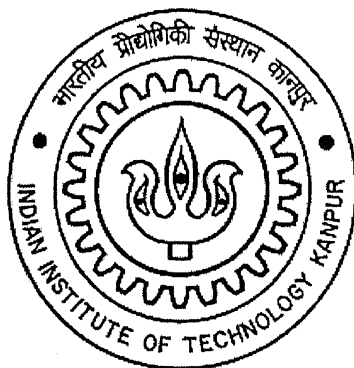# DEVELOPMENT AND CHARACTERIZATION OF TiB_2 BASED MATERIALS FOR HIGH TEMPERATURE APPLICATIONS

A THESIS SUBMITTED

IN PARTIAL FULFILMENT OF THE REQUIREMENTS FOR THE DEGREE OF MASTER DEGREE TECHNOLOGY
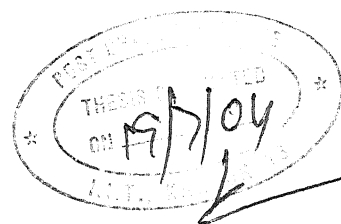
By

T.S.R.Ch. Murthy

ROLL NO. Y210628

Guides: *R.Balasubramaniam*
Bikramjit Basu
Ashok Kumar Suri

TO THE

DEPARTMENT OF MATERIALS AND METALLURGICAL ENGINEERING

INDIAN INSTITUTE OF TECHNOLOGY – KANPUR

July 2004

CERTIFICATE

This is to certify that the work contained in the thesis entitled "Development and characterization of TiB_2-based materials for high temperature applications" by T.S.R. Ch. Murthy (Roll No. Y210628) has been carried out under our supervision and to the best of our knowledge, this has not been submitted elsewhere for a degree.

(Dr. Bikramjit Basu)
Asstt. Prof.
IIT-Kanpur

Prof. R. Balasubramaniam
Professor
IIT-Kanpur

Dr. A.K. Suri
Asso. Dir. (P)
Materials Group
& Head, MPD, BARC

Dedicated to ....

Late Prof. V.S.R. Murthy and my Parents

ACKNOWLEDGEMENTS

Table of contents

Abstract

TiB_2 is a potential candidate material for high temperature structural and nuclear applications due to the attractive combination of properties e.g. high melting point, high thermal and electrical conductivities, high elastic modulus, high hardness, good corrosion resistance and high neutron absorption cross-section. Despite having useful properties, the application of monolithic TiB_2 is rather limited due to poor sinterability, exaggerated grain growth and poor oxidation resistance. To overcome this problem, various metallic and nonmetallic binders have been used to obtain dense borides. An extensive research has been reported on the role of metallic binders (e.g. Ni, Fe, Co) on the densification of TiB_2 and >99% theoretical density (ρ_{th}) was achieved by liquid phase sintering. However, the presence of metallic binder is not desirable for high temperature structural applications. Therefore studies have also been carried out with non-metallic additives to improve sinterability and also to retain mechanical properties at high temperature with good oxidation resistance. Several nonmetallic additives such as AlN, ZrO_2, SiC, Si_3N_4, CrB_2, B_4C, TiC, TaC, WC, TiN, ZrN, ZrB_2 were used for attaining the densification of TiB_2 with good mechanical properties. However, critical literature analysis reveals that most of the earlier work concentrated on developing TiB_2 sintered with ceramic binders for room temperature applications.

Considering the importance of high temperature applications and the difficulty in sintering of TiB_2 materials, the present work was undertaken to develop TiB_2-$MoSi_2$ composites. Both hot pressing as well as pressureless sintering was attempted for densification. $MoSi_2$ was selected because of its high thermal conductivity and good oxidation resistance at high temperature. The densification results indicated that > 97% ρ_{th} can be obtained with 10 wt. % $MoSi_2$ at 1700°C. The sintered microstructure was characterized by homogeneous distribution of $MoSi_2$ in a fine TiB_2 matrix (grain size ~ 2-3 microns). $TiSi_2$ is a limited reaction product of TiB_2 and $MoSi_2$ was identified in TiB_2-20 wt % $MoSi_2$ composite by using XRD. It was further confirmed with EPMA and TEM (EDS and spot pattern). Vickers hardness of the TiB_2-10 wt % $MoSi_2$ composite was around 24-26 GPa. Fracture toughness of the developed composites was in the range of 4 to 5.5 $MPa.m^{1/2}$. Additionally, the thermal property data were acquired using LASERFLASH thermal diffusivity measuring system and electrical conductivity was obtained using four probe methods. The experimental measurements had revealed that the newly developed materials have high thermal (~60 W/m/k) as well as high electrical conductivity (~10^4 order).

The objective of the tribology study is to analyze the role of $MoSi_2$ addition and load on the fretting wear of TiB_2 and TiB_2-$MoSi_2$ composites. The friction and wear properties of TiB_2-$MoSi_2$-/steel contacts are studied under fretting contacts with variation of load and compared to those of monolithic TiB_2/steel contacts. Low coefficient of friction (COF) (0.11) is recorded in case of TiB_2-10 wt. % $MoSi_2$ composite at 10 N load, while 0.5 COF recorded in case of monolithic TiB_2 and TiB_2-20 wt. % $MoSi_2$ composite. TiB_2–10 wt % $MoSi_2$ composite exhibits significantly low wear volume and highest wear resistance. Detailed microstructural investigation was done in order to understand the fretting wear mechanism on the worn surfaces of TiB_2 and its composites using SEM with EDS. Elemental X-ray mapping is also performed on monolithic TiB_2 worn surfaces. TiB_2-10 wt % $MoSi_2$ exhibits mild wear due to the formation of lubricate nature, continuous and stable tribooxide layer during fretting. Severe wear is observed in case of monolithic TiB_2 and TiB_2-20wt % $MoSi_2$ composite. It is due to domination of adhesive and abrasive wear mechanisms.

As TiB_2 is a potential candidate material for high temperature applications, the thermal stability of monolithic TiB_2 needs to be studied. The oxidation of TiB_2 can exert a negative influence on the mechanical and physical properties and on the performance of components made of these ceramics. The isothermal oxidation behavior of monolithic TiB_2 and TiB_2–20 wt % $MoSi_2$ composite has been evaluated at $850^\circ C$ in air. The monolithic TiB_2 exhibited continuous weight gain with increasing time. The TiB_2-$MoSi_2$ composite showed continuous weight gain till 16h and afterwards the weight gain decreased markedly. The weight loss observed in composite after 16h has been related to the formation and subsequent vaporization of MoO_3. The surfaces of the oxidized samples were characterized by XRD and SEM with EDS. The XRD analysis indicated that the predominant phase present in the oxide was TiO_2 (rutile). The cracking of the surface scales on oxidized surfaces was observed for the composite and monolithic TiB_2. Elemental compositional analysis across oxide cross section of the 64 h oxidized samples indicated enrichment of B_2O_3 on the surface of TiB_2 and SiO_2 in the case of the composite.

LIST OF FIGURES

ix

obtained from the middle of the image in (a)

LIST OF TABLES

CHAPTER 1
INTRODUCTION

It is well recognized that the progress of human civilization is intimately connected with the availability and development of two major resources – materials and energy. What is perhaps less appreciated is the inextricable relation between materials development and energy generation. This interdependence has been continuously growing and it is engineering materials that hold the key to the large-scale production of any form of energy. Among the engineering materials, high temperature ceramics like borides, carbides, nitrides had received wider attention in the past two decades.

1.1 High Temperature Materials

Because of high refractoriness and high strength retention at elevated temperature, structural ceramics are well appreciated in high temperature application [1]. To this end, titaniumdiboride (TiB_2) is one of the materials of growing interest in the materials community [2]. Moreover, it is anticipated that TiB_2 will be the base material for a range of new high performance materials [3]. TiB_2 is a refractory compound with many attractive properties including exceptional hardness ($\approx$ 25-33 GPa at room temperature) up to high temperatures, high melting point, good creep resistance, good thermal conductivity (65 W m^{-1} $°C^{-1}$), high electrical conductivity and considerable chemical stability. When compared to the most commonly used hard materials, TiB_2 (33.38 GPa) is harder than TiC (31.52 GPa), WC (23.29 GPa) and TiN (19.80 GPa) [3]. TiB_2 is considered as an interesting material because it is very similar to TiC, an important base material for cermets, in many of its properties, namely hardness, thermal conductivity, electrical conductivity [7] and its oxidation resistance is better than that of TiC [4,5,6,7]. The unique combination of properties, as mentioned above, makes TiB_2 a candidate material for heavy duty wear applications, in particular at elevated temperatures.

With respect to the chemical stability, which can be a decisive factor in high temperature applications, TiB_2 is more stable in contact with pure iron than WC and Si_3N_4. It can be noted that TiB_2-based materials should be preferred over WC-based materials for high temperature applications. The chemical inertness at high temperatures

and the good electrical conductivity of TiB_2 (electrical resistivity $\approx 13 \times 10^{-8}$ Ωm) make it an excellent candidate for special electrical applications, e.g. cathodes used in aluminium electrosmelting or vaporising elements for vacuum metal deposition installations [8].

The relatively low fracture toughness of monolithic TiB_2 (≈ 5 MPa m$^{1/2}$) and its sensitivity to slow subcritical crack growth, however, limits its use in many engineering applications [9]. Pure TiB_2 is also very difficult to densify, due to low coefficient of diffusivity (due to predominant covalent bonding). All these shortcomings have triggered considerable research work to improve both toughness and sinterability [10,11].

One of the avenues to improve the sinterability/toughness of the boride/carbide materials had led to the development of an important class of structural materials, popularly known as cermets* [12,13]. In Japan, much attention has been focused on the development of cermets. About 40 % of all cutting tools in Japan are based on TiC and Ti(C,N) [14]. The first generation of cermets was a titanium carbide-molybdenum carbide (TiC-Mo$_x$C) solid solution with a nickel binder phase. In the early seventies, titanium carbonitrides Ti(C,N) were introduced. The latest generation of cermets are very complex: commercial materials made of Ti(C,N), Mo$_x$C, VC, WC, TaC and NbC with a nickel-cobalt binder [14,15,16]. The further development of cermet materials is supported by an intensive research towards the production of boride/carbide/carbonitride starting powders with finer particle sizes. A commercial production process using a recently patented process based on self-propagating high temperature synthesis (SHS) produces high purity submicron (≈ 0.5 μm) grained TiB_2 powders [15]. Recently some Indian researchers have also reported the synthesis of fine boride powders [16]. A production route to obtain gram quantities of nanometer sized TiB_2 powder is now feasible [17]. Commercial availability of fine boride powders is typically preferred in order to obtain better densification and superior mechanical properties.

---

* Theoretically, all ceramic materials with a metal binder are classified as cermets, including the cemented carbides. However, the cutting tool industry considers only the TiC, Ti(C,N) and TiB_2 based materials to be cermets, while the WC based materials are classified as cemented carbides.

Cemented borides with a metallic binder have recently been developed in the TiB_2-Fe system [18]. Compared to WC-based hardmetals, this possesses higher hardness at 16-20 vol. % Fe-binder content. Bending strength of 550-900 MPa and fracture toughness of 6-10 MPa m$^{1/2}$, however, are still lower than for the commercial hardmetals (WC-Co) with intermediate binder contents. The TiB_2-based materials will contain TiB_2 as a major phase, bonded with non-metallic phase (silicides, carbides) and metallic phase (Co/Ni). These materials will form a novel lower density (having potentially higher hardness) substitute for the WC/Co system.

As reinforcement, TiB_2 is also incorporated in several ceramic microstructures to obtain improved structural and mechanical properties. The addition of TiB_2 to an Al_2O_3 or Si_3N_4 matrix greatly increases their hardness, strength and fracture toughness [19]. In addition, these composites can be used as wear parts, cutting tools and heat exchangers. TiB_2 as well as TiN or TiC are not only used to toughen Al_2O_3 and Si_3N_4 matrices, but are also used to obtain electro conductive materials [19]. These electro conductive toughened ceramics can be shaped by electro discharge machining (EDM) to manufacture complex components, largely increasing the number of industrial applications of these ceramic materials. Thus, it is evident that complex shaped engineering components can be machined out of the sintered TiB_2-based materials with non-metallic additives.

Since densification of borides has been a major challenge, the fundamentals of sintering theory are discussed in the following section.

1.2 Sintering of Ceramics

Ceramic processing is based on the sintering of powder compacts rather than melting /solidification/cold working widely used for metallic alloys and some polymers. This is due to the following reasons:

- Ceramics melt at high temperatures ($T_m \geq 2000^{\circ}C$)
- As-solidified microstructures can not be modified through additional plastic deformation and recrystallisation due to brittleness of ceramics.
- The coarse grains, if present in the microstructure, would act as fracture initiation sites.

- Low thermal conductivities of ceramics (<30-50 W/m/K), in contrast to high thermal conductivity of metals (in the range 50-300 W/m/K) cause large temperature gradients, resulting in thermal stress and shock during melting/solidification of ceramics.

However, some ceramic refractories, such as Al_2O_3, Al_2O_3/ZrO_2, can be manufactured through the melting/casting/solidification process. If made properly, they are superior to the sintered. The processing costs of large, ~ 1 m tall blocks, is lower [20].

Sintering commonly refers to processes involving heat treatment of powder compacts at elevated temperatures, usually at $T>0.5\ T_m$ [in Kelvin], i.e. in the temperature range where diffusional mass transport is appreciable. Successful sintering usually results in a dense polycrystalline solid. However, sintering can proceed only locally (i.e. at contact point of grains), without any appreciable change in the average overall density of a powder compact. Schematic illustration of three sphere sintering model is shown in Fig. 1.1.

Sintering is not only used to densify ceramic materials, but also used to produce powder metallurgy (P/M) products including refractory metals like W, Ta etc. In the production of small metal objects, it is often not practical to cast them. Through chemical or mechanical procedures, a fine powder of the material can be produced. When the powder is compacted into the desired shape and heated, i.e., sintered, for up to three hours, the particles composing the powder join together to form a single solid object.

Ceramics can not be fabricated either by melting or mechanical forming, since they possesses high melting point and highly brittle. So ceramics can be fabricated by sintering with or without applying external pressure. Moreover near net shapes can obtained with sintering. High pure ceramics or composites can produce with 100% yield by sintering.

The principal variables that control shrinkage at all stages of sintering are: temperature, time, pressures, particle size, chemical composition of starting powder mixture, and the sintering environment.

1.2.1 Basic Thermodynamics of Sintering

The driving force for sintering is the overall decrease in the surface free energy of powder compacts. Thermodynamically, sintering is an irreversible process in which a

free energy decrease is brought about by a decrease in surface area i.e. by replacing solid-vapour interfaces (surface energy Γ_{sv}) with solid-solid interfaces (Γ_{ss}), where $\Gamma_{ss} < \Gamma_{sv[}$ [20].

For typical specific surface area (S) of ceramic powders, S=1-10 m^2/g and Γ_{sv}=1-2 J/m^2, the resulting excess in surface energy of Γ_{sv}=1-20 J/g is small compared with the heat of chemical reactions (>1 KJ/g), but still sufficient to drive the sintering processes. Some mechanisms can lead to a change of sintering driving force without assisting densification. These are the grain coarsening mechanisms, which are driven by the same force as sintering.

The change in system energy dE due to sintering is composed of an increase due to the creation of new grain boundary areas, $dA_{ss} > 0$, and due to the annihilation of vapour-solid interfaces, $dA_{sv} < 0$. The necessary global thermodynamic condition for the sintering to proceed is:

$$dE = \Gamma_{ss}\, dA_{ss} + \Gamma_{sv}\, dA_{sv} < 0 \qquad\qquad (1)$$

Sintering process will stop when dE= 0, i.e. $dE = \Gamma_{ss}\, dA_{ss} + \Gamma_{sv}\, dA_{sv}$=0 or $\Gamma_{ss}/\Gamma_{sv} = -dA_{sv}/dA_{ss}$

At the start of sintering, all surface area equals the free surface area, since no grain boundaries exist, $A_{sv} = A_{svo}$ and $A_{ss}= 0$. As sintering proceeds, A_{sv} decreases and A_{ss} increases, in such a way that a monotonically decreasing curve is obtained with the slope $- dA_{sv} / dA_{ss}$. If, at any point during sintering, the value of the slope reaches Γ_{ss}/Γ_{sv}, the sintering must stop due to the above equilibrium condition. The principal objective of sintering is the elimination of porosity, i.e. a minimum A_{sv}, possibly $A_{sv} = 0$ and A_{ss} large, meaning little grain growth. It is thus desirable that the maximum densification condition is reached when the slope dA_{sv}/dA_{ss} close to zero, i.e. Γ_{ss}/Γ_{sv}. Through this type of thermodynamic considerations it is suggested that sintering can be encouraged through manipulation of the doping and/or the environment, so the surface energy is maximized [20].

It can be note that the global decrease of system free energy is a necessary, but not sufficient, condition for sintering. The sintering process will proceed only if driven by the local differences in chemical potential due to differences in curvatures between the grain and the neck.

1.2.2 Classification of sintering

The majority of non-silicate ceramics are processed through high-temperature treatment and sintering of powder compacts with little (<2 vol %) or no liquid phases. This is defined as solid state sintering, with predominant mass transport (i.e. densification mechanism) through solid-state diffusion. In case of Solid-state sintering, the densification is achieved through changes in particle shape, without particle rearrangement or the presence of liquid. However, most silica containing ceramics, including traditional porcelains as well as advanced silicon nitride, sinter in the presence of viscous glass-type liquids, with predominant mass transport (i.e. densification mechanism) through viscous flow. This is defined as viscous sintering. If the liquid component of the sintering system has low viscosity (e.g. molten cobalt in the "classical" system of WC/Co), the process is defined as liquid sintering. In this system, the predominant densification mechanism is through rearrangement of the solid particles "submerged' in and wetted by the low viscosity liquid, followed by dissolution and re-precipitation of the solid.

The development of microstructure and densification during sintering is a direct consequence of mass transport through several possible paths with one of these paths usually predominant at any given stage of sintering:

- Gas phase (evaporation/condensation)
- Liquid phase (solution/precipitation)
- Solid phase (lattice diffusion)
- Interfaces (surface diffusion, grain boundary diffusion)
- Viscous or plastic flow, under capillary pressure (internal) or externally applied pressure (pressure-sintering, hot-pressing, hot-isostatic pressing)

Since certain mechanisms of mass transport can be dominant in some systems, two broad categories of sintering are recognized. The second is liquid-phase sintering, where some liquid forms at sintering temperatures and subsequently aids in consolidation. The grain rearrangement occurs in the initial stage, followed by a solution-reprecipitation stage. In many instances, solid state sintering may proceed in the presence of previously undetected (or transient) small amounts of liquid (perhaps introduced as impurities during the powder preparation stage, such as silicates in oxide ceramics Al_2O_3, ZrO_2) [20].

Liquid phase sintering is effective for difficult-to-sinter ceramics, because it accelerates mass transport enormously. A small wetting angle for liquid phase sintering is required in order that wetting occurs efficiently and faster. It is critical that the liquid phase wets the solid phase, so that wherever contacts have developed between particles, or the grain boundary presents, the liquid can penetrate and replace the grain boundary with liquid. The criterion for this is simply that $2\gamma_{sl} < \gamma_{gb}$ [20], where γ_{sl} is solid-liquid interfacial energy, γ_{gb} is grain boundary interfacial energy. Liquids also allow for particle rearrangement by effectively lubricating the particles so that they can slide past one another. Elimination of voids is accelerated if the solid can dissolve in the liquid phase, to a limited extent. Diffusion rates in liquids are typically three to four orders of magnitude faster than in solids.

Stages of Sintering

Simple model experiments with spheres or rods illustrate sintering phenomena, and the three stages of sintering are discussed below.

1. **Initial stage of sintering**

At the initial stage, the following processes take place:

a) Local point of contact formation or fusion, without shrinkage of compact. This is accompanied by smoothing of the free surface of particles.

b) Neck formation at the contact point, with the resulting concave curvature δ_n (where $\delta_n = 1/r_n$) at the neck, in contrast to the convex curvature on the particle surface of radius r, where $r >> r_n$. The two radiuses of the neck curvature, r_n and r, represent an experimental justification for the two-sphere model of sintering.

The above processes result in densification of the sintering component by ~10%. That is, if the relative green density after forming of the particle compact was 60%, the density after initial stage would be about 70% of the theoretical density (TD). However, the 10% densification in the initial stage is reached very quickly (seconds or minutes) after exposing powder to high temperature, because of the large surface area and the high driving force for sintering. Five mass transport mechanisms, with respect to initial stage (neck formation) are represented in the Fig.2. These mechanism are vapor transfer, boundary diffusion, surface diffusion, bulk diffusion and dislocation diffusion.
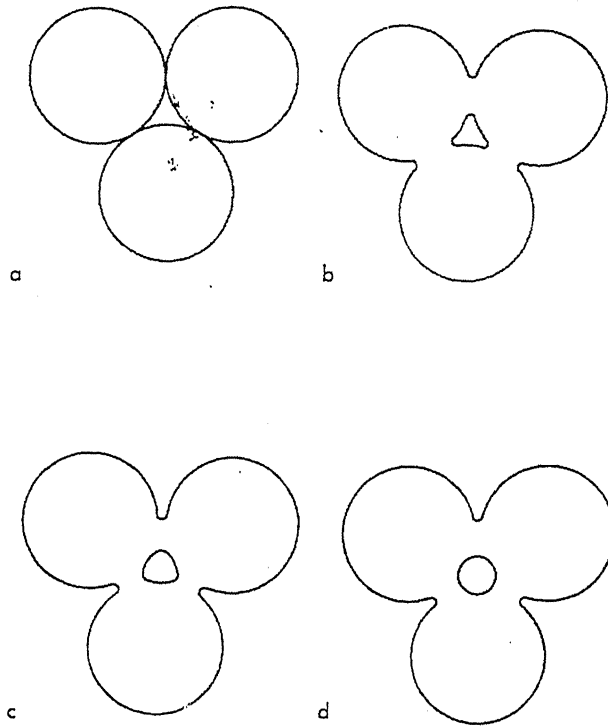
Fig. 1.1: Schematic illustration of three sphere sintering model: (a) original point contacts, (b) neck growth, (c) and (d) pore rounding [21]
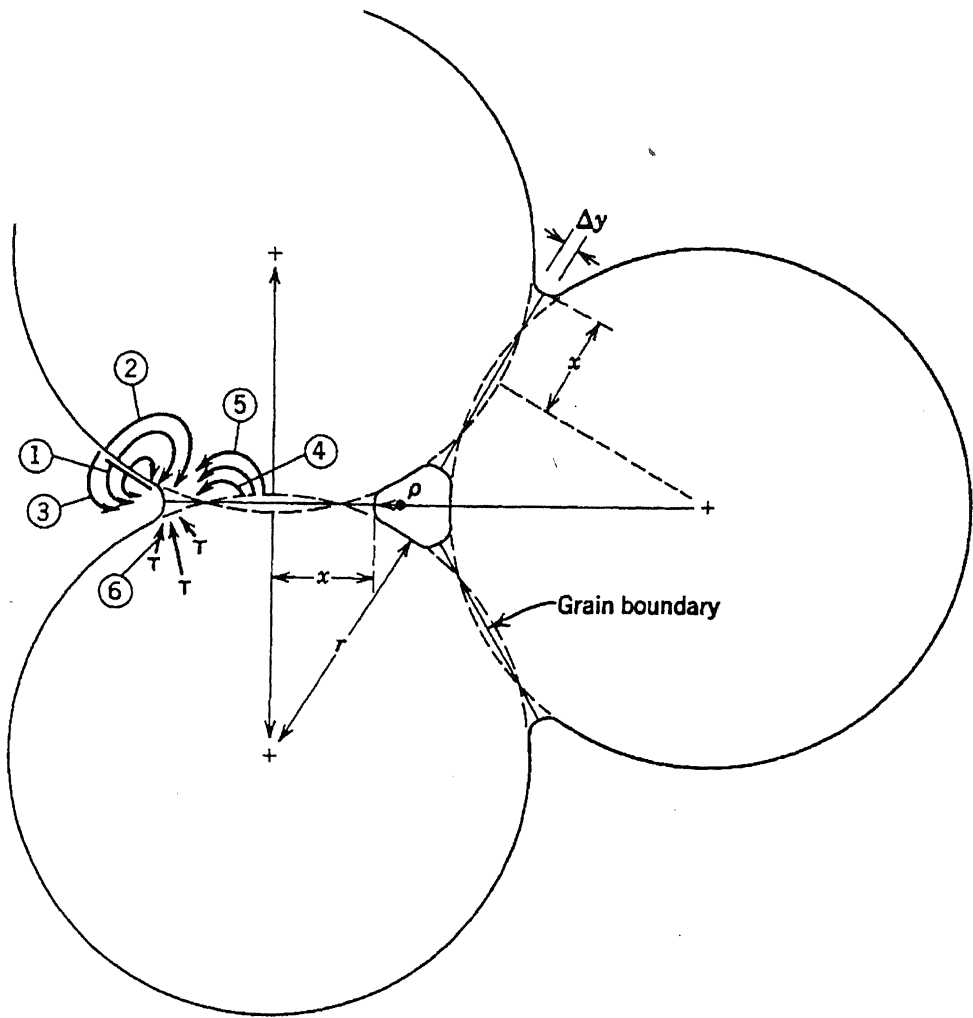
1. Vapor transfer 2. Boundary diffusion (grain boundary) 3. Surface diffusion 4. Bulk diffusion
5. Dislocation diffusion

Fig. 1.2: Various paths for matter transport during the initial stage of sintering

2. Intermediate stage of sintering

The physics of the process involves:

a) neck growth,

b) pores forming arrays of interconnected cylindrical channels

c) particle centers approaching one another, with the resulting compact shrinkage.

The shrinkage in the intermediate stage can result in additional densification by as much as 15-20%, or to a total of maximum~90% of TD (theoretical density). However, shrinkage does not necessarily have to take place during the intermediate stage of sintering. For example, shrinkage would not occur if matter was transported from the particle surface, and preceded through either gas, solid or along interface as surface diffusion.

Densification in the intermediate stage takes place only if mass is transported from the particle volume, or mass is transported from the grain boundary, and proceeds through the solid as volume diffusion or along a boundary as grain boundary diffusion towards the neck forms between the sintering particles.

The origin of mass transport during sintering determines the ability of the compact to shrink and eliminate porosity. There are material systems where sintering proceeds vigorously through evaporation/condensation or through surface diffusion, without any shrinkage of the compact. In most cases this is an undesirable phenomenon, whenever residual porosity is undesirable. In some systems e.g. recrystallised SiC, this technique of bonding ceramic particles is acceptable.

3. Final stage of sintering

In the final stage, the following processes take place:

a) Isolation of pores, i.e. relative density exceeding – 93%

b) Elimination of porosity

c) Grain growth

The final sintering stage begins at about ~90% of TD, when the pores are already isolated. Ideally, at the end of this stage all porosity is eliminated. The complete elimination of porosity in the final stage of sintering can only happen when all pores are connected to form fast, short diffusion paths along grain boundaries (or, equivalently, if the grain boundaries remain attached to the pores).

This favorable situation happens only if the pores follow the movement of the grain boundaries and are not trapped within grains. This means that discontinuous grain growth (i.e. few grains growing at a very large rate at the expense of all other grains, trapping porosity on its path) is suppressed through grain growth limiting additives, such as secondary phase particles at grain boundaries, and/or appropriate time and temperature control of the sintering process.

In the final stage of sintering, small pores attached to grain boundaries move quickly to collapse together and thus reduce surface energy. Along with pores, grain boundary movement is accelerated, leading eventually to discontinuous grain growth, when pores do not pin any more the grain boundaries. This leads to rapidly moving grain boundaries that consume small grains.

Thus, some grains appear with many highly curved sides and therefore, grain boundary motion further accelerates, leaving behind closed porosity that is trapped within large grains. Closed porosity is difficult to eliminate, because it involves relatively slow diffusion through lattice of the gas trapped in the pore. The critical grain size r_c at which discontinuous grain growth starts can be expressed as $r_c=r_p/f$, where r_p and f are the average pore radius and pore volume fraction respectively.

Pores trapped within large grains are much more difficult to eliminate in the final sintering stage, because diffusion paths are long and slow, because lattice diffusion is the rate controlling step. Moreover, trapped gas resists the densification. The closed porosity at the final sintering stage allows external gas pressure to be applied isostatically in order to accelerate the final densification. This approach is commercially known as gas pressure sintering (GPS).

During sintering, if the only material transport mechanism originates on the surface of particles, no compact shrinkage takes place. In such a case, change of the shape and size of pores and particles is observed, and commonly defined as grain growth or coarsening. Grain growth/coarsening deplete the surface energy and effectively inhibit the densification of the compact, even if mass transport mechanisms other than evaporation/condensation or surface diffusion become operational. Optimally, the coarsening process decreases the driving force for sintering and therefore the sintering rate, expressed as shrinkage versus time, decreases in the intermediate stage. The driving force, which propels sintering (i.e. elimination of excessive surface energy) also leads to

grain growth during sintering. In this process, larger particles grow at the expense of smaller particles, according to the following expression;

$$R^n - r_0^n = k\,\Gamma_{sv}\,t \qquad\qquad (2)$$

where r is average particle size after time t, r_0 = initial average particle size at t=0, Γ_{sv} = surface energy, k, n = constants, n= 3 to 4. The growth of large grains at the expense of small grains is defined as Ostwald ripening, with the grain size $\infty\ t^{1/3}$.

1.2.3 Mechanisms of mass transport and neck growth in solid state sintering

A macroscopically measured quantity (for example by dilatometer), indicative of densification during sintering is the compact shrinkage $\Delta L/L$. For the idealized model of a dense uniform arrangement of spherical particles of radius r, the relative centers approach by h/r, which is equal to the overall shrinkage of the compact $\Delta L/L$. In real systems, these quantities are generally not equal, because of particle shift and rearrangement, formation and break-up of contacts, and interactions with porosity [20].

a. The mass transport from surfaces: evaporation-condensation

The mass transport can proceed through a gas phase, driven by a differential in vapour pressure. Evaporation-condensation takes place because the vapour pressure p_1 on a curved surface of radius r_1 is different from that on a flat surface (p_0, $r_0 = \infty$) or any other surface at r_2. This is expressed by the Kelvin equation:

$$\ln(p_1/p_2) = (\Omega\,\Gamma_{sv}/\,RT)(1/r_1 + 1/r_2) \qquad\qquad (3)$$

where Ω is the molar volume of the species. For simple case of $r_2 = r_0 = \infty$ and $p_2 = p_0$ (that is, for a flat surface), the above equation simplifies to:

$$\ln(p_1/p_2) \approx (p_1-p_0)/p_0 = \Delta p/p_0 \qquad\qquad (4)$$

Therefore $\qquad\qquad \Delta p/p_0 = (\Omega\,\Gamma_{sv})/(RT\,r_1) \qquad\qquad (5)$

Accordingly, convex surfaces show overpressure ($r_1 > 0$, $\Delta p > 0$), whereas concave surfaces show under pressure ($r_1 < 0$, $\Delta p < 0$). The pressure gradient results in faster evaporation from convex surfaces (i.e. from grains, especially small grains), transport under the pressure gradient, and condensation within concave surfaces (i.e. within necks). Quantitatively, the effect is not large. For example $\Delta p/p_0 = 1.02$ for SiO_2 of $r_1 = 10^{-7}$ m (0.1 μm) at 1700°C.

The most important case of evaporation-condensation mass transport is from the surface of convex (spherical) particles ($r>0$) to the surface of concave necks ($r_n <0$) where $|r_n| << |r|$ at the contact region. No shrinkage occurs in this process and y^3 is a linear function of time:

$$y^3 = \alpha_2 t \text{ and } h/r = \Delta L/L = 0 \qquad (6)$$

where y is mass transport rate, α_2 is constant.

This type of transport dominates at the relatively high vapor pressures of 10^{-4} atmospheres, found for halides (e.g. NaCl at 700°C). The log-log plot of the neck size versus time has a slope close to 1/3. The evaporation condensation process is expected to stop the sinterability of some non-oxide ceramics (such as SiC, B_4C) at very high temperatures $>2100^\circ$C.

b. The model for mass transport from surfaces: surface or volume diffusion from surface

Similar to evaporation/condensation, no shrinkage results from the other two mechanisms of mass transport from particle surfaces to necks through the two possible diffusion paths.

a. Volume diffusion from particle surfaces to necks:

$$y^4 = \alpha_3 t \text{ and } h/r = \Delta L/L = 0 \qquad (7)$$

where α_3 is volume diffusion constant.

b. Surface diffusion, along particle surfaces to necks:

$$y^7 = \alpha_4 t \text{ and } h/r = \Delta L/L = 0 \qquad (8)$$

where α_4 is surface diffusion constant.

c. The model for mass transport from within the particle volume or from the grain boundary

For mass transfer originating in the particle volume or at the grain boundary, the particle centers approach ($h>0$) and shrinkage takes place.

a) for volume diffusion from grain boundary:

$$y^5 = \alpha_5 t \text{ and thus } (h/r)^{2.5} = (\Delta L/L)^{2.5} \qquad (9)$$

b) for grain boundary diffusion from grain boundary:

$$y^6 = \alpha_6 t \text{ and } (h/r)^3 = (\Delta L/L)^3 \qquad (10)$$

All the above models explain the kinetics of diffusion. The swelling or shrinkage of sample depends on the dominant mass transport mechanism. These models are helpful to estimate the densification mechanism during sintering process.

1.2.4. Sintering kinetics

The sintering kinetics is accelerated for fine grained materials (high surface energy) or at elevated temperatures. The powder composition and sintering atmosphere intervene in the densification through modification of the diffusion coefficient (D). However, increasing the temperature far beyond $T = 0.5 \, T_m$ does not guarantee an increased sintering rate and full densification. This is due to the coarsening of grains (as explained above through evaporation/condensation and surface diffusion) that can effectively stop densification (compaction through volume diffusion and grain boundary diffusion).

Typically, ceramics are composed of at least two elements (typically oxygen, boron or nitrogen and metal ions) and both ionic species must diffuse together to maintain the electrical neutrality of the system. Therefore, it is the diffusion coefficient of the slowest moving ion along its fastest path that controls mass transfer, and therefore densification during solid state sintering. To enhance sintering, the slowest moving ion must be identified and its diffusion along the fastest path should be "encouraged" through:

- chemical doping,
- atmospheric control
- an appropriate time/temperature cycle
- external pressure (in case of hot pressing or HIP)

For an example, consider sintering of silicon carbide. The pressureless sintering of SiC requires B and C as additives, which affect the relative diffusion coefficients. The formation/presence of silica in SiC can enhance evaporation-condensation mechanisms through a volatilization reaction:

$$SiO_2 \text{ (solid)} + SiC \text{ (solid)} \rightarrow SiO \text{ (gas)} + CO \text{(gas)} \quad (11)$$
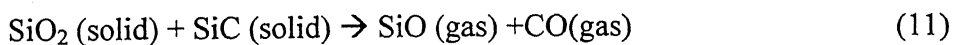
Carbon removes SiO_2 and Si from the surface of SiC according to the carbothermal reduction reaction:

$$SiO_2 + 3C \rightarrow SiC + 2CO \quad (12)$$

$$C + Si \rightarrow SiC \quad (13)$$

14

Thus, fewer defects are present at the surface and diffusion along the surface decreases. This slows down the coarsening mechanisms. Simultaneously, boron has been found to selectively segregate towards grain boundary regions, where its role is unclear, i.e. it is expected that it lowers the grain boundary surface energy Γ_{ss} and thus increases the macroscopic driving force Γ_{sv}-Γ_{ss}. This introduces additional defects (silicon vacancies) and enhances grain boundary diffusion.

Liquid phase sintering

Liquid phase sintering refers to those cases for which the sintering temperature is high enough so that one or more components of the material is present as a liquid during all or part of the sintering process. In the majority of cases, the use of liquid phase sintering is to produce a very high density sintered material with little residual porosity. That is, substantial densification is usually associated with liquid phase sintering [21].

Stages of Liquid phase sintering:

The first stage has been termed "rearrangement" or "liquid flow" and corresponds to the large scale bulk movement of particles within the liquid phase. This movement leads to a rearrangement of the particles and densification.

The second stage has been termed "accommodation" or "dissolution and reprecipitation" and can only take place if there is limited solubility of the solid in the liquid phase. It too leads to densification, but at a slower rate than the first stage. Because the solubility of the solid in the liquid increases with increasing convexity (decreasing particle size), small particles dissolve and disappear, while the larger ones grow and take on a rounded shape.

The third stage is termed "coalescence" or "solid phase bonding." If wetting of the solid with the liquid is incomplete, then there is some contact between solid particles, rather than complete separation of the particles by the liquid.

1.3 Tribological properties

Tribology is broadly defined as the science and technology of interacting surfaces in relative motion. The fundamental point to be noted here is that tribology is a system dependent property. It encompasses study of friction, wear and lubrication. Tribology is known for its positive aspects (polishing and soldering by friction) as well as for its negative aspects (wear and wear particles, vibration and noise, reduction of useful tool life, and system reliability).The importance of tribological study in controlling of wear and its consequences could lead to an enormous economic benefit.

The following factors influence the tribological properties of a system:

- equipment used (contact geometry)
- materials in contact
- surface treatment undergone
- normal force applied, F_n
- normal Hertzian contact pressure, P_a
- slide distance
- time t (or number of cycles, frequency)
- sliding speed V
- ambient or test temperature T
- atmosphere and relative humidity RH %
- area of contact
- physico-chemical state of surfaces in friction (roughness, oxide layers)
- crystallographic structure and mechanical properties of the material (hardness)
- absence or presence of a lubricant
- presence of active agents in friction (anti-wear additives)

One of the important industrial aspects of tribology is to study the lubrication behavior of different tribological components. The principal role of a lubricant is to reduce friction and wear by introducing a film between surfaces that are in relative movement to each other. Lubricants may be solid, liquid or gas. Lubricants should contain the following properties.

- low shear strength
- high viscosity

16

- high thermal conductivity
- inert (does not react)
- provides chemical protection against corrosion

Solid lubricants: The solid lubricants, a class of inorganic soft nonmetals, include molybdenum disulfide (MoS_2), graphite, talc, and other inorganic salts. MoS_2 and graphite have lubricating abilities because of their layered lattice structure. In MoS_2, low shear strength is an intrinsic property, whereas in others, notably graphite, the presence of adsorbed gases or impurities between the basal planes appears to be necessary to develop desirable friction properties. The maximum temperature of lubrication with MoS_2 and graphite in air atmosphere is limited by oxidation to about 315^0C and 430^0C, respectively [22]. Soft solid lubricants (MoS_2, graphite, and PTFE) are also used as additives in oils, greases, polymers, and other solid materials.

The friction force (F) is proportional to the applied load (W) as per the relation

$$F = \mu W \qquad (14)$$

where μ is coefficient of friction. Friction force is independent of apparent area of contact. Frictional force does not depend on velocity (not always so: static μ usually greater than sliding μ). Friction is well characterized enough to make a reasonably "stable" parameter to measure for given materials under given conditions.

1.3.1 Wear

Wear is defined as the continuous removal of materials from contacting surfaces in relative motion. Typically wear is quantified with wear rate. Wear rate means volume worn or depth of wear per unit load and unit traversed distance. Based on wear rate or intensity of wear, one can judge the whether it is a mild or severe wear. Wear is a consequence of friction, and occurs at the zone of contact. The parameters that influence wear include:

- Surface interactions at asperities
- Displacement of material and altering the surface properties.
- Removal of material either to other counter body or in the form of wears debris or formation of third body at interface.
- Although definition is based on material loss or material damage with no net change in weight or volume also called wear.

- Wear mechanical/chemical process accelerated by frictional heating

Depending on the quantity of material lost by an active element in a tribosystem, can distinguish the following classes of wear:

- **Mild or ultra- mild wear**: where the system is worn away very little, the surfaces remain smooth, and the particles have dimensions of the order of micrometers.

- **Severe wear**: where the body surfaces are changed and the size of the particles exceeds 100 microns.

- **Catastrophic wear**: where the life expectancy of the machine is reduced enormously.

Wear debris are particles which become detached from a worn away surface, during the process of wear.

1.3.2 Wear Mechanisms

Wear occurs by mechanical and/or chemical means and is generally accelerated by frictional heating. Principal wear mechanisms include (1) adhesive, (2) abrasive, (3) fatigue, (4) impact by erosion and percussion, (5) chemical, and (6) electrical-arc-induced wear. Other, but not distinct, mechanisms are fretting and fretting corrosion, a combination of adhesive, corrosive, and abrasive forms of wear. Wear by all mechanisms, except by fatigue mechanism, occurs by gradual removal of material. Of the aforementioned wear mechanisms, one or more may be operating in one particular machine. In many cases, wear is initiated by one mechanism and it may proceed by other wear mechanisms, thereby complicating failure analysis.

In brief, adhesive, abrasive and chemical wear are the fundamental wear mechanisms, which can explain other wear process, such as fretting. This fretting is a common occurrence, since most machinery is subjected to vibration, both in transit and in operation. In the following, the physics and mechanisms of wear process are discussed individually.

Adhesive wear:

Adhesive wear occurs because of adhesion at asperity contacts at the interface. These contacts are sheared by sliding, which may result in detachment of a fragment from one surface to another surface. As the sliding continues, the transferred fragments may come off the surface on which they are transferred and be transferred back to the original surface, or else form loose particles. The formation of loose particle is another

reason for wear of material. The wear volume can be calculated by using Archard's equation, where volume of wear (υ) of contacts going through plastic deformation is proportional to normal load (W) and sliding distance (x) inversely proportional to the hardness (H) of the surface being worn away.

$$\upsilon \propto \frac{1}{3}\frac{Wx}{H} = \frac{kWx}{H} \tag{15}$$

Several mechanisms have been proposed for the detachment of a fragment of a material. In an early theory of sliding wear (still well recognized), it was suggested that shearing can occur at the original interface or in the weakest region in one of the two bodies (Figure 1.3) [23].

In most cases, interfacial adhesion strength is expected to be small as compared to the breaking strength of surrounding local regions. Thus, the rupture during shearing occurs at the interface (path1) in most of the contacts and no wear occurs in that sliding cycle. In a small fraction of contacts, the rupture may occur in one of the two bodies (path 2) and a small fragment (shaded region in the figure) may become attached to the other surface. These transfer fragments are irregular and occur in blocks.

In another mechanism, plastic shearing of successive layers of an asperity contact leads to detachment of a wear fragment. According this theory, plastic shearing of successive layers (see Figure 1.4) based on a slip line field (along the planes AC and so on) occurs in conjunction with the propagation of a shear crack (AD and so on), along which the fragment detaches [24]. This process results in thin wedge-shaped transfer fragments. The fragment is detached from one surface and transferred to mating surface because of adhesion. Further sliding causes more fragments to be formed either of the two mechanisms. The wear fragments may remain adhering to a surface; transfer to the mating surface, or to become detached as large loose wear particles. These particles may be of roughly equal size in each dimension. In addition, during this process, surface asperities undergo plastic deformation and strain hardening with surface micro hardness as much as factor of two higher than the bulk hardness, is measured.
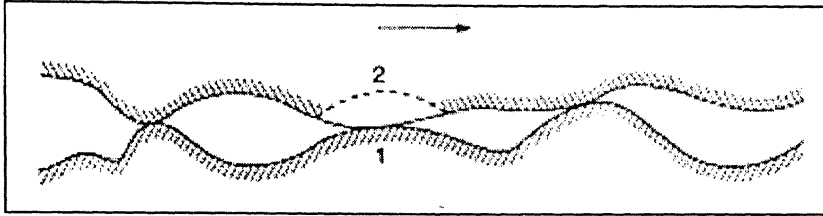
Fig. 1.3: Schematic showing two possibilities for the rupture of adhesive bonds (1 and 2) during shearing of a tribological interface.
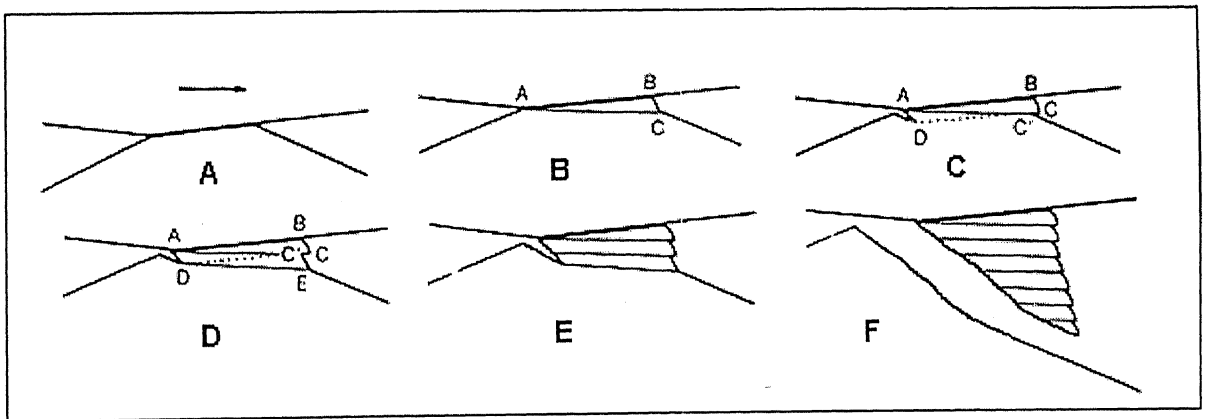
Fig. 1.4: Schematic showing the stages (A to F in order) in the detachment of fragment of a material due to plastic shearing of successive layers of an asperity contact

Abrasive wear:

Abrasive wear occurs when asperities of a rough, hard surface or hard particles slide on a softer surface, and damage the interface by plastic deformation or fracture in the case of ductile and brittle materials, respectively. In many cases, there are two general situations for abrasive wear.

In the first case, the hard surface is the harder of two rubbing surfaces (two-body abrasion see Figure 1.5a). For example, 2-body abrasion occurs in mechanical operations, such as grinding, cutting and machining. While, in second case, the hard surface is a third body, generally a small particle of abrasive, caught between the two surfaces and sufficiently harder to be able to abrade either one or both of the mating surfaces (three-body abrasion). Example: free-abrasive lapping and polishing (Figure 1.5b).

In many cases, the wear mechanism at the start is adhesive, which generates wear particles that get trapped at the interface, resulting in a three-body abrasive wear. In most abrasive wear situations, scratching is observed with series of grooves parallel to the direction of sliding. During sliding, like adhesive wear, asperities on or beneath the surface undergo plastic deformation and strain hardening occurs with an increase in hardness. Abrasive wear rate is a function of surface roughness and, in contrast to adhesive wear mechanism; it increases with an increase in surface roughness.

The wear equation for two-body abrasive wear is also valid for three-body abrasive wear and follows similar formation like equation 15 with appropriate wear coefficient. However, wear rate will be lower by about an order of magnitude because many particles will tend to roll rather than slide. If the wear takes place with fresh abrasive medium wear continues at a steady state, whereas, if a limited amount of abrasive medium is used as the sliding continues, the wear rate generally decreases as a function of time.

A decrease in wear rate as a function of time is believed to occur primarily as a result of blunting of the abrasive surfaces in two-body wear or abrasive particles in three-body wear, as shown in Figure 1.6a. In addition, clogging of the abrasive surface by abraded debris occurs during wear (Figure 1.6b). If at any instance, wear debris is larger than abrasive particles, it may leave the material being abraded above the level of the abrasive grains and result in no additional wear. In case of abrasive wear, the abrasive material must be harder than the surface to be abraded, and this wear mechanism

influenced by hardness and sharpness. Usually, brittle solids have sharp corners and subjected to high stress and abrasion. In high stress abrasion condition, the sharp asperity of brittle solids follows a plastic deformation wear mechanism at low load regime (Fig.1.7). Above the threshold load, brittle fracture occurs, and the wear occurs by lateral cracking at a sharply increased rate. The threshold load is proportional to $(K_{Ic}/H)^3 K_{Ic}$ [25]. The H/K_{Ic} is known as index of brittleness, where H is hardness (resistance to deformation) and K_{Ic} is fracture toughness (resistance to fracture).
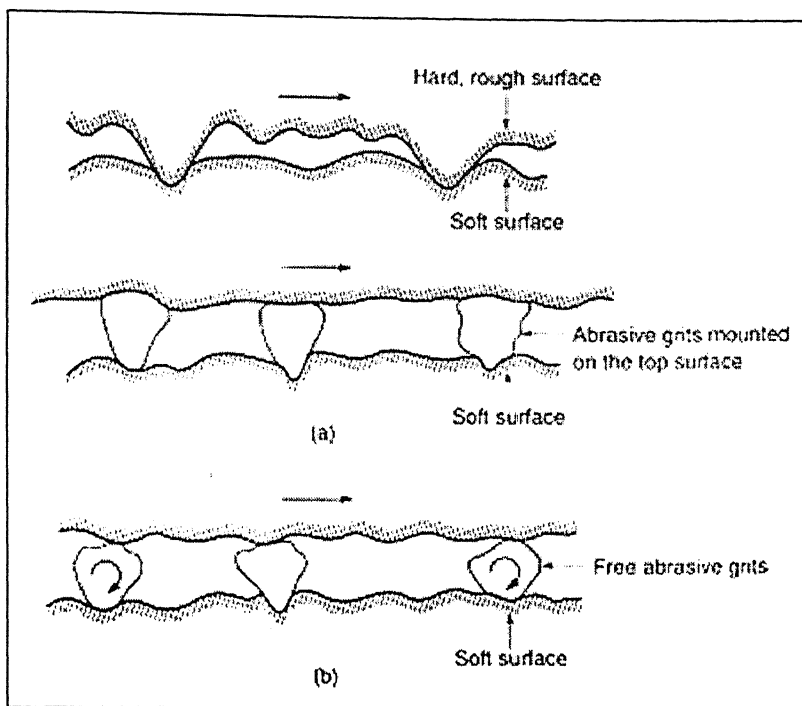
Fig. 1.5: Schematic of a rough, hard surface mounted with abrasive grits sliding on a softer surface (a), and free abrasive grits caught between the surfaces with at least one of the surfaces softer than the abrasive grits (b)
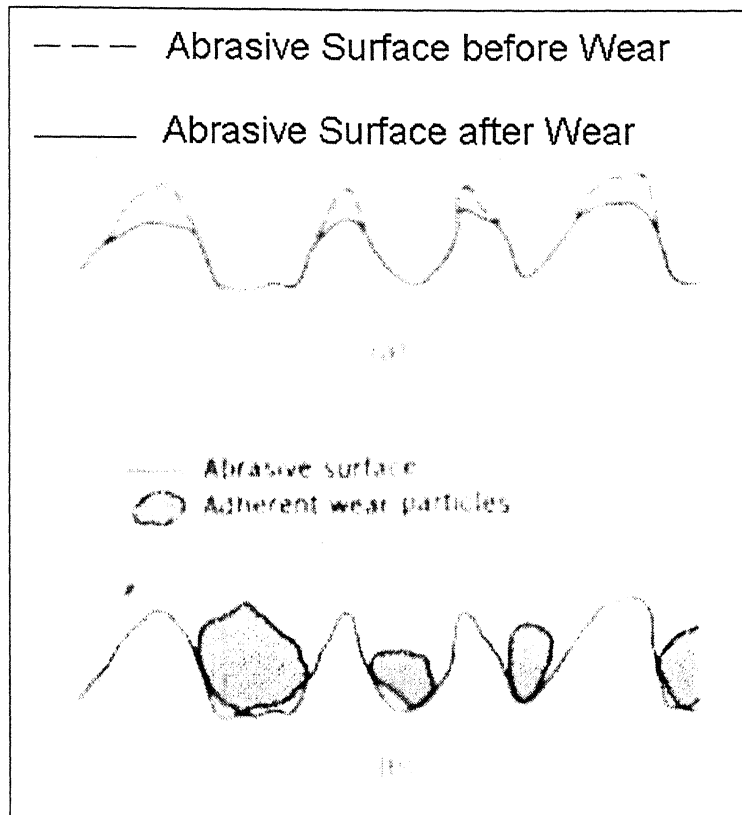
Fig. 1.6: Schematic illustration of an abrasive surface before and after wear showing blunting (a) and an abrasive surface clogged by wear debris (b)
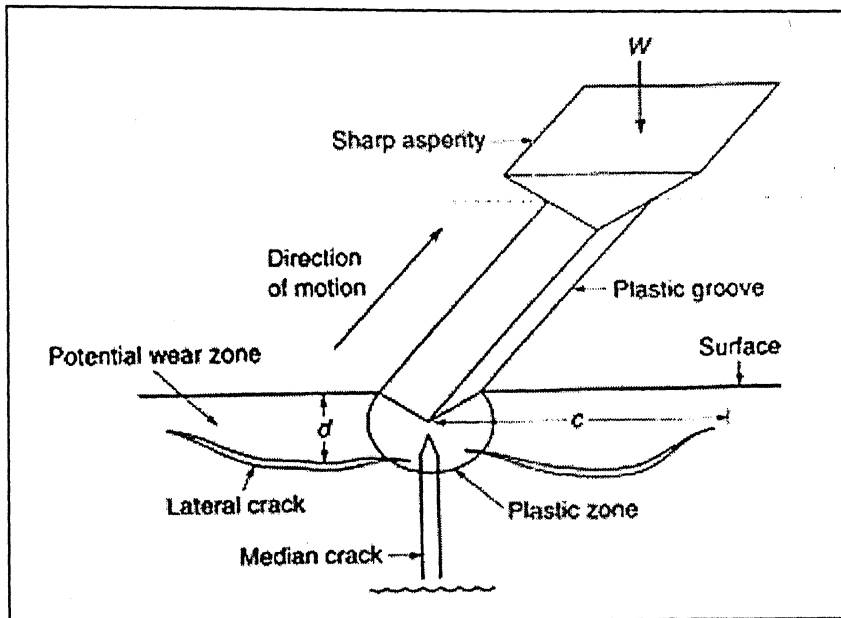
Fig. 1.7: Schematic illustrating the mechanism of wear by a sharp asperity sliding on the flat surface of a brittle material causing lateral fracture.

The lateral crack length c for a sliding asperity contact is given by [26],

$$c = \alpha_1 \left[\frac{(E/H)^{3/5}}{K_c^{1/2} H^{1/8}} W^{5/8} \right] \qquad (16)$$

Where, α_1 is a material-independent constant that depends on the asperity shape. The depth d of the lateral crack d is given by;

$$d = \alpha_2 \left(\frac{E}{H} \right)^{2/5} \left(\frac{W}{H} \right)^{1/2} \qquad (17)$$

Where, α_2 is another material-independent constant. The maximum volume of material removed due to per asperity encounter per unit sliding distance is 2dc. If N asperities contact the surface with each carrying load W, then from Equ 16 and 17, the volume of wear per unit sliding distance of the interface is given by;

$$\upsilon = \alpha_3 N \frac{(E/H) W^{9/8}}{K_c^{1/2} H^{5/8}} \qquad (18)$$

Where, α_3 is a material-independent constant. The ratio (E/H) does not vary by much for different hard brittle solids. Therefore, wear rate is inversely proportional to the (fracture toughness)$^{1/2}$ and (hardness)$^{5/8}$. Wear rate is proportional to (normal load)$^{9/8}$, which implies that wear rate by lateral fracture increases more rapidly than linearly with the applied load as in plastic deformation.

Due to this wear, debris particles are produced. The size and shape of debris particles are one of the important parameter for mild to severe wear transition. Usually, at low load regime the submicron debris are generated. The indentation fracture mechanics concept is illustrated that the minimum load required for fracture due to abrasion is [27]:

$$P* = \frac{54.47\,\beta}{\pi\,\eta^2\,\theta^4} \left(\frac{K_{IC}}{H} \right)^3 K_{IC} \qquad (19)$$

Where, P* = Minimum load required to produce fracture from a point contact (N), β the constant relating hardness to diagonal (2.16 for Vickers Indentation), θ the geometrical constants (≈ 0.2), K_{Ic} the Fracture toughness of the material indented (MPa. m$^{1/2}$), H the hardness of the material

Chemical wear:

Chemical wear in air is generally called as oxidative wear, requiring both chemical reaction and rubbing. Frictional heating modifies the kinetics of chemical reactions of sliding bodies with each other, and with the gaseous or liquid environment, to the extent that reactions normally occur at high temperatures occur at moderate or even ambient temperatures during sliding. Chemistry dealing with this modification of chemical reaction by friction or mechanical energy is referred to as tribochemistry, and wear controlled by this reaction is referred to as tribochemical wear. In addition with chemical reaction, the interface temperatures produce at asperity contacts during sliding of two counterbody, which is known as flash temperature. This temperature is responsible for thermal oxidation and produce oxide films in several microns thick. At low ambient temperatures, oxidation occurs at asperity contacts from frictional heating and at higher ambient temperatures, general oxidation of the entire surface occurs and affects wear.

Fretting Wear:

Fretting occurs where low-amplitude oscillatory motion (a few tens of nanometers to a few tens of micrometers) takes place between contacting surfaces, which are nominally at rest [28]. A rapid increase in wear rate occurs with slip amplitude over an amplitude range. This is a common occurrence, since most machinery is subjected to vibration, both in transit and in operation. In general there are three modes of fretting, which are illustrated in Figure 1.8.
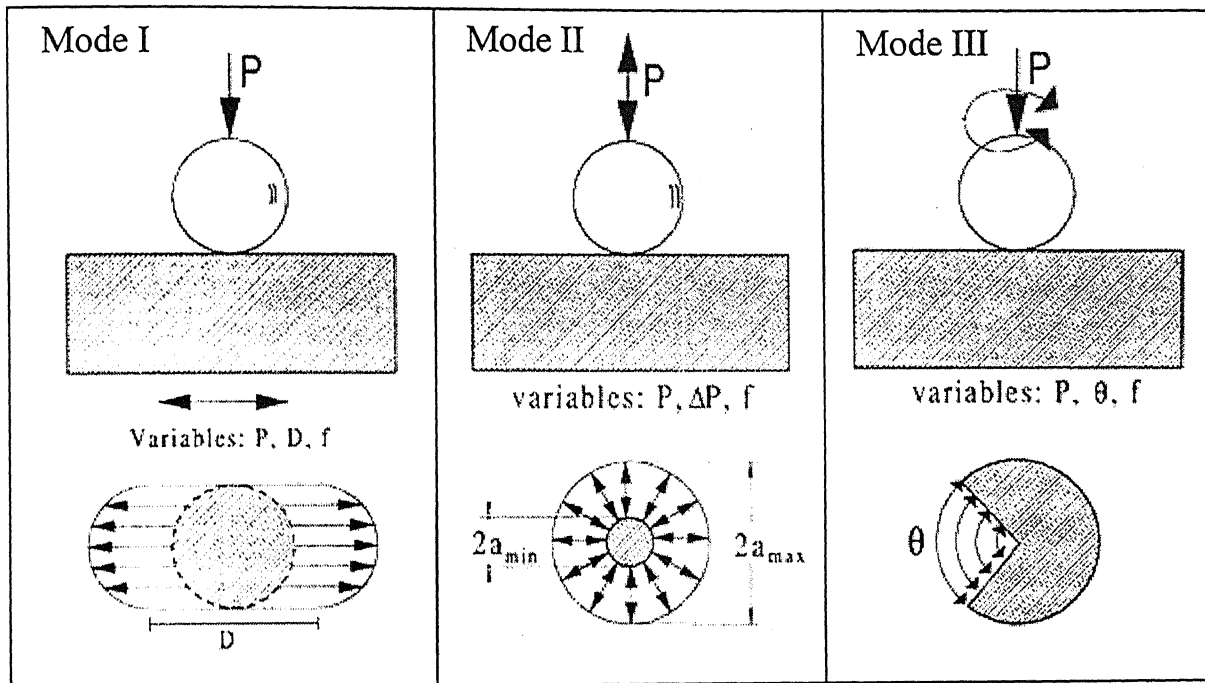
Fig. 1.8: Schematic of different mode of fretting

28

Model (Linear motion): Here fretting is induced by small amplitude linear relative displacement with constant frequency. Here the normal force is maintained constant. The contact displacement may be partial or gross slip.

Mode 2 (Radial trajectory): Here the normal force keeps oscillating as a consequence of this the contact boundary oscillates between 2 points a_{min} and a_{max}, while the central portion is always sticking to the surface. This mode is generally noticed in the ball bearing and the electrical fittings.

Mode 3 (Circumferential trajectory): This takes place under twisting relative displacement in motion. The surface damage consists of an undamaged locked zone surrounded by a damaged slip zone. All though there are three modes of fretting the first mode of fretting is important because of it's wider application. Hence all the experiments are done based on the linear motion principle. In the following experiments, only the normal force that is applied is taken as the variable and the rest of the variables are maintained constant, so that the results that are obtained can compared.

Basically, fretting is a form of adhesive or abrasive wear, where the normal load causes adhesion between asperities and oscillatory movement causes ruptures, resulting in wear debris. These wear particles are abrasive in nature. Because of the close fit of the surfaces and the oscillatory small amplitude motion (on the order of few tens of microns), the surfaces are never brought out of contact, and therefore, there is little opportunity for the products of the action to escape. Further oscillatory motion causes abrasive wear and oxidation (chemical wear), and so on. Therefore, the amount of wear per unit sliding distance due to fretting may be larger than that from adhesive and abrasive wear.

1.4 Oxidation of Materials

High temperature oxidation is a form of corrosion that does not require the presence of a liquid electrolyte. Sometimes, this type of damage is called "dry corrosion" or "scaling". The term oxidation is ambivalent since it can either refers to the formation of oxides or to the mechanism of oxidation of a metal, i.e. its change to a higher valence than the metallic state. Strictly speaking, high temperature oxidation is only one type of high temperature corrosion.

High temperature corrosion is a widespread problem in various industries such as: power generation (nuclear and fossil fuel),aerospace and gas turbine, heat treating, mineral and

metallurgical processing, chemical processing, refining and petrochemical, automotive, pulp and paper, waste incineration.

The long-term viability of machine components operating at high temperatures in an oxidising environment often relies on the integrity of a thin, protective layer of oxide, typically chromia, alumina or silica. Understanding the mechanisms of the formation of such a protective layer and the processes which affect its mechanical integrity, particularly during temperature changes are major challenges to the larger oxidation research community. The compositions of commercial alloys are generally optimized to produce such protective oxide layers but in some applications, such as gas turbines where components may be highly stressed, good oxidation resistance is incompatible with the need for high creep strength. In these cases, oxidation-resistant coatings are applied

1.4.1 Pilling-Bedworth Ratio

In a pioneering work in 1923, Pilling and Bedworth [29] first correlated the porosity of a metal oxide with the specific density. The Pilling-Bedworth ratio, (P-B ratio) R, of a metal oxide is defined as the ratio of the volume of the metal oxide, which is produced by the reaction of metal and oxygen, to the consumed metal volume:

$$R = Md/amD \qquad (20)$$

Where M and D are the molecular weight and density of the metal oxide whose composition is $(Metal)_a(oxygen)_b$; m, and d are the atomic weight and density of the metal.

Pilling and Bedworth realized that, when R is less than 1, a metal oxide tends to be porous and non-protective because it cannot cover the entire metal surface. Later researchers found that, for excessively large R (>1), large compressive stresses are likely to exist in metal oxide, leading to buckling and spalling. In addition to R, factors such as the relative coefficients of thermal expansion and the adherence between metal oxide and metal should also be favorable in order to produce a protective oxide layer.

Using the P-B ratio, Chalmers, and McKay classified protective metal oxides from non-protective metal oxides. Table 1.1 lists protective and non-protective metal oxides and their corresponding P-B ratios.

Table 1.1 Pilling-Bedworth ratios of different elements [29].

Protective oxides	Non protective oxides
Be 1.59	K 0.45
Cu 1.68	Ag 1.59
Al 1.28	Cd 1.21
Cr 1.99	Ti 1.95
Mn 1.79	Mo 3.40
Fe 1.77	Hf 2.61
Co 1.99	Sb 2.35
Ni 1.52	W 3.40
Pd 1.60	Ta 2.33
Pb 1.40	U 3.05
Ce 1.16	V 3.18

The list can be readily applied to the protective metal oxides used in integrated circuits. The intrinsic protective metal oxides, including the oxides of Be, Cu, Al, Cr, Mn, Fe, Co, Ni, Pd, Pb, and Ce, may be able to replace silicon oxide. On the other hand, a few popular metal oxides, e.g. Ti oxide and Ta oxide, are non-protective, suggesting a possible reason why these oxides have not been successfully used in commercial products after years of research. Besides oxides of elemental metal, the P-B ratio can be applied to oxides of metal alloy, metal nitrides and other metal ceramic systems.

1.4.2 Thermodynamic Principles

The stability of materials at high temperature can be thermodynamically analyzed using plots of the standard free energy of reaction (ΔG_0) as a function of temperature, commonly known as Ellingham diagrams. Such diagrams can help to visualize the relative stability of metals and their oxidized products. The values of ΔG_0 on an Ellingham diagram are expressed as kJ per mole O_2 to normalize the scale and be able to compare the stability of these oxides directly, i.e. the lower the position of the line on the diagram the more stable is the oxide.

For a given reaction ($M + O_2 = MO_2$) and assuming that the activities of M and MO_2 are taken as unity, the following equations can be used to express the oxygen partial pressure at which the metal and oxide coexist, i.e. the dissociation pressure of the oxide:

$$P_{O_2}^{M/MO_2} = e^{\frac{\Delta G^0}{RT}} \tag{21}$$

or its logarithm form

$$\log(P_{O_2}^{M/MO_2}) = \frac{\Delta G^0}{2.303 RT} \tag{22}$$

Table 1.2 lists the coexistence equations, temperature ranges and standard Gibbs energy changes that can be used to construct such diagrams. Ellingham diagrams (Figure 1.9) may, of course, be constructed for any class of compounds. It is possible to use plots of the free energy of formation of metal oxides vs. temperature to predict the temperatures at which a metal is stable and the temperatures at which it will spontaneously oxidize. For

temperatures at which the free energy of formation of the oxide is positive, the reverse reaction is favored and the oxide will spontaneously decompose to the metal.

The vapor species that form in any given high temperature corrosion situation often have a strong influence on the rate of attack, the rate generally being accelerated when volatile corrosion products form. Gulbransen and Jansson [29] have shown that metal and volatile oxide species are important in the kinetics of high temperature oxidation of carbon, silicon, molybdenum, and chromium. Six types of oxidation phenomena were identified:

- At low temperature, diffusion of oxygen and metal species through a compact oxide film.

- At moderate and high temperatures, a combination of oxide film formation and oxide volatility.

- At moderate and high temperatures, the formation of volatile metal and oxide species at the metal-oxide interface and transport through the oxide lattice and mechanically formed cracks in the oxide layer.

- At moderate and high temperatures, the direct formation of volatile oxide gases.

- At high temperature, the gaseous diffusion of oxygen through a barrier layer of volatilized oxides.

- At high temperature, spalling of metal and oxide particles.
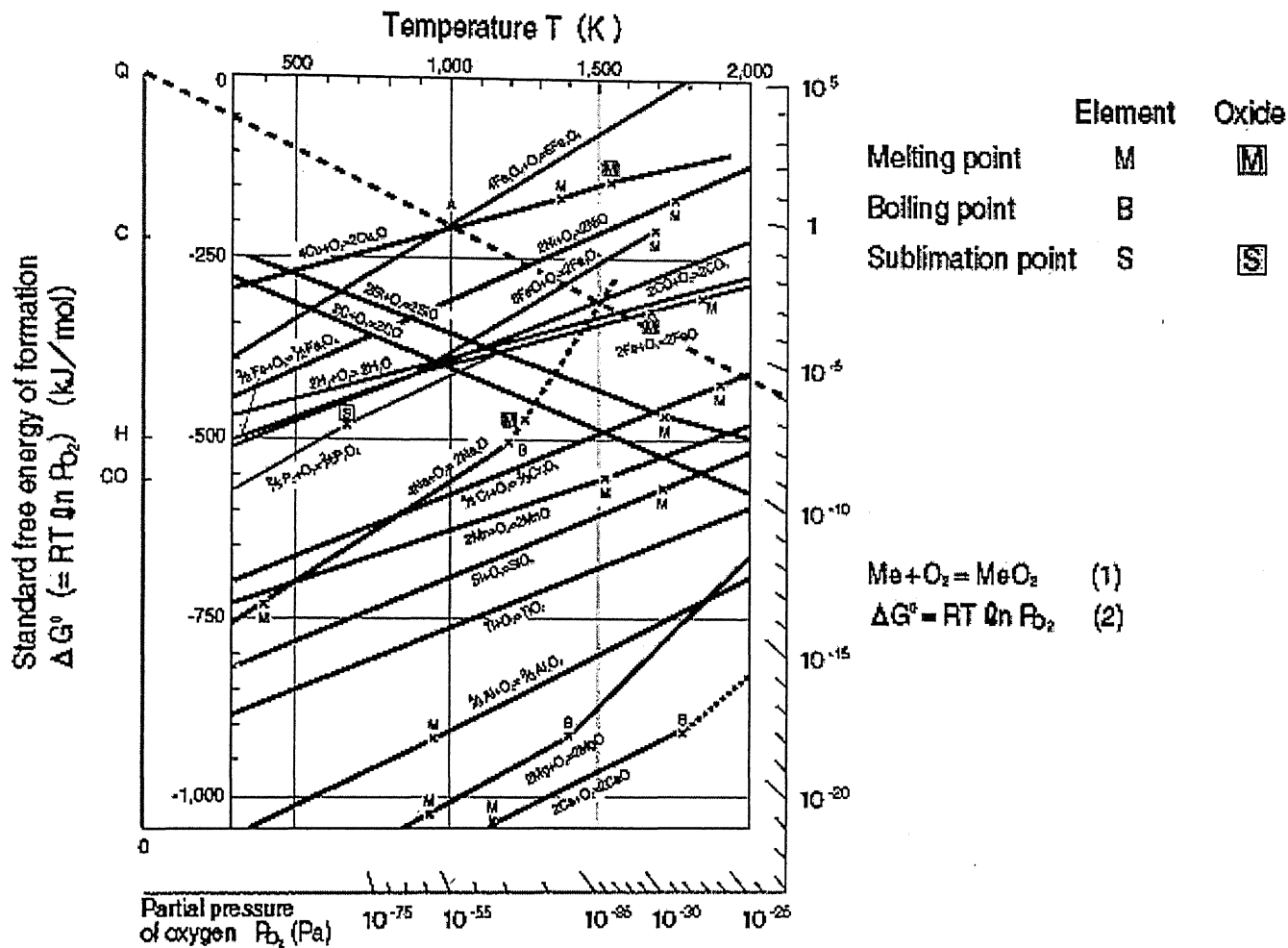
Fig. 1.9: Ellingam diagram for metal oxides [30]

Table 1.2 Thermodynamic data for the oxidation of metals [29]

Temperature Range (K)	Coexistence Equation (Oxidation Reaction)	Standard Free Energy Change (J)
900-1154	$Pd + 0.5\ O_2 = PdO$	$-114,200 + 100\ T\ (°K)$
884-1126	$2\ Mn_3O_4 + 0.5\ O_2 = 3\ Mn_2O_3$	$-113,360 + 92.0\ T$
298-1300	$3\ CoO + 0.5\ O_2 = Co_3O_4$	$-183,200 + 148\ T$
892-1302	$Cu_2O + 0.5\ O_2 = 2\ CuO$	$-130,930 + 94.5\ T$
1396-1723	$1.5\ UO_2 + 0.5\ O= = 0.5\ U_3O_8$	$-166,900 + 84\ T$
878-1393	$U_4O= + 0.5\ O_2 = 4/3\ U_3O_8(-2)$	$-164,400 + 82\ T$
967-1373	$2\ Fe_3O_4 + 0.5\ O_2 = 3\ Fe_2O_3$	$-246,800 + 141.8\ T$
1489-1593	$2\ Cu + 0.5\ O_2 = Cu_2O$	$-166,900 + 43.5T$
1356-1489	$2\ Cu + 0.5\ O_2 = Cu_2O$	$-190,300 + 89.5\ T$
924-1328	$2\ Cu + 0.5\ O_2 = Cu_2O$	$-166,900 + 71.1\ T$
992-1393	$3\ MnO + 0.5\ O_2 = Mn_3O_4$	$-222,540 + 111\ T$
1160-1371	$Pb + 0.5\ O_2 = PbO$	$-190,580 + 74.9\ T$
772-1160	$Pb + 0.5\ O_2 = PbO$	$-215,000 + 96.0\ T$
911-1376	$Ni + 0.5\ O_2 = NiO$	$-233,580 + 84.9\ T$
1173-1373	$Co + 0.5\ O_2 = CoO$	$-235,900 + 71.5\ T$
973-1273	$10\ WO_{2.9} + O_2 = 10\ WO_3$	$-279,400 + 112\ T$
973-1273	$10\ WO_{2.72} + O_2 = 10\ WO_{2.90}$	$-284,000 + 101\ T$
973-1273	$1.39\ WO_2 + 0.5\ O_2 = 1.30\ W\ O_{2.72}$	$-249,310 + 62.7\ T$
973-1273	$0.5\ W + 0.5\ O_2 = 0.5\ WO_2$	$-287,400 + 84.9\ T$
949-1273	$3\ FeO + 0.5\ O2 = Fe_3O_4$	$-311,600 + 123\ T$
770-980	$Sn + 0.5\ O_2 = SnO_2$	$-293,230 + 108\ T$
903-1540	$Fe + 0.5\ O_2 = FeO$	$-263,300 + 64.8\ T$

Temperature Range (K)	Coexistence Equation (Oxidation Reaction)	Standard Free Energy Change (J)
1050-1300	$2\,NbO_2 + 0.5\,O_2 = Nb_2O_5$	$-313,520 + 78.2\,T$
693-1181	$Zn + 0.5\,O_2 = ZnO$	$-355,890 + 107.5\,T$
1300-1600	$0.66\,Cr + 0.5\,O_2 = 0.33\,Cr_2O_3$	$-371,870 + 83.7\,T$
1050-1300	$NbO + 0.5\,O_2 = NbO_2$	$-360,160 + 72.4\,T$
923-1273	$Mn + 0.5\,O_2 = MnO$	$-388,770 + 76.3\,T$
1539-1823	$Mn + 0.5\,O_2 = MnO$	$-409,500 + 89.5\,T$
1073-1273	$0.4\,Ta + 0.5\,O_2 = 0.2\,Ta_2O_5$	$-402,400 + 82.4\,T$
1050-1300	$Nb + 0.5\,O_2 = NbO$	$-420,000 + 89.5\,T$
298-1400	$0.5\,U + 0.5\,O2 = 0.5\,UO2$	$-539,600 + 83.7\,T$
1380-2500	$Mg(v) + 0.5\,O2 = MgO$	$-759,600 - 30.83\,T \log T + 317\,T$
923-1380	$Mg(l) + 0.5\,O2 = MgO$	$-608,200 - 1.00\,T \log T + 105\,T$
1124-1760	$Ca + 0.5\,O2 = CaO$	$-642,500 + 107\,T$
1760-2500	$Ca(v) + 0.5\,O2 = CaO$	$-795,200 + 195\,T$

1.5 Objectives

The major aim is to develop TiB_2–based advanced structural materials with non-metallic additive $MoSi_2$ and to gain an insight into the microsturcture, properties and the degradation behavior, in particular friction, wear, and high temperature oxidation properties with reference to microstructure and mechanical properties. Some salient objectives are listed below:

- To optimise the material parameters, starting powder composition and refine the processing parameters to develop dense TiB_2–based materials for high temperature application.

- To evaluate the mechanical (hardness and fracture toughness) and physical properties (thermal conductivity and electrical conductivity)

- To perform high temperature oxidation tests in order to evaluate the thermal stability of titanium diboride and composite.

- To investigate the tribological performance under different tribological conditions (varying load, cycles) on a fretting wear (mode I) and acquisition of fundamental understanding of the wear mechanisms.

1.6 Structure of thesis

Three different areas are involved in this thesis report. The first part of the thesis deals with the synthesis of starting powders such as TiB_2 and $MoSi_2$ and their subsequent processing into sintered compacts of monolithic TiB_2 and TiB_2-$MoSi_2$ composites. To understand the dominant sintering mechanisms, further detailed characterization of the compacts was done using X-ray diffraction (XRD), Scanning electron microscope (SEM), Electron probe microanalyzer (EPMA) and Transmission electron microscope (TEM).

The second part deals with the evaluation of tribological behavior of hot pressed monolithic TiB_2 and TiB_2-$MoSi_2$ composites, in which the frictional and wear characteristics are analyzed in detail. Wear mechanisms were studied using Scanning electron microscope (SEM) equipped with Energy dispersive spectroscopy (EDS). Raman spectroscopy was also used to identify the compounds formed during wear. All tests were performed on small amplitude reciprocating friction and wear (Fretting, mode-I type) testing equipment with a ball- on-flat configuration.

The third part deals with the high temperature oxidation behavior. Isothermal oxidation tests were performed at 850°C, in order to understand the thermal stability of titanium diboride and the composite. SEM with EDS and X-ray diffraction (XRD) were used for evaluating the oxidation mechanisms and reaction products.

References

1. R.A. Cutler, "Engineering Properties of borides, in Engineered materials handbook," vol. 4, ceramics and glasses, ASM international, The Materials Information Society, USA (1991).

2. R. Telle, "Boride and carbide ceramics," in Materials Science and Technology. Ed. R.W. Cahn, P. Haasen, E.J. Kramer. Vol. 11: Structure and Properties of Ceramics. Ed. M. Swain. VCH, Weinheim, Germany, (1994), p.175.

3. G.V.D. Goor, P. Sägesser and K. Berroth, *"Solid State Ionics,"* 1163 (1997) 101-103.

4. P. Ettmayer, H. Kolaska, W. Lengauer, and K. dreyer, "Ti(CN) Cermets-Metallurgy and Properties," *Int. J.Refract. Met.Hard Mater.,* 13, (1995) 343-51.

5. G.E. D'Errico, S. Bugliosi, and E. Gugliemi, "Tool-Life Reliability of Cermet Inserts in Milling Tests," *J..Mater.Proc. Technol.,* 77 (1998), 337-43.

6. D. Moskowitz and M. Humenik Jr., "Cemented Titanium Carbide Cutting Tools," *Mod. Dev. Powder Metall.,* 3, (1966) 83-94.

7. S. Put, J. Vleugels, O.V.D Biest, "Electrophoretic shaping of functionally graded hardmetals," *P/M Science & Technology Briefs,* 3 (3), (2001) 14-17.

8. Y. Liu, X Liao, F. Tang & Z. Chen, "Observations on the operating of TiB_2-coated cathode reduction cells," In: "Light Metals". Ed. E. Cutshall. The Minerals, Metals and Materials Society, Warrendale, PA, (1991) 427-29.

9. F. De Mestral & F. Thevenot, "Ceramic composites: TiB_2-TiC-SiC, Properties and microstructures in the ternary system," *J. Mater. Sci,* 26 (1991).

10. B. Basu, J. Vleugels and O.V.D Biest, "Development of ZrO_2-ZrB_2 Composites," *J. Alloys and Compounds,* 334 [1-2] (2002) 200-204.

11. B. Basu, "Zirconia-titanium boride composites for tribological applications," Ph.D. thesis, Katholieke Universiteit Leuven, 2001.

12. S. Zang, "Titanium Carbonitride-Based Cermets: Process and Properties," *Mater. Sci. Engg.A,* 163 (1993) 141-48.

13. W.D. Schubert, A. Bock and B. Lux, *"Int. J. of Refractory Metals & Hard Materials,"* 13 (1995) 281-296.

14. T. Yamamoto, A. Jaroenworaluck, Y. Ikuhara, and T. Sakuma, *"J. Mat. Res.,"* 14 [11] (1999) 4129-31.

15. "Advanced Engineered Materials," Bell Park drive, woodstock, USA.

16. (a) S. K. Mishra (pathak), S. K. Das, A. K. Ray and P. Ramchandrarao, "Effect of nickel on sintering of self-propagating high-temperature synthesis produced titanium carbide," *J. Mat. Res.,* 14 [9] (1999) 3594-3598.

    (b) S. K. Mishra (pathak), S. Das, S. K. Das and P. Ramchandrarao, "Sintering studies on ultrafine ZrB_2 powders produced by a self-propagating high-temperature synthesis process," *J. Mat. Res.,* 15 [11] (2000) 2499-2504.

17. S. Bates, W. Buhro, C. Frey, S. Sastry and K. Kelton, "Synthesis of TiB_2 nanocrystallites by solution-phase processing," *J. Mater. Sci.,* 10 (1995) 2599-2612.

18. L. S. Sigl & K.A. Schwetz, *"Powder Metall. Int.,"* 23 (1991) 221.

19. A. Bellosi, G. De Portu and S. Guicciardi, "Preparation and properties of electroconductive Al_2O_3-based composites," *J. Europ. Ceram. Soc.,* 10 (1992) 307-315.

20. G.C. Kuczynski, "Phys. Sinter," *J. Int. Inst. Sci. Siner,* 5 (1973) 67.

21. J. Hirschhorn, S. Joel, Introduction to powder metallurgy, 238-240.

22. J.P.G. Farr, "Molybdenum Disulphide in Lubrication: A Review," *Wear* 3(1975)1-22.

23. J.F.Archard, "Contact and Rubbing of Flat Surfaces," *J.Appl. Phys.* 24 (1953) 981-988.

24. T. Kayaba and K. Kato, "Adhesive Transfer of the slip-Tongue and the Wedge," *ASLE Trans.* 24, 164-174.

25. B.R. Lawn and D.B. Marshall, "Hardness, Toughness, and Brittleness: An Indentation Analysis," *J.Amer. Ceram.Soc.* 62, (1979) 347-350.

26. A.G. Evans and D.B. Marshall, "Wear Mechanisms in Ceramics In Fundamentals of friction and Wear of Materials," *Amer. Soc. Metals*, Metals Park, Ohio (1981) 439-452.

27. S.G.Roberts, "Depths of Cracks Produced by Abrasion of Brittle Materials", *Scripta Materialia,* 40 [1] (1999) 101-108.

28. P.L. Hurricks, "The Mechanism of Fretting-A Review," *Wear* 15, (1970) 389-409.

29. http://www.corrosionsource.com/technicallibrary/corrdoctors/Modules/HotCorros ion/ellingham.htm

30. F.D. Richardson, "Ellingham diagrams," JISI (1948) (http:// www.chem.ox.ac.uk/.../ lecture3/ellingham.html.)

CHAPTER 2
LITERATURE REVIEW

2.1 Processing of TiB₂–based composites

TiB$_2$ is a potential candidate material for high-temperature structural applications due to the excellent combination of attractive properties e.g. high melting point, high thermal and electrical conductivities, high elastic modulus, high hardness and good corrosion resistance [1]. TiB$_2$ is a stable phase, as can be observed in the Ti-B binary phase diagram (see Fig. 2.0). MoSi$_2$ is being considered as a candidate material for high temperature structural applications in view of its excellent oxidation resistance, high melting point (2020°C), and relatively low density (6.31 g/cc)[2]. Some important physical and mechanical properties of TiB$_2$ and MoSi$_2$ are described in Table 2.1. Despite having useful properties, the applications of monolithic TiB$_2$ is rather limited due to poor sinterability, exaggerated grain growth and poor oxidation resistance. To overcome this problem, various metallic and non-metallic binders are used to obtain dense borides. In the present work, MoSi$_2$ is selected as binder phase to densify TiB$_2$. Since densification has been a major challenge to obtain dense borides, the sintering of borides will be discussed in details.

2.1.1 Difficulties in sintering

Densification of single phase and pure ceramics of transition metal diboride is complicated by three characteristics of these compounds: the high melting point, low self-diffusion coefficient and the comparatively high vapor pressure of the constituents. As a rule, sintering temperatures exceeding 70% of the absolute melting temperature have to be applied. TiB$_2$ (T$_m$ ~3250°C) requires firing temperatures of the order of 1800–2300°C to initiate grain boundary and volume diffusion, to obtain more than 95% of the theoretical density. One disadvantage is that the borides undergo a similar abnormal grain growth at high temperatures [3]. Furthermore, at comparatively lower temperatures, evaporation–condensation reactions are enhanced, which induces growth of faceted crystals. The occurrence of microcracking at the grain boundaries is promoted with the increase in grain size, as will be discussed later. Thus, it is nearly impossible to achieve completely dense borides by pressureless sintering, as no shape accommodation occurs without external pressure and the large pores tend to coarsen [3].

Table 2.1 Summary of important physical and mechanical Properties of TiB$_2$ [1] and MoSi$_2$ [4].

Property	TiB$_2$	MoSi$_2$
Melting Point (^{o}C)	3200	2030
Thermal conductivity (W/m/K)	60 – 120	53
Density (g/cc)	4.52	6.24
Coefficient of linear expansion (^{0}C^{-1})	8.1 X 10^{-6}	8.5 X 10^{-6}
Electrical resistivity ($\mu\Omega$ – cm)	10 – 30	21.6
Fracture toughness K$_{IC}$ (MPa.m$^{1/2}$)	5 – 7	3-4
Hardness (G Pa)	32	12
Elastic modulus (G Pa)	~500	~450
Oxidation Resistance	≤1000°C	≤1400°C
Friction coefficient (Self mated)	0.9	_____
Specific heat (J/Kg/K)	617	_____
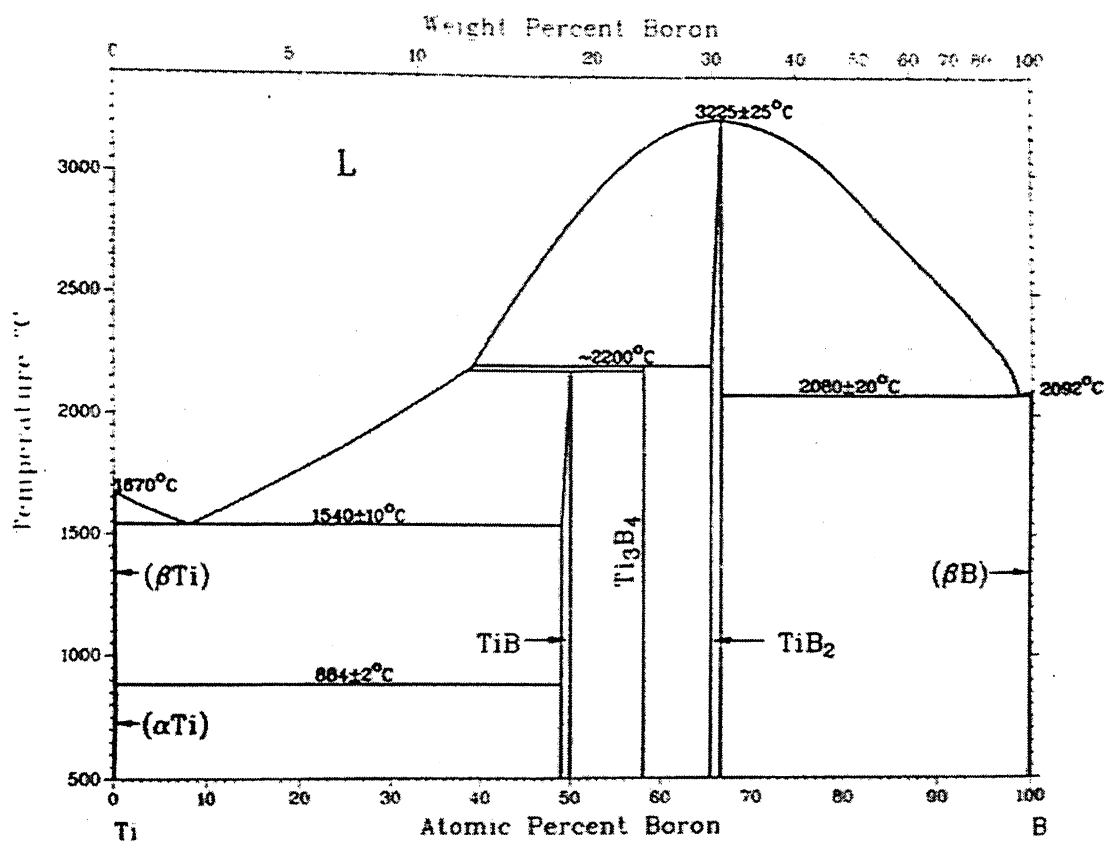
Fig. 2.0: Ti-B binary phase diagram [72].

The reasons for poor sinterability of TiB_2 can be summarized as follows. Very high sintering temperatures are required for densification due to the presence of predominantly covalent and ionic bonds in TiB_2. Moreover a low self diffusion coefficient, which causes delay in densification, so requires long sintering time. Additionally, a thin oxygen rich layer (mainly TiO_2 and B_2O_3) on the surface of TiB_2 powder is found to be very detrimental to densification [5]. Eventually high sintering temperature and time leads to the grain growth. Baik and Becher [6] analyzed the adverse effect of oxygen contamination often introduced during synthesis and/or subsequent processing on densification of TiB_2. They found that the presence of oxygen promoted the grain coarsening by increasing evaporation–condensation kinetics and limited the maximum attainable density in the case of hot pressing (1400–1700^{0}C). The primary oxygen-bearing species is B_2O_3, which can be reduced effectively by the addition of carbon. In the case of pressureless sintering (1700^0 to 2050^{0}C), oxygen remained primarily as titanium oxides and increased grain and pore coarsening by increasing surface diffusivity. In order to achieve higher densities and inhibit abnormal grain growth, it was suggested that the total oxygen content of the powder must be limited to less than 0.5 wt% or strong reducing additives be used to remove TiO_X below 1600^{0}C.

The effect of sintering on the microstructure and properties of TiB_2 ceramics has also been studied. Ferber and co- workers [7] reported that anisotropic materials, such as TiB_2, often develop microcracks, relieving localized residual stresses produced as the material is cooled after hot pressing. Such stresses arise primarily from thermal expansion mismatch between individual grains. For example, the TiB_2 thermal expansion coefficients along the crystallographic a and c axes are 7.19×10^{-6} /^{0}C and 9.77×10^{-6} /^{0}C, respectively [7]. The micro-cracking phenomenon generally requires that the average grain size exceed a critical value. The microscopic observations of TiB_2-based ceramics have suggested that the critical grain size is $\sim$ 15 μm.

Wang and co-workers investigated the influence of hot pressing temperature and sintering time on microstructure and mechanical properties of TiB_2 ceramics [8]. Initially, the density of sample increases rapidly with increasing sintering time (initial few minutes), and later on, the density increases slowly (Fig 2.1a). This indicates that the sintering mechanisms are different at different sintering stage. Plastic flow and diffusion

creep are the main sintering mechanisms at initial sintering stage and last stage, respectively. Hot pressing temperature has a remarkable influence on the density of sintered sample. With increasing sintering temperature, sample density increases rapidly. At 2173 K, the TiB_2 ceramics is nearly fully dense. This result indicates that in order to prepare TiB_2 ceramics with high density, high sintering temperature is necessary. At high sintering temperature, TiB_2 grains will grow rapidly and irregularly. It is also known that grains size and shape of TiB_2 ceramics can have an important influence on the mechanical properties. In order to prevent the abnormal grain growth, the optimum hot pressing parameters have to be determined by experiments [8]. Fig. 2.1b illustrates the effect of sintering parameters on the grain size of TiB_2.

2.1.2 Preparation of TiB_2 powder

Bates and co-workers [9] have prepared nanocrystalline TiB_2 of 5–100 nm size via an initial solution phase reaction of $NaBH_4$ and $TiCl_4$, followed by annealing the obtained amorphous precursor at 900–1100^{0}C. Axelbaum and co- workers [9] have developed a gas phase combustion process that can directly yield non-agglomerated, low-oxygen TiB_2 nano-particles by the reaction of sodium vapor with $TiCl_4$ and BCl_3. However, the products were contaminated with metallic titanium and titanium oxide.
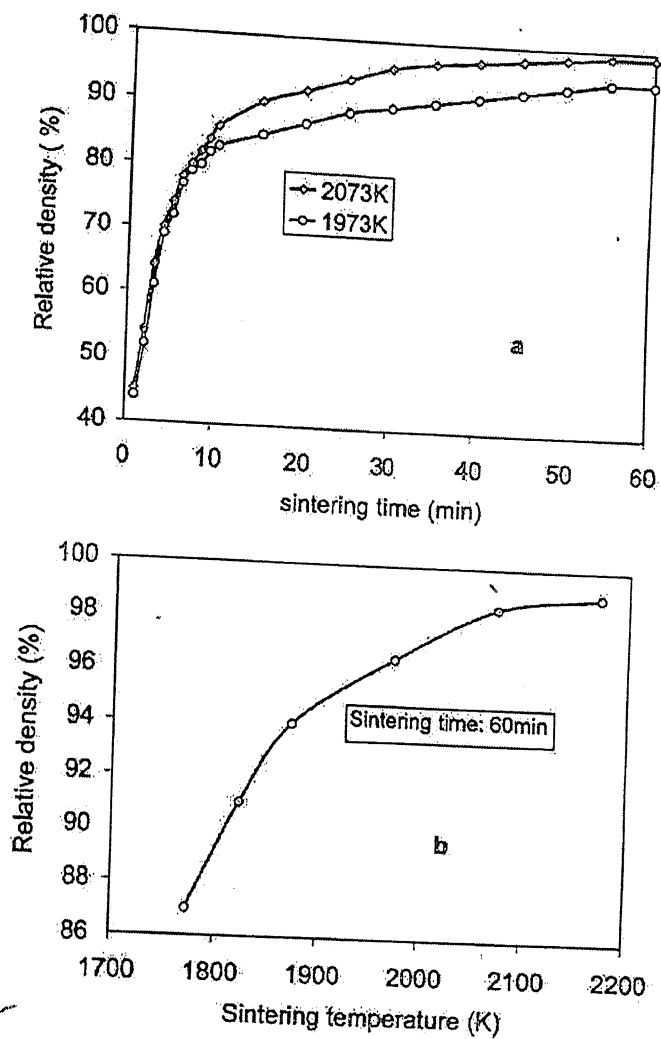
Fig. 2.1a: Influence of sintering time (a) and temperature (b) on relative density of monolithic TiB$_2$ [8].
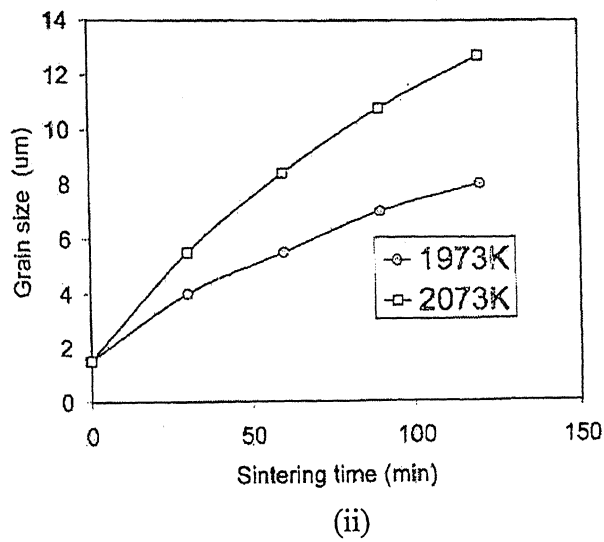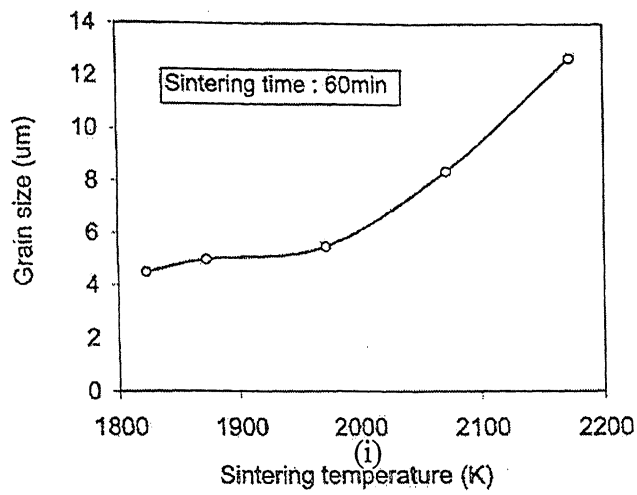
Fig. 2.1b: Influence of sintering temperature (i) and time (ii) on average grain size of TiB₂ ceramics [8].

Recently, Yunel and co-workers [9] developed a novel route to prepare nano crystalline titanium diboride via a solvothermal reaction of metallic sodium with amorphous boron powder and TiCl$_4$ at 400^{0}C. It can be represented by the following equation.

$$TiCl_4 + 2B + 4Na \text{ (benzene @ 400}^0\text{C)} \rightarrow TiB_2 + 4NaCl \qquad (23)$$
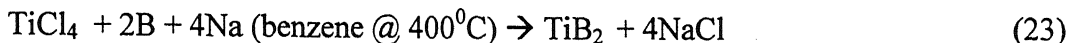
Active nascent titanium generated by the reduction of TiCl$_4$ by metallic sodium helps in the formation nano-crystalline TiB$_2$. Benzene serves as reaction medium to control the rate of reaction and particle size. By confirming the reaction within an anaerobic environment, the product was free of oxide impurity. However, sample surface oxidation may occur during the purification process.

Hwang and Lee reported [10] the synthesis of sub micrometer-sized TiB$_2$ powder by mechanical alloying the mixture of elemental Ti and B powders in argon atmosphere using a steel jar. The amorphization reaction is a common process during mechanical alloying. However, it has not been observed by then and the starting raw material directly converted into final stable phase. No amorphization process had occurred during mechanical alloying because of the much negative heat of formation of the TiB$_2$. It was found that size of the transition metal and the heat of formation of borides greatly affected the time for mechanical alloying of TiB$_2$.

2.1.3 Metallic binders

Extensive research has reported the role of metallic binders on the densification of TiB$_2$ [11,12,13]. Earlier sintering experiments using metallic additives like such as nickel, iron, cobalt, stainless steel, and manganese have demonstrated that 99% ρ_{th} can be achieved by liquid phase sintering. Ferber et al [7] have used up to 10 wt% Ni to achieve more than 99% theoretical density by hot pressing route (1425^{0}C). The transition metals (Ni, Co, Cr) react with TiB$_2$ forming various metal borides with a low melting point (approx. 900-1100°C) with a suitable wetting behavior. In the case of Ni-bonded TiB$_2$, a ternary τ-phase with the composition, Ni$_{21}$Ti$_2$B$_6$ forms by the dissolution of TiB$_2$. At 800^{0}C, the τ-phase is in equilibrium with Ni, Ni$_3$B, Ni$_3$Ti, and TiB$_2$. Typical metal contents required for successful liquid phase hot pressing of TiB$_2$ are 5 to 25 wt.% (2 to 12 at.%) of either Ni or Co. In order to avoid reactions consuming TiB$_2$, the borides of Ni

or Co have also been used [3]. By this method, the sintering temperatures have been decreased from 2100^0C to 1400^0C. The liquid phase intensifies the mass transport but causes accelerated grain growth. However, extensive nickel phase transformation was found to have deleterious effect on both fracture strength and fracture toughness. However, the strength and toughness are significantly enhanced for TiB_2 ceramics with a fine grain size (4 μm) and modest Ni content (<2 wt%). Fig. 2.2a A illustrates the microcracks formation in coarse grained TiB_2 and absence of microcracks in fine grained TiB_2 material (Fig. 2.2a B). It explains the effect of grain size on microcrack formation. If the grain size is beyond the critical size (15 μm), then the microcracking would occur. The reason for forming the microcracks is due to difference in the thermal expansion coefficients along the crystallographic a = 7.19 X 10^{-6}/^{0}C and c = 9.77 X10^{-6}/^{0}C of TiB_2, since it is a non cubic crystalline structure (hexagonal).

Kang et al [12] have observed that simultaneous addition of 0.5 wt % Fe and 0.5 wt% Cr enhances the densification of TiB_2 in the temperature range of 1800-1900^0C. They have shown that when small amount of Fe (0.5 wt %) is added, abnormal grain growth occurs and the sintered density is low. In case of B_4C addition along with 0.5 wt % Fe, abnormal grain growth was suppressed remarkably and there was an increase in sintered density up to 95%. Microstructural observation confirmed the existence of Fe-rich phase at the triple junction and at grain boundaries. However, the presence of metallic binder was not desirable for high temperature structural applications as the low melting point of metallic elements leads to incipient fusion and consequently the degradation in the properties. Therefore, non-metallic additives are used with an aim to improve sinterability without promoting grain growth and also to retain high temperature properties with good oxidation resistance.

Fig. 2.2a: Microstructures of monolithic TiB$_2$. (A) Coarse-grained TiB$_2$ (fabricated at 2000°C) showing microcracking (arrows). (B) Fine-grained TiB$_2$ (fabricated at 1800°C) showing uniformly sized grains and absence of microcracking.

The microstructures of the TiB_2 composites prepared by liquid phase sintering are similar to those of other hard metals like WC-Co etc. The TiB_2 particles form a rigid skeleton of faceted crystals, whereas the binder forms compounds of Fe, Cr, or Co e.g., Ni_3B, Ni_2B, Ni_3B_4. Depending upon the wetting behavior, typically influenced by the surface oxidation of the hard material phase, round pores may accumulate at particle/matrix interfaces or close to triple junctions, which have not been completely infiltrated by the liquid phase. Moreover, the evaporation of Fe-, Co-, or Ni- borides may cause entrapped gas pores. Hence, hot-pressing is required for a homogeneous distribution of the liquid phase, particle rearrangement, and complete removal of the residual porosity. In contrast to hard metals, the matrix phase is very brittle, e.g., the K_{IC} of Ni_3B equals 1.4 –1.9 MPa $m^{1/2}$ [3], and hence does not improve the mechanical properties.

The fabrication of TiB_2 based cermets, resembling the well-known WC-Co hard metal, combines the high toughness and ductility of a metallic binder with the hardness of the boride phase. This is recently achieved by using Fe instead of Ni and Co [3]. Although there are still some controversies concerning the phase diagram, TiB_2 is in a eutectic equilibrium with liquid Fe at 1340^0C (eutectic concentration 6.3 Mol%TiB_2), which enables liquid phase sintering. Discrepancies exist for the phase equilibria at lower temperatures because of the problem of whether the observed Fe_2B is an equilibrium phase or results from impurities present in the staring powders. It is, however, obvious that oxygen and carbon contaminants, introduced by the manufacturing processes of the starting powders significantly affect the wetting behavior of the liquid Fe. Both constituents do indeed cause dramatic changes in the phase equilibria and sintering kinetics, and thus have to be compensated for by the addition of metallic Ti, Mo or Nd to form TiC, or Ti_2O_3 and Nd_2O_3, respectively, to act as a carbon or oxygen trap [3].

Since the eutectic concentration in the quasi-binary TiB_2-Fe system with 14 vol.% TiB_2 is considerably closer to the metal-rich side than in the similar WC-Co system (32 vol.% WC), a much smaller amount of liquid phase is generated upon sintering which makes densification more difficult [3]. A simple increase in temperature cannot satisfactorily balance the lack of liquid, because it is accompanied by accelerated coarsening of TiB_2 due to Oswald ripening. The volume fraction of binder phase thus

ranges between 10 and 30%. A typical microstructure is very similar to that of WC-Co hard metals (see Fig. 2.2b). TiB_2 particles are embedded in a continuous Fe matrix. The densification mechanisms are typically dissolution-reprecipitation as well as coalescence, i.e., rearrangement and intergrowth of particles with common faces of the same orientation. The latter mechanism is active if the volume fraction of liquid exceeds 30%, but may result in the growth of elongated platelets. The residual porosity after pressureless sintering at $1500-1800^0C$ depends upon the initial liquid phase composition. At 1500^0C, 88% of the theoretical density has been obtained for the TiB_2-Fe system (99% ρ_{th} at 1800^0C); whereas at 1450^0C, Ti addition results in 98% theoretical density and combined Ti-Nb additives result in 96.7% theoretical density. Hot pressing and hot isostatic pressing can yield densities > 98% with a lower binder content [3].

Pressureless sintering of titanium diboride with nickel, nickel boride and iron additives has also been experimented. Einarsrud and co-workers [14] reported the effect of relatively small additions (1–5 wt%) of nickel, nickel boride (NiB), and iron to promote the liquid-phase sintering of titanium diboride (TiB_2). Carbon was also added to some samples, in order to reduce the amount of oxygen impurities in the TiB_2 ceramics. The green bodies, formed by uniaxial pressing were sintered in a graphite furnace at 1300°-1700^oC, both under vacuum and in a 500 mbar argon atmosphere. High densities (>94% of theoretical density) were obtained at temperatures greater than or equal to 1500^oC. The weight loss of the samples during sintering was shown to be dependent on the densification rate and the final density was not governed solely by the thermodynamics of the system. Significant exaggerated grain growth was observed in samples with binders like nickel, NiB, and iron during sintering at 1700^0C. The exaggerated grain growth was observed to be closely related to the oxygen content of the samples and sintering temperature. The addition of carbon strongly reduced the density and the oxygen content and, thereby, inhibiting the grain growth. They have proposed that, exaggerated grain growth is enhanced by surface diffusion in a titanium-oxide-rich layer on the TiB_2 grains. The rate of exaggerated grain growth (or the number of large grains) in the system was decreased by a) lowering the sintering temperature, b) adding 1.5 wt% of iron instead of 1.5 wt% nickel, c) performing the sintering under vacuum instead of in an argon atmosphere, and d) decreasing the nickel content from 5 wt % to

1.5 wt%. Also, the exaggerated grain growth seems to be correlated to the weight loss or the content of the secondary phases. Einarsrud and co workers [14] proposed that the exaggerated grain growth in TiB_2 ceramics is enhanced by oxygen impurities. For the samples with added carbon in addition to nickel, the grain growth was inhibited (under vacuum)/limited (in an argon atmosphere), and these samples were shown to contain small amounts of oxygen. However, because the density of these samples was quite low, exaggerated grain growth was not expected to occur.

Baik and Becher [6] have noted the importance of oxygen as an active species to increase surface diffusion and grain growth during the pressureless sintering of TiB_2. Bellosi et.al [15] also observed the grain growth for TiB_2 powders containing oxygen impurities during hot pressing. The mechanism for grain growth in liquid-phase sintering is dissolution-reprecipitation, smaller grains are dissolved and reprecipitation occurs on the larger grains.

Kang and Kim [12] reported the pressureless sintering and properties of titanium diboride ceramic containing chromium and iron. Simultaneous addition of 0.5 wt% Cr and Fe was found to enhance the densification of TiB_2. The densities of specimens that were sintered for 2h at 1800^0C and 1900^0C were 97.6% and 98.8% of the theoretical value, respectively. The mechanical properties of the specimen sintered at 1800^0C, (strength of 506 MPa and a fracture toughness of 6.16 $MPa.m^{1/2}$), were much better than those observed in the specimen sintered at 1900^0C. Table 2.2 presents the summary of the literature reports revealing the influence of metallic binders on the microstructure and mechanical properties of TiB_2-based materials.
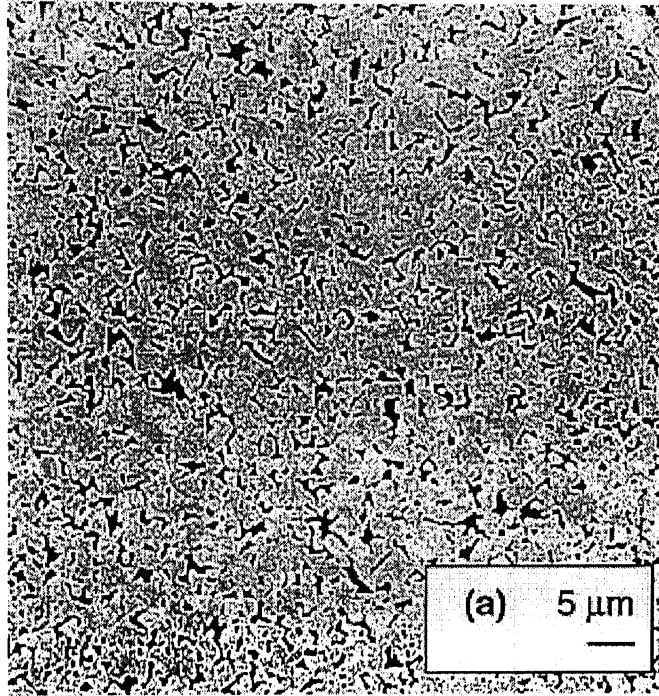
Fig. 2.2b: Microstructure of WC-8 wt % Co sintered at 1450°C, black phase representing the liquid Co [11].

Table 2.2 Overall summary of metallic additives influence on microstructure and mechanical properties.

Composition	Processing	Sintered density (% theoretical ρ_{th})	Microstructure	Vickers Hardness, GPa	Fracture Toughness, MPa.m$^{1/2}$	Strength, MPa	Reference
TiB$_2$-7.9Ni	Hot pressed	>99	coarse grained(7µm)	-	4	420	7
TiB$_2$-1.4Ni	Hot pressed	>99	Fine Grained(4µm)	-	6.4	670	
TiB$_2$-0.5Cr-0.5Fe	Pressureless(1800^0 C,2h)	97.6	Fine, uniform (4µm)	27.0±2.5	6.16±0.88	506.0±8.2	5
TiB$_2$-0.5Cr-0.5Fe	Pressureless(1900^0 C,2h)	98.6	-	31.3±2.9	5.90±0.93	262.1±14.8	
TiB$_2$-0.5Fe-10B$_4$C	Pressureless@200 0^{0}C,Ar 30Min	97.5	4.2µm Fe rich Phase at triple junction& Grain Boundaries	-	5.50	400	71

2.1.4 Non-metallic additives

Different non-metallic additives such as AlN, ZrO_2, SiC, Si_3N_4, CrB_2, B_4C, TaC, TiC, WC, TiN, ZrN, ZrB_2 has been used for attaining densification of TiB_2 with good mechanical properties [16-29]. Shirotorizuka et al. [19,23] observed the formation of grain boundary liquid phase (amorphous SiO_2), when SiC was used as an additive. Moreover, they identified partial liquid phase $(Ti, Zr)_5Si_3$ formation at triple point in TiB_2-19.5 wt% ZrO_2- 2.5/5.0 wt% SiC composite, processed via the hot isostatic pressing (HIP) route. Watanabe et. al [30] reported the formation of (Ti, Zr) B_2 solid solution in hot pressed TiB_2-30 wt. % ZrO_2 composites. Telle et. al [17] also reported the formation of $(Zr,Ti,)O_2$ solid solution in addition to $(Ti,Zr)B_2$ solid solution when 25 vol. % ZrO_2 added to TiB_2. In another interesting investigation, Torizuka et al. [21] has not reported any solid solution formation when 20 wt. % ZrO_2 binder was used to densify TiB_2 via HIP route. According to Murata et al. [28], TaC and TaN were quite effective for densification of TiB_2. In their work, (Ti, Ta) B_2 and (Ta, Ti) (C, N) solid solutions were observed to form when TaC was added to TiB_2 and the composite was hot pressed at 2000^0C. In another work, Park et.al [25] reported the formation of different reaction products like TiN and BN in TiB_2–2.5-10 wt% Si_3N_4 composites (sintered at 1800^0C) and observed that Si_3N_4 acted as a grain growth inhibitor.

Muraoka et.al. [18] reported the hot isostatic pressing of TiB_2- ZrO_2 composite. Dense sintered composites of TiB_2 and ZrO_2 (2 mol% Y_2O_3) have been fabricated by HIPing for 2h at 1500^0C under 196 MPa. The ZrO_2 particles in the composites consisted of more of m-ZrO_2. They have not identified any reaction products of TiB_2 and ZrO_2. The fracture toughness and bending strength of the composites with 30-mol% ZrO_2 content were 11.2 $MPa.m^{1/2}$ and 680 MPa, respectively.

Li et.al. [16] investigated the densification and mechanical properties of titanium diboride with aluminium nitride as a sintering aid. Titanium diboride (TiB_2) was hot pressed at 1800^0C with aluminum nitride (AlN) as a sintering aid. They recognized the presence of AlN had a strong influence of the sinterability and mechanical properties of TiB_2 due to the following mechanism. When a small amount of AlN ($\leq$ 5wt%) was added to the TiB_2, the rutile (TiO_2) present on the surface of the TiB_2 powder was eliminated by a reaction with AlN to form TiN and Al_2O_3, according the following reaction.

$$3TiO_2 (s) + 4AlN(s) \rightarrow 3\ TiN\ (s) + 2Al_2O_3(s) + 1/2\ N_2\ (g) \qquad (24)$$
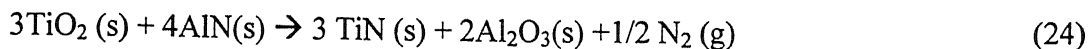
The elimination of TiO_2 markedly improved the sinterability and consequently the mechanical properties of TiB_2. However, when too much AlN was added ($\geq$ 10 wt. %), the sinterability and the mechanical properties decreased, apparently due to the remaining unreacted AlN.

The effect of SiC and ZrO_2 on sinterability and mechanical properties of titanium nitride, titanium carbonitride and titanium diboride was investigated by Torizuka et.al. [19]. ZrO_2 and SiC additions were effective in improving sinterability and mechanical properties of TiB_2. The density of TiB_2 and TiB_2-20%ZrO_2 after sintering at 1700^0C were 70 % of their theoretical densities. The addition of ZrO_2 had little effect in improving the sinterability of TiB_2. On the other hand, the density of TiB_2-19.5%ZrO_2-2.5%SiC was 97 % ρ_{th}. Although TiB_2 and TiB_2-20%ZrO_2 are lacking sinterability, the addition of SiC was very effective in improving the density after sintering due to the following reason. TiO_2 existing on the surface of TiB_2 powder reacts with SiC and formed TiC and SiO_2, according to the following chemical reaction.

$$TiO_2 + SiC \rightarrow TiC + SiO_2 \qquad (25)$$

In the case of TiB_2-2.5wt% SiC sintered compacts, the added SiC was all transformed to SiO_2, Approximately 3.5 vol% of SiO_2 would form in this reaction. Residual TiO_2 and B_2O_3 contributed to lowering the melting point of SiO_2 and increasing the liquid volume.

Holcombe et.al. [26] reported the microwave sintering of titanium diboride. Using a 2.45 GHz, 6 KW microwave furnace adapted for inert gas sintering, titanium diboride (TiB_2) was rapidly microwave-sintered to >90% of theoretical density with sintering temperatures of 1900 to 2100^0C and soak times of 30 min or less. Densification behavior with low-level additives was evaluated and chromium diboride (CrB_2, 3Wt.%) was found to be an excellent sintering additive and grain growth inhibitor. A special covering system was used to produce oxide free TiB_2. Comparison with conventional sintering indicated that microwave sintering of TiB_2–3wt% CrB_2 occured at lower temperatures (i.e. 200^0C lower) and yielded material with significantly improved hardness, grain size, and fracture toughness.

Wen et.al [31] have reported the reaction synthesis of TiB_2–TiC composites with enhanced toughness. In-situ toughened TiB_2-TiC_x composites were fabricated using reaction synthesis of B_4C and Ti powders at high temperatures. The resulting materials possessed very

high relative densities and well developed TiB_2 plate-like grains, leading to rather high fracture toughness (up to 12.2 MPa m$^{1/2}$) .The reaction products mainly consisted of TiB_2 and TiC_x. No other phases, e.g. Ti_3B_4, TiB, Ti_2B_5 and free Ti, were observed. The microstructural morphology was characterized by TiB_2 plate-like grains distributed uniformly in the TiC_x matrix. The very high reaction temperature was believed to be responsible for the formation of plate-like grains, which, in turn, was responsible for the much-improved mechanical properties. The main toughening mechanisms were likely to be crack deflection, platelet pullout and the micro-fracture of TiB_2 grains. Tough TiB_2-TiC composites have also been successfully synthesized by means of in-situ reaction of B_4C and Ti powder mixtures at relatively high temperatures [31]. Powder mixtures of Ti:B_4C molar ratios of 3:1 (3Ti-B_4C) and 4.8:1(4.8Ti-B_4C) were completely transformed to high density (TiB_2-TiC_x) composites, when hot pressed at 1700^{0}C~1800^{0}C under 35 MPa for 6 min. Ti_3B_4, TiB, Ti_2B_5 and free Ti phases were not identified in the samples by XRD and EDAX analysis. The high sintering temperature is believed to be the key to achieving the high relative density and the well-developed plate-like morphology of the TiB_2 grains. As a result, the sintering reaction, densification and grain growth proceeded by a transient liquid mechanism. The transformation of Ti_3B_4 and TiB_2, and the flow and/or vaporization of Ti also occurred in the local high-temperature environment. The rapid growth of the TiB_2 grains led to many inclusions and defects within the TiB_2 grains. Rather high fracture toughness (K_{IC} up to 12.2 MPam$^{1/2}$) has been obtained by the hot pressing to high density and the existence of well-developed TiB_2 plate-like grains. The main toughening mechanisms remain crack deflection and the pullout and fracture of the TiB_2 plate like grains.

Baumgartner and Steiger [32] reported the sintering and properties of TiB_2 made from powder synthesized in a plasma-arc heater. Their work describes the essentially complete densification of titanium diboride powder by pressureless sintering. The high purity micron sized titanium diboride powder was produced in arc plasma by the reaction of titanium tetrachloride and boron trichloride gases in the presence of excess hydrogen according to the following reaction:

$$TiCl_4 (g) + 2BCl_3 (g) + 5H_2 (g) \rightarrow TiB_2 (s) + 10HCl (g) \qquad (26)$$
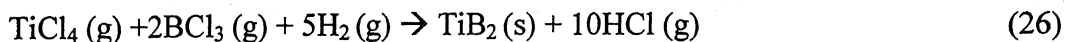
A chlorinated hydrocarbon was used into the reactor to introduce a small amount of carbon into the titanium diboride powder. The carbon assists densification by inhibiting grain growth of the diboride. Titanium diboride may be pressureless sintered to greater than 99% of theoretical density by use of a sub micrometer-sized powder produced in arc plasma. Densification proceeds by self-diffusion and requires a high grain-boundary surface area (small grain size) to reach completion. Previous difficulties in achieving fully dense titanium diboride by the pressureless sintering of carbothermic powder are attributed to rapid grain growth prior to complete densification. The activation energy for grain growth in titanium diboride is 1.02 MJ/mol (244 Kcal/mol). The internal stresses, caused by anisotropic thermal expansion coefficients, strongly influenced the physical properties of the material. The influence on modulus, strength, electrical and thermal conductivity were most pronounced, if the grain size was large enough to induce microcracking. The strength was significantly affected by internal stresses even in the absence of microcracking. The stresses adversely affected the strength and produced a positive strength temperature coefficient. Relatively pure titanium diboride (grain size $\leq 4\mu m$) does not exhibit intrinsic slow crack growth at temperatures up to 1400^0C. A time-dependent mechanism exists, which blunts flaw tips and strengthens the material at low stressing rates. A negative slow crack growth exponent in dynamic tests manifests the strengthening mechanism.

The synthesis of dense TiB_2–TiN nanocrystalline composites through mechanical and field activation was investigated by Lee and Munir [33]. The starting materials were powders of Ti (99.7% pure), amorphous B (95%-97% pure), and BN (99.9% pure). The initial particle size ranges for the three powders were 20-45, 1 and 2-3 μm, respectively. The powders were blended in a stoichiometric ratio to promote the following reaction.

$$Ti + 0.5B + 0.5 \ BN \rightarrow 0.5 \ TiB_2 + 0.5 \ TiN \qquad (27)$$
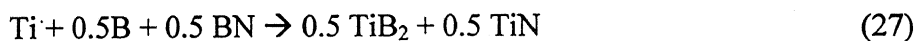
Powder mixtures of Ti, BN, and B were mechanically activated via ball milling. Some powders were milled to reduce crystallite size but to avoid initiating a reaction. In other cases, the powders were milled and allowed to partially react. All these were subsequently reacted in a spark plasma synthesis (SPS) apparatus. The products were composites with equimolar nitride and boride components with relative densities ranging from 90.1% to 97.2%. Crystallite size

analyses using the XRD for the TiN and TiB_2 components indicated sizes in the range 38.5-62.5 and 32.2-58.8 nm, respectively. Vickers microhardness measurements (at 2N) on the dense samples provided values ranging from 14.8 to 21.8 GPa and fracture toughness (at 20 N) values ranging from 3.32 to 6.50 MPa $m^{1/2}$.

Synthesis of $MoSi_2$–titanium boride composites via in situ displacement reactions was reported by Silva et. al [34]. In-situ solid-state displacement reactions were used to synthesize $MoSi_2$–molybdenum boride and $MoSi_2$–TiB_2 composites at temperatures lower than 0.7 T_m (where T_m is the melting pint of the boride). The $MoSi_2$-TiB_2 composites, produced by in-situ displacement reactions possessed very fine microstructures that could not be achieved when the staring materials were elemental powders, i.e. when no displacement reaction is involved. No evidence of liquid phase formation could be found in any of the samples, while the formation of intermediate silicides seems to be an important part of the process. When the elemental powder reacts, no intermediate boride phases could be identified. Although these mechanism remarks are relevant and helpful to understand some of the aspects of the process occurring, there is no clear explanation for the difference in scale of the microstructure of the $MoSi_2$-TiB_2 composites and its relationship to the reactants involved. Presently, it is speculated that the magnitude of the driving force for the synthesis reaction may play a role in defining the scale of the microstructure. Standard free energy change (ΔG^0_{298}) for the two paths for production of $MoSi_2$-TiB_2 composites are as follows.

$$3/7\ Mo_5Si_3 + Ti_5Si_3 + 10\ B = 15/7\ MoSi_2 + 5\ TiB_2 \qquad (28)$$
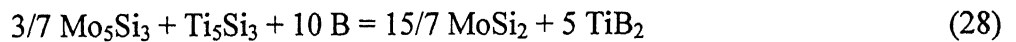
$$\Delta G^0_{298}\ (KJ) = -1124.5,\ \Delta H^0_{298}\ (KJ) = -1149.6$$

$$5Ti + 10\ B + 15/7\ Mo + 30/7\ Si = 15/7\ MoSi_2 + 5\ TiB_2 \qquad (29)$$

$$\Delta G^0_{298}\ (KJ) = -1840.3,\ \Delta H^0_{298}\ (KJ) = -1861.9$$

where ΔH^0 is standard change in enthalpy at 298 K.

Itoh et.al. [35] fabricated TiB_2 sintered compacts by hot pressing. A sintered compact of titanium diboride (TiB_2) was prepared by hot pressing the synthesized TiB_2 powder, which was obtained by a solid-state reaction between TiN and amorphous boron. Densification of the

sintered compact occurred at 1800^{0}C under 20MPa pressure for 5 to 60 min with the aid of a reaction sintering, including the TiB$_2$ formation reaction between excess 20 at% amorphous boron in the as-synthesized powder (TiB$_2$ +0.2B) and intentionally added 10 at% titanium metal. A homogeneous sintered compact of a single phase TiB$_2$, prepared by hot pressing for 30 min from the starting powder composition [(TiB$_2$ + 0.2 B) + 0.1 Ti], exhibited a fine-grained microstructure composed of TiB$_2$ grains with diameters of 2 to 3 μm. The bulk density was 4.47 g/cc, i.e. 98% of ρ_{th}. The microhardness, transverse rupture strength and fracture toughness of the TiB$_2$ sintered compact were 2850 Kg/mm^{-2}, 48 Kg/mm^2 and 2.4 MPa.m$^{1/2}$ respectively.

Table 2.3 presents the summary of results obtained using non-metallic additives on the densification and mechanical properties of TiB$_2$.

Table 2.3 Summary of research results illustrating the effect of different non metallic sinter additives on microstructure and mechanical properties of TiB$_2$.

Composition	Processing	Sintered density (% theoretical ρ_{th})	Microstructural Phases	Hardness GPa	K_{IC}, MPa m$^{1/2}$	Flexural Strength MPa	References
TiB$_2$	HP, 1800°C, 1hr, 30MPa, Ar Atmosphere	89.0	TiB$_2$	(load 2.94N) 12.5GPa	4.5	360	16
TiB$_2$+2.5% AlN	"	94.0	TiB$_2$, BN, TiN	16.09	5.0	500	
				22.0	6.8	650	
TiB$_2$+5% AlN	"	98.0	TiB$_2$, BN, TiN, Al$_2$O$_3$	14.0	5.2	500	
TiB$_2$+10% AlN	"	87.0	Additional to above AlN	12.0	4.6	400	

No.	Sample	Process	Density (%)	Phases / Notes		Value	Bending
17	TiB₂+0%ZrO₂	PS: 2150°C HR:50K/min	93.1	TiB₂	-	5.4	-
	TiB₂+25%ZrO₂(Vol%)	Ar Atmosphere HP:1700°C@ 24MPa for 1 hr, Ar Atmosphere	98.0	TiB₂, ZrO₂, (Ti,Zr)B₂, (Zr,Ti)O₂ solid sol	-	9.5	-
18	TiB₂+0mol%ZrO₂(2wt% ZrO₂)	HIP, Ar gas@ 196MPa, 1500°C for 2 hr	97.6	No reaction between ZrO₂ & TiB₂ due to lower sintering temp Avg.TiB₂ six: 1.75µm(no GG) ZrO₂ size:1.30yn		3.7	(Bending) 650
	TiB₂+10mol%ZrO₂	"	98.1			5.6	800
	20mol%ZrO₂	"	98.6	"		7.1	900
	30mol%ZrO₂	"	98.4	"		11.2	680
				"		7.1	550

Material	Conditions	Density	Microstructure	Hardness (0.98N for 15 sec)	Strength	Toughness	Ref
40mol%ZrO2	"	96.4			480	6.1	
50mol%ZrO2	"	94.1					24
TiB2-0wt%SiC	PS 1700°C, Vaccum+HIP	62.0	Amorphous SiO2, liquid phase along		(3-point) 450	3.3	
TiB2-2.5wt%SiC	1600°C, 200MPa of	96.0	G.B.		660	4.3	
TiB2-5wt%SiC	Ar	93.0	TiB2, SiC & TiC		850	4.9	25
TiB2+0 wt%Si3N4			Grain growth (7µm) Grain Size of	(0.98N for 15 sec) 23	(4-point) 380	(196N, 15sec) 5.8	
TiB2-2.5wt%Si3N4	HP 1800oC for 1 hr Ar atmosphere	99.0	TiB2 : 3µm	27	810	5.1	
			TiB2,TiN,BN	21	510	4.8	
TiB2-5wt%Si3N4		99.0	"	20	400	4.4	

Material	Condition	Density (%)	Microstructure	Fracture toughness	Strength	Ref
TiB₂	(Argon Atmosphere) H.P.				(3-Point)	8
	1600°C,1h	91.0	4.8μm grain size (avg)	4.1	305	
	1700°C,1h	95.0	5.0μm grain size (avg)	4.3	498	
	1800°C,0.5h	96.0	5.3μm grain size (avg)	5.3	545	
	1800°C,1h	97.0	8.1μm grain size (avg)	5.7	558	
	1800°C,1.5h	-	10.5μm irregular grains	6.3	538	
	1800°C,2h	-	12.68μm irregular grains	6.8	475	
	1900°C,1h	-	12.2μm irregular grains	6.2	521	
TiB₂-3wt%CrB₂	(Flowing Argon Atmosphere) MW, 1900°C,30min	95.0	4μm grain size (avg)	6.24	DPH-1Kg load(GPa) 28.9	26

	Commercial, 1900 °C,30min	84.0	4μm grain size (avg)	17.8	5.66
	MW, 2100°C,30min	98.0	4μm grain size (avg)	27.0	6.10
	Commercial, 2100 °C,30min	90.0	12μm grain size (avg)	17.9	6.10
			20μm grain size (avg)	26.7	
TiB_2	HP, 2000°C, 1h, 13.8MPa	-	11μm grain size		4.78
	HP, 1800°C		11μm grain size	-	4.4
TiB_2+10wtB_4C+ 0.5wt%Fe			7μm grain size	1656HV	4.6
TiB_2+10wtB_4C+	HP, 1800°C	-		2623HV	4.6

Material	Processing	Density (%)	Microstructure	Hardness	K	Strength	Test / value	
3wt%Fe								
TiB$_2$+30wtB$_4$C+ 0.5wt%Fe	HP, 1800°C	96.0-99.9	7μm grain size	2705HV	4.4	570	-	
TiB$_2$+30wtB$_4$C+ 3wt%Fe	HP, 1800°C	"	4μm grain size	2658HV	4.5	-		
TiB$_2$+50wtB$_4$C+ 0.5wt%Fe	HP, 1800°C	"	4μm grain size	2712HV	4.6	620		
TiB$_2$+50wtB$_4$C+ 3wt%Fe	HP, 1800°C	"				-		
33.3TiB$_2$+66.7A IN	Mechanochemical synthesis HP, 2000°C, 1h, 25MPa	96.8		GPa 17.8	5.21	352	4-point	16

68

33.0TiB$_2$+64.0A IN	HP, 1740°C, 0.5h, Gas pressure sintering,		98.2	9.5	5.05	539
10.0TiB$_2$+88.0A IN***	1750°C,1h,0.2MPa Pressure sintering,		96.5		3.7	220
45.7TiB$_2$+54.3A IN	1700°C,2h Ti+Al+BN: Mechanochemical synthesis		96.1	12	4.6	172
		Effective additives TaC>TaN>TiC>WC>TiN>Si$_3$N$_4$>ZrN>				
TiB$_2$+0(wt%)	HP,2000°C, 2600PSi,30 min		90.0	(Superficial) 96.0(RN$_{15}$)		28
95%TiB$_2$+5%Ta C	" "	ZrB$_2$	97.6	98.4		
5TaN	" "		96.8	98.2		
5TiC	" "		96.5	98.0		

5WC	"	95.9		94.3
5TiN	"	95.0		98.1
5Si$_3$N$_4$	"	86.0		87.0
5ZrN	"	83.9		92.8
5ZrB$_2$	"	79.6		88.4
99%TiB$_2$+1TaC	"	98.0	(Ti,Ta)B$_2$ and (Ta,Ti)(C,N) type solid solutions had formed	97.8
99%TiB$_2$+5TaC	" 60min	99.4		98.2
90%TiB$_2$+10Ta	"	99.4		98.4
C	"	99.8		97.8
85%TiB$_2$+15Ta	"	100.0		97.9
C	"	97.4		97.8
80 +20TaC	HP			

	2000,2600Psi, 30 min		
25TaC	99.6		96.9
30TaC	99.6		96.4
40TaC	98.4		96.9
50TaC	98.3		97.2
50 +50TaC			97.6
"	HP 2100,2600Psi ,30min	99.4	97.9
"	HP 2000,2600Psi ,60min	98.7	97.5
"	HP 2000, 5200Psi,30min	99.8	
"	HP 2100,		

71

Composition	Processing	Density (%)	Microstructure	Hardness (HV)	Fracture toughness (Load 98N)	Strength (3-Point)	
TiB₂+Ti	5200Psi,30min	99.6	Needle of fibre type TiB₂	(HV) 19GPa	4.5	(3-Point) 360MPa	35
TiB₂-1vol%Fe	HP, 1900°C,2hr,28.5Mpa, Argon atmosphere	99.0	TiB₂ avg size:6.38μm		(Load 98N) 6.6	(3-Point) 520	27
TiB₂-10vol%B₄C-1vol%Fe	HP, 1700°C,1hr,35Mpa, Argon atmosphere	99.5	TiB₂-4.38μm B₄C -2.97μm		7.2	700	
TiB₂-20vol%B₄C-1vol%Fe	"	99.5	TiB₂-4.42μm B₄C -4.12μm		7.6	660	
TiB₂-30vol%B₄C-1vol%Fe	"	97.5	TiB₂-4.28μm B₄C -4.54μm		7.1	600	
TiB₂-	PS		Grain boundary glassy phase was		5	(3-Point)	56

Material	Processing	Density (%)	Observations	Hardness	Toughness	Strength (MPa)	Ref
19.5wt%ZrO_2	1700°C+HIP 1600 PS	70	observed		3.3	1250MPa	30
TiB_2-19.5wt%ZrO_2 +2.5%SiC	1700°C+HIP 1600	97.0			-	420 / 1200	
TiB_2	"		$(Ti\ Zr)B_2$ solid soln formed	(3000N load VH) 18GPa	5	(3-Point) 800	
TiB_2-20wt%ZrO_2	HP 1900°C,30min,20MPa,Vacuum	-					
TiB_2-30wt%ZrO_2							
TiB_2	HPS: (high pressure sintering),2250K,300sec,3 GPa	94.6-97.9	1.4μm TiB_2	19.2	-		29
"	2500K " "	98.2		21.7	2.8		
"	2750K " "	99.3		24.5	3.2		
TiB_2+15%TiC	2250K " "			22.6	3.5		
Ti+B (1:2)	2500K " "	97.82		23.9	3.9		

"	HPCS:high pressure self combustion synthesis 2250K (NH:No bonding)	98.04	23.6	3.5
"		98.03	24.0	3.8
"	2500K "	98.72	23.9	3.6
"	2750K "	98.86	24.2	3.9
"	2250K (300sec) "	99.19	24.5	3.8
"	2500K " " 2750K " "		24.6	4.5
Ti+B+C	2250K, NH,	98.5	22.7	4.3
TiB$_2$+15%TiC	"		23.8	4.2
"	2250K	99.1	23.5	4.6

74

Composition	Processing	Density (%)	Phases / Grain size	Hardness (Vickers)	(4-Point)	(3-Point)	Ref
TiB$_2$-0.7vol%Ni	HP, 2250°C, 30Mpa, 20min	97.9	Grain Size : 1.5μm; Traces: Ni$_4$B$_3$, Ni$_3$B	23.3 ± 1.4	5.81 ± 0.23	716 ± 75	
	2500K "" (300sec)	99.0					20
TiB$_2$-10vol%B$_4$C-0.7vol%Ni	HP, 1600°C, 30Mpa, 20min	97.9	1.6μm; Ni$_3$B$_2$O$_6$, Ni$_4$B$_3$, in small amount Ni$_3$B, Ni$_3$C-traces	19.3 ± 0.4	6.22 ± 0.15	717 ± 84	
TiB$_2$-	HP, 1600°C, 30Mpa, 15min	95.6	TiB$_2$, B$_4$C, 2.6μm	15.9 ± 1.6	5.69 ± 0.49	736 ± 54	
TiB$_2$-10vol%B$_4$C-10vol%*2Y-ZrO$_2$-07vol%Ni	HP, 1650°C, 30Mpa, 60min	97.0	Low amounts of ZrTiO$_4$ & Ni$_4$B$_3$; " 3.5μm	15.0 ± 1.3	6.80 ± 0.34	734 ± 47	
TiB$_2$-10vol%B$_4$C-10vol%*2Y-ZrO$_2$-1.2vol%Ni	HP, 1750°C, 30Mpa, 20min	-					
	HIP, 1600°C,		Grain growth	(Vickers) 3.5		(3-Point)	22

Material	Conditions	Relative density (%)	Microstructure	Hardness (GPa)	HV 10	Fracture toughness	450MPa	
TiB$_2$	200Mpa, 2hr Argon gas atmosphere			26		3.7	880	23
TiB$_2$-5 wt%2Y-ZrO$_2$			TiB$_2$: 2μm →4-6μm, ZrO$_2$: 0.1μm →2-5μm	25		4.6	1180	
TiB$_2$-10 wt%2Y-ZrO$_2$			Grain growth controlled	24		5.2	1200	
TiB$_2$-20 wt%2Y-ZrO$_2$			TiB$_2$: 2μm →2-5μm, ZrO$_2$: 0.1μm →1-3μm	21.0		5.1	1280	
TiB$_2$-20 wt%2Y-ZrO$_2$-2.5% SiC		59.0	SiC act as a grain growth inhibitor.	23		5.2	1280	
TiB$_2$-5 wt%2Y-ZrO$_2$-5% SiC	HIP, 1600°C,	98.0		23.1		7.4	860	
TiB$_2$-11vol% ZrO$_2$(Monoklin)	HP, 1500°C, Ar	98.1		19	1787 ± 38	4.89 ± 0.43	607 ± 152	
-18.3 vol% ZrO$_2$(Monoklin	"	96.9			1708 ± 102	5.45 ± 0.56	671 ± 52	

76

Composition	Method	Density %				Comments	Ref
27.3 vol% ZrO₂(Monoklin)	"	97.8	1429 ± 42	6.47 ± 0.67	622 ± 23		
TiB₂-7.1(vol%3mol% Y₂O₃tetragonal ZrO₂)	"	97.3	1923 ± 46	5.34 ± 0.28	660 ± 106		
-18.7 "	"	96.8		5.99 ± 0.54	598 ± 54		
26.9 "	"	96.2	1737 ± 116	6.70 ± 0.52	269 ± 75		
		97.8	1630 ± 51				
TiB₂-19.5wt%(2mol %Y₂O₃-ZrO₂)	HIP 1600°C	68.0				SiC addition improved the sinterability drastically, grain boundary phases Ti,Siₓ Zr at Triple point (TiZr)₅Si₃ Partial liquid phase at the sintering temp of 1700°C	23
TiB₂-19.5wt%(2mol %Y₂O₃-ZrO₂)-2.5-5.0 wt%SiC "	"	96.0					

HP : hot pressing; HIP: hot isostatic pressing; MW: microwave; HV: vickers hardness; RN: Rockewll superficial (N scale);

2.2 Tribological behavior of hard materials

In 1966, the concept of Tribology was enunciated in a report of the, Department of Education and Science, UK. Typically, tribology covers the interdisciplinary science and technology of interacting surfaces in relative motion and associated subjects and practices. Surface interactions in a tribological interface are highly complex, and their understanding requires knowledge of various disciplines including physics, chemistry, solid mechanics, fluid mechanics, thermodynamics, heat transfer, materials science, rheology, lubrication, machine design, performance and reliability. An alternative definition is that tribology is the art of applying operational analysis to problems of great economic significance, namely, reliability and wear of technical equipment, ranging from spacecraft to household appliances. A popular English language equivalent of 'Tribology' is *friction* and *wear* or *lubrication* science [36].

Mercer and Hutchings [37] reported the friction and wear behavior of CP titanium and Ti-6Al-4V against alumina in different testing environment (air,Ar,O_2,N_2). The analysis of reported wear data indicated that wear loss of Ti-6Al-4V is highest in O_2 atmosphere and lowest in inert atmosphere (Ar). The major wear mechanism in different atmosphere is identified as abrasion. High purity single-crystal Si is used for semiconductor applications, and sometimes as a smooth substrate for tribological application [38]. From a structural standpoint, some nickel alloys are among the toughest known materials. The Ni alloys have ultra-high strength and high moduli comparable with steel. Ni-based alloys are strong, tough, and ductile at cryogenic temperatures. However, Ni-based alloys in metal-to-metal sliding usually exhibit poor galling resistance. Mo and/or Co is normally added to obtain superior sliding characteristics. This is probably because of the formation of beneficial oxide-films [39]. In a recent research report, it is observed that laser melted ternary metal silicide, $Cr_{13}Ni_5Si_2$ alloy has excellent wear resistance compared to hardened 0.45%C steel and 1.0%C-1.5%Cr containing tool steel under sliding wear conditions at 98-196N load, measured on a ball-on-wheel tribometer [40].

Friction of Ceramics

Fracture toughness plays an important role in friction of ceramics. Under certain tribo-conditions, brittle fracture can occur in contact zone; often intergranular in polycrystalline ceramics. Since the fracture process provides an additional energy dissipation mechanism at

sliding contact, the occurrence of fracture leads to increased friction. The recently compiled measurements of specific wear amount (w_s) and friction coefficient (μ) data for several ceramics (Si_3N_4, SiC, ZrO_2 and Al_2O_3 against themselves) are illustrated in Figure 2.3. It is noticed that specific wear rate can change by six orders of magnitude for even same friction coefficient [50].

At low loads, plastic grooving on SiC occurs without any fracture and COF is low. But with increase in load, brittle fracture occurred around the sliding track, leading to a higher COF. Both diamond and TiN exhibit high COF in vacuum for self mated couple. The COF of diamond is 0.05-0.1 in air and 0.1-0.2 for TiN. Significant surface oxidation of TiN leading to TiO_2 formation causes low friction. Diamond has dangling C-bonds on the surface and it is reactive, H-absorbs readily on the surface of diamond and adsorbed hydrogen from the environment forms a hydrocarbon layer, which reduces friction. High thermal conductivity dissipates frictional heat energy and is believed to result in low friction and wear.

Several studies have been performed to investigate the wear behavior of advanced structural ceramics [41,42]. The fretting wear behavior of boride containing composites under dry sliding conditions against bearing steel has been reported and a tribochemical wear model has been formulated [43]. The influence of fracture toughness, an important property for brittle materials, on the wear behavior of Y-TZP ceramics has been also investigated [44].

The tribological behavior of TiC-based ceramics against high speed steel was studied using a pin-on-disk tribometer [45]. Oxidative wear coupled with adhesive and abrasive wear was the major mechanism for material removal. Rainforth [46] investigated the micromechanical and microchemical processes involved in dry sliding of several structural ceramics (Y-TZP, Mg-PSZ and ZTA) against bearing steel and zirconia toughened alumina (ZTA) ceramic counterfaces. The wear mechanism in these tribocouples was dominated by the tribochemical reactions at the sliding contacts. The role of zirconia phase transformation was found to be negligible.

The fretting wear behavior of TiB_2–containing composites against ball bearing steel in lubricating medium was investigated and reported in literature [47]. The wear behavior of WC-based materials was also reported [48]. Mukerji et al. studied the wear performance of sialon-based composites with varying amount of TiC or BN (up to 20 vol %) against ball bearing grade steel under dry sliding conditions [49].

It can be noted here that TiB_2–containing materials have great potential for tribo-applications due to two reasons: high hardness and the lubrication efficiency of the boric acid film produced at the tribological interface. Although tribological studies on several structural ceramics have been reported in the literature, none of the studies has evaluated the wear performance of TiB_2–based materials with non-metallic additives.

Role of Debris Particles:

The size and shape of debris may change during sliding in dry lubricated systems, therefore the condition of a system can be monitored by nature of debris. Mild wear is characterized by finely divided wear debris (typical 0.01-1μm in particle size). The worn surface in case of mild wear is relatively smooth. Severe wear, in contrast, results in much larger particles, typically on the order of 20-200 μm in size, which may be visible even with naked eye and the worn surface is rather rough. Debris particles can be classified based on wear mechanism or their morphology. Regarding the particles present in wear debris, these are generally classified based on their morphology – plate-shaped, ribbon-shaped, spherical and irregular-shaped. The load dependence of the formation of wear debris particles is reported in one of our recent work. The newly developed WC-ZrO_2 nanocomposite exhibits very low wear rate ($X10^{-8}$ mm^3/N.m) in contact with steel, which produce very finer irregular shaped debris particle at 2N load and relatively larger at higher load (see Figure 2.4a &b) [51].

Based on the adhesion theory of friction, Rabinowicz proposed that the average diameter of a loose wear debris particle (d) is dependent on work of adhesion:

$$d = 60,000 \frac{W_{ad}}{H} \qquad (30)$$

Where, W_{ad} is work of adhesion, H = hardness of the material and d = debris diameter.

From (30), it is clear that the size of wear debris particles, being directly proportional to the work of adhesion, is strongly dependent on normal load and tangential force. In fact, COF linearly increases with W_{ad} [52]. This can be rationalized from the fact that in order to maintain relative motion at frictional contact, higher frictional force is necessary to break the adherent bonds between interlocking asperities at higher loads.

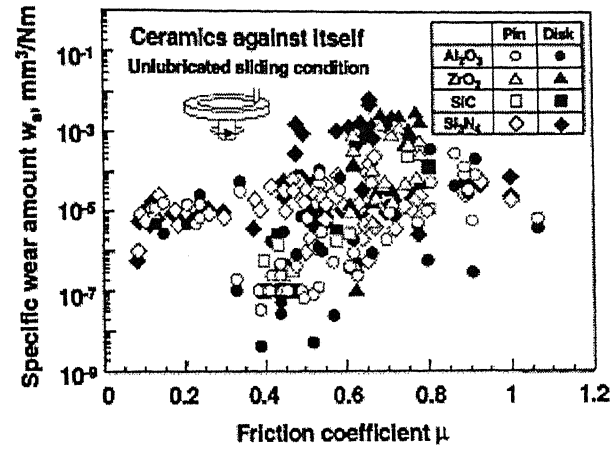Fig. 2.3: Specific wear rate amount (w_s) of ceramics in relation to friction coefficient (μ) measured in unlubricated sliding in air [50].
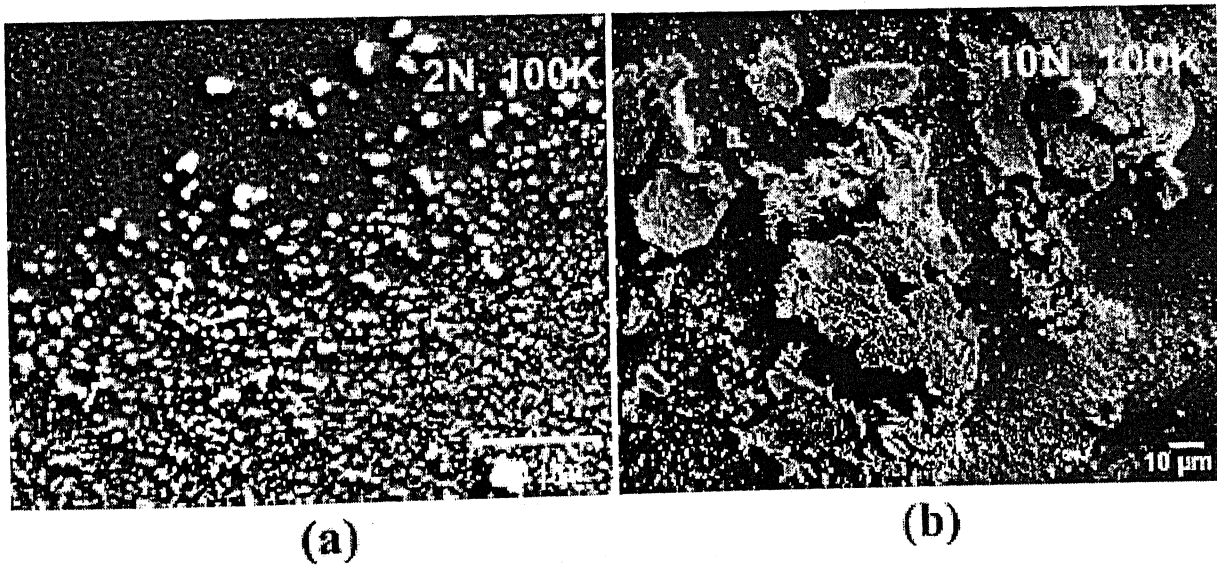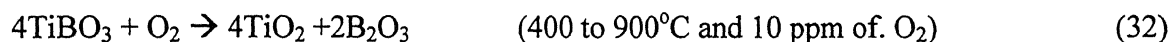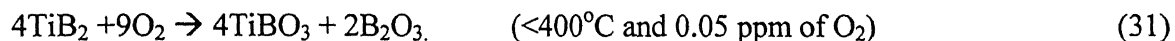

(a) (b)

Fig. 2.4: Variation of debris particle size in case of mild wear (a) and severe wear (b) of ceramics.

2.3 High Temperature oxidation behavior of TiB$_2$- based materials

In high temperature applications, the oxidation resistance is an important property to be critically considered. Titanium diboride powder itself is associated with surface oxides like TiO$_2$, TiBO$_3$ and B$_2$O$_3$ [53]. Monolithic TiB$_2$ has poor oxidation resistance compared to TiB$_2$ with Si or Al based additives [55,58]. These additives can form protective glassy SiO$_2$ [55,64] or Al$_2$O$_3$ [58] layer on the surface of composites. Koh et.al [60] reported the improved oxidation resistance of TiB$_2$ due to coating of protective amorphous SiO$_2$ layer on the surface.

Oxidation mechanism of TiB$_2$ depends on the temperature, partial pressure of oxygen, time of exposure, porosity and the nature of sintering additives. Kulpa et.al [62] reported that the oxidation of TiB$_2$ powders starts below 400°C and identified the formation of TiBO$_3$. They proposed that the oxidation mechanism at different temperatures and oxygen pressures was as follows:

$$4TiB_2 + 9O_2 \rightarrow 4TiBO_3 + 2B_2O_3 \qquad (<400°C \text{ and } 0.05 \text{ ppm of } O_2) \qquad (31)$$

$$4TiBO_3 + O_2 \rightarrow 4TiO_2 + 2B_2O_3 \qquad (400 \text{ to } 900°C \text{ and } 10 \text{ ppm of. } O_2) \qquad (32)$$

Reactions (31) and (32) occur concurrently in the temperature range of 400 to 900°C.

Tampieri and Bellosi investigated the oxidation of monolithic TiB$_2$ (hot pressed at 1850°C for 60 min and at 30MPa), Al$_2$O$_3$-TiB$_2$ [63] and Si$_3$N$_4$-TiB$_2$ [64] composites. It was observed that TiB$_2$ starts to oxidize at around 400°C. They found that the oxidation reaction was governed by a diffusion mechanism up to 900°C. The crystalline TiO$_2$ and B$_2$O$_3$ were detected in the oxide scale. Fig 2.5 illustrating the isothermal weight gain at various temperatures for a) TiB$_2$;b) Al$_2$O$_3$-(30 vol %) TiB$_2$; c) Si$_3$N$_4$-(20 Vol%)TiB$_2$. The overall oxidation reaction was represented by

$$TiB_2 + 5/2 \, O_2 \rightarrow TiO_2 + B_2O_3. \qquad (33)$$

Crystalline B$_2$O$_3$ was identified on the surfaces of monolithic TiB$_2$ after oxidation at 700°C and 800°C [63]. Diffusion controlled oxidation kinetics was observed up to 900° C [63]. A linear behavior was noted for longer periods (8 and 13 h) of oxidation at 1000°C and 1100°C. Fig 2.6 shows the oxidized surfaces of monolithic TiB$_2$ and Al$_2$O$_3$-TiB$_2$ composite, oxidized at 1000°C in air. Highly textured rutile can be seen in Fig. 2.6a. Arhenius plot of oxidation rate constants of TiB$_2$, Al$_2$O$_3$-TiB$_2$ and Si$_3$N$_4$-TiB$_2$ are shown in Fig. 2.7.

The large volume expansion that occurred during the oxidation of TiB_2 to TiO_2 caused cracking in the oxide layer, resulting in an increase in the active area for oxidation and heterogeneous diffusion in the barrier layer [64]. It was observed that the oxide scale was composed of only highly textured TiO_2 crystals [64].

The oxidation kinetics of TiB_2 (71.6wt%) cermets containing Fe-Ni-Al-Cr showed two kinetic range, a parabolic one up to 775°C and a linear one above 800°C(Fig. 2.8) [65]. Koh et.al [61] investigated the oxidation behavior of hot-pressed TiB_2–2.5wt% Si_3N_4 composite at temperatures between 800° and 1200°C for up to 10h in air. It was reported that TiB_2 exhibited two distinct oxidation behavior depending on the exposure temperature. At temperature below 1000°C, parabolic weight gains were observed as a result of the formation of TiO_2 and B_2O_3 (*l*) on the surface (Fig.2.9). The oxide layer was severely cracked during cooling after the oxidation due to the thermal expansion mismatch between the layer and the substrate (Fig. 2.10a). At temperatures above 1000°C, crystalline TiO_2 was identified along with gaseous B_2O_3. In this case, the surface was covered with only thick crystalline TiO_2 layer. Fig. 2.10b shows the spheroid crystalline phase of TiO_2 on the oxidized surface of TiB_2–2.5 wt% Si_3N_4 at 1000°C in air.

Graziani et.al investigated the oxidation of TiB_2–12.06wt. %B_4C–2.1wt.% Ni composite [66], which was processed by hot pressing. They reported a behavior similar to monolithic TiB_2 up to 900°C, with parabolic kinetics indicating a diffusion-limited reaction. The morphology of the oxidized surfaces showed the formation of a scale of increasing thickness and smoothness with the presence of glassy bubbles (B_2O_3) and cracks. Highly textured TiO_2 (rutile) and crystalline B_2O_3 were observed in increasing amounts with increasing temperature. The traces of $TiBO_3$ and $Ni_3B_2O_6$ were also detected on the oxidized surface. At 1000°C, the best fit of the data was obtained with the Ginstiling-Brounshtein equation [[1-(2/3)\alpha] - (1-\alpha)^{2/3} \approx kt$ (where $\alpha \approx \Delta w/s$)] which considers a three-dimensional diffusion process associated with a decrease in the reaction surfaces as the process proceeds, owing to the growth of a product layer around the reactants, considered as spherical particles.
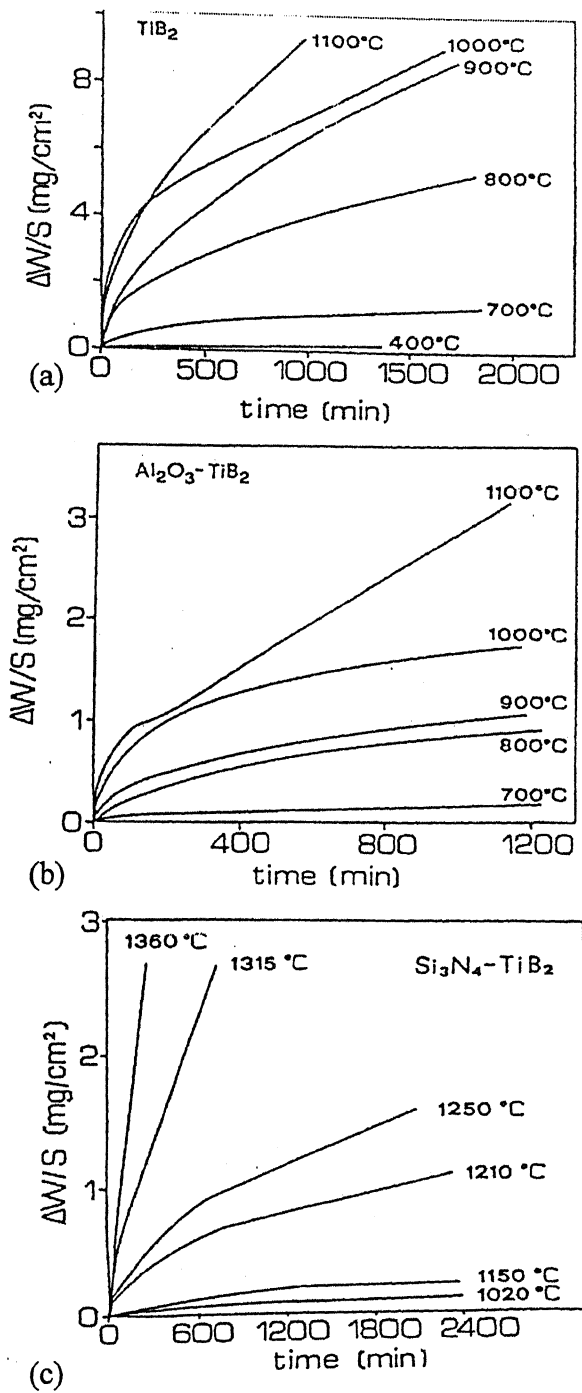
Fig. 2.5: Isothermal weight gain at various temperatures for: a) TiB₂ b) Al₂O₃-(30 vol %) TiB₂; c) Si₃N₄-(20 Vol %) TiB₂ [63]
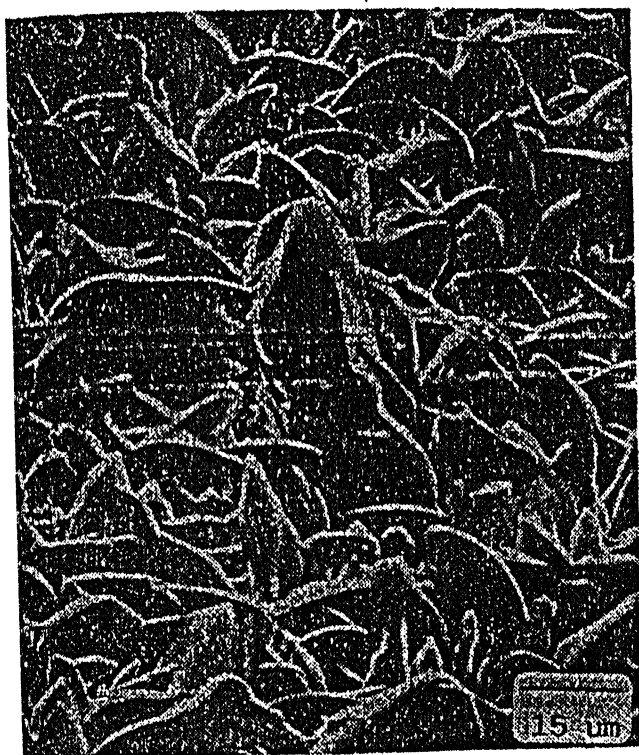
(a)

(b)

Fig. 2.6: Microstructure of th oxidized surface at 1000°C of : a) TiB_2; b) Al_2O_3-TiB_2 [63]
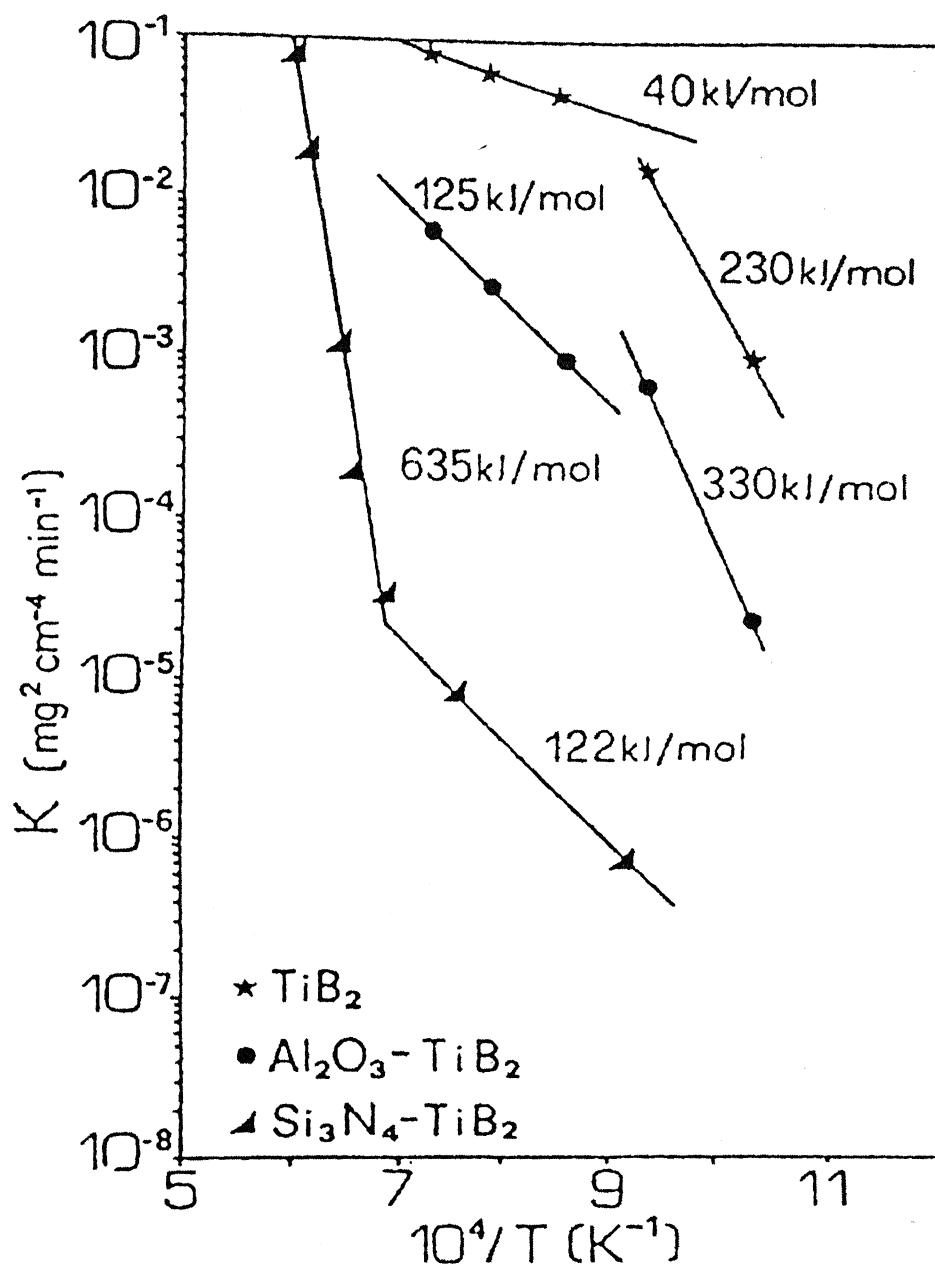
Fig. 2.7: Arhenius plot of oxidation rate constants of TiB₂, Al₂O₃-TiB₂ and Si₃N₄-TiB₂ [63]

86
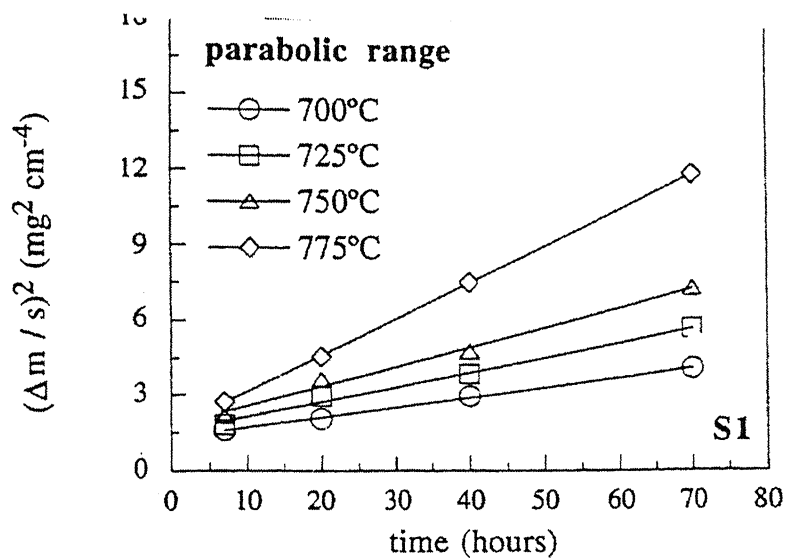
(a)
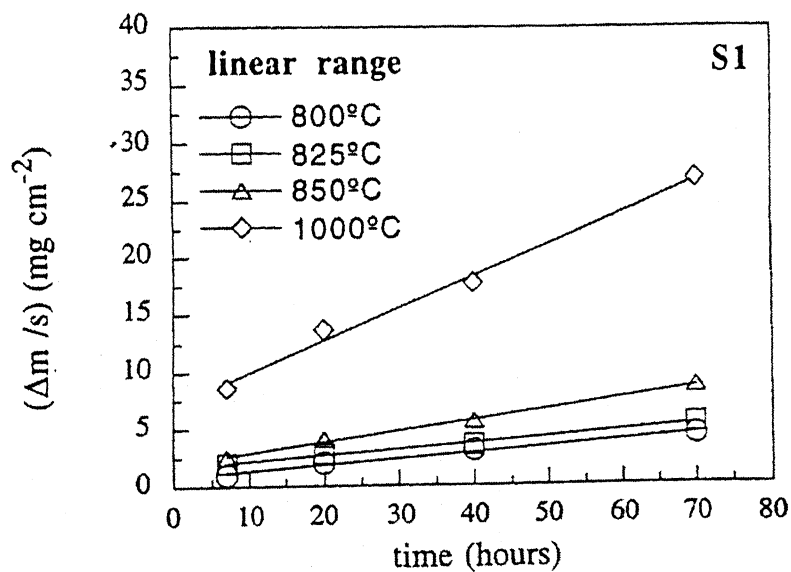
(b)

Fig. 2.8: Oxidation kinetics for specimen TiB_2-Fe-Ni-Al cermet indicating (a) a parabolic type and (b) a linear type of kinetics for temperature ranges 700-775°C and 800-1000°C, respectively [65]
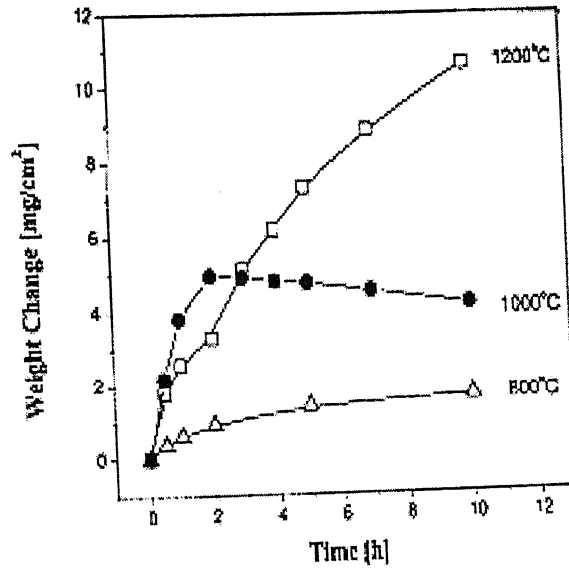
Fig. 2.9: Weight changes of TiB$_2$–2.5wt% Si$_3$N$_4$ specimens exposed to air at elevated temperatures for up to 10h [61]
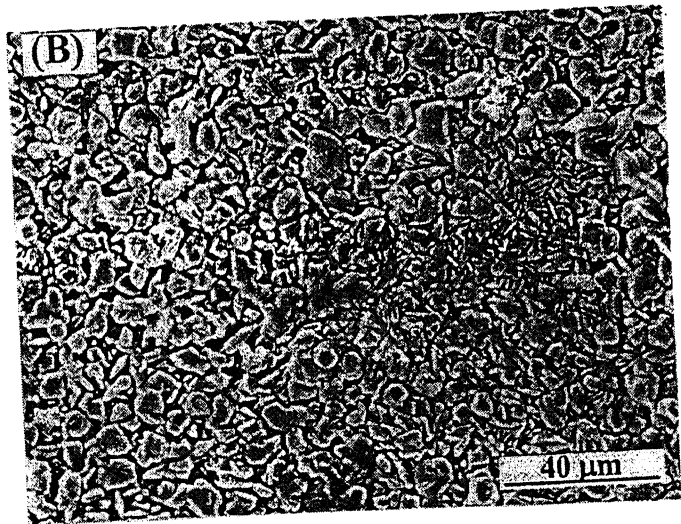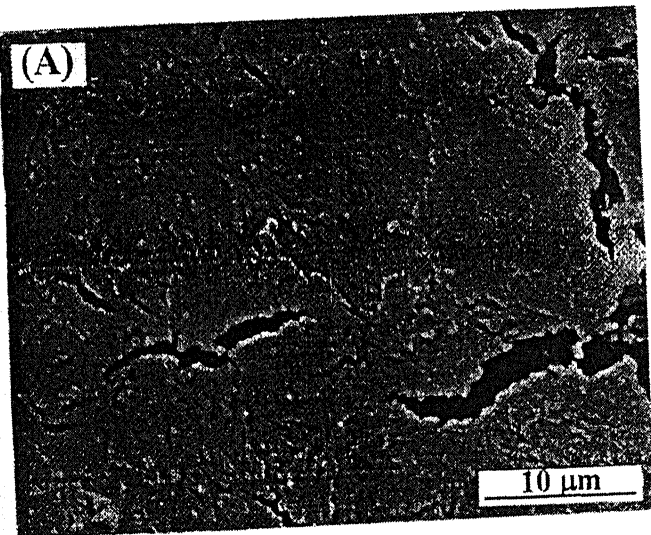
Fig. 2.10: SEM micrographs of oxidized surfaces of TiB$_2$–2.5wt% Si$_3$N$_4$ speciment exposed to air for 10h at (A) 800°, and (B) 1000°C [61]
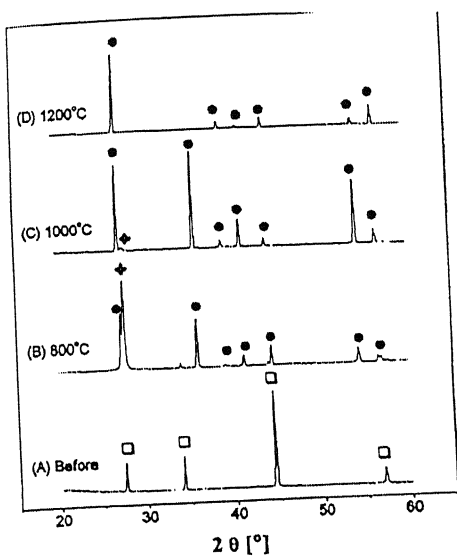
(a)
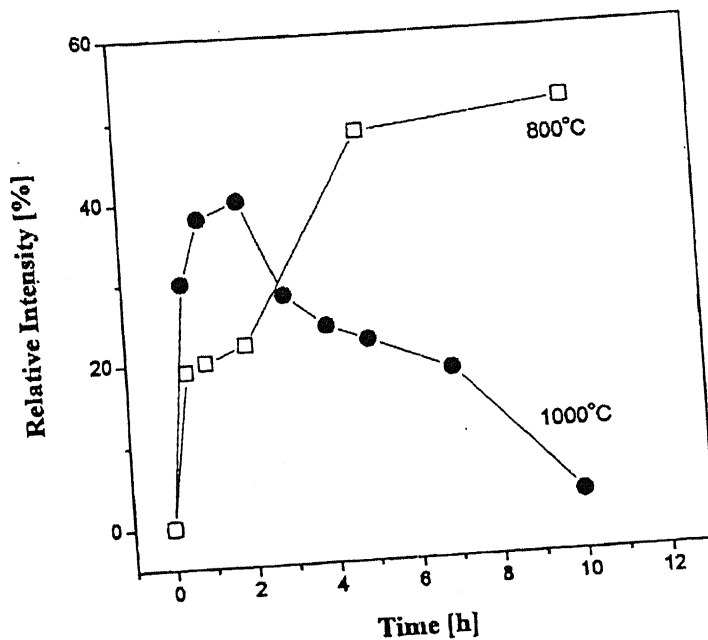
(b)

Fig. 2.11: X-ray diffraction patterns of TiB_2–2.5wt% Si_3N_4 specimens (A) before oxidation and after oxidation to air for10 h at (B) 800°, (C) 1000°, and (D) 1200°C; (□) TiB_2, (●) TiO_2, (♦) B_2O_3. Variation in relative intensity of B_2O_3 peak with respect to TiB_2 peaks after exposure at 800° and 1000°C (b) [61]

As regards the kinetics, the formation of oxide product B_2O_3 would occur initially, because of the small radius of the boron atom [67,68]. Its diffusion to the surface is more intensive than the diffusion of the atom of the boride metal and this leads to the formation of large amounts of B_2O_3. The glassy nature of the B_2O_3 films provides additional diffusion barrier for atmospheric oxygen during interaction.

Molybdenum disilicide ($MoSi_2$) is well-known for its excellent oxidation and corrosion resistant properties at high temperatures. It has been widely used for heating elements and as a protective coating for high temperature structures. Because of the combination of high temperature stability and electrical conductivity, $MoSi_2$ also finds many applications as contacts and interconnects in VLSI technology [69]. Despite its superior environmental protective capabilities $MoSi_2$, like most of the other intermetallics, also suffers from low temperature brittleness and poor strength at high temperatures. Specifically, the yield stress (250-350 MPa) of $MoSi_2$ decreases drastically at temperatures above 1200°C. It has been well-established that the excellent oxidation resistance of $MoSi_2$ at high temperatures is attributed to the formation of a self-healing, glassy silica (SiO_2) layer. But during low temperature (400-600°C) oxidation, it exhibits pest behavior. Pest means disintegration of the material (the disintegrated $MoSi_2$ results in powdery products) (Fig. 2.12).

The following reactions explain the oxidation mechanisms of $MoSi_2$ at different temperature ranges in air [70]:

Low temperatures (400 – 600°C):

$$2MoSi_2 + 7O_2 \rightarrow 2MoO_3 + 4SiO_2 \tag{34}$$

High temperatures(> 750°C):

$$5MoSi_2 + 7O_2 \rightarrow Mo_5Si_3 + 4SiO_2 \tag{35}$$

As TiB_2 is a potential candidate material for high temperature applications, the thermal stability of monolithic TiB_2 needs to be studied. The oxidation of TiB_2 can exert a negative influence on the mechanical and physical properties and on the performance of components made of these ceramics.
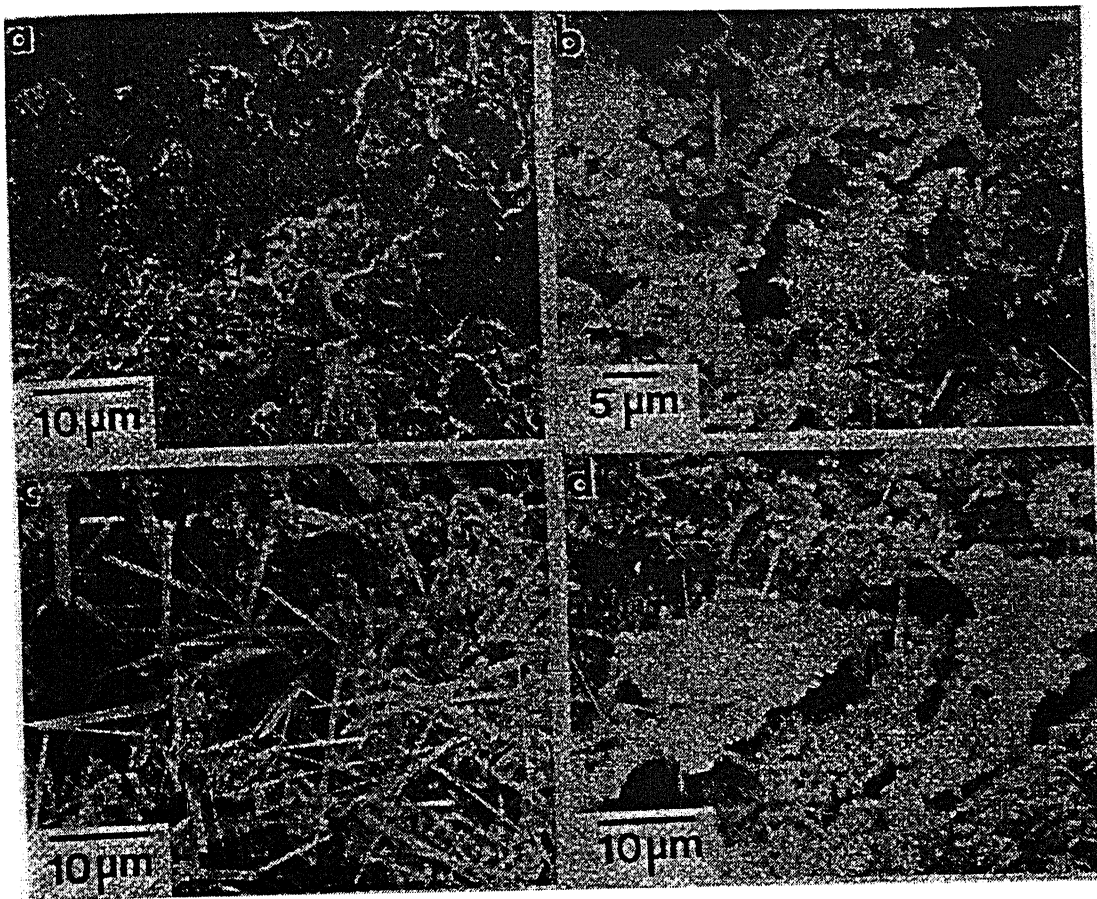
Fig. 2.12: SEM micrographs showing the surface characteristics of (a) unpested (b) lightly pested, and (c) severely- pested regions from the sample oxidized at 500°C for 21 h. (d) MoO_3 whiskers are noted to nucleate primarily at cracks and interparticle boundaries[69].

CHAPTER 3
EXPERIMENTAL PROCEDURE

In this chapter, the details of the powders, densification, and characterization of sintered materials as well as the different equipments will be discussed.

3.1 Processing and Microstructure

3.1.1 Starting powder preparation and characterization

TiB_2 and TiB_2 based composites are synthesized via powder metallurgy route. The details of starting powders are summarized in Table 3.1. The mean particle diameter and particle size distribution was measured using laser particle analyzer (Analysett 22). The specific surface area was measured by BET (COULTER, SA300) method. The morphology of the starting powders was investigated using SEM. The in-house processed TiB_2 and $MoSi_2$ powders were selected as starting powders for composite production. TiB_2 powder was produced by borothermic reaction:

$$2TiO_2 + B_4C + 3 C \rightarrow 2 TiB_2 + 4 CO \qquad (3.1)$$

Oxygen and carbon are the main impurities in TiB_2. Synthesized TiB_2 powder was further ground to break down the agglomerates to form finer particles having D_{50} around 1.1 μm.

$MoSi_2$ was synthesized from elemental powders Mo (>99% purity, Leco Industries, U.S.A) and Si (> 99% purity, supplier Merck, Germany). Mechanical grinding reduces the size of $MoSi_2$ powder after synthesis to finer particle size with D_{50} around 1.4 μm. SEM images of starting powders are shown in Fig. 3.1. While finer equiaxed TiB_2 particles can be observed in Fig.3.1a, the morphology of $MoSi_2$ was rather irregular.

3.1.2 Hot pressing and pressureless sintering

Appropriate amount of powders with various compositions (0 wt.% $MoSi_2$, 10 wt.% $MoSi_2$, 15 wt.% $MoSi_2$, 20 wt.% $MoSi_2$, and 25 wt.% $MoSi_2$), were mixed using a tungsten carbide (WC) grinder. The densification was performed by hot pressing under vacuum, using a 10 mm diameter graphite die with 32 MPa pressure. The samples were hot pressed at 1650°C, 1700°C and 1800°C with a heating rate of 15 °C/min. Hot press (Supplier: GCA/ vacuum Industries, U.S.A.) contains the graphite heating elements

92

graphite wool insulation; High-density Graphite die is used for making the pellets. Plungers (root and top) are used for applying pressure on that powder. The die is charged with the powder and this kept on vibrator to achieve a high tap density. Hot pressing was carried out under vacuum with 32 MPa pressure, for different compositional samples (Monolithic, 10%MoSi$_2$, 15%MoSi2, 20%MoSi$_2$, 25%MoSi$_2$) with varying temperature. Temperature was measured by Optical Pyrometer (model Marathon Series, Raytek, U.S.A). After completion of hot pressing, the vacuum and pressure were maintained till the end of cooling. The pellets were ejected from die with hydraulic press. The thickness of the hot pressed pellets was around 6-8 mm.

To study the feasibility of pressureless sintering, green pellets of various TiB$_2$–MoSi$_2$ composite (without organic binder) were used. The green density of the cold pressed specimens was 65 % of theoretical density. Graphite heating furnace was used for sintering (supplier: Hind Hivac, Bangalore).the green samples were sintered for 2 hours at 1900°C at a heating rate of 15^{0}C/minute in a reducing atmosphere (Ar + H$_2$). Prior to sintering experiments, the vacuum chamber was evacuated and backfilled with Ar to ensure the absence of any residual oxygen. After completion, the samples are cooled down to room temperature and then removed from the furnace.

Hot pressed and sintered samples were thoroughly cleaned. The cleaned dense pellets, were weighed and density measured by using Archimedes principle. Fluid is distilled water. Balance model AT 261 Delta Ra (supplier Mettler Toledo). Density was calculated by taking the ratio of weight in air to the volume of displaced water.

Cutting of TiB$_2$ sample is very difficult and requires diamond wafering blade ISOCUT cutting Fluid (11 – 1193 grade) was used as a lubricant and coolant. The sintered samples were mounted in mounting machine (model Simplimet 1000, Buehler, U.S.A) and then polished for microstructural studies.

93
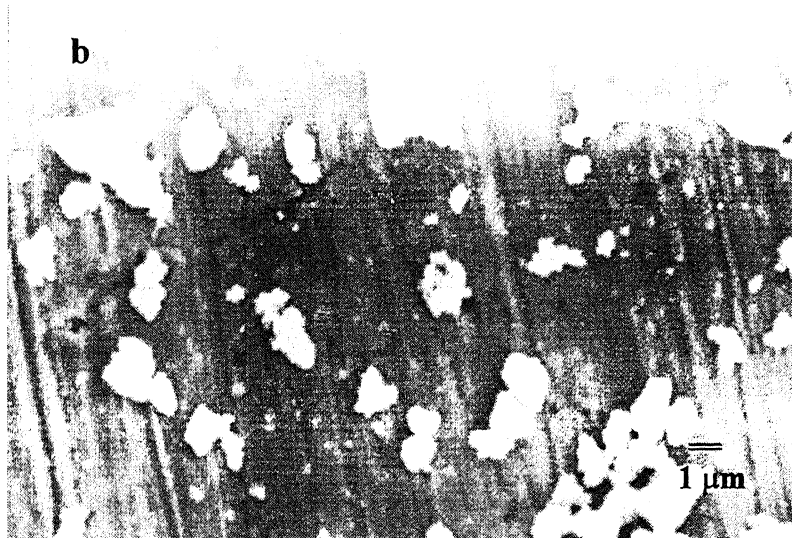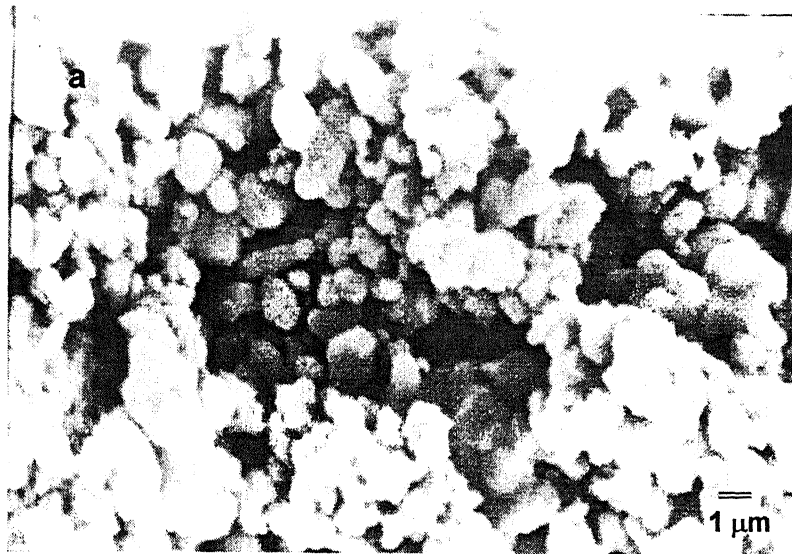
Fig. 3.1: SEM images showing the morphology of a) TiB$_2$ and b) MoSi$_2$

Table 3.1 Details of the starting powders used in the present work.

Powder	Supplier	Carbon (wt. %)	Oxygen (wt. %)	Nitrogen (wt. %)	Metallic Impurities (wt. %)	Median particle diameter D_{50} (μm)	Surface area (m^2/g)
TiB_2	In-house	0.6	0.5	0.6	-	1.1	1.360
$MoSi_2$	In-house	0.37	0.3	-	-	1.4	0.389
TiO_2	Merck, Germany	-	-	-	Pb$\leq$0.005 As$\leq$0.0005 Fe$\leq$0.005	0.8	-
B_4C	In-house	19.5	-	-	Fe ~ 2000ppm Si~ 2000ppm	6.7	-

3.1.3 Phase identification and Microstructural characterization

The crystalline phases in the starting powders and hot pressed sample were analyzed using XRD. XRD patterns were obtained using Cu Kα (λ = 1.5404 A) radiation in a Rich-Seifert, 2000D diffractometer. The patterns were later analyzed using Diffrac[Plus] software (Bruker Advanced X-ray Solutions, Germany) and JCPDF database. Microstructural investigation of the phase assemblage was performed by means of SEM (JSM-840A, JEOL) on polished surfaces and the nature of fracture was observed on fractured surfaces. The detailed microstructural analysis was also performed using EPMA (WDS analysis) (JAX 8600 MX, JEOL) and 200 kV TEM (JEM2000FXII). Prior to SEM observation, the oxidized samples were sputter-coated with a thin Au-Pd coating in order to obtain sufficient conductivity on the surface and to avoid charging of the surface in the SEM. Thin foil for TEM was prepared by the following method.

Initially, a thin slice of nearly 150 micron was cut by diamond saw cutter. Following this, a 3 mm disc was cut by ultrasonic cutter. The grinding of thin disc was performed up to 60 micron thickness. Subsequently, the dimple grinding was performed up to 20 micron thickness. The Ion milling was performed to obtain central perforation (nearly 70 to 90 h), that ensured transparent region at the vicinity of the opening. Finally, a thin carbon coating was sputter coated on thin foil in order to obtain sufficient conductivity on the surface. EDS analysis and spot patterns was collected from triple pockets of the structure with TEM, Point to point resolution is about 1.5 A.

3.1.4 Physical and Mechanical properties characterization

Thermal conductivity and Electrical conductivity measurements

Thermal diffusivity of the samples in the temperature range of RT-500^{0}C was measured using a LASERFLASH thermal diffusivity measuring system, which works on the Flash or the Pulse technique. The sample used was a disc of diameter 10 mm and thickness 1 mm. The thermal diffusivity data was corrected for radiation losses and finite pulse width effects. The thermal diffusivity (λ) was calculated using the definition of thermal diffusivity

$$\lambda = \frac{k}{\rho C_p}$$ (3.2)

Where k is the thermal conductivity, ρ is the geometrical density and C_p is the specific heat capacity.

Electrical conductivity at room temperature was measured by using the conventional 4-probe method. Rectangular cross sectional (dimensions: 1mmX2mmX6mm) samples were prepared for conductivity measurement. All sides of sample were smoothly polished. Four copper probes were connected to the sample with the help of silver paste. Two probes were located on the two sides of longitudinal, which were connected to the programmable current source (KEITHLEY: 224) and remaining two probes were connected on the top surface of transverse direction with 1 mm apart, which were connected to Nanovoltemeter (KEITHLEY: 2182), which recorded the out put voltage when 100 mA current was passed through the sample. Electrical conductivity was calculated using the following expression:

$$\text{Conductivity} = IL/VA \qquad (3.3)$$

Where I is current (100 mA), L distance between two probes, which are connected to voltmeter (1mm), V is recorded voltage in nanovoltemeter, A is the cross-sectional area of the specimen (mm^2).

Evaluation of Hardness and Toughness

The hardness was measured at different indent loads of 50, 100 and 200N with time of 5sec. Fracture toughness (K_{IC10}) calculations were based on the crack length measurements of the radial crack pattern produced by Vickers H_{V10} indentations, according to the formula given by Anstis et al.[20]. The reported values were the average of data obtained from three indentation tests. Fracture toughness values were calculated by using the Anstis empirical relation [20]:

$$K_{Ic} = 0.016 \, (E/H)^{1/2} \, X \, (P/C^{3/2}) \qquad (3.4)$$

where K_{Ic} is the fracture toughness, E – Elastic modulus, H – hardness, P – load, 2C – full crack length. Elastic modulus value was estimated theoretically by using the rule of mixture and considering the presence of porosity in the sintered samples. Elastic modulus values are tabulated in Table 3.2.

Table 3.2 Theoretical Elastic modulus values of TiB_2 and its composites.

Material	Elastic modulus, E (GPa)	Porosity%	Elastic modulus, E (GPa) (after considering porosity)
TiB_2	500	2.5	487
$MoSi_2$	450	-	-
TiB_2- 10 wt % $MoSi_2$	495	5	470.25
TiB_2- 20 wt % $MoSi_2$	400	5	380

3.2 Tribological Properties

Monolithic TiB_2 and $TiB_2 - MoSi_2$ composites containing 10 and 20 wt. % $MoSi_2$ particulate reinforcement were used for the tribological study. The hot pressed pellets were cut into small discs of 2mm thickness and smoothly polished to $R_a = 1$ μm. Polished monolithic TiB_2 and TiB_2-composites were used as flat (moving) materials. 8 mm diameter bearing grade steel balls (commercial SAE 52100 grade, hardness 63-65 HRc, data from supplier) were used as counterbodies (stationary).

3.2.1 Equipment

The fretting experiments were performed using a computer-controlled fretting machine (Fig.3.2) (DUCOM TR281-M), which produces a linear relative oscillating motion with ball-on-flat configuration. By a stepper motor, the flat sample is made to oscillate with a relative linear displacement of constant stroke and frequency. An inductive displacement transducer monitors the displacement of the flat sample and a piezoelectric transducer is used to measure the friction force. Variation in tangential force is recorded and the corresponding coefficient of friction is calculated on-line with the help of a computer-based data acquisition system.

Prior to the fretting tests, both the flat and ball were ultrasonically cleaned in acetone. The fretting experiments were performed on monolithic TiB_2 and TiB_2-$MoSi_2$ composites against steel balls with varying load (P) of 2, 5 and 10 N at 8Hz oscillating frequency and 100μm linear stroke for 10,000 cycles duration. Moreover, the combination of testing parameters results in the gross slip fretting contacts. All experiments were conducted in air at room temperature (30 ± 2^0C) with relative humidity (RH) of $45\pm5\%$. The schematic of the experimental arrangement is shown in Fig. 3.3.
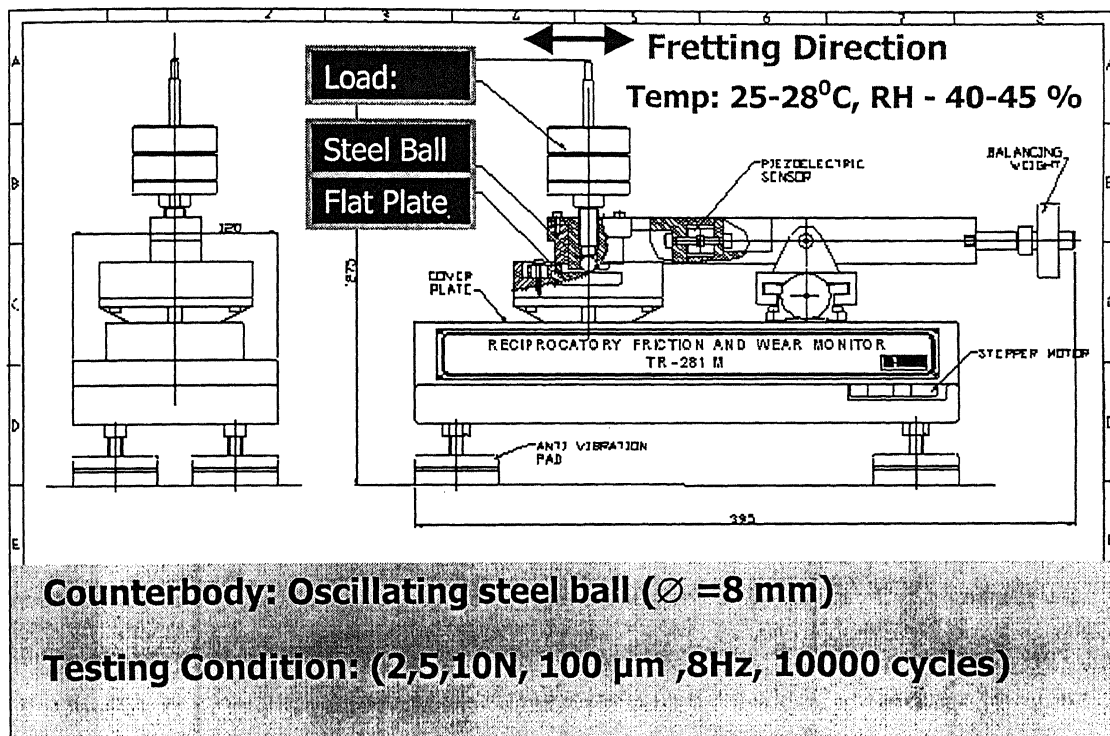
Fig. 3.2. Schematic of the fretting wear tester, manufactured by DUCOM, India.

100

3.2.2 Wear rate calculations

The wear volumes of both flat and ball were calculated from the measured transverse wear scar diameters as per the equation given by Klaffke [76].

$$V = \left[\frac{\pi d}{8} + \frac{4A}{3} \right] \left(\frac{d^3}{8R} \right)$$
(3.5)

where V = wear volume; R is the radius of ball (8mm), d is the diameter of wear scar in the transverse direction, A is displacement amplitude (100 μm). From the estimated wear volume, the specific wear rates were calculated.

Wear rate = Wear volume / (load X distance)
(3.6)

The use of this equation is reported to be justified for the present fretting conditions (providing errors less than 5%) when the wear scar diameter is larger than twice the Hertzian contact diameter, as was the case in our experiments.

3.2.3 Characterization of worn surfaces

After each test, the worn surfaces of both the flat and the ball were observed using an optical microscope (Zeiss). Further detailed characterization of the worn surfaces was performed using a scanning electron microscope (JEOL-JSM840). Raman laser spectroscopy (SPEX-1877E Triplemate) and electron microprobe analyzer (EPMA JEOL-JXA8600) with wavelength dispersive X-ray analysis (WDX) were used to identify the triboproducts formed on the worn surfaces. Prior to SEM observation, the oxidized samples were sputter-coated with a thin Au-Pd coating in order to obtain sufficient conductivity on the surface and avoid charging of the surface in the SEM.
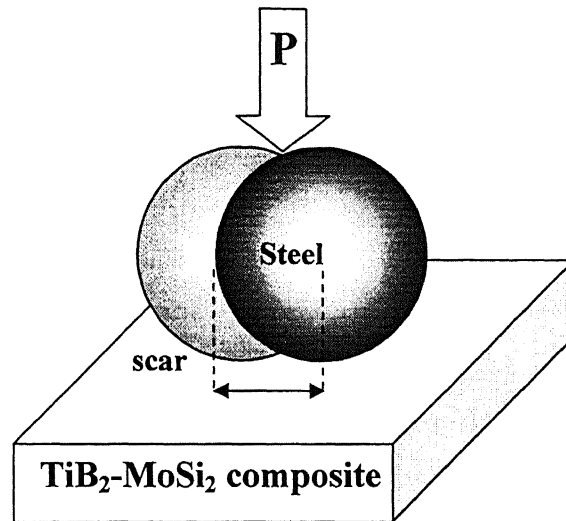
Fig. 3.3. Schematic of the fretting test set-up. Test conditions: Constants-Stroke length 100 μm, Oscillation frequency 8Hz and Cycles 10000. Variables- Normal load, P (2-10N).

3.3 Oxidation behavior

3.3.1 Materials

Two materials were considered for the oxidation study. The monolithic TiB_2 and TiB_2–$MoSi_2$ (20 wt. %) composites were fabricated by hot pressing at 1700°C for 60 min and at 32MPa in vacuum. Hot pressed pellets of diameter 10 mm were sectioned into 2mm thick discs using high speed diamond cutter. These discs were polished with emery papers (1/0,2/0,3/0,4/0) and finally with diamond paste up to 1 μm finish. The polished discs were ultrasonically cleaned in acetone for 10 minutes.

3.3.2 Experimental apparatus

Oxidation tests were conducted in a vertical tube furnace. In order to avoid oxidation during heating, the samples were directly inserted into the furnace after the furnace temperature reached 850°C. Temperature was measured using a chromel–alumel thermocouple with an accuracy of ± 10°C. Samples were placed in an alumina crucible and suspended inside the furnace. A total of eight samples, for each material, were oxidized for different time intervals (0.5h to 64h) at 850°C. The dimensions of the samples were accurately noted using vernier caliper. Each sample was carefully weighed before and after exposure, to determine the weight change during the oxidation process. Duplicate experiments were performed for selected time intervals to check for the reproducibility of the test results.

3.3.3 Characterization of oxidized samples

The surfaces of the oxidized samples were characterized using X-ray diffraction (XRD) and scanning electron microscopy (SEM). XRD patterns were obtained from the surface of the oxidized samples using Cu Kα (λ = 1.404 A) radiation in a Rich-Seifert 2000D diffractometer. The patterns were later analyzed using Diffrac[Plus] software (Bruker Advanced X-ray Solutions, Germany) and JCPDF database (JCPDF 2001).

103

The morphology and nature of oxide layer was understood by observing the surface in a JSM-840A JEOL scanning electron microscope. The cross section of the oxidized monolithic and composite samples for 64h was studied in details. Elemental X-ray maps were obtained on the cross sections of 64h oxidized monolithic and composite. Line scan across the cross section of 64 h oxidized composite was performed using a FEI QUANTA 2000 HV SEM. Prior to SEM observation, the oxidized samples were sputter coated with a thin Au-Pd coating in order to obtain sufficient conductivity on the surface and to avoid charging of the surface in the SEM.

CHAPTER 4

RESULTS AND DISCUSSIONS

4.1 Processing:

4.1.1 Hot pressing:

The densification data of the hot pressed samples are presented in Table.4.1.1 and Figure 4.1.1. For monolithic TiB_2, poor densification of ~ 88 % ρ_{th} was obtained after hot pressing at 1700°C, while excellent densification of ~ 98 % ρ_{th} was achieved at 1800°C. The attainment of such high density for binderless TiB_2 by hot pressing route had not been reported in literature till todate. Critical observation of data presented in Table 4.1.1 shows that the sintered density of TiB_2 increases with amount of $MoSi_2$ sinter-additive and the maximum of 99% ρ_{th} can be obtained with 10 % $MoSi_2$ addition at 1700°C. For 20% $MoSi_2$ reinforced composites, similar high density of around 98% ρ_{th} is obtained at 1700°C. Additional hot pressing experiments at 1700°C revealed that 98-99% ρ_{th} can be obtained with 15% $MoSi_2$ and 25% $MoSi_2$ additions. Because of the excellent densification achieved with higher amount of $MoSi_2$ additions and in order to study the feasibility of densifying them at lower temperature, limited experiments were carried out by hot pressing TiB_2-15 % $MoSi_2$ and TiB_2-20 % $MoSi_2$ composites at lower temperature of 1650°C for 1 hour. The densification results reveal that 87-89% ρ_{th} can be obtained with these composites with the lower density for higher silicides additions. From the above observations, it should be clear that $MoSi_2$ improves sinterability of TiB_2 and by optimizing the 'processing and compositional window', more than 95% ρ_{th} can be obtained by hot pressing route. Considerable weight loss (during sintering) of around 4-9% is measured depending on the sintering temperature and $MoSi_2$ content.

To this end, it can be noted that Torizuka et. al [24] achieved 95% ρ_{th} with TiB_2–2.5 wt % SiC composite, when hot pressed at 1700°C. Also 98% ρ_{th} was obtained with TiB_2-5 wt % AlN, hot pressed at 1800°C by Li et. al [16]. Park et. al [25] achieved 99% ρ_{th} using 2.5 wt % Si_3N_4 additives for TiB_2 hot pressed at 1800°C for 1h. Thus, comparing our experimental results with literature reports, it can be said that obtaining high density in TiB_2-10 wt. % $MoSi_2$ composites at 1700°C, in the present case, is a new and promising result. More experiments are planned for future to densify TiB_2 with lower amount of silicides additives (< 10 wt. %).

Table 4.1.1 Densification data and properties of the Hot pressed materials.

Sample designation*	Hot pressing temperature (^{o}C)	Theoretical density (g/cc)	Density (g/cc)	Relative density (%)	% Wt loss	Hardness (KH) (GPa)
TiB_2-10% $MoSi_2$						
HP0	1700	4.65	4.62	99.35	4.4	18-26
TiB_2 – 15% $MoSi_2$						
HP1	1650	4.71	4.17	88.53	6.4	
HP1	1700	4.71	4.65	98.42	7.6	19-26
HP1	1800	4.71	4.62	98.08	5.7	17-25
TiB_2-20% $MoSi_2$						
HP2	1650	4.78	4.18	87.44	5.8	16-22
HP2	1700	4.78	4.60	98.72	8.3	21-25
HP2	1800	4.78	4.65	97.28	7.1	22-30
TiB_2-25% $MoSi_2$						
HP3	1700	4.85	4.83	99.58	9.4	23-31
Monolithic TiB_2						
HP4	1700	4.52	3.99	88.27	6.0	6 - 7
HP4	1800	4.52	4.41	97.56	6.0	23 - 26

* HP: hot pressed sample. The digits represent composition $0 - 10\% MoSi_2 + TiB_2$; $1 - 15\% MoSi_2 + TiB_2$ $2 - 20\% MoSi_2 + TiB_2$; $3 - 25\% MoSi_2 + TiB_2$; $4 - 0\% MoSi_2 + TiB_2$
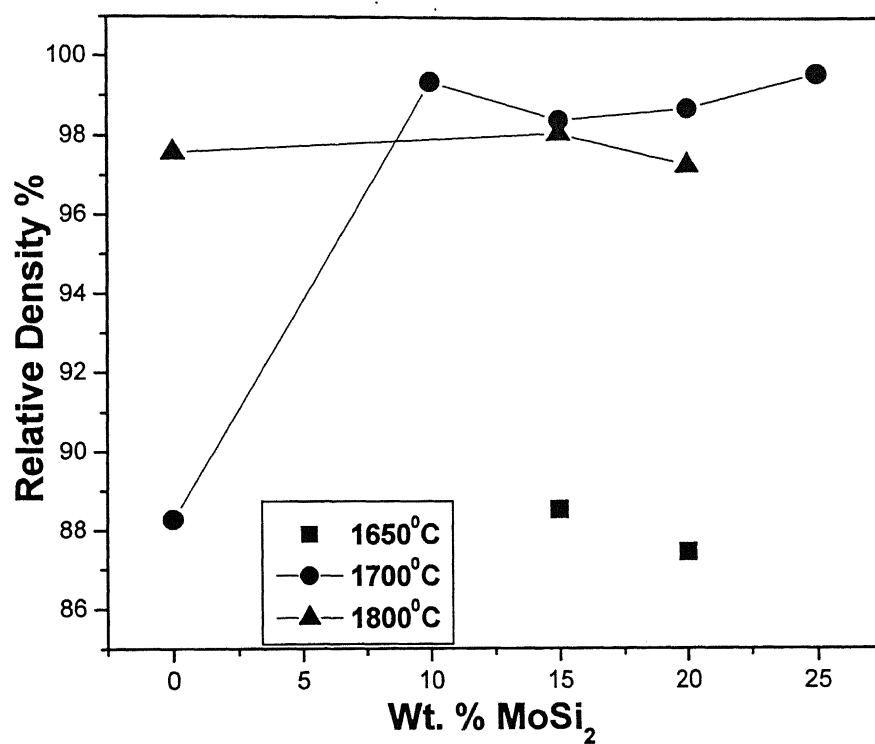
Fig. 4.1.1: Relative density of hot pressed samples as a function of MoSi$_2$ content. The lines joining the data points are connecting the densification data obtained with varying hot pressing temperature.

107

Pressureless sintering

Table 4.1.2 presents the densification results of pressureless sintering experiments, carried out at 1900^0C for 1 hour in inert (Ar + H_2) atmosphere. The sintered density of the composites increases with increasing $MoSi_2$ content. A maximum sintered density of 91% ρ_{th} is obtained with 25 wt % $MoSi_2$ addition. The weight loss during sintering varies between 4.4 and 6.2 wt % for different $MoSi_2$ additions and the measured weight loss is observed to increase with increase in $MoSi_2$ content.

Summarizing our experimental results clearly indicate that the densification of TiB_2 critically depends on $MoSi_2$ content and sintering temperature. An optimum combination of 10 % $MoSi_2$ sinter-additive and the hot pressing temperature of 1700^0 C are found to be suitable for producing dense boride materials. With pressureless sintering, a maximum of 91 % ρ_{th} could be obtained at $1900^{\circ}C$ for TiB_2-25% $MoSi_2$ composites.

Since the major purpose of the materials development work is to obtain dense borides with minimal sinter-additive content, detailed microstructural and other properties (physical, mechanical and degradation) were investigated in details for borides with 10 and 20 % silicides additives. A comparison has also been made with the monolithic borides.

Table 4.1.2 Details of the densification data for ceramic samples, pressureless sintered at 1900^0C for 1 hr in (Ar+ H_2) atmosphere

Sample designation[*]	Theoretical density (g/cc)	Density (g/cc)	Relative density (%)	% Wt. loss
PS0	4.65	3.83	82.36	4.4
PS1	4.71	4.00	84.92	5.0
PS2	4.78	4.23	88.49	5.6
PS3	4.85	4.43	91.34	6.2
PS4	4.52	—	—	1.1

[*] PS: Pressureless Sintered sample. Digit represents composition $0 - 10\%$ $MoSi_2$ + TiB_2; $1 - 15\%MoSi_2$ + TiB_2

$2 - 20\%$ $MoSi_2$ + TiB_2; $3 - 25\%$ $MoSi_2$ + TiB_2; $4 - 0\%$ $MoSi_2$ + TiB_2

4.1.2 Physical properties

Thermal conductivity measurements

Because of lack of availability of LASERFLASH equipment, the thermal properties of the monolithic TiB_2 (hot pressed at $1700°$ C, 1 hour) could only be measured. Thermal diffusivity, specific heat and thermal conductivity of monolithic TiB_2 as a function of temperature (up to $600°$ C) are plotted in Fig.4.1.2. The thermal diffusivity monotonically decreases from 0.22 cm^2/Sec (room temperature, RT) to 0.16 cm^2/Sec ($600°$ C). On the other hand both specific heat capacity (C_p) and thermal conductivity (λ) decreases initially up to $300°C$, then further increases with increase in temperature up to $500°C$. RT thermal conductivity of monolithic TiB_2 was measured to be around 50 W/m/K, while that at $500°C$ is around 60 W/m/K. This observation matches well with the literature data [1].

Electrical Conductivity data

The measured conductivity data are summarized in Table 4.1.3. The electrical conductivity was measured on hot pressed ($1700°$ C, 1h) sample. The electrical conductivity of all the investigated samples varies over the same order of magnitude. However, the addition of $MoSi_2$ appears to decrease the electrical conductivity from 6.6 x 10^4 siemens/cm (pure TiB_2) to 2.612 x 10^4 siemens/cm (TiB_2-10 % $MoSi_2$). Also, a modest increase in conductivity to 4.065 x 10^4 siemens/cm is recorded for 20 % $MoSi_2$ composites.
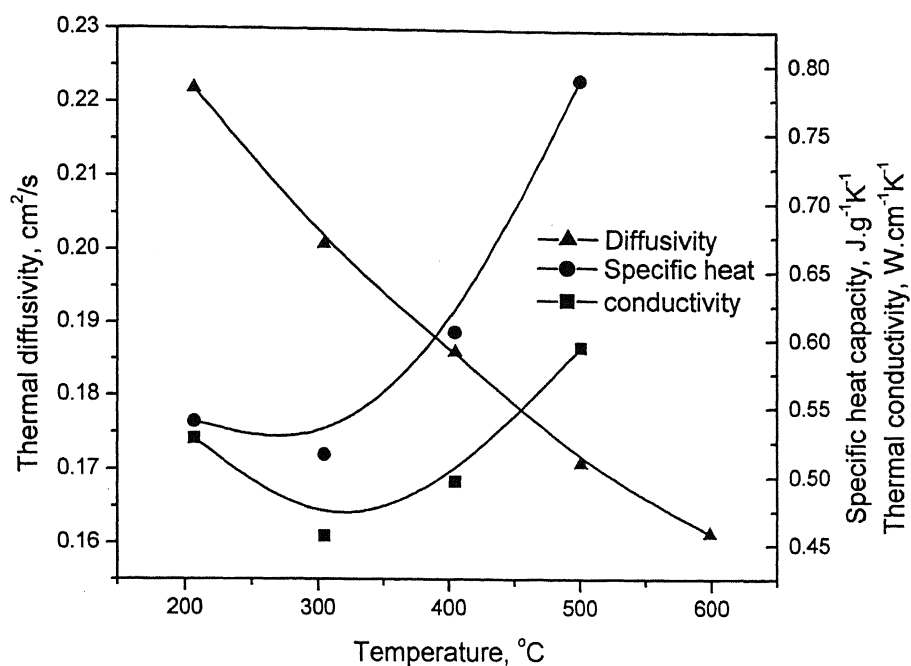
Fig.4.1.2: The thermal property data of monolithic TiB₂

Table 4.1.3 The measured physical properties (Electrical conductivity and Thermal conductivity) of the investigated materials

Sample	Relative Density (%)	Electrical conductivity (siemens/cm) (at RT)	Thermal conductivity (w/m/K) (at 500°C)
Monolithic TiB₂	97.56	6.6×10^4	59.442
TiB₂ – 10 wt.% MoSi₂	95.91	2.612×10^4	
TiB₂ – 20 wt.% MoSi₂	96.50	4.065×10^4	

4.1.3 Microstructural Characterization

XRD

XRD analysis of starting powders and hot pressed specimens were carried out and the results are shown in Figure 4.1.3. These results indicate that the microstructure of developed composites predominantly contain TiB_2 and $MoSi_2$. However, addition of 10 wt. % and 20 wt. % $MoSi_2$ result in the formation of small amount of $TiSi_2$, which was further confirmed by TEM analysis.

SEM

SEM images of starting powder TiB_2 and $MoSi_2$ are shown in Fig 3.1. SEM images of fracture surfaces of monolithic TiB_2 and TiB_2-10 wt. % $MoSi_2$ composite, both hot pressed at 1700^0C are shown in Fig 4.1.4. The average grain size of the monolithic TiB_2 particles in hot pressed samples is around 2-3 μm. The presence of finer $MoSi_2$ particles (~ 2-3 μm) is observed in the composite sample and a slight decrease in the TiB_2 grain size (~ 1.5-2 μm) is noted in the composites. Considering the starting particle size of TiB_2 (D_{50} ~1.1μm) and $MoSi_2$ (D_{50} ~1.4μm), the above observation indicates that hot pressing at 1700^0C does not promote any significant grain growth and $MoSi_2$ inhibits grain growth of TiB_2 in the composites. It can be noted here that Torizuka et al. [19] have observed extensive grain growth at 1700^0C when using 20-wt % ZrO_2 as a sintering additive. The above observation thus indicates that $MoSi_2$ can act as grain growth inhibitor for TiB_2.
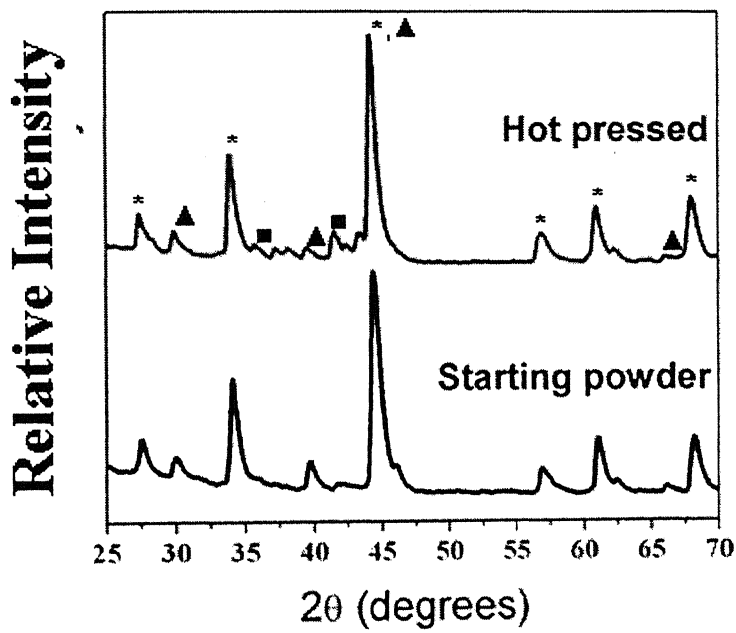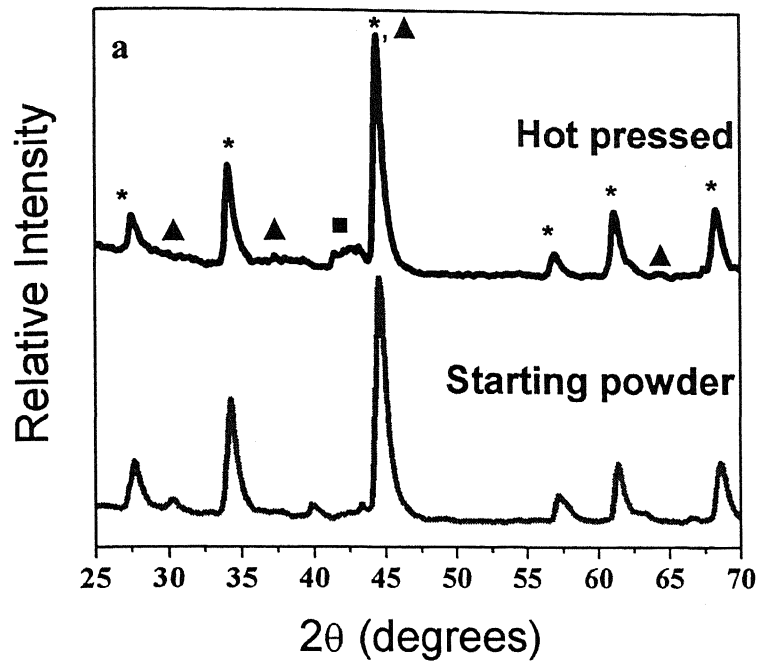
Fig. 4.1.3: Phase analysis of starting powder and hot pressed samples (a) TiB$_2$ –
10wt.%Mosi$_2$ (b) TiB$_2$–20wt.% MoSi$_2$. The different crystalline phases are identified:
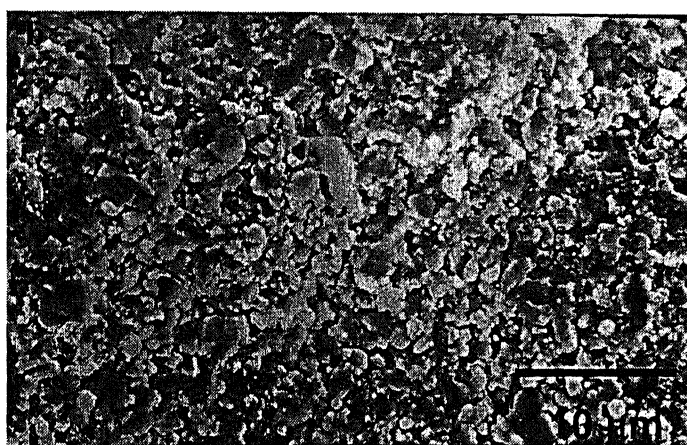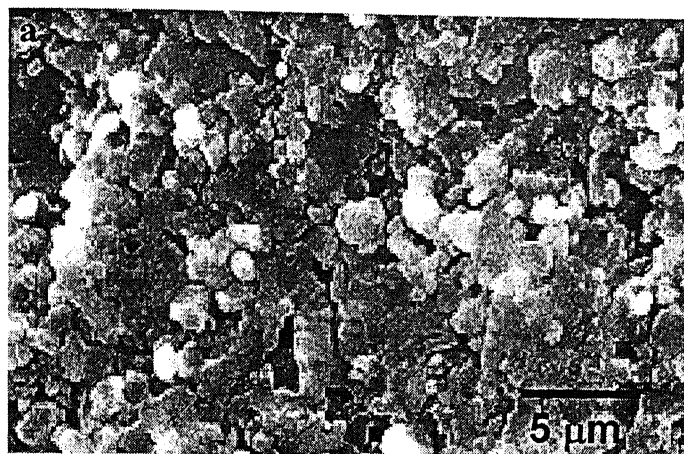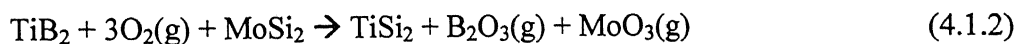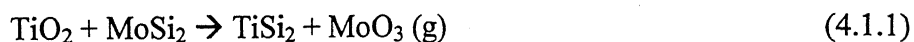TiB$_2$ (*); MoSi$_2$ (▲); TiSi2 (■).

113

Fig. 4.1.4: SEM images of the fracture surfaces of the newly developed ceramics, hot pressed at 1700°C for 1 hour: (a) Monolithic TiB_2 (b) $TiB_2 - 10wt.$ % $MoSi_2$ composite.

TEM

TEM analysis of TiB_2 –20% $MoSi_2$ is carried out and the bright field images are shown in Fig. 4.1.5. The presence of finer faceted TiB_2 particles (~0.1-0.2 µm) can be seen in Fig. 4.1.5b, while the dispersion of coarser shaped $MoSi_2$ particles is observed in Fig. 4.1.5c. Typical aspect ratio of elongated silicides particles is around 4-5. Closer observation of Fig. 4.1.5c reveals the defect substructure i.e. the dislocation activity within $MoSi_2$ grain. However, TiB_2 grains (Fig. 4.1.5b) does not exhibit any observable defect substructure i.e. dislocation etc. Fig. 4.1.5d and e reveals some interesting information. The formation of $TiSi_2$ is commonly observed at grain boundary triple pockets. EDS analysis from the triple pocket (Fig. 4.1.5f) shows a strong Ti peak. Because of the use of Si-detector (EDS system), the X-ray counts for Si peak is rather weak. This along with XRD and EPMA results suggests that $TiSi_2$, a reaction product forms at grain boundary triple pockets during sintering.

4.1.4 Densification Mechanism

The existence of the grain triple pocket phase ($TiSi_2$) provides some insight into the densification mechanism. Since the melting point of $TiSi_2$ is 1500^0C, liquid $TiSi_2$ presumably forms during the hot pressing (sintering temperature 1700^0C). Therefore, it is quite likely that the densification of TiB_2 with $MoSi_2$ sinter-additive occurs via liquid phase sintering, which typically involves the rearrangement of grains by capillary action in the presence of wetting second phase. It is reported in literature that a surface layer of TiO_2 and B_2O_3 exists on the surface of TiB_2 particles [6]. Also, literature report indicates that B_2O_3 Vaporizes rapidly above 1127^0C [68]. In our hot pressing experiments, 4-6 % weight losses are measured and this can be attributed to the evaporation of the volatile oxides. The reaction mechanism for the formation of $TiSi_2$ can be explained by the following reaction:

$$TiO_2 + MoSi_2 \rightarrow TiSi_2 + MoO_3 \text{ (g)} \tag{4.1.1}$$

$$TiB_2 + 3O_2(g) + MoSi_2 \rightarrow TiSi_2 + B_2O_3(g) + MoO_3(g) \tag{4.1.2}$$

Based on the available data for the free energy of formation of different compounds, it was found that the overall free energy change for reaction (4.1.1): $\Delta G_1 > 0$ at high temperature (>1773K). Hence, the first reaction involving chemical interaction of TiO_2 and $MoSi_2$ resulting in the formation of $TiSi_2$ is thermodynamically not feasible. However, the thermodynamic calculations reveal that the overall free energy change for second possible reaction, i.e. $\Delta G_2 < 0$ at and above 1773K (1500^0C). For example, ΔG_2 at 1800 K is

- 183.018 Kcal. At T > 1800 K, ΔG_2 becomes more negative. Hence, the second reaction leading to formation of $TiSi_2$ is thermodynamically feasible. The Gibbs energy and reaction rate constant (K) values for reaction (4.1.2) at different temperatures are tabulated in Table 4.1.4. It can be noted here that this reaction can take place even at low oxygen partial pressure, as relevant for the hot pressing experiments. Also, XRD clearly shows the formation of $TiSi_2$ and the weight loss measured after sintering explains the formation of volatile compounds like B_2O_3 (g) and MoO_3 (g), which evaporate at hot pressing temperature of 1700°C.

Table 4.1.4 Thermodynamic data of $TiSi_2$ formation at different temperatures (T) for the following reaction: $TiB_2 + 3O_2$ (g) + $MoSi_2$ = $TiSi_2$ + B_2O_3 (g) + MoO_3 (g). The thermodynamic data for $TiSi_2$ is extrapolated from the existing data available for T=1773K [79]. ΔH is the enthalpy change, ΔS is the entropy change, ΔG is the overall Gibbs free energy change, K is the rate constant for the above mentioned reaction.

| T	ΔH	ΔS	ΔG	K	Log(K)
K	kcal	cal/K	kcal		
1200.000	-217.517	-19.153	-194.533	2.706E+035	35.432
1300.000	-217.506	-19.144	-192.618	2.425E+032	32.385
1400.000	-217.514	-19.150	-190.704	5.925E+029	29.773
1500.000	-217.545	-19.171	-188.788	3.226E+027	27.509
1600.000	-217.600	-19.207	-186.869	3.367E+025	25.527
1700.000	-217.680	-19.255	-184.946	6.003E+023	23.778
1800.000	-217.786	-19.316	-183.018	1.672E+022	22.223
1900.000	-217.918	-19.387	-181.083	6.776E+020	20.831
2000.000	-218.076	-19.468	-179.140	3.777E+019	19.577

(a)

(b)

(c)

(d)

(e)

(f)
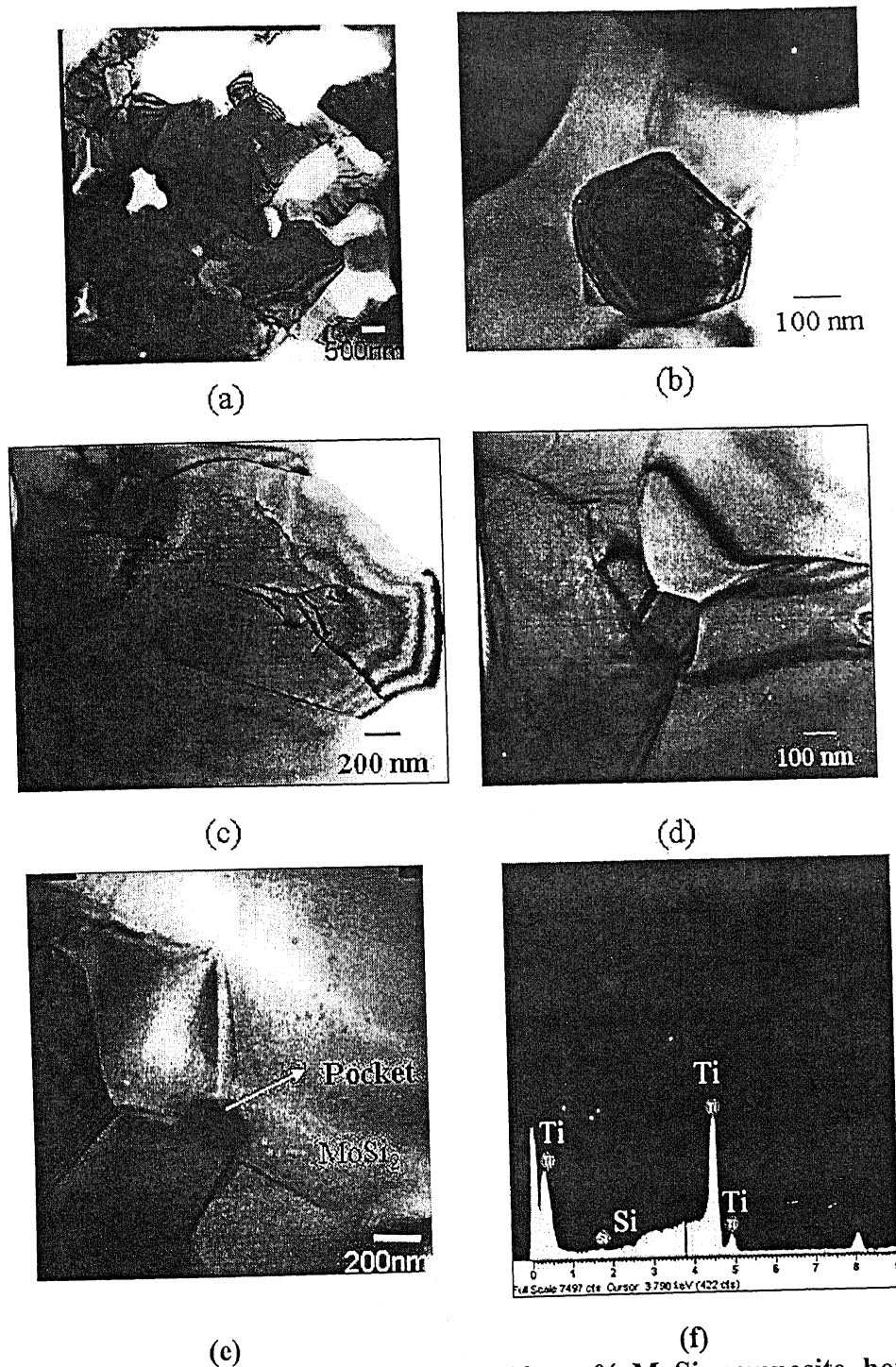
Fig. 4.1.5: Bright field TEM images of TiB$_2$–20 wt. % MoSi$_2$ composite, hot pressed at 1700° C showing the overall microstructure (a), the presence of equiaxed finer TiB$_2$ grains (b), the platelet shaped MoSi$_2$ grains (c), the presence of TiSi$_2$ phase at grain boundary triple pockets (d,e). EDS spectrum obtained from the grain boundary triple pocket also shown (f).

117

4.1.5 Mechanical Properties

The mechanical properties, in particular the Knoop hardness of the composites are compared with monolithic TiB_2 in Table 4.1.1. An increase in hardness with $MoSi_2$ content is typically observed for samples, hot pressed at 1700^0C. Additionally, the mechanical properties are also measured using Vickers indentation technique. The Vickers hardness, recorded using 10 kg indent load, is plotted against $MoSi_2$ content in Fig. 4.1.7. The hardness varies in the range of 21-29 GPa. While monolithic TiB_2 exhibit average hardness of 26 GPa, slightly lower average hardness of 24 GPa is recorded for TiB_2-20 % $MoSi_2$ composites. No observable increase in hardness is observed for TiB_2-10 % $MoSi_2$ composites, as compared to monolithic TiB_2. A maximum hardness of around 25 GPa is obtained for TiB_2–20 % $MoSi_2$ composites. It can be noted here that similar high hardness of 19 GPa, 22-23 GPa and 28 GPa is measured with TiB_2–10 vol. % B_4C [20], TiB_2-15 wt. % TiC [29] and TiB_2–3 wt. % CrB_2 [26] composites respectively.

Based on the indentation crack length measurements and assuming theoretical elastic modulus values for TiB_2 and TiB_2-$MoSi_2$ composites, the indentation toughness is evaluated. The measured toughness of the investigated materials varies in the range of 4-6 $MPa.m^{1/2}$. While the average toughness of monolithic TiB_2 and TiB_2-20 % $MoSi_2$ lies around 5.1 $MPam^{1/2}$, a little lower toughness of 4.3 $MPa.m^{1/2}$ is recorded for TiB_2-10 % $MoSi_2$ composites. Further investigation should be carried out to improve the toughness of these materials.
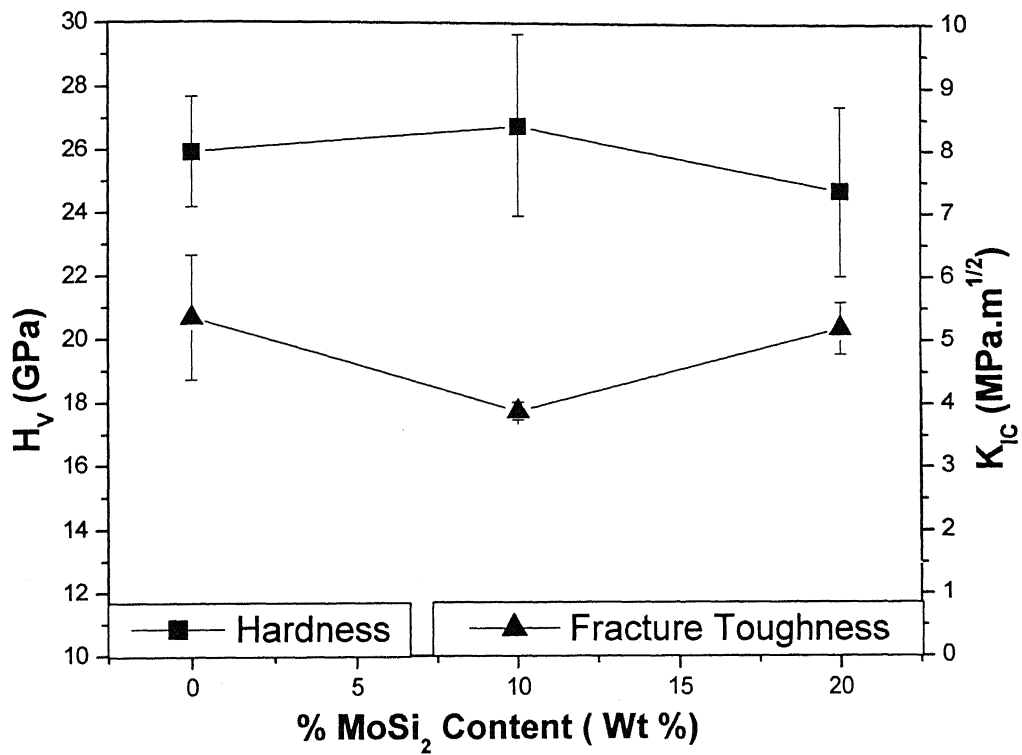
118

Figure 4.1.6: Vickers Hardness and Indentation Toughness as a function   of $MoSi_2$
content. Monolithic TiB_2 is sintered at 1800^0C whereas the composites containing $MoSi_2$
are hot pressed at 1700^0C.

Considerable interest has recently been shown in investigating the crack patterns, produced during the indentation of brittle surfaces. The individual indentation fracture event serves as a convenient "basic microscopic unit" in the description of wide range of engineering properties (degradation, abrasion, erosion, wear etc) of ceramics. Also, the indentation method provides a novel means for measuring the important fracture parameters (e.g. fracture surface energies, crack velocities). The concentrated contact forces can generate high local stresses, even if the load is <1 mN [73]. Indentation studies in case of silicate glasses and crystalline ceramic materials have demonstrated that the contact damage zones beneath sharp indenters consist arrays of concentrated shear or slip faults, which were activated at stresses close to the cohesive strength of materials [74]. A simplified view of the geometry also reveals that the dimensions of the shear or slip faults are confined within the immediate contact zone. The cracks, largely emanating from the corners of the indentations, propagate around the contact zone and complete themselves in a half penny configuration of radius 'c', with characteristic radial traces on the top surface. The radial cracks, initiated either at sufficiently high indentation loads or under the action of tensile stresses play a major role in degrading the strength properties. One interesting fact to note is that the smoothness of indentation surface belies the presence of underlying intense damage. The radial cracks, clearly visible at higher loads are suppressed at lower loads. Of the two indenters, sharp and blunt, sharp indenter (cone and pyramid) produces more complex fracture patterns and it has gone largely unstudied. It is the sharp indenter, which is more pertinent in real contact situation where severity of surface damage is of prime concern. Sharp indenters produce two basic types of crack patterns: radian-median and lateral (Law & Wilshaw 1975) [74].

In addition to mechanical property measurements, efforts have also been put forward to understand the indentation damage behavior of the newly developed materials. For this purpose, the polished surfaces are indented with varying loads and subsequently observed under SEM. In case of 5 kg load, perfect indentations are visible in both monolithic and composites, but in case of 10kg load, monolithic TiB_2 reveals the classic example of "Indentation Fracture", giving diffused indentation. It is apparent from the Figure 4.1.8c that the lateral crack is much more pronounced than the radial one. But this is not observed in TiB_2-10 wt % $MoSi_2$ composite. The hardness value is quite high around 22-27 GPa with standard deviation of ±10 %, but the fracture toughness is relatively low, around 4-6

MPa.m$^{1/2}$. A closer look at the 10kg indentation, in case of monolithic TiB$_2$, reveals interesting facts. The load is high enough to cause the indentation fracture. In Figure 4.1.8d, it is clearly visible that the fracture outside the indentation region is intergranular in nature. Figure 4.1.8a shows that the cracks are parallel. One interesting observation is the anisotropy of the indentation-induced damage with lower area showing highly deformed zone as opposed to the top area, where there is no visible deformation. The damage, just adjacent to indentation, is not as much pronounced as the bottom one. Figure 4.1.8e shows the shear deformation. Also, the severity of deformation confirms that plastic deformation has occurred outside the indentation region. Linear dimension of the crack zone is greater than the crack length in that particular zone. The damaged zone varies from 40 μm to 115μm whereas the crack length varies from 35 μm to 68 μm.
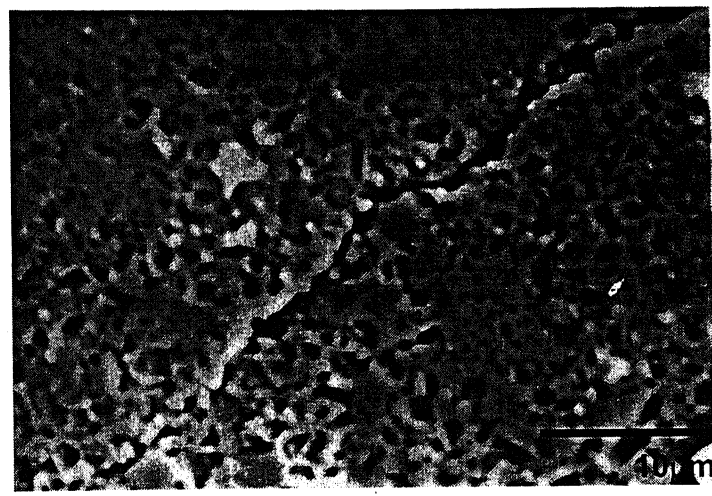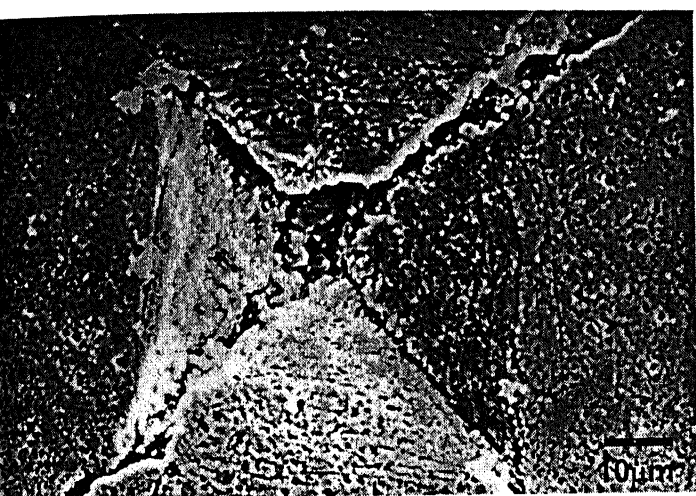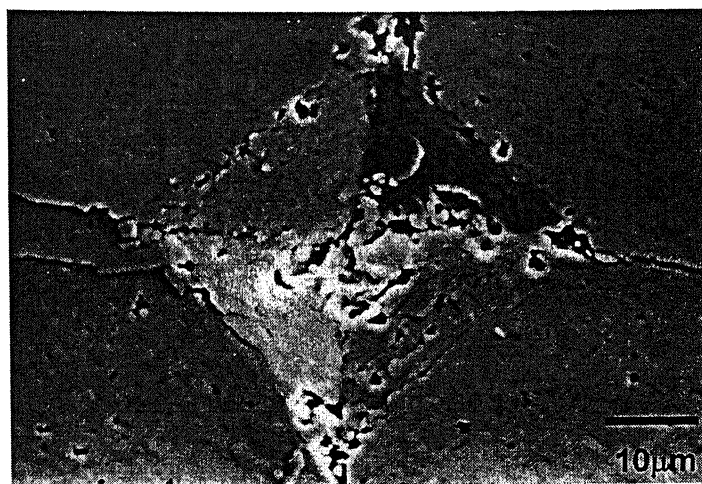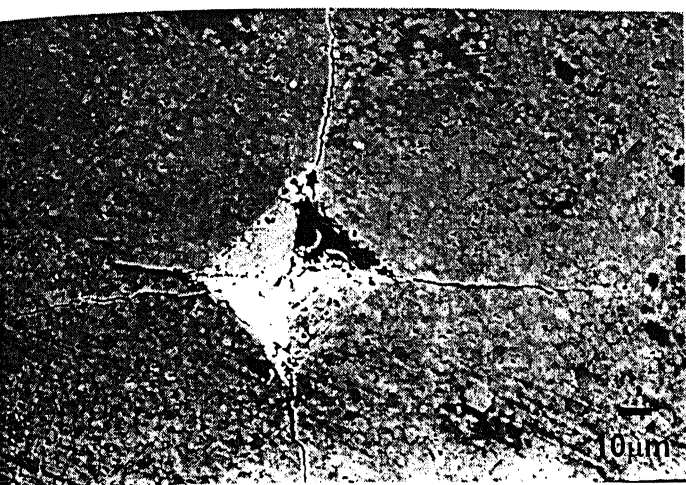
c   d

Figure 4.1.7: SEM images showing the Vickers indentation (a, b) on monolithic TiB$_2$ (HP) at 50N indent load (c) in TiB$_2$-10%MoSi$_2$ composite at 100N load. (d) The crack propagation in TiB$_2$-10% MoSi$_2$
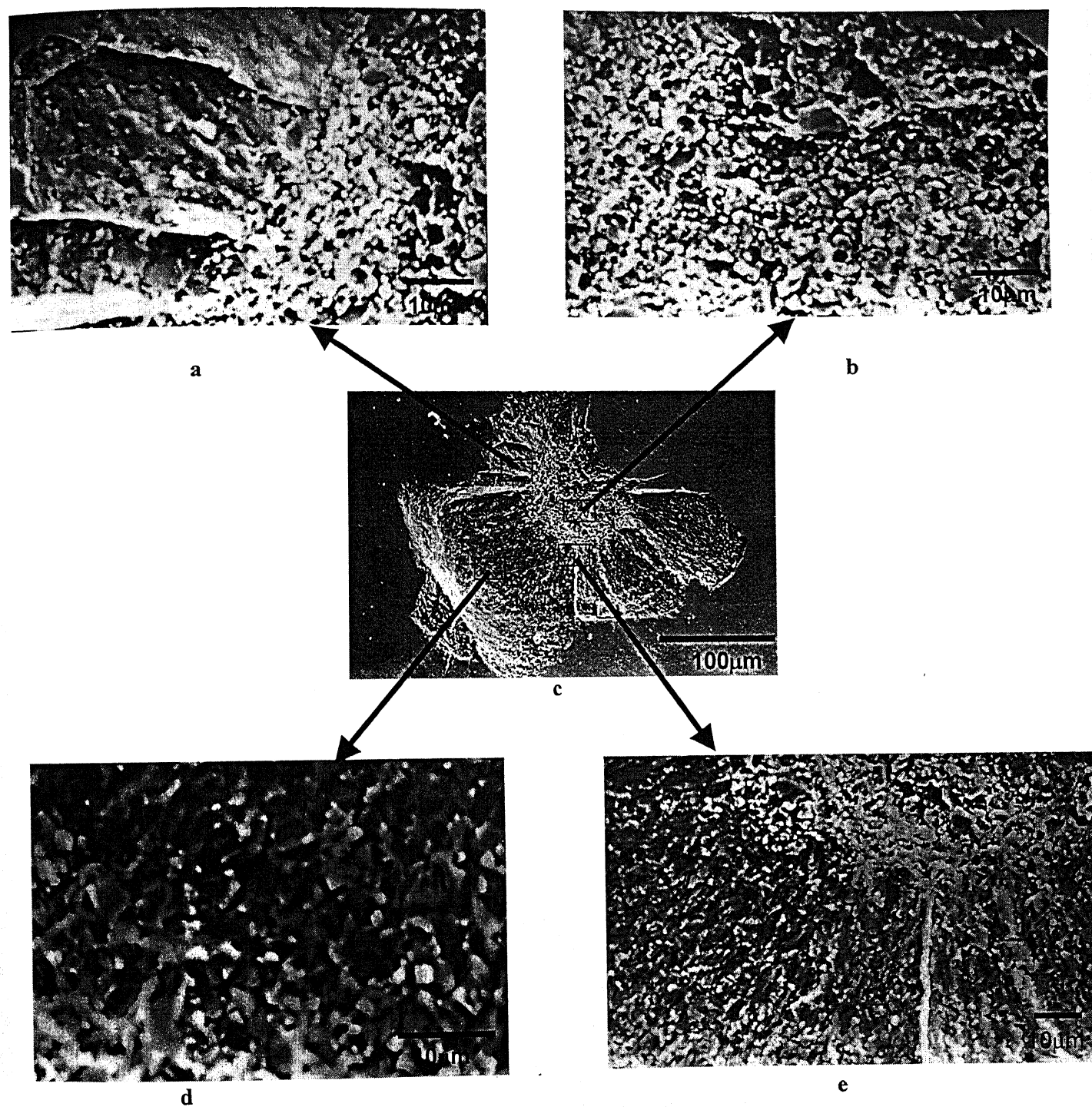
122

Figure 4.1.8: Typical SEM image illustrating the indentation-induced damage of monolithic TiB$_2$ at 100N indent load (c) The detailed view of the different parts of the indented zone (b) and the damage zone , adjacent to Vickers indentation (a, d and e) are also shown.

4.2 Tribological studies

4.2.1 Friction data

The friction and wear properties of monolithic TiB_2 and its composites were studied under fretting contacts against bearing steel. The effect of load was investigated by keeping other fretting variables (10,000 cycles, 100 μm amplitude and 8 Hz frequency) constant. The COF plots of TiB_2 and $MoSi_2$ reinforced TiB_2 at different loads are shown in Fig.4.2.1. For monolithic TiB_2 in running-in-period (first 1000 cycles), COF values increase to a high value and then decrease to attain a steady state value. However, there is variation in the peak and steady state values depending on the materials and load (Table 4.2.1). The following observations can be made from the COF data obtained with TiB_2 and its composites: a) Monolithic TiB_2 exhibits COF values of 0.67 and 0.71 at 2 and 5N respectively. In contrast at 10N, COF value is lower and around 0.5. At 2 and 5N, peak COF values during running-in-period are around 0.71 and 0.85 respectively. At 10 N, peak COF value during running-in-period is only 0.56. The reason for low COF value at higher loads is yet to be clear. In one of the earlier investigations, So et. al [75] reported that the higher the pressure and sliding speed, the thicker was the extruded layers and the shorter was the time interval for a layer to be extruded from the contact interface. In the present study, similar tribooxidation is expected to take place and could cause higher COF. b) TiB_2- 10 wt. % $MoSi_2$ composite exhibits COF values of 0.12, 0.10, and 0.11 at 2, 5 and 10N respectively. At 2, 5 and 10N peak COF values during running-in-period are 0.14, 0.10 and 0.13 respectively. In this case COF is almost same at all loads due to the formation of lubricated nature tribooxide layer, as will be revealed from SEM images of wear scars. C) TiB_2–20 wt.% $MoSi_2$ composites exhibits steady state COF values of 0.67, 0.79 and 0.51 at 2, 5 and 10N respectively. At 2, 5 and 10N, peak COF values during running-in-period are 0.80, 0.80 and 0.55 respectively. In the fretting wear process, formation of triboxoidation products and subsequent fracture and removal of debris/tribochemical layer results in the observed high COF in friction curves, as noticed in Monolithic TiB_2 and TiB_2- 20 wt. % $MoSi_2$ composite.

124

Table 4.2.1 Peak and steady – state COF values at different loads

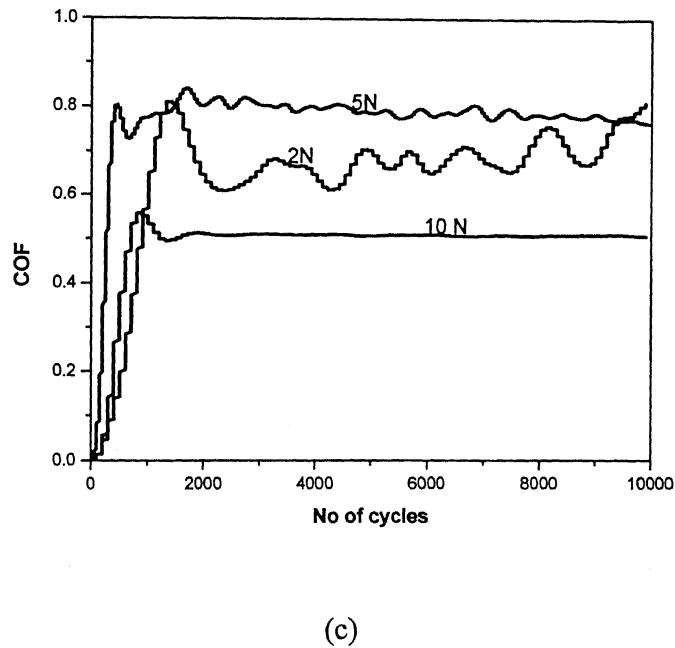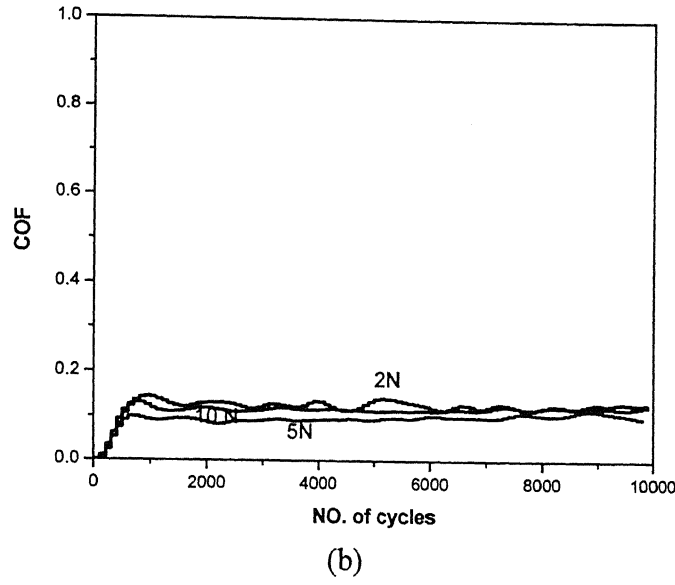| Material	COF values					
	2N		5N		10N	
	Peak value	Steady - State value	Peak value	Steady - State value	Peak value	Steady - State value
Monotlithic TiB$_2$	-	0.58	0.70	0.65	-	0.50
TiB$_2$–MoSi$_2$ (10 wt.%)	0.14	0.12	0.10	0.10	0.13	0.11
TiB$_2$–MoSi$_2$ (20 wt.%)	0.80	0.67	0.80	0.79	0.55	0.51

(a)

(b)

(c)
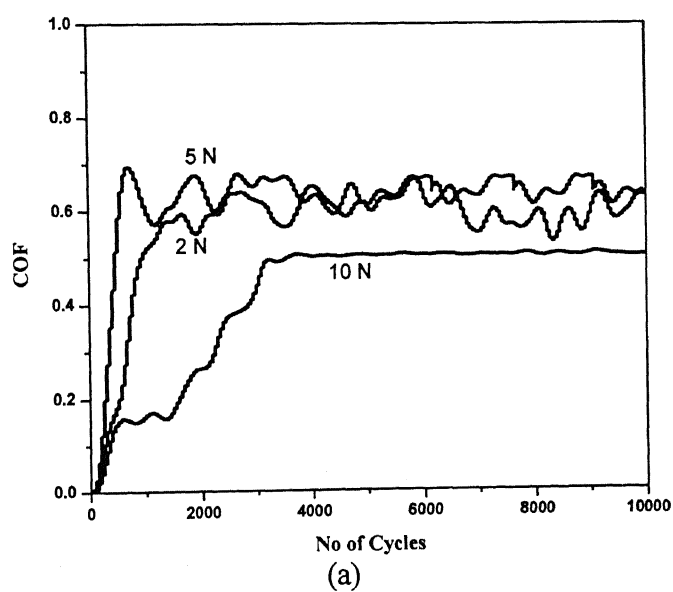
Fig. 4.2.1: The frictional behavior of monolithic TiB$_2$ and its composites: (a) Monolithic TiB$_2$, (b) TiB$_2$–MoSi$_2$ (10 wt %) composite and (c) TiB$_2$–MoSi$_2$ (20 wt %) composite, during fretting against bearing steel. Fretting conditions: 2-10N load, 10,000 cycles, 8Hz frequency and 100 μm stroke length.

4.2.2 Wear data

The wear volumes of TiB_2 and its composites are computed by measuring wear scar diameter in the transverse direction on the worn samples and following the Klaffke's equation [76], as already mentioned in Chapter 3. Wear scar diameter in the transverse direction of both flat and ball are presented in Table 4.2.2. The specific wear rates, calculated based on the wear volume, load and total fretted distance are plotted in Fig.4.2.2 In case of monolithic TiB_2 and TiB_2-20wt % $MoSi_2$ composite the wear volume and specific wear rate exhibited in higher range. However, in the case of TiB_2-10 wt % $MoSi_2$ is showing significantly low wear volume as well as low specific wear rate due to the formation of stable lubricative nature oxide layer. The wear volume of steel is more than that of the ceramic in all cases and is evident from the large difference in hardness.

Summarizing the tribological data, it should be evident that the lowest steady state COF and lower wear rate could be achieved with TiB_2-10 wt % $MoSi_2$ composites. No clear correlation between COF and load is observed for the investigated materials. Also, the frictional behavior of this composite is stable as can be realized from the absence of any observable fluctuations in the friction plot. However, the frictional behavior of monolithic TiB_2 as well as for TiB_2-20 wt % $MoSi_2$ is similar to that of steels, as the steady state COF for self-mated steel varied between 0.5-0.6. However, the wear rate of the investigated materials is superior compared to that of steels.

Table 4.2.2 Wear scar diameter in the transverse direction of both flat and ball. Fretting conditions: 10,000 cycles, 8Hz frequency and 100 μm stroke length.

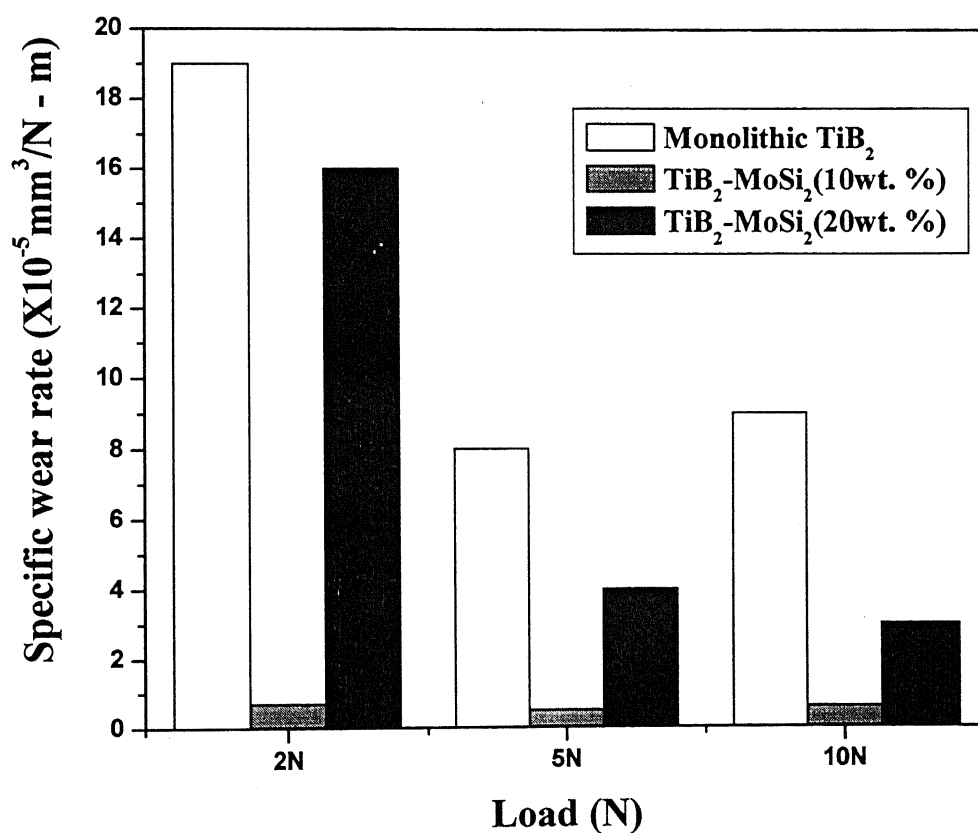| Fretting couple	Transverse wear scar diameter (μm)					
	2N		5N		10N	
	Flat	ball	Flat	ball	Flat	ball
TiB₂/steel	181.5	700.0	163.0	900.0	219.0	652.0
TiB₂ -10% MoSi₂/steel	40.0	-	52.0	-	68.4	211
TiB₂ -20% MoSi₂/steel	276.0	282.5	226.0	426.0	238.0	258.7

Fig. 4.2.2: Variation of specific wear rate for monolithic TiB_2 and TiB_2 – $MoSi_2$ composites against bearing steel at different loads. Fretting conditions: 10,000 cycles, 8Hz frequency and 100 μm stroke length, counterbody: steel ball. About 10 % deviation in the wear data is measured in our experiments.

4.2.3 Morphology of worn surfaces and wear mechanism

Detailed microstructural investigation using SEM was performed in order to understand the fretting wear mechanism for monolithic TiB_2 and its composites. The overall topographical features of worn scars formed on monolithic TiB_2 flats are shown in Fig. 4.2.3. The abrasion was commonly observed under all loads. At 2N load, severe wear occurred due to delamination and fracture of discontinuous tribochemical layer (Fig. 4.2.3a-b). Similarly at 5N, severe wear took place due to the non-protective nature of discontinuous tribolayer, which further results in delamination and fracture of the surface. On the other hand at 10N load, extensive wear occurred due to similar delamination and intergranular fracture of the surface. EDS analysis revealed that the presence of B, O, Ti and Fe on the worn surface of monolithic TiB_2 of all loads. An interesting observation is the relative amount of Fe and O increases with increasing load (Fig. 4.2.4). Since the hardness of steel is lower than that of TiB_2, so iron has transferred from the counterbody (bearing steel). Elemental X-ray mapping on the worn surface of 10 N load monolithic TiB_2 revealed the distribution of elements (B, Ti, O and Fe) on the tribosurface as shown in Fig. 4.2.5. The steel balls also surfer extensive fretting damage (Fig. 4.2.6) with increased severity as the load is increased from 2N to 10N. The transverse wear scar diameter on steel is an indicative parameter for severity of wear damage, increases from 700 to 900 μm as load increases from 2N to 5N. The major wear mechanisms appear to be abrasion, adhesion and tribochemical wear.

In contrast to monolithic TiB_2, TiB_2-10 wt % $MoSi_2$, exhibits mild wear due to the formation of soft tribooxide layer, which is continuous throughout wear scar under all loads (Fig. 4.2.7). Further, no signs of debris formation on or around the wear scar were observed. The contrast between the reaction products indicated a difference in the chemistry (Fig. 4.2.7). This tribooxide layer is soft due to lubricative nature and spreads easily on the surface. This protective layer causes low COF and wear rate under unlubricated condition. The lower COF and wear rate for TiB_2-10 % $MoSi_2$, attributable to the adherent tribochemical layer is rather a new result. The possible tribochemical reactions that can occur during fretting actions include:

$$TiB_2 + O_2 \rightarrow TiO_2 + B_2O_3 \qquad (4.2.1)$$

$$MoSi_2 + O_2 \rightarrow MoO_3 + SiO_2 \qquad (4.2.2)$$

From the above reactions, it is plausible that the tribochemical layer is enriched with TiO_2 and SiO_2. B_2O_3 may form some glass and MoO_3 can evaporate. Additionally, TiO_2 can further react with SiO_2 to form complex compounds. Detailed Raman analysis needs to be carried out in future to prove this point. Furthermore the steel counterbody suffers less wear (Fig. 4.2.8) as compared to that against monolithic TiB_2 and TiB_2- 20 % $MoSi_2$ composites. For 2N and 5N load, the wear scars on steel ball were not visible under optical microscope. For 10N load, the wear scar diameter on steel ball is around 211 μm (see Table 4.2.2).

Fig. 4.2.9 shows the overall and detailed view of the fretted scars on TiB_2–20 wt % $MoSi_2$ composite. When compared with TiB_2–10wt % $MoSi_2$ fretted surface, an additional feature that is observed is the formation of wear debris (see Fig. 4.2.7 and Fig. 4.2.9).TiB_2–20 wt % $MoSi_2$, exhibits high COF and wear rate due to the formation of discontinuous tribooxide layer. At 2 N and 5N, severe wear occurred due to the extensive fracture of tribochemical layer and it turned into coarse wear debris, which further accelerated the wear rate. At 10N spalling of tribochemical layer and agglomerated wear debris at the vicinity of wear scar were observed. These debris are formed due to fracture of tribochemical layer. The important features like accumulation of oxide at the periphery of scar, smearing, fracture and removal of oxide layer (as sheets) is illustrated in Fig. 4.2.9. It was observed that formation and smearing of tribochemical reaction product starts at 2N itself. The steel balls also suffer extensive fretting damage (Fig. 4.2.10) like counterbody of monolithic TiB_2. The wear scar transverse diameter increases systematically from 282.5 μm to 426 μm as load increases from 2N to 5N.

Ceramics are chemically more stable than metals, so that wear and friction of ceramics should be less sensitive to environmental effects. But tribo-chemical effects on wear and friction of some ceramics (especially non-oxide) are considered as an important factor under certain conditions and its effect is complicated. [77] The tribo-chemical effects of ceramics are closely related with surface chemistry and physics of the tribological process. Because of their inherent brittleness, ceramics can wear by chipping. The surface and subsurface cracks form, join, and release small chips of material. A fine powder is produced as this wear debris is ground up during the wear process. Ceramics are also sensitive to strain rate and typically exhibit an increased tendency to crack with

increased sliding velocity, in addition to the frictional heating. Oxidational wear is a form of wear that primarily occurs during nominally unlubricated conditions of sliding [78]. It is usually, but not always, beneficial by forming a protective layer. In monolithic TiB_2 and TiB_2-20 wt. % $MoSi_2$, oxidation of both the steel and the ceramic are the causes for such high wear rate and friction. In case of TiB_2–10 wt. % $MoSi_2$ the wear of ceramic and steel ball are significantly less. Moreover the ceramic was not found adhering to the surface of the wear scar in the ball like as monolithic and TiB_2-20 wt. % $MoSi_2$ composite, which indicates the non-seizing and non-adhering character of the composite to steel. Therefore, adhesive wear plays negligible role in the wear of TiB_2-10 wt. % $MoSi_2$ composite. While tribochemical wear is the major wear mechanism for all the investigated materials, the adhesive and abrasive wear by brittle microfracture of tribolayer also contribute to more wear in case of monolithic TiB_2 and TiB_2-20 wt. % $MoSi_2$ composites.
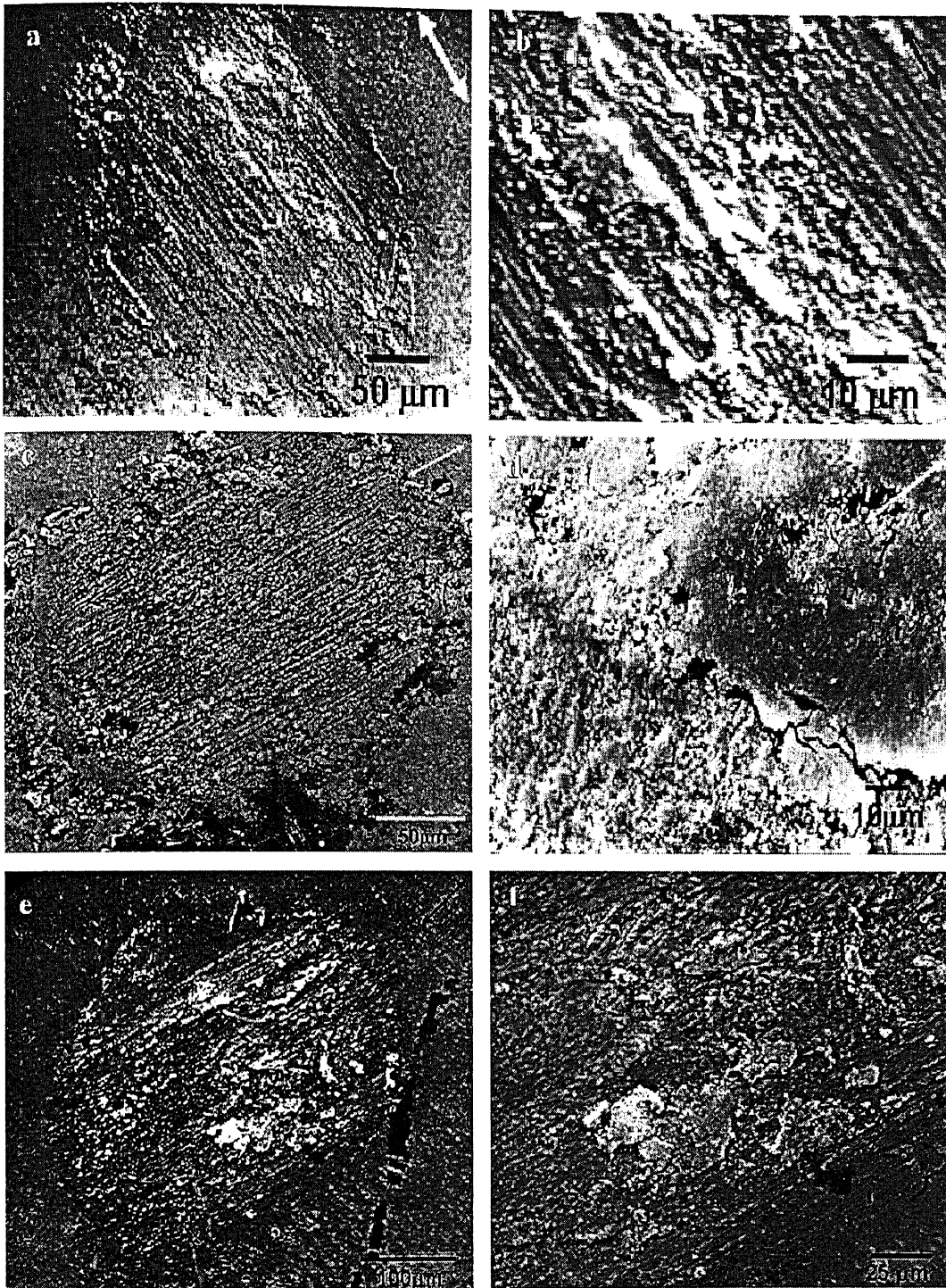
Fig. 4.2.3: SEM images showing the overview and details of the worn surfaces on monolithic TiB$_2$ at different loads: (a-b) 2N (c-d) 5N (e-f) 10N (overall and detailed). Arrow indicates the fretting direction. Fretting conditions: 10,000 cycles, 8Hz frequency and 100 μm stroke length. Counterbody: bearing steel.
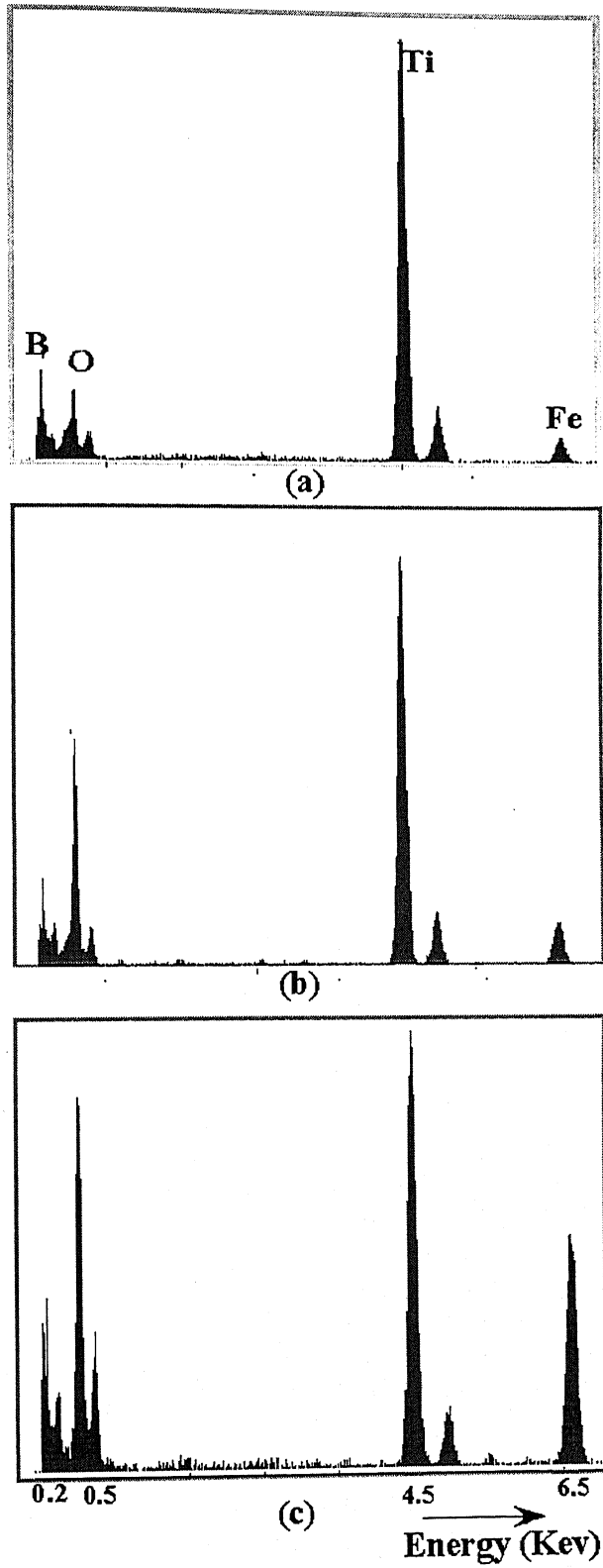
132

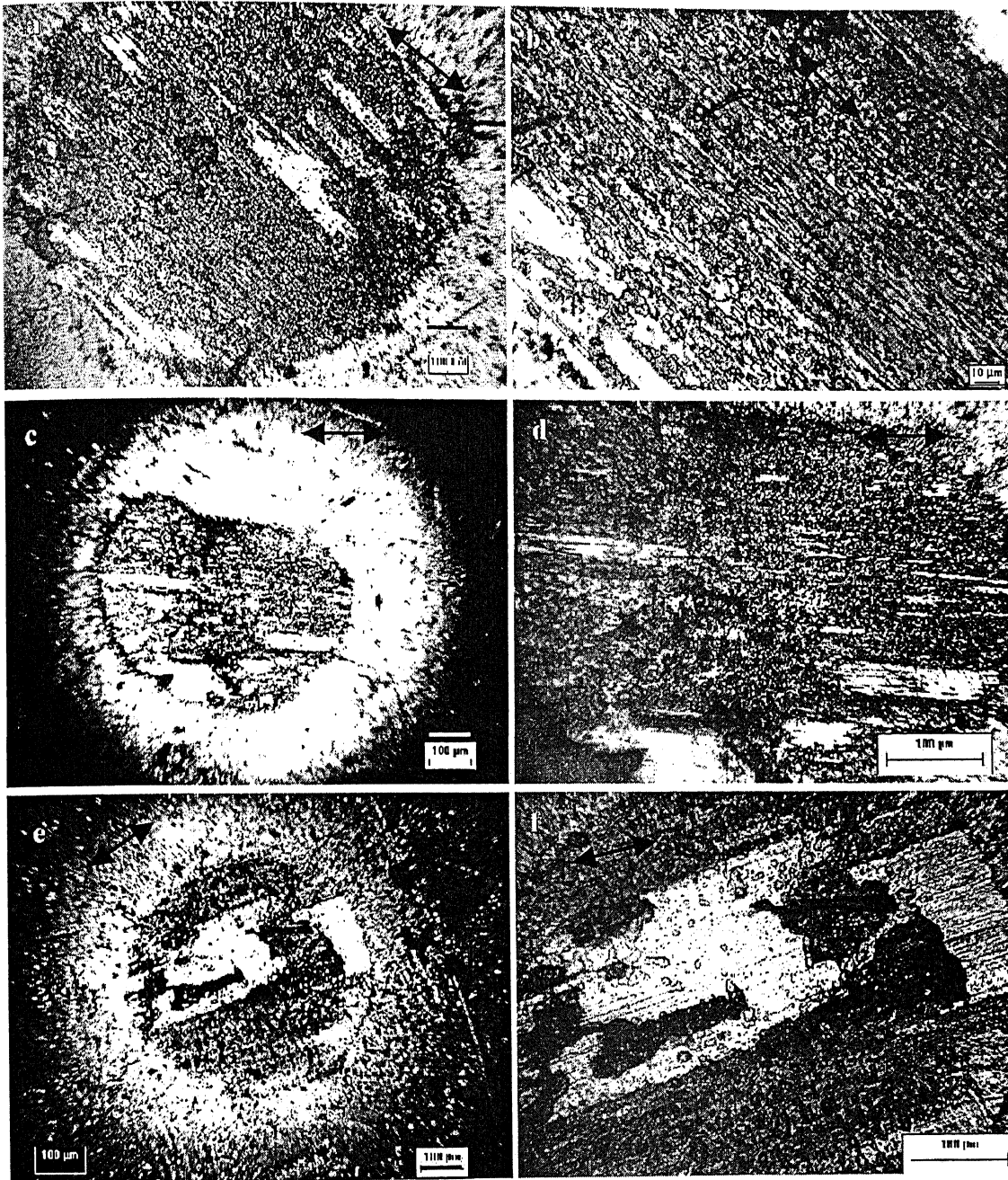Fig. 4.2.4: EDX analysis on the tribolayer of monolithic TiB$_2$ at different loads: 2N (a), 5N (b), 10N (c). Fretting conditions: 10,000 cycles, 8Hz frequency and 100 μm stroke length. Counterbody: bearing steel.
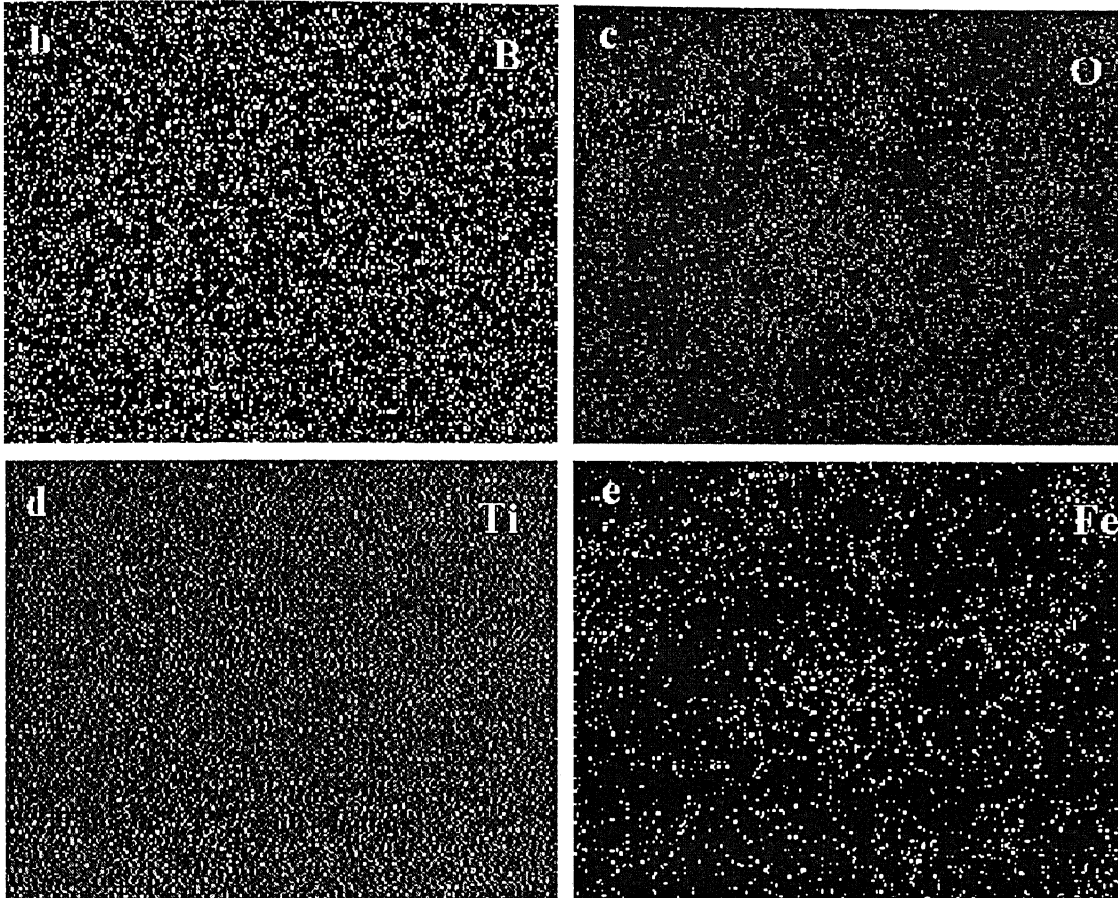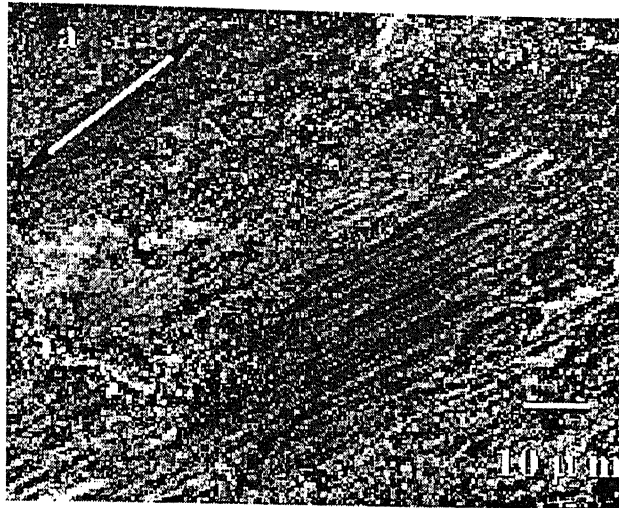
Fig. 4.2.5: X-ray mapping of different elements (b) boron (c) oxygen (d) titanium (e) iron on the worn surface of TiB_2 shown in (a). Arrow indicates the fretting direction. Fretting conditions: 10N load, 10,000 cycles, 8Hz frequency and 100 μm stroke length. Counterbody: bearing steel.

Fig. 4.2.6: Optical images showing the overview and details of the worn surfaces on steel ball at different loads: (a-b) 2N (c-d) 5N (e-f) 10N (overall and detailed). Arrow indicates fretting direction, Fretting conditions: 10,000 cycles, 8Hz frequency and 100 μm stroke length. Counterbody: Monolithic TiB_2.
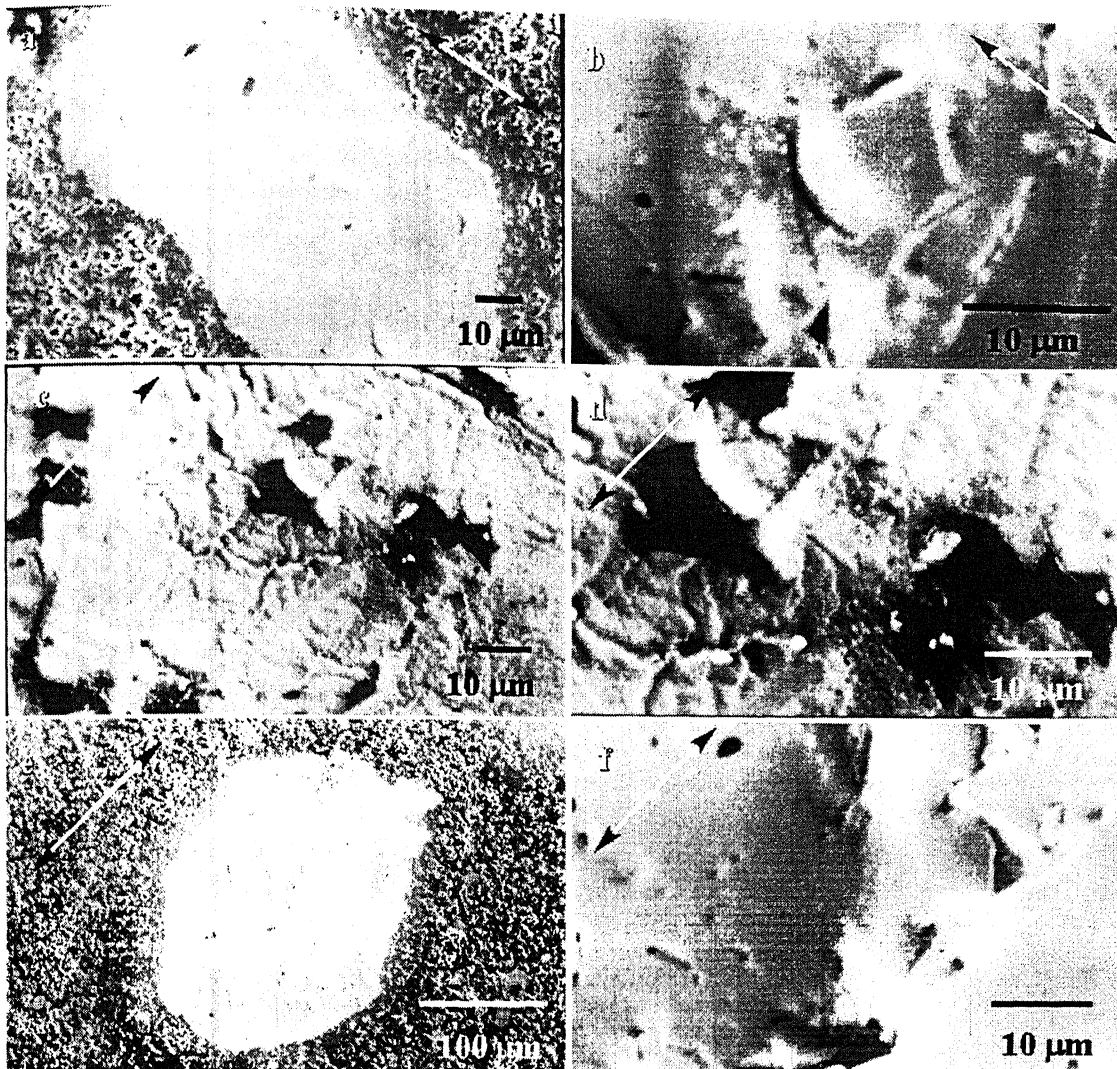
Fig. 4.2.7: SEM images revealing the overall and details of the fretted surfaces on TiB$_2$ - MoSi$_2$ (10 wt. %) composite at different loads: (a-b) 2N (c-d) 5N (e-f) 10N (overall and detailed view). Arrow indicates the fretting direction. Fretting conditions: 10,000 cycles, 8Hz frequency and 100 μm stroke length. Counterbody: bearing steel.
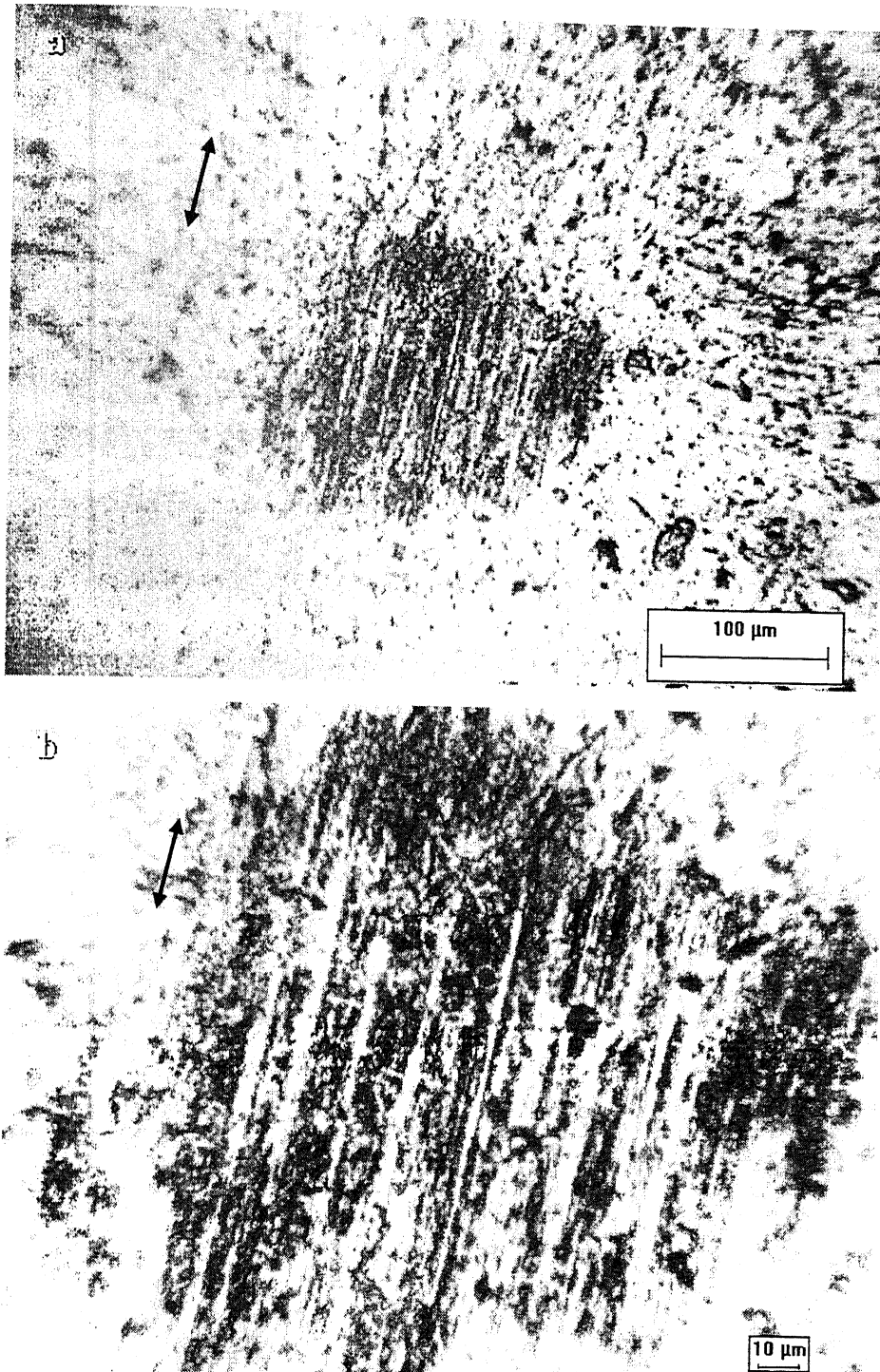
Fig. 4.2.8: Optical images showing the overview and details of the worn surfaces on steel ball at 10N load. Arrow indicates fretting direction, Fretting conditions: 10,000 cycles, 8Hz frequency and 100 μm stroke length. Counterbody: TiB$_2$-10 % MoSi$_2$ composite.
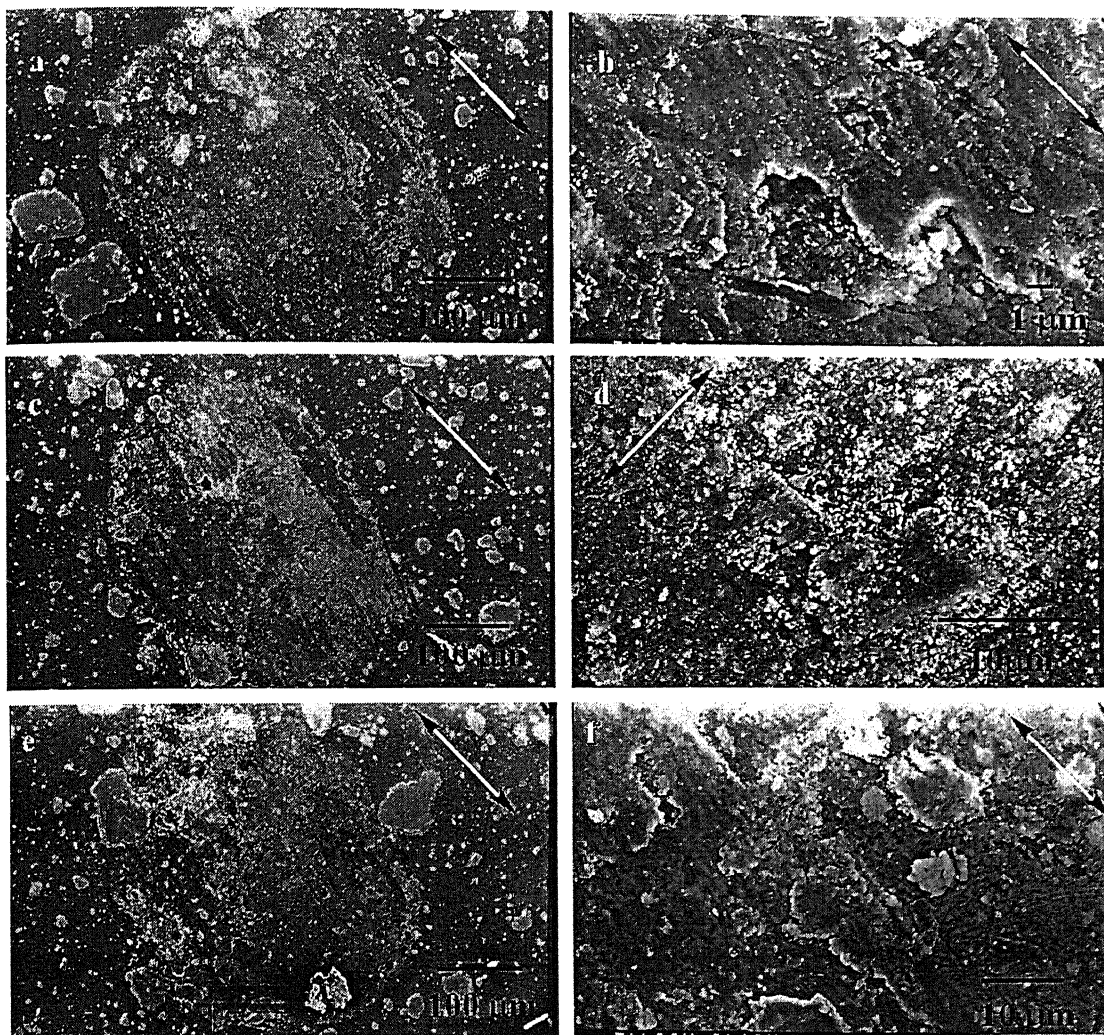
Fig. 4.2.9: SEM micrographs reveals the overview as well as details of the fretted worn surfaces of TiB$_2$–MoSi$_2$ (20 wt.%) composite at varying loads of 2N (a-b), 5N (c-d), 10N (e-f). Arrow indicates the fretting direction, Fretting conditions: 10,000 cycles, 8Hz frequency and 100 μm stroke length. Counterbody: bearing steel.
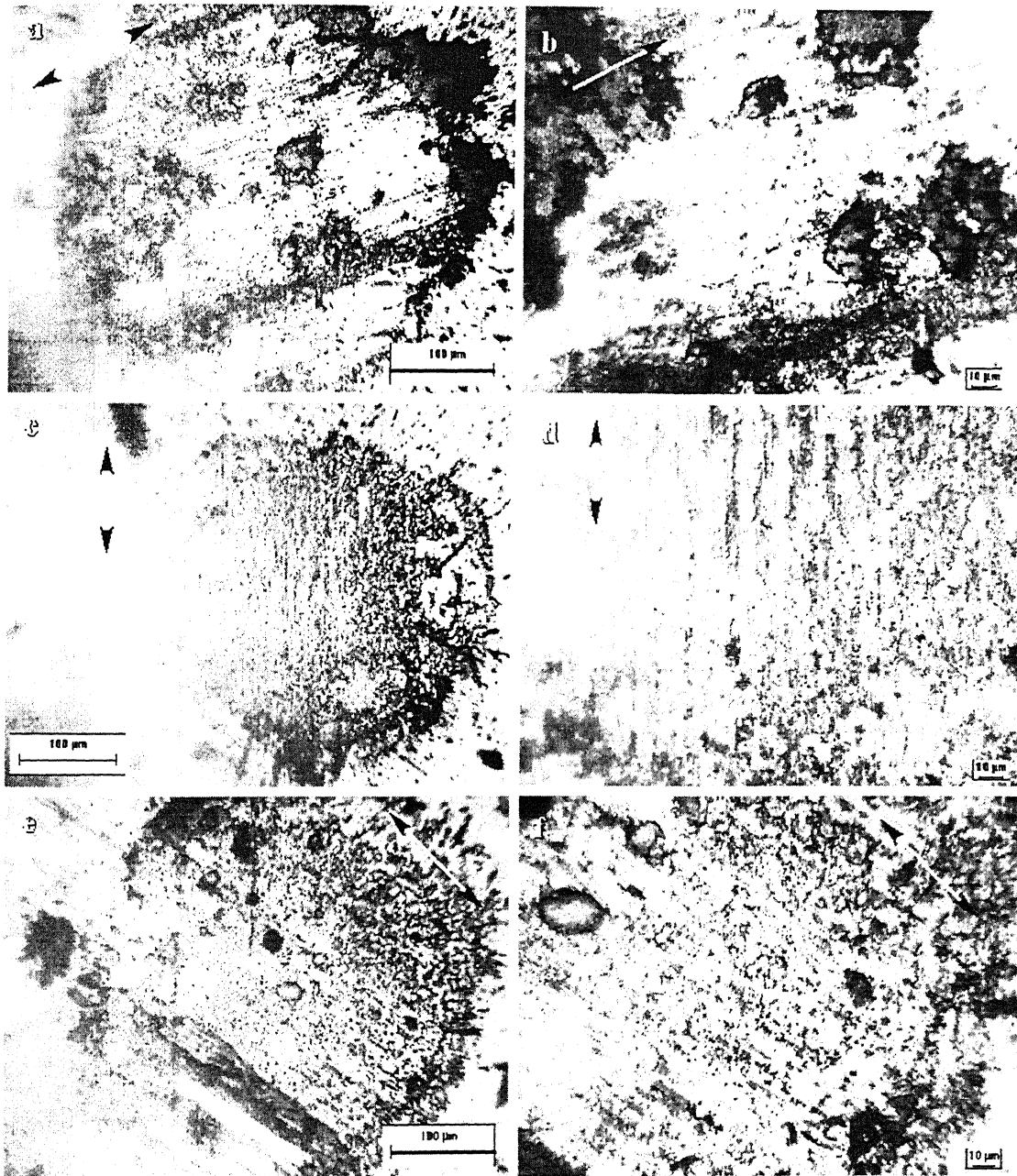
Fig. 4.2.10: Optical images showing the overview and details of the worn surfaces on steel ball at different loads: (a-b) 2N (c-d) 5N (e-f) 10N (overall and detailed). Arrow indicates the fretting direction, Fretting conditions: 10,000 cycles, 8Hz frequency and 100 μm stroke length. Counterbody: TiB$_2$-20 % MoSi$_2$ composite.

4.3 Oxidation studies

For the oxidation study, monolithic TiB_2 and TiB_2-$MoSi_2$ composites having densities of 88% ρ_{th} and 95% ρ_{th} (theoretical density), were respectively selected. SEM image of the fracture surfaces of monolithic TiB_2 and TiB_2–$MoSi_2$ composite, hot pressed at 1700°C are shown in Fig 4.1.5. The presence of pores can be easily distinguished in the structure. The addition of $MoSi_2$ was beneficial in improving the sintered density of TiB_2. The relatively lower sintered density of the monolithic TiB_2 is due to the lower temperature of hot pressing. Tampieri et. al [64] reported a hot pressed of 98% ρ_{th} for the case of TiB_2 hot pressed at 1850°C for 60 min at 30 MPa. The samples hot pressed by Tampieri et. al [64] were also evaluated for oxidation at different temperatures and their results will be compared with the results of the present study.

4.3.1 Kinetics of oxidation

The weight gain curves as a function of time for both monolithic TiB_2 and TiB_2-20% $MoSi_2$ composites are presented in Fig 4.3.1a. The actual weight gain data is provided in Table 4.3.1. In the case of monolithic TiB_2, the weight gained continuously with time. However, the weight gain of the composite was dependent on the exposure time. TiB_2-$MoSi_2$ composite exhibited continuous weight gain till 16h, after which there was a drop in the weight gain. In order to understand the kinetics of oxidation, the data were analyzed using the parabolic law, i.e.

$$(\Delta w/A)^2 = K_p t \qquad\qquad (4.3.1)$$

where Δw is the change in weight, A is the surface area of the sample, t is the oxidation time and K_p is the parabolic rate constant. For analysis, the data obtained only up to 16h was utilized for the TiB_2-$MoSi_2$ composite. The weight gain curves as per the parabolic rate law are provided in Fig. 4.3.1b. The parabolic rate constants have been presented in Table 4.3.2 and they were similar for the oxidation of TiB_2 up to 64h and of TiB_2-$MoSi_2$ up to 16h. This indicates that the mechanism of oxidation in the case of composite was at least similar to that of monolithic TiB_2 up to 16h of oxidation.

The parabolic rate constant determined in the present study for monolithic TiB_2 were about three orders of magnitude higher than that determined by Tampieri et. al [64] for oxidation of TiB_2 at 850°C. Tampieri et.al [64] have provided weight gain data at

800°C and 900°C (Figure 2.5) from which the K_p was estimated at these two temperatures. As the apparent activation energy for oxidation is also known between 800°C and 850°C (E_a= 40 KJ/mol) [64], the K_p at 850°C was calculated. These results are presented in Table 4.3.3. The higher K_p obtained for the monolithic TiB$_2$ in the present study may be related to the higher amount of porosity. It can be related that the hot pressed condition used by Tampieri et. al [64] resulted in monolithic TiB$_2$ with a higher sintered density (98 % ρ_{th}).

In order to understand the nature of oxidation, the data used in the parabolic law analysis above was also fit to the general rate equation

$$(\Delta w/A)^m = K_m t \qquad (4.3.2)$$

where Δw is the change in weight, A is the surface area of the sample, t is the oxidation time and K_m is the rate constant. These results are also tabulated in Table 4.5. The oxidation nature can be termed as para linear because the value of m was closer to 1.5 for both materials. Moreover, the nature of oxidation (up to 16h) appears to be similar for both materials. The nature of oxidation changed after 16h in the case of the composite (Fig. 4.3.1a) and this needed to be understood.

Table 4.3.1 Actual weight gain data of monolithic TiB_2 and TiB_2-$MoSi_2$ composite after oxidation in air at 850°C.

Time (seconds)	Monolithic TiB_2 ($\Delta w/A$) x 10^2 Kg/m^2	TiB_2-$MoSi_2$ composite ($\Delta w/A$) x 10^2 Kg/m^2
1800	7.79	18.54
3600	.24.15	31.15
7200	38.11	29.72
14400	102.34	124.09
28800	150.78	120.97
57600	155.89	186.58
86400	-	22.27
115200	213.38	9.75
172800	-	19.87
230400	305.23	35.08

Table 4.3.2 Summary of rate constants processed from the data of the isothermal oxidation experiments. The data only up to 16 h was considered for composite materials.

Material	K_p (Kg^{2}m^{-4}s^{-1}) X 10^5	K_m X 10^4	m
Monolithic TiB_2	4.087	2.246	1.414
(TiB_2–$MoSi_2$) composite	5.992	3.349	1.423

Table 4.3.3. K_p values of monolithic TiB_2 at different temperatures evaluated in the study of Tampieri et. al [64].

Temperature (^oC)	K_p value $Kg^2/m^4/sec$	Reference	Material
800	3.1×10^{-8}	Tampieri et. al [11]	Monolithic TiB_2
850	6.0×10^{-8}	Tampieri et. al [11]	Monoltihc TiB_2
900	6.6×10^{-8}	Tampieri et. al [11]	Monoltihc TiB_2
850	4.0×10^{-5}	Present study	Monoltihc TiB_2
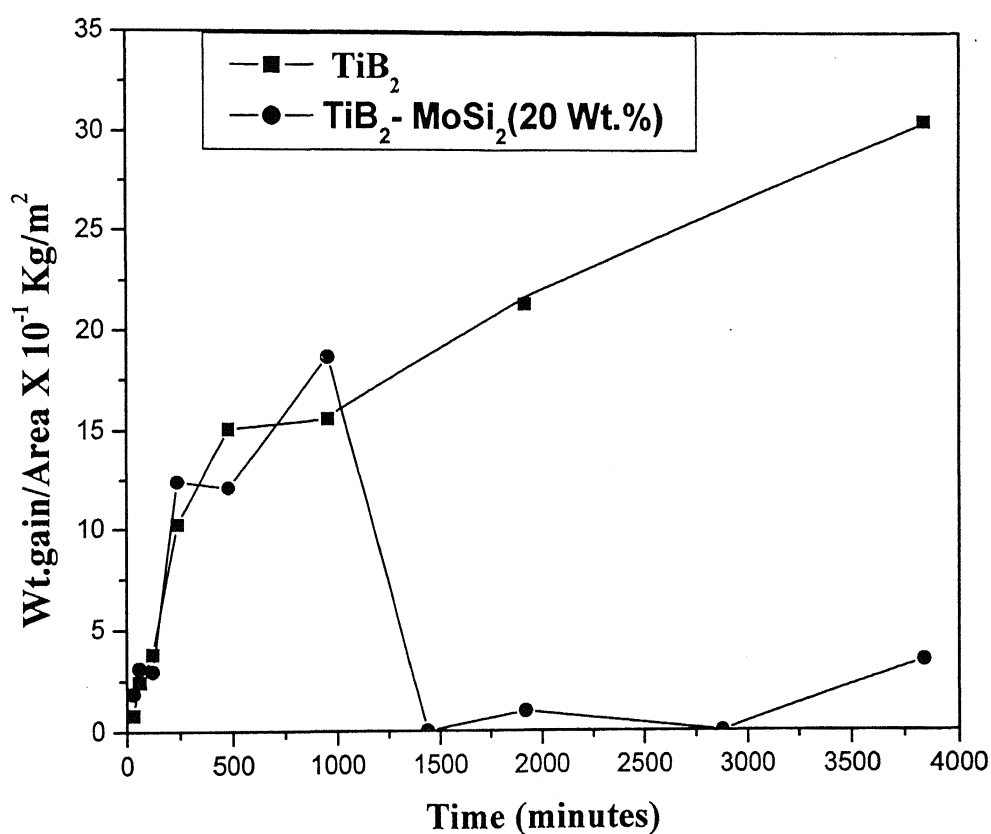
Fig. 4.3.1a: Weight gain curves for oxidation of monolithic TiB_2 and TiB_2-$MoSi_2$ (20 wt. %) composite in air at 850^oC. The lines joining the data points are for visual aid only

143

Fig. 4.3.1b: Variation of $(\Delta w/A)^2$ as a function of time for the isothermal oxidation of monolithic TiB_2 and TiB_2-$MoSi_2$ (20 wt. %) composite in air at $850^\circ C$. The lines joining the data points are for visual aid only

144

4.3.2 XRD results

XRD patterns obtained from the surface at different oxidation times have been presented in Fig. 4.3.2. X-ray diffraction analysis of the hot pressed samples indicated that TiB_2 phase was present in monolithic and TiB_2, $MoSi_2$ and $TiSi_2$ phases were present in the composite. After oxidation, only crystalline rutile (TiO_2) could be unambiguously identified in both monolithic and composite samples. Minor phases like $TiBO_3$, MoO_3 and SiO_2 could not be identified by XRD investigations, although they have been reported to form [55,62,66]. This could be due to their low volume fraction in the surface oxide volume from where the XRD information was obtained or due to their possible presence as non-crystalline phases. The identification of B_2O_3 was a little more tricking. According to Koh et. al [61], the B_2O_3 phase was identified on the oxide scale of TiB_2. A detailed search through the JCPDF data base for B_2O_3 indicated several possibilities (Table 4.3.4). The B_2O_3 identified by Koh et. al [61] was the less common of the B_2O_3 (the second entry in Table 4.3.4) and this phase was assumed while identifying B_2O_3 in the oxide. The maximum intensity peak for this phase ($2\theta = 27.76$) was almost close to that for TiO_2 ($2\theta = 27.436$). Therefore, unambiguously identification of B_2O_3 was generally not possible. However, its presence was indicated in the case of composite samples after 1h and 4h oxidation (Fig. 4.3.2b). In the case of the composite, B_2O_3 was the major phase on the surface for samples oxidized for 1h and 4h. In these cases, this B_2O_3 peak was the most prominent peak. For the samples oxidized beyond 4h, the oxide was composed of mainly TiO_2.

Table 4.3.4 Available JCPDF data for B_2O_3

JCPDF Number	Year	Crystal Structure	Lattice parameters	Quality
06-0634	1953	Hexagonal	a=4.334 c= 8.334	not indexed
13-0570	-	-	-	deleted
44-1085	1991	Hexagonal	a=4.336 c= 8.34	calculated
72-0626	1970	Hexagonal	a=4.335 c= 8.339	calculated
73-2100	1952	Hexagonal	a=4.325 c= 8.317	calculated
73-1550	1953	Hexagonal	a=4.334 c= 8.334	calculated
76-1655	1968	Hexagonal	a=4.330 c= 8.390	calculated

146
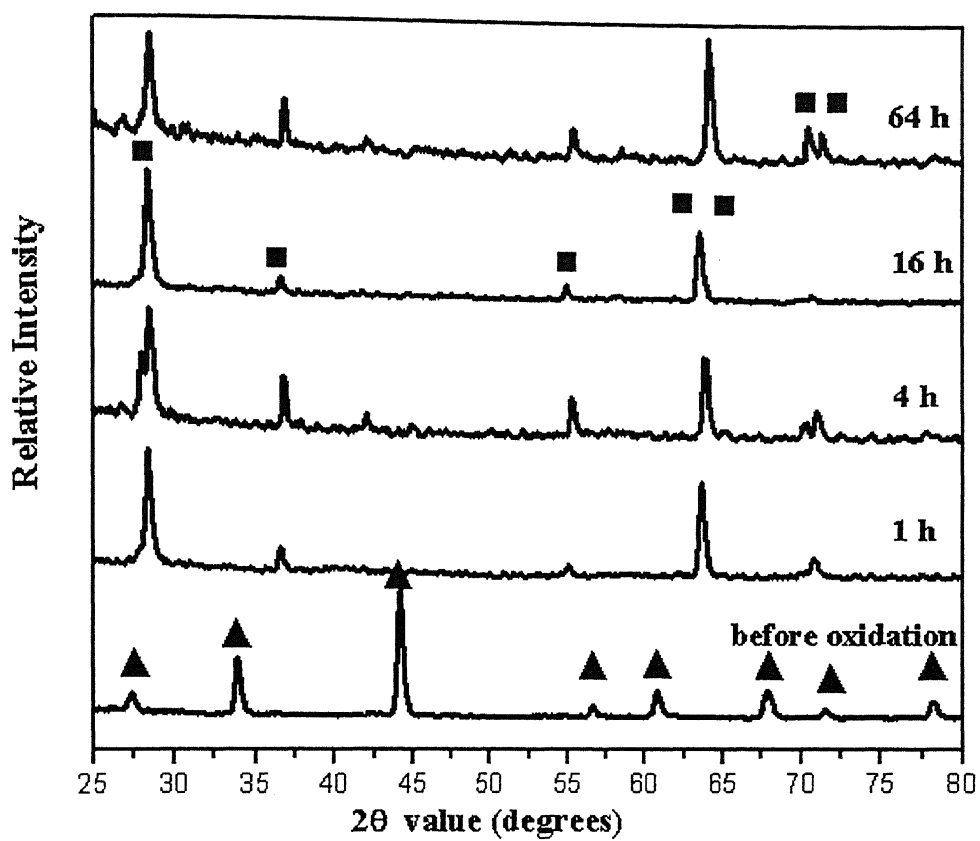
Fig. 4.3.2a: X-ray diffraction patterns from the surface of TiB_2 after oxidation for different times. The phases identified have been marked: ▲ TiB_2 (JCPDF:35-0741), ■ TiO_2 (JCPDF:21-1276)
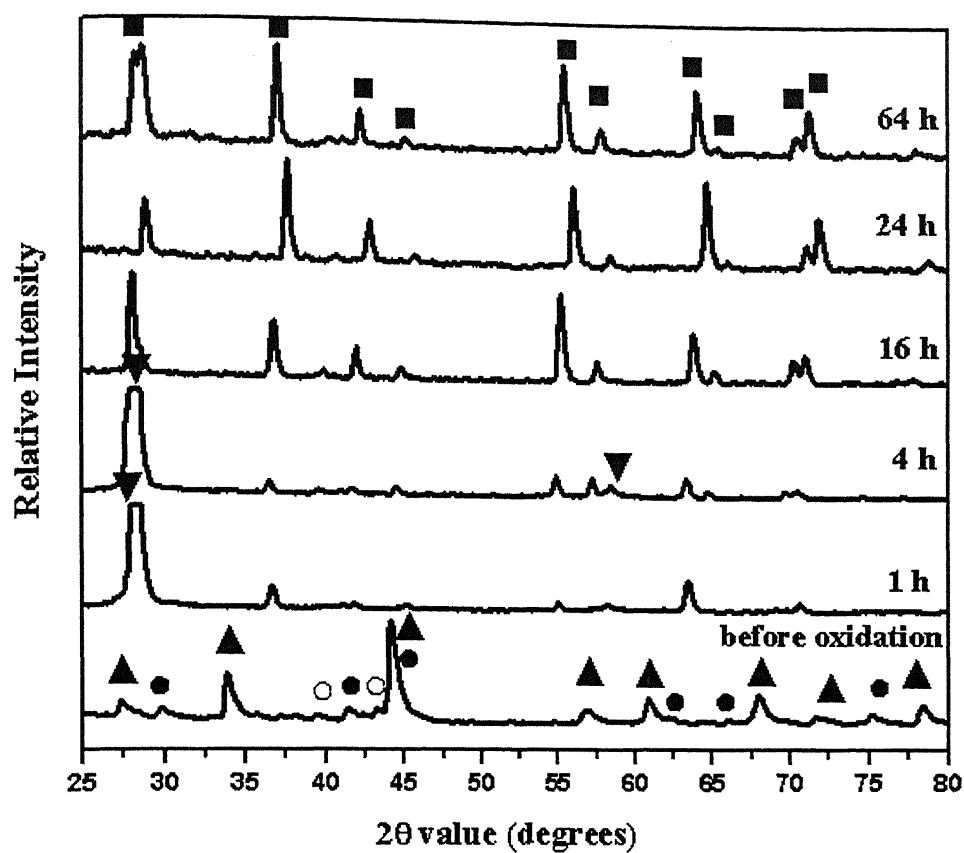
Fig. 4.3.2b: X-ray diffraction patterns from the surface of TiB_2-$MoSi_2$ composite after oxidation for different times. The phases identified have been marked: ▲ TiB_2 (JCPDF:35-0741), ● $MoSi_2$ (JCPDF:41-0612), ■ TiO_2 (JCPDF:21-1276), ○ $TiSi_2$ (JCPDF:35-0785), ▼ B_2O_3 (JCPDF:73-1550)

4.3.3 SEM and EDS results

Scanning electron micrographs of the surface oxide scales of monolithic TiB_2 after oxidation at 850°C for different times are presented in Fig. 4.3.3. The oxide surfaces were cracked. The surface of the 64h oxidized sample appeared as if a liquid film was present on the surface. It may be due to the formation of liquid B_2O_3 during oxidation. The fusion point of B_2O_3 is ~500°C and its boiling point is ~1100°C [65]. It has also been reported that due to the small radius of the boron atom, it can diffuse easily to the surface during oxidation of TiB_2 [67,68]. Koh et.al [66] identified a double layered oxide with the thickness of about 50 μm on the fracture surface of the TiB_2-2.5wt % Si_3N_4 composite oxidized at 800°C for 10h. The outer layer consisted of B_2O_3 crystallites imbedded in a boron-rich glassy phase, while the inner layer was mainly composed of crystalline TiO_2.

The presence of glassy B_2O_3 could not have been determined by XRD studies possibly because of its non-crystallinity. In order to understand the possible formation of B_2O_3 on the surface of the oxide, the cross-section of the monolithic TiB_2 sample oxidized for 64h was mounted in epoxy and the same was compositionally mapped for the elements Ti, B and O in the SEM (Fig. 4.3.4). Oxygen and titanium were found throughout the oxide scale, confirming that the oxide was indeed primarily composed of rutile (TiO_2). The boron map revealed that there it was also distributed fairly uniformly throughout the oxide scale. However, there was a slight enhancement in its concentration towards the metal oxide-environment interface. Compositional analysis determined directly on the surface of the 64h oxidized sample provided strong signals for the presence of B (Fig 4.3.5). Therefore it was concluded that the relative amount of B_2O_3 was higher on the surface of the oxide. In the case of monolithic TiB_2, the oxide was primarily composed of TiO_2 and possibly enriched with B_2O_3 phase on the surface.

The surface morphology of oxide scales on the composite has been presented in Fig. 4.3.6. Cracks were observed on the surface, severe for the sample oxidized for 1h (Fig. 4.3.6a). The surface of the sample after oxidation for 16h and 24h indicated evidence for pesting (Fig. 4.3.6c-f). Pest behavior can be defined as disintegration of structure. $MoSi_2$ exhibits pest behavior at lower temperatures (400°C – 600°C), wherein

$MoSi_2$ decomposes into MoO_3 and SiO_2 [69,70]. The oxidation of $MoSi_2$ under these conditions can be described by the following reaction.

$$2MoSi_2 + 7O_2 \rightarrow 4SiO_2 + 2MoO_3 \uparrow \qquad (4.3.3)$$
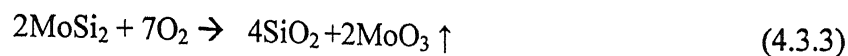
Pesting behavior in $MoSi_2$ has typically been associated with whisker MoO_3 and formation of SiO_2 cluster [69,70].

In the present study, the presence of fine whiskers was clearly indicated at several locations on surface of the composite sample oxidized for 24h (Fig. 4.3.6 c-e). In fact, the microstructure presented in Fig 5e indicates a structure similar to that reported by Chou and Neih [69] for the surface of oxidized $MoSi_2$, showing MoO_3 whiskers on top of discontinuous SiO_2 cluster. The protruding nature of MoO_3 whiskers has been proposed to open the structures and accelerate the disintegration of $MoSi_2$ [69,70]. The vapor pressure of MoO_3 is quite high at high temperature (9×10^{-3} Pa) at 500°C [69]. Therefore, the formation of volatile MoO_3 assists disintegration. The morphology of the whiskers observed in the composite surface indicated that the thickness of whiskers was less than 1 μm and the length varied from 5 to 20 μm.

The cross section of the oxide on the composite after 64h oxidation at 850°C, shown as the inset in Fig. 4.18, was compositionally analyzed. X-ray mapping of the oxide cross section after 64h oxidation indicated the presence of boron, titanium, silicon and oxygen throughout the cross section while Mo was present only in traces (Fig. 4.3.7). From Fig. 4.3.7 d, e and f, the formation of SiO_2 in agglomerated cluster morphology can be confirmed. The presence of B_2O_3 is also indicated by the B and O compositional maps. The presence of clusters of SiO_2 was also confirmed by compositional line scan obtained across the oxide (marked black in inset of Fig. 4.3.8) (Fig.4.3.8). These results indicated that the outer surface layer of oxidized sample could be enriched with SiO_2. It has been reported that glassy SiO_2 can form on the surface of Si-based ceramics and composites during oxidation [60]. Tampieri et. al have observed the formation of SiO_2 layer on the surface during the oxidation of Si_3N_4-TiB_2 (20 vol %) composite [64]. Therefore, the results of the present study indicate that the weight loss noticed in the case of the composite sample after 16h of oxidation must be related to the oxidation nature of $MoSi_2$. The non-protective nature of $MoSi_2$ oxidation may have resulted in the observed weight loss for the composite sample. Moreover, it has been reported that the formation

of whisker MoO_3 and cluster SiO_2 on $MoSi_2$ [69] is a nucleation and growth process. The rate limiting step has been shown to be MoO_3 whisker formation. Therefore, the delayed weight loss behavior in case of composite sample can be related to the delay in formation of MoO_3 whiskers. Interestingly, MoO_3 formation is accelerated when oxygen exposure is limited and this condition would occur beneath the TiO_2 and B_2O_3 initially formed. With subsequent growth of MoO_3 and formation of SiO_2, the nature of oxidation for the composite changed from that seen in the monolithic TiB_2 (Fig. 4.3.1a).

Koh et. al observed parabolic weight gain for TiB_2-2.5wt % Si_3N_4 composite exposed in air at $800^{\circ}C$ [66], while Graziani et.al reported parabolic kinetics for TiB_2-20 vol%B_4C [65] composite up to $900^{\circ}C$. In present study, paralinear kinetics were observed for monolithic and composite when exposed in air at $850^{\circ}C$. Surface cracks were observed on the oxide in the present study. The thickness of the oxides on the surface of the monolithic and composite samples after 64h oxidation at $850^{\circ}C$ was 150 μm and 25 μm. The presence of cracks in the oxide can result in control of the oxidation process by a diffusion controlled as well as phase boundary controlled reaction, thereby resulting in paralinear behavior.
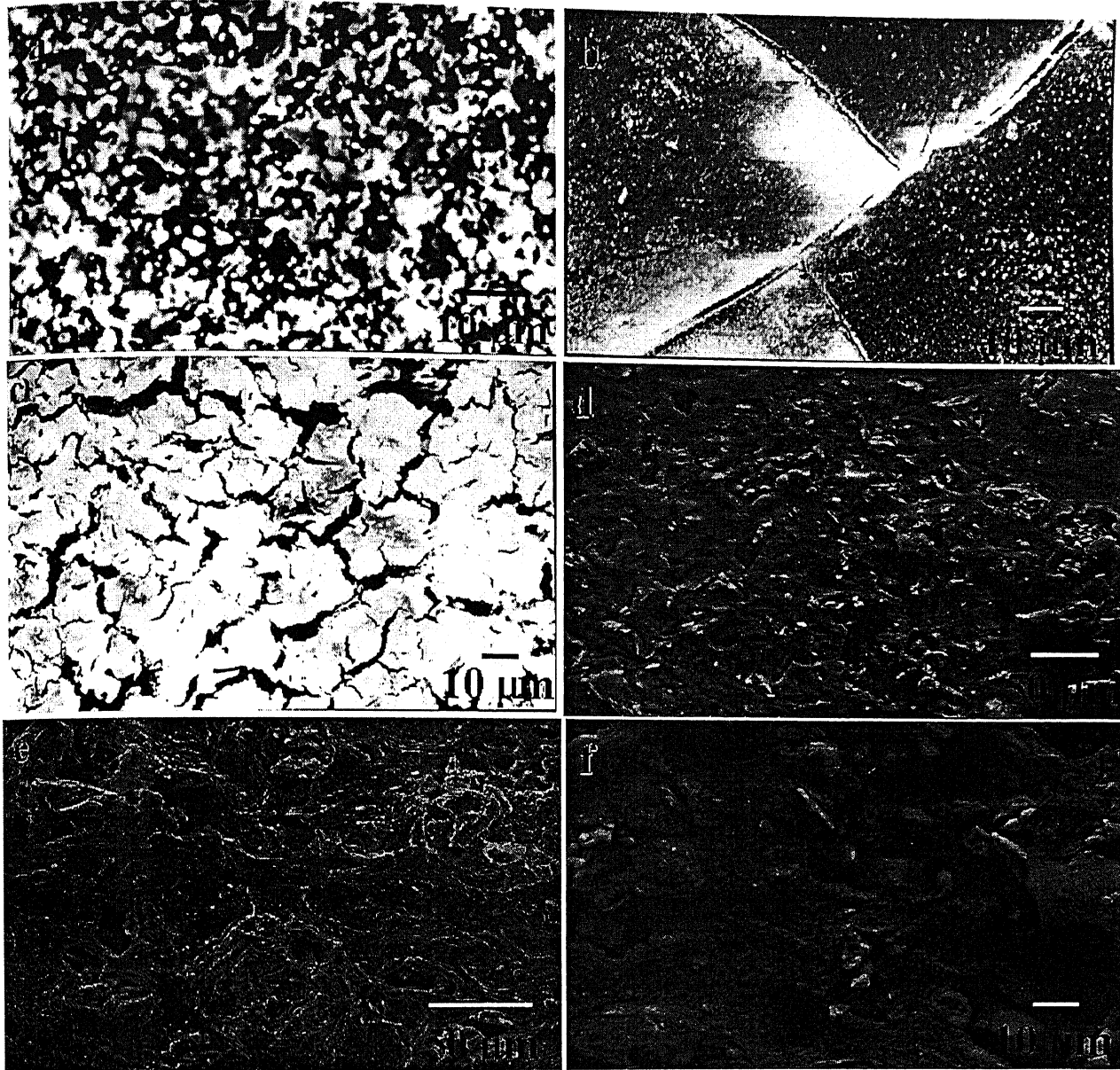
Fig. 4.3.3: SEM micrographs of surface of oxide scales of monolithic TiB$_2$ after oxidation at 850°C for (a) 0.5h, (b) 1h, (c) 4h, and (d-f) 64h
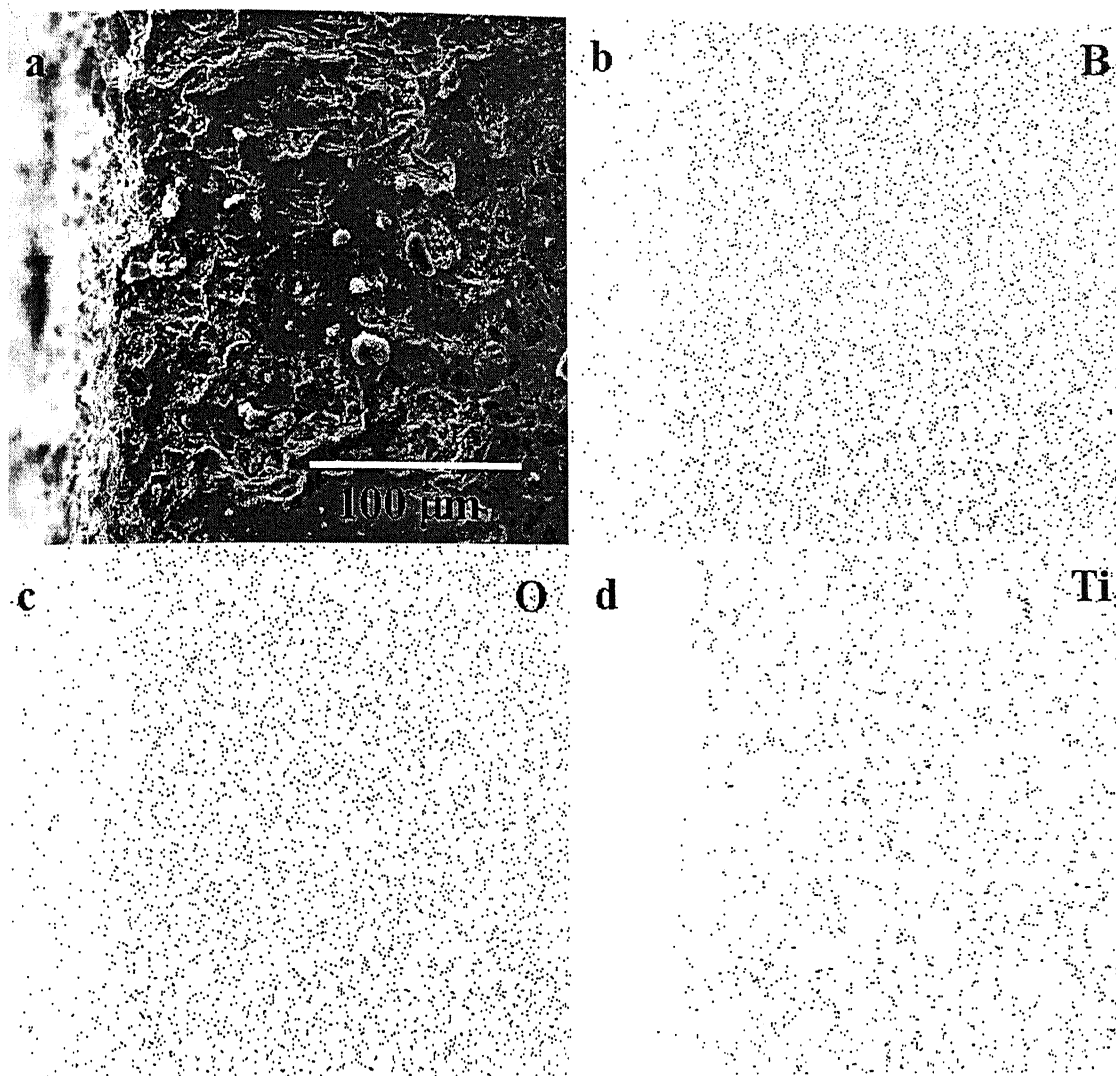
Fig.4.3.4: X-ray mapping of 64h oxidized monoltihc TiB$_2$ cross section (a) cross section image (b) X- ray map of boron (c) X- ray map of oxygen (d) X- ray map of titanium
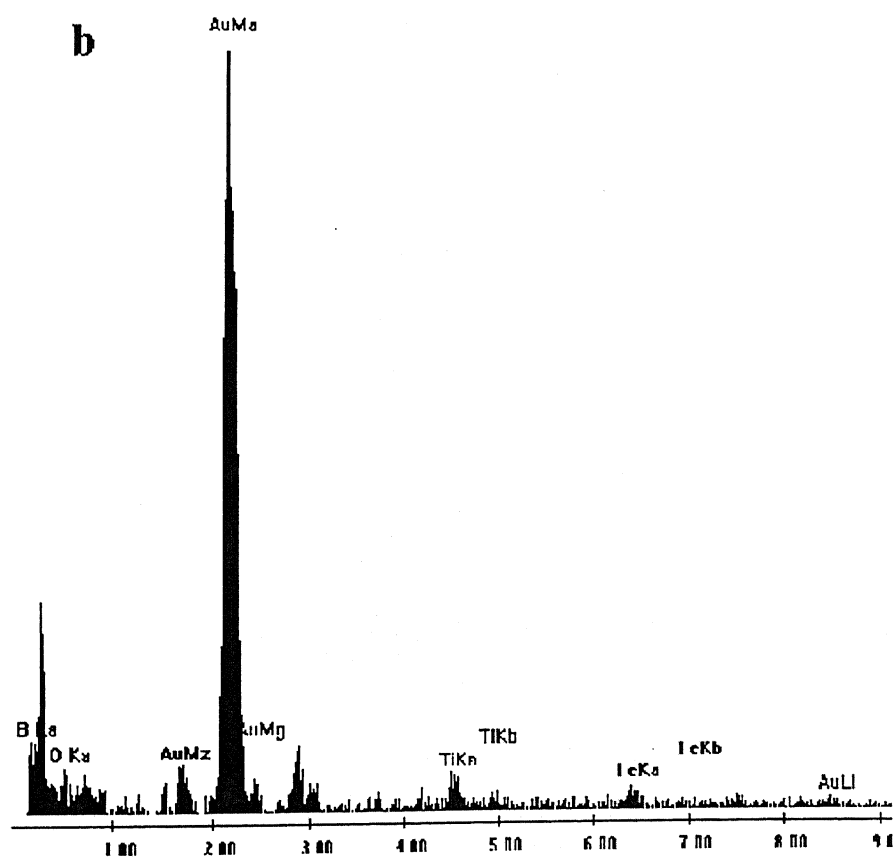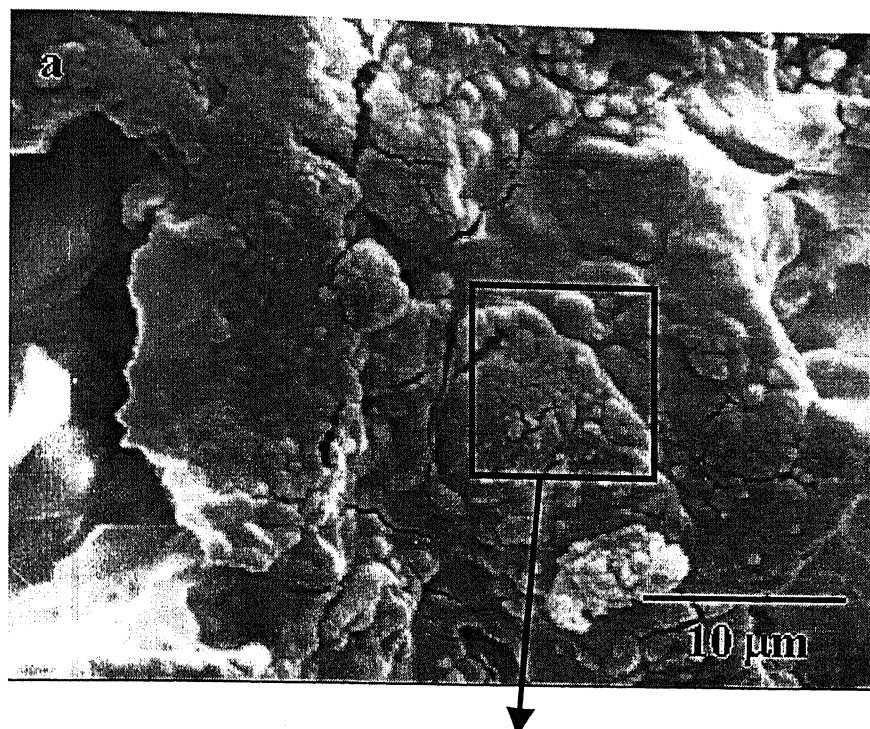
ig 4.3.5: (a) SEM image of 64h oxidized surface of monolithic TiB₂ (b) EDS ectrum obtained from the middle of the image in (a)
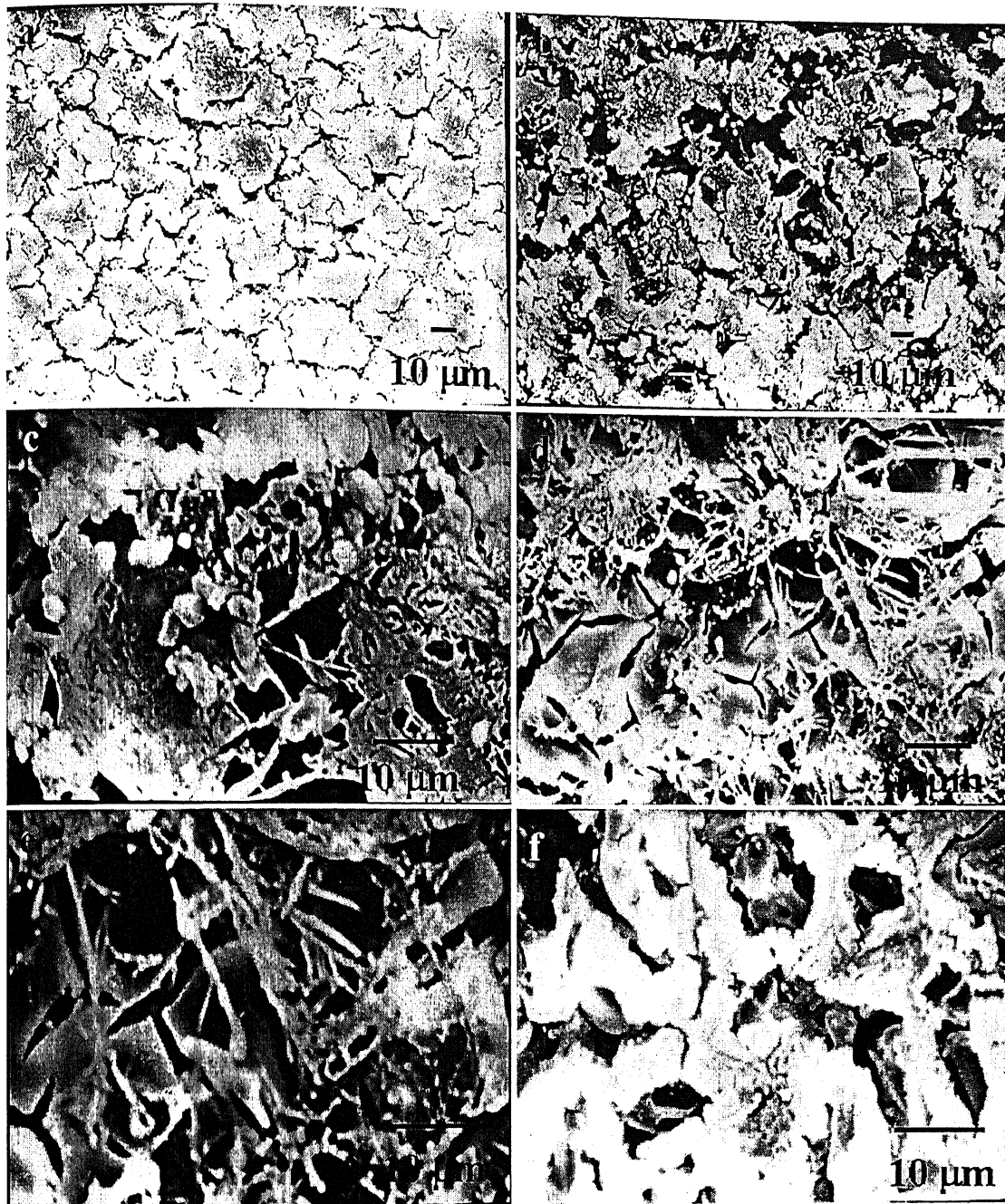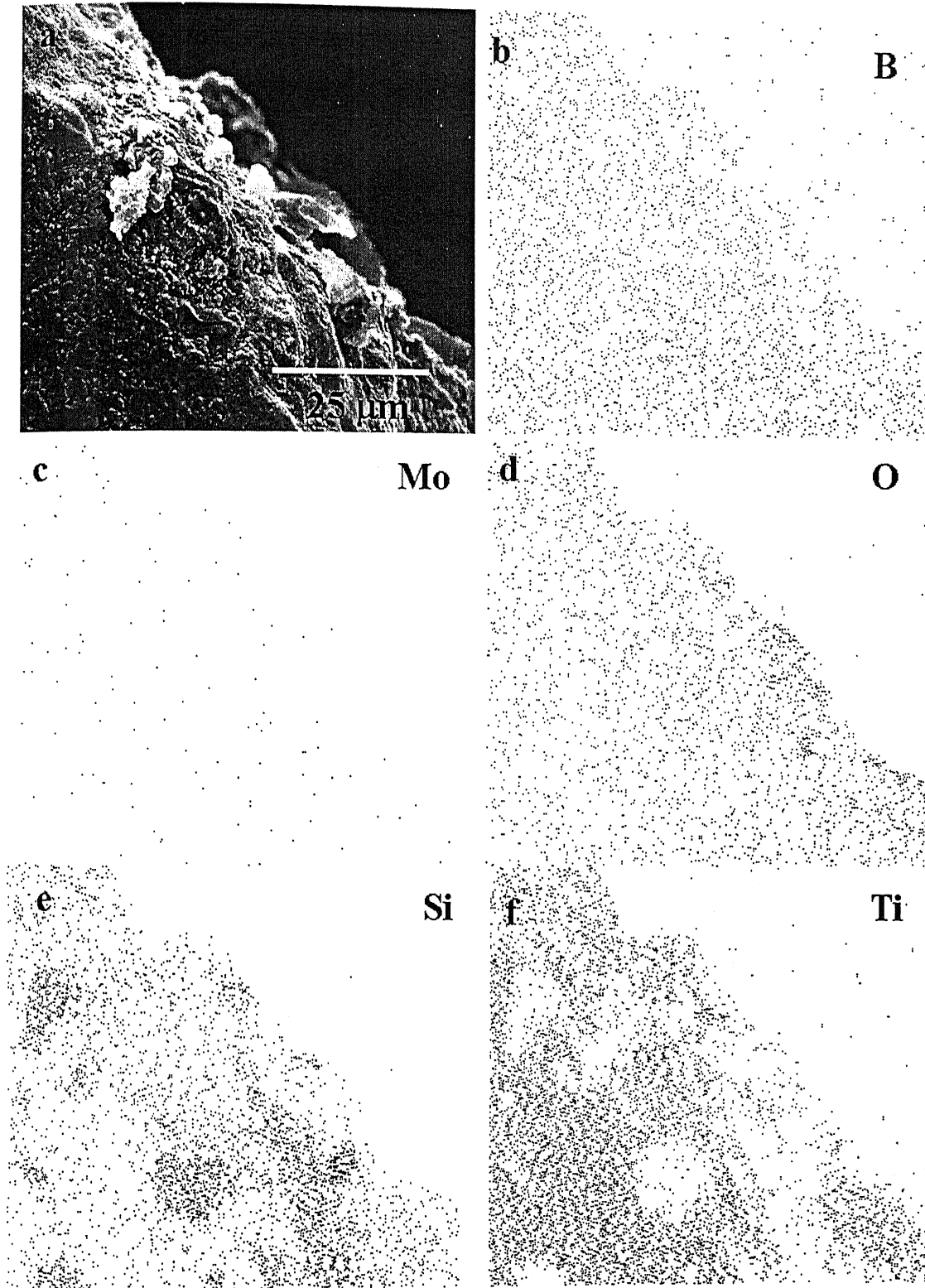
154

Fig. 4.3.6: SEM micrographs of surface of oxide scales of composite (TiB$_2$-MoSi$_2$) after oxidation at 850°C for (a) 1h, (b) 16h, (c-e) 24h and (f) 64h

Fig. 4.3.7: X-ray mapping of 64h oxidized composite cross-section (a) cross-section image (b) X- ray map of boron (c) X- ray map of molybdenum (d) X- ray map of oxygen (e) X- ray map of silicon (f) X- ray map of titanium
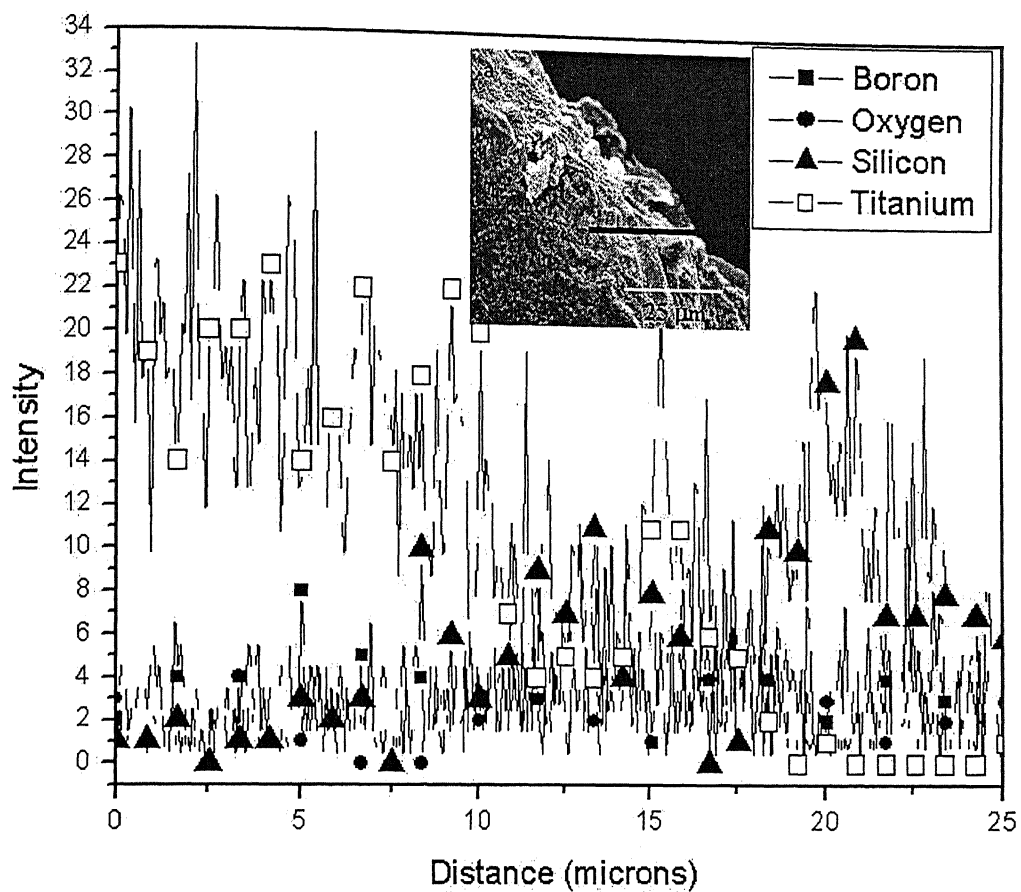
Fig. 4.3.8: Compositional line scan obtained across the black line marked in the inset for the 64h oxidized composite

CHAPTER 5
SUMMARY

5.1 Conclusions

5.1.1 Processing results

In the processing experiments, the amount of $MoSi_2$ sinter-additive and the sintering temperatures are varied. The salient results are as follows:

a) The use of finer TiB_2 powders, synthesized by borocarbothermic reactions, and the lower hot pressing temperature of 1800°C results in obtaining ~98% ρ_{th} dense TiB_2 with finer microstructure (~ 1-2 µm).

b) Our experimental results also reveal that $MoSi_2$ can be used as sinter-additive for densification of titanium boride at lower hot pressing temperature. The optimum conditions for obtaining a density of 97% ρ_{th} in the composites are: 10wt. % $MoSi_2$ addition and hot pressing at 1700° C for 1 h. In case of pressureless sintered materials, a maximum of 91% ρ_{th} is obtained with 25% $MoSi_2$ composites, when sintering is carried out at 1900°C for 1h.

c) The Presence of finer $MoSi_2$ dispersion is observed to prevent the grain growth of TiB_2 during sintering, while obtaining full densification.

d) The optimized composite (TiB_2-10 wt.% $MoSi_2$) exhibits significantly higher hardness (H_v ~ 26 GPa) and indentation toughness (K_{IC} ~ 4.3 MPa.m$^{1/2}$).

e) XRD and EPMA results indicate the formation of $TiSi_2$, a reaction product formed during hot pressing at 1700°C. TEM analysis also confirmed the presence of $TiSi_2$ at grain boundary triple packets. $TiSi_2$, being liquid at hot pressing temperature, promotes liquid phase sintering and hence enhances densification.

5.1.2 Tribological studies

In an effort to evaluate the tribological potential, the fretting wear experiments were carried out on monolithic TiB_2, TiB_2-10% $MoSi_2$ and TiB_2-20% $MoSi_2$ composites against bearing steel under varying load. The important observations are as follows:

a) Lowest Coefficient of Friction (COF) of less than 0.15 recorded for TiB_2–10 % $MoSi_2$ composite at all loads (2N, 5N and 10N).

158

b) Monolithic TiB_2 and TiB_2–20 wt % $MoSi_2$ composite exhibit COF value in the range of 0.5 to 0.8, under varying load.

c) TiB_2–10 % $MoSi_2$ composite exhibits significantly low wear volume and highest wear resistance.

d) TiB_2–10 wt % $MoSi_2$ exhibits mild wear due to formation of a continuous protective tribochemical layer which is very clear in SEM images.

e) SEM-EDS analysis revealed higher amount of transferred Fe on monolithic TiB_2 with increasing load.

f) While the tribochemical wear is the dominant wear mechanism for all the investigated materials, the adhesive and abrasive wear contribute to more wear for monolithic TiB_2 and TiB_2-20 wt % $MoSi_2$ composite.

5.1.3 Oxidation studies

The oxidation behavior of TiB_2 and TiB_2-20% $MoSi_2$ composite was investigated in air at 850°C and important results are as follows:

a) In case of monolithic TiB_2, the weight gain increased continuously with time. TiB_2-$MoSi_2$ composite exhibited continuous weight gain only up to 16h, after which there was a drop in the weight gain.

b) The detailed analysis of the oxidation data using parabolic rate constant indicated slightly improved oxidation resistance for TiB_2 compared to the composite.

c) Crystalline rutile (TiO_2) could be identified unambiguously on the oxidized surfaces of both TiB_2 and composite by XRD analysis.

d) The surface scales were severely cracked. The formation of B_2O_3 during oxidation of TiB_2 and its enrichment on the surface was indicated by SEM analysis.

e) In the case of TiB_2-$MoSi_2$ composite, whisker type MoO_3 oxide formation on the surface was noted after 24h and 64h of oxidation.

f) Enrichment of Si was also noted on the surface of the composite sample after 64h of oxidation. The oxidation behavior in the case of the composite has been related to the nucleation and growth of MoO_3 and SiO_2 in the oxide.

5.2 Scope of future work

5.2.1 Processing

> It is observed that relative density sharply increases with addition of 10 % $MoSi_2$. In future, some careful experiments need to be carried out with varying composition in the range of 0-10 wt % $MoSi_2$.

> In this work, only hot pressing and pressureless sintering was used for densification. Advanced processing techniques like Hot Isostatic pressing (HIP), Spark Plasma Sintering (SPS) etc can be attempted in future for the densification of monolithic TiB_2 and TiB_2-$MoSi_2$ composites and compared with hot pressing.

> In the present study, detailed microstructural characterization (XRD,EPMA, SEM and TEM) was performed only for TiB_2-20 wt % $MoSi_2$ composite. Similar study is extended to other composites.

5.2.2 Tribological studies

> In this work, the number of cycle or test duration is constant for each load. The fretting wear for more extended time or varying test cycles are not performed, which should be carried out in future.

> The debris analysis is not performed. The shape and chemical composition of debris should throw more light on the damage mechanism of TiB_2 and TiB_2-20 wt% $MoSi_2$ composite surfaces.

> In our experiments, only steel is used. In future, different counterbodies like Al_2O_3, SiC, Si_3N_4 etc can be used to evaluate the wear of TiB_2 and TiB_2- $MoSi_2$ composites in different tribological systems.

> In this work, only studied monolithic TiB_2, TiB_2-10 wt % $MoSi_2$ and TiB_2-20 wt% $MoSi_2$ composites, further can extend these fretting wear studies on different compositional composites (2.5%, 5%, 15% and 25% $MoSi_2$).

5.2.3 Oxidation studies

> In this work, isothermal oxidation behavior was studied only at $850^\circ C$ temperature. The oxidation studies at different temperatures (400-$1200^\circ C$), can be carried out in future.

> The oxidation studies can be extended to composites with varying $MoSi_2$ content (2.5%, 5%, 15%, 20% and 25%).

160

References:

1. R. Telle and G. Petzow, "Strengtheing and toughening of boride and carbide hard material composites," *Mat. Sc.Engg, A 105/106* (1988) 97-104.

2. A.C. Silva and M.J. Kaufman, "Synthesis of $MoSi_2$-boride composites through in situ displacement reactions," *Intermetallics 5* (1997) 1-15.

3. M.V. Swain, "structure and properties of ceramics", in: *Materials Science and NY(USA)*,V.11 (1993)175-258.Technology, ed. R.W.Cahin, P.Haasen, and E.J.Kramer, VCH publishers Inc.

4. T.C. Chou and T.G. Nieh, "New Observations of $MoSi_2$ Pest at 500° C," *Scripta Met. Et. Mat.*, Vol. 26, (1992) 1637-42.

5. S.H. kang and D.J. Kim, "Pressureless sintering and properties of Titanium Diboride Ceramics Containing Chromium and Iron," *J.Am.Ceram.Soc.*84 [4] (2001) 893-95.

6. S. Baik and P.F. Becher, "Effect of oxygen contamination on densification of TiB_2," J.Am.Ceram.Soc, 70[8] (1987) 527-30.

7. M.K. Ferber, P.F. Becher, and C.B. Finch, "Effect of Microstructure on the properties of TiB_2 ceramics," Communications of the American Ceramic Society, January 1983, C-2, C-3.

8. W. Wang, Z. Fu, H. Wang and R. Yuan, "Influence of hot pressing sintering temperature and time on microstructure and time on microstructure and mechanical properties of TiB_2 ceramics," *Journal of the European Ceramic Society,* 22 (2002) 1045 – 1049.

9. F.Thevenot, "A review on boron carbide", *Key Engineering Materials,* Vol 56-57 (1991) 59-88.

10. Y. Hwang and J.K. Lee, "Preparation of TiB_2 powders by mechanical alloying," *Materials Letters* 54 (2002) 1-7.

11. C.H. Allibert, "Sintering features of cemented carbides WC-Co processed from fine powders," *Int. J. Refr. Met. & Hard Mat.* 19 (2001) 53-61.

12. S. Kang and D.J. kim, E.S. Kang and S. S. Baek, "Pressureless Sintering and properties of Titanium Diboride Ceramics containing Chromium and Iron," *J.Am.Cer.Soc,* 84[4] (2001) 893-95.
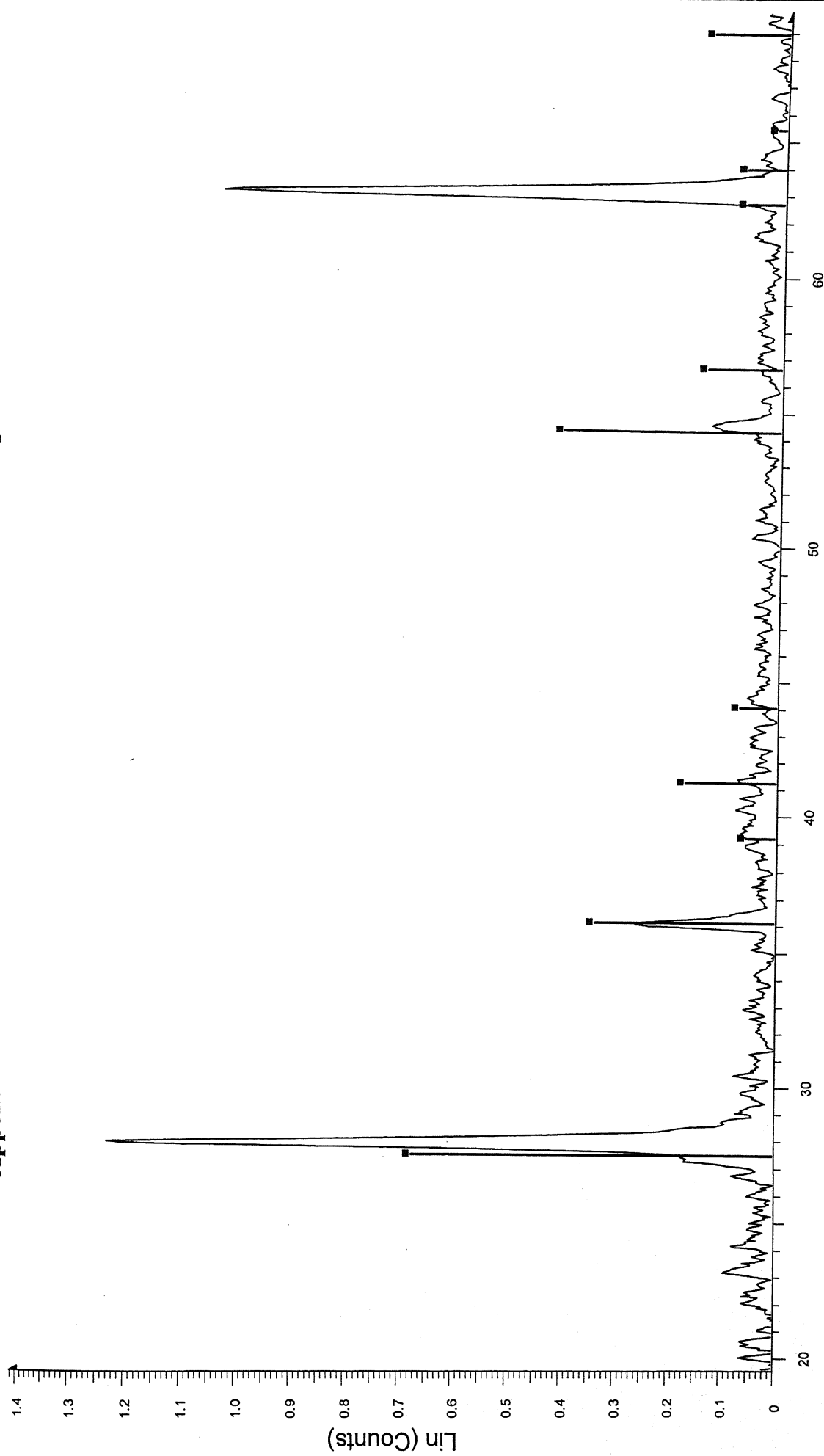
13. E.S. Kang, C.W. Jang, C.H. Lee, C. H. Kim, and D. K. Kim, "Effect of Iron and Boron Carbide on the densification and mechanical properties of Titanium Diboride Ceramics," *J.Am. Ceram soc.,* 72[10] (1989) 1868-72.

14. Mari–Ann Einarsrud & coworkers Reported, *J.Am. Ceram.Soc. 80[12]* (1997) 3013-20.

15. D.E.Mahagin and R.E.Dahl, "Nuclear applications of boron and the borides", in: *Boron and refractory borides, ed.* V.I.Matkovich, Springer- Verlag Berlin Heidelberg (1977) 613-632.

16. L. H. Li, H.E. Kim and E.S. Kang, "Sintering and mechanical properties of titanium diboride with aluminum nitride as a sintering aid," *Journal of the European Ceramic Society* 22 (2002) 973-77.

17. R. Telle, S .Meyer, G. Petzow and E.D. Franz, "Sintering Behavior and Phase Reactions of TiB_2 with ZrO_2 Additives," *Materials Science and Engineering* A105/106(1988) 125-129.

18. Y. Muraoka, M. Yoshinaka, K. Hirota and O. Yamaguchi. "Hot Isostatic Pressing of TiB_2-ZrO_2 (2 Mol% Y_2O_3) composite powders," *Materials Research Bulletin,* Vol.31.No.7. (1996) 787-792.

19. S. Torizuka and T. Kishi, "Effect of SiC and ZrO_2 on sinterability and mechanical Properties of Titanium Nitride, Titanium Carbonitride and Titanium Diboride," *Materials Transactions,* JIM, Vol. 37, No.4 (1996) 782-787.

20. T. Graziani and A. Bellosi, "Sintering and Characterization of TiB_2-B_4C-ZrO_2 Composites," *Materials and Manufacturing Processes,* Vol.9, No.4, (1994) 767-780.

21. S. Torizuka, J. Harada, and H. Nishio, "High Strength TiB_2," *Ceram.Eng.Sci.Proc.* 11[9-10], (1990) 1454-1460.

22. J. Schneider, K.H.Z Gahr, R .Muller and E.D Franz, "Einflub des ZrO_2–Zusatzes auf mechanische Eigenschaften und den ungeschmierten Gleitverschleib von TiB_2–ZrO_2–Mischkeramiken," *Mat.-wiss.u.Werkstofftech.27,* (1996) 359-366.

23. S. Torizuka, K. Sato, J. Harada, H. Yamamot and H. Nishio, "Microstructure and Sintering Mechanism of TiB_2-ZrO_2-SiC Composite," *J.Ceram.Soc.Japan* 100 [4] (1992) 392-397.

24. S. Torizuka, K. Sato, H. Nishio and T. Kishi, "Effect of SiC on Interfacial Reaction and Sintering Mechanism of TiB_2," *J.Am.Ceram.Soc.* 78 [6] (1995) 1606-1610.

25. J.H. park, Y. Koh, H. Kim C. Hwang and E. Kong, "Densification and Mechanical Properties of Titanium Diboride with Silicon Nitride as Sintering Aid," *J.Am.Ceram.Soc.* 82 [11] (1999) 3037-3042.

26. C.E. Holcombe and N.L. Dykes, "Microwave Sintering of titanium diboride," *Journal of Materials Science* 26 (1991), 3730-3738.

27. E.S. kang and C.H. Kim, "Improvements in mechanical properties of TIB_2 by the dispersion of B_4C particles," *Journal of Materials Science* (1989), 580-584.

28. Y. Murata, H.P. Julien and E.D. Whitney, "Densification and Wear Resistance of Ceramic Systems: I. Titanium Diboride," *Ceramic Bulletin,* Vol 46, No.7 (1967).

29. S.K. Bhaumik, C. Diwakar, A.K. Singh and G.S. Upadhyaya, "Synthesis and sintering of TiB_2 and TiB_2-TiC composite under high pressure," *Materials Science and Engineering* A279 (2000) 275-281.

30. T. Watanbe and K. Shoubu, "Mechanical Properties of Hot–Pressed TiB_2-ZrO_2 Composites," *J.Am.Ceram.Soc.* 68[2] (1985) C-34-C-36.

31. G. Wen, S.B. Li, B.S. Zhang and Z.X. Guo, "Reaction Synthesis of TiB_2 – TiC composites with enhanced Toughness" *Acta Mater.* 49 (2001) 1463-1470.

32. H.R. Baumgartner and R.A. Steiger, "Sintering and Properties of TiB2 made from Powder Synthesized in a plasma – Arc Heater," *J.Am.Ceram.Soc,* 67[3] 1984 207-212.

33. J.W. Lee and Z. A. Munir, "Synthesis of Dense TiB_2 – TiN Nanocrystalline Composites through Mechanical and Field Activation," *J.Am.Ceram.Soc,* 84[6] (2001) 1209-16.

34. A.C. e Silva & M.J. Kaufman, "Synthesis of $MoSi_2$ – boride composites through in situ displacement reactions," *Intermetallics* 5 (1997) 1-15.

35. S. naka and H. Hamamoto, "Preparation of TiB_2 sintered compacts by hot pressing," *Journal of Materials Science* 25 (1990) 533-536.

36. B. Bhusan and B.K. Gupta, "Handbook of Tribology," *Materials, Coatings, and Surface Treatments,* McGraw-Hill, New York (1991).

37. M.I. Hutchings and A.P. Mercer, "The influence of atmosphere composition on the abrasive wear of titanium and Ti-6Al-4V," *Wear,* 124, (1988) 165-176.

163

38. C.A. Hampel, "Rare Metals Handbook," 2nd edition, Reinhold, London,1961.

39. Anonymous, Metals Handbook, Vol 1: Properties and Selection: Iron, Steels and High Performance Alloys, 10th edition, ASM International, Materials park, Ohio.

40. H.B. Tang, Fang YL, Wang HM., "Microstructure and dry sliding wear resistance of a $Cr_{13}Ni_5Si_2$ ternary metal silicide alloy,' *Acta Mater* 52 (2004) 1773.

41. B. Basu, R.G. Vitchev, J. Vleugels, J.P. Celis and O.V.D. Biest, "Influence of humidity on the fretting wear of self-mated tetragonal zirconia ceramics," *Acta Materialia,* 48 (2000) 2461-2471.

42. B. Basu, J. Vleugels, M. Kalin and O.V.D. Biest, "Friction and wear mechanism of sialon ceramics under fretting contacts," *Mat. Sc. Engg.,* A359 (2003) 228-236.

43. J. Vleugels, B. Basu, K.C. Hari Kumar, R.G. Vitchev and O.V.D. Biest, "Unlubricated fretting wear of TiB_2 containing composites against bearing steel," *Metallurgical and Materials Transactions A* (in Press, 2002)

44. B. Basu, J. Vleugels and O.V.D Biest, "Microstructure-Toughness-Wear relationship of tetragonal zirconia ceramics," *J. Eur. Cer. Soc.* 24 [7] (2004) 2031-2040.

45. Z. Xingzhong, L. Jiajun, Z. Baoliang, O. Jinlin and X. Qunji, *"Ceramics International,"* 24 (1998) 13-18.

46. W. M. Rainforth, *"Ceramics International,"* 22 (1996) 365-372.

47. B. Basu, J. Vleugels and O.V.d Biest, "Influence of lubrication on the fretting wear performance of TiB_2 based materials," *WEAR* 250 (2001) 631-641.

48. R.B. Bhagat et al, "Tribological performance evaluation of WC-based cermets and development of a fracture mechanics wear model" *Wear* 201 (1996) 233-243.

49. J. Mukerji and B. Prakash, *"Ceramics International,"* 24 (1998) 19-24.

50. K. Kato and K. Adachi, "Wear of Advanced Ceramics," *Wear,* 253 (2002) 1097-1104,

51. T. Venkattsharwan, D. Sarkar and B. Basu, "Tribological properties of $Wc-ZrO_2$ nanocomposites," *J.Am.Cer.Soc.* (in press 2004).

52. E. Rabinowicz, "Friction and Wear of Materials," second edition, Wiley, New York (1995).

53. S. Baik and P.F. Becher, "Efect of Oxygen Contamination on Densification of TiB_2" *J.Am. Ceram.Soc.,* 70[8] (1987) 527-30.
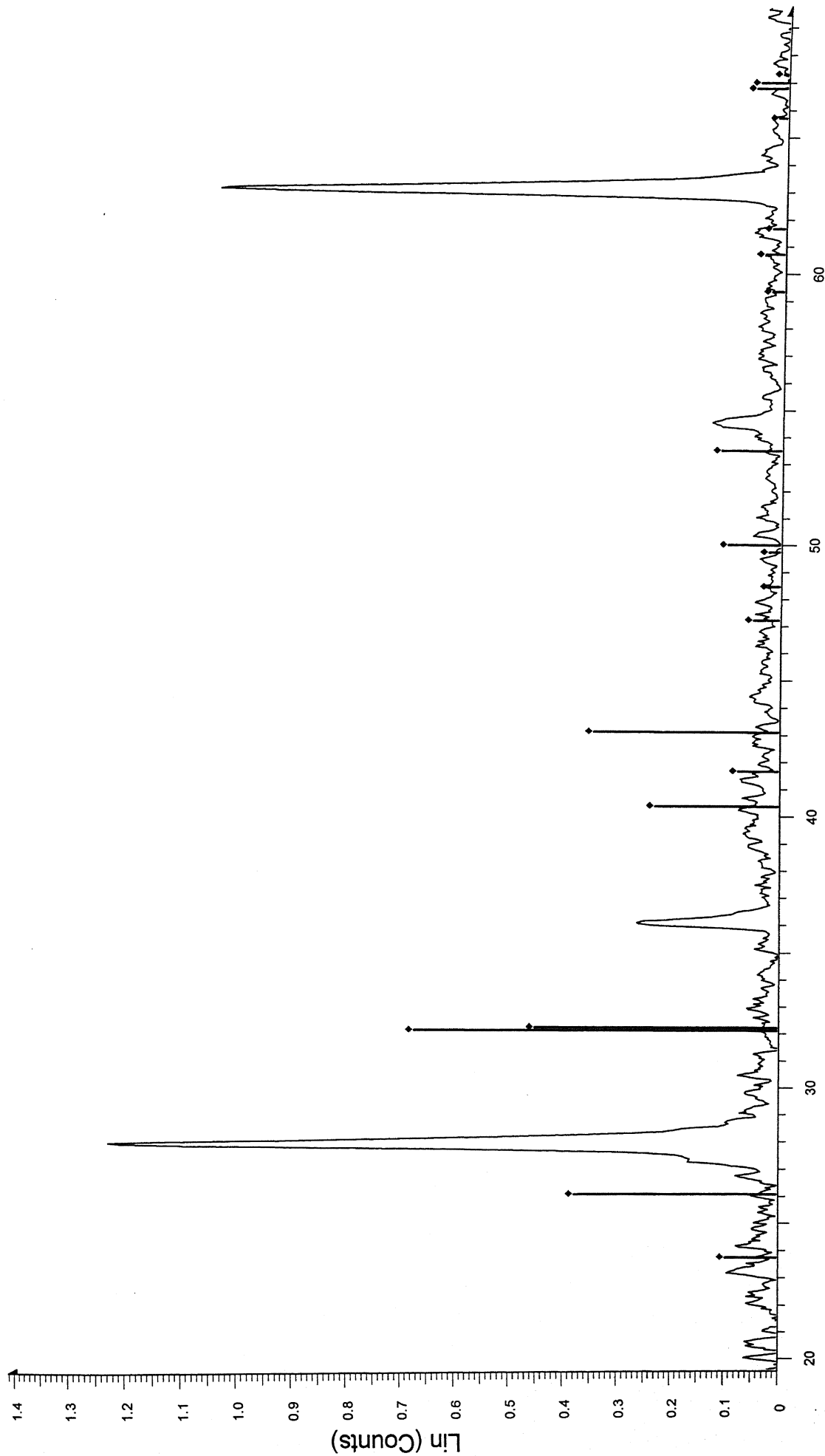
54. M. Einarsrud, E. Hagen, G. Pettersen, and T. Grande, "Pressureless sintering of Titanium Diboride with Nickel, Nickel Boride, and Iron additivies," *J. Am. Ceram. Soc.*, 80[12] (1997) 3013-20.

55. S. Torizuka, K. Sato, H. Nishio, and T. Kishi, "Effect of SiC on Interfacial reaction and sintering Mechanism of TiB2," *J.Am.Ceram.Soc.*, 78[6] (1995) 1606-10.

56. S.Torizuka and T. Kishi, "Effect of SiC and ZrO_2 on sinterability and mechanical Properties of Titanium Nitride, Titanium Carbonitride and Titanium Diboride" Materials Transactions, *JIM,* Vol. 37, No.4, (1996) 782-787.

57. J.H. park, Y. Koh, H. Kim, C. Hwang and E. Kong, "Densification and Mechanical Properties of Titanium Diboride with Silicon Nitride as Sintering Aid," *J.Am.Ceram.Soc.* 82 [11] (1999) 3037-3042.

58. L.H. Li, H.E. Kim, E.S. Kang, "Sintering and mechanical properties of titanium diboride with aluminum nitride as a sintering aid," *Journal of the European Ceramic Society* 22, (2002) 973-77.

59. T.S.R.Ch. Murthy, A. Shrivastava, B. Basu, R. Balasubramaniam, A.K. Suri, C. Subramanian and R.K. Fotedar, "Processing and properties of novel TiB_2- based composites," (submitted to J. Am. Ceram. Soc., 2004).

60. Y.H. Koh, H.W. Kim and H.E. Kim, "Improvement in oxidation resistance of TiB_2 by formation of protective SiO2 layer n surface," *J.Mater.Res.,* Vol 16, No.1, Jan (2001).

61. Y.H. Koh, S.Y. Lee and H.E. Kim, "Oxidation behavior of Titanium boride at elevated temperatures," *J.Am.Ceram.Soc.* 84[1] (2001) 139-41.

62. A. Kulpa and T. Troczynski, "Oxiation of TiB2 powders below 900^0C, J.Am.Ceram.Soc" 79[2] (1996) 518-20.

63. A. Tampieri and A. Bellosi, "Oxidation of monolithic TiB_2 and of Al_2O_3 $-TiB_2$ Composite," *J.Mat. Sci.* 28, (1993).

64. A. Tampieri, E .Landi and A .Bellosi, "On the oxidation behaviour of monolithic TiB2 and Al2O3 and Si3N4 $-TiB2$ compoistes," *Journal of Thermal Analysis,* Vol. 38, (1992) 2657-68.

65. M.G. Barandika, J.J. Echeberria, and F. Castro, "Oxidation resistance of two TiB2- based cermets." *Materials Research Bull.* Vol 34, No.7, (1999) pp 1001-11.

66. T. Graziani, E. Landi, and A. Bellosi, "Oxidation of TiB$_2$-20 vol % B$_4$C composite,"*J.Mat.Sci.letters* 12 (1993) 691-694.

67. V.A. Lavrenko, S.S. Chuprov, A.P. Umanskii, T.G. Protsenko, and E.S. Lugovskaya,"High-Temperature oxidation of composite materials based on Titanium diboride," *Soviet Powder Met. & Metal ceramics,* (1987) 761-2.

68. M. Singh and H. Wiedemeier, "Chemical interactions in diboride-reinforced oxidematrix composites," J.Am.Ceram.Soc., 74[4] (1991) 724-27.

69. T.C. Chou and T.G. Nieh, "New observations of MoSi$_2$ pest at 500^{0}C," Scripta Metallurgica et Materialia; Vol.26, (1992) 1637-42.

70. C.D. Wirksus and D.R. Wilder, "High-Temperature Oxidation of Molybdenum Disilicide," *J.Am.Ceram.Soc.,* 49[4] (1966) 173-177.

71. S.Tuffe, J. Dubois, G. Fantozzi and G. Barbier, "Densification, microstructure and mechanical properties of TiB$_2$-B$_4$C composites," *Int. J. of Refr. Met. & hard mat.,* 14 (1996) 305-310.

72. J.L. Murray, P.K. Liao and K.E. Spear, "The B-Ti (Boron-Titanium) system," *Bulletin of alloy phase diagrams,* Vol. 7 No. 6 (1986) 550-554

73. B.R. Lawn, E.R. Fuller, "Equilibrium penny-like cracks in indentation fracture," *J. of Mat. Sci.* 10 (1975) 2016-2024.

74. B. Lawn, R. Wilshaw, "Review indetnation fracture: principles and applications," *J.of Mat. Sci* 10 (1975) 1049-1081.

75. H. So, D.S. Yu, C.Y. Chuang, "Formation and wear mechanism of tribo-oxides and the regime of oxidation wear of steel," *Wear* 253 (2002) 1004-1015.

76. Klaffke D, "Fretting wear of ceramics," *Tribology Int* 22(2) 1989, 89-01.

77. H. Kong, M.F. Ashby, "wear mechanisms in brittle solids," *Acta met. Mat.* Vol 40 No 11 (1992) pp 2907-2920.

78. T.F.J. Quinn, "Oxidation wear," ASM handbook Vol 18, 290-289.

Appendix A

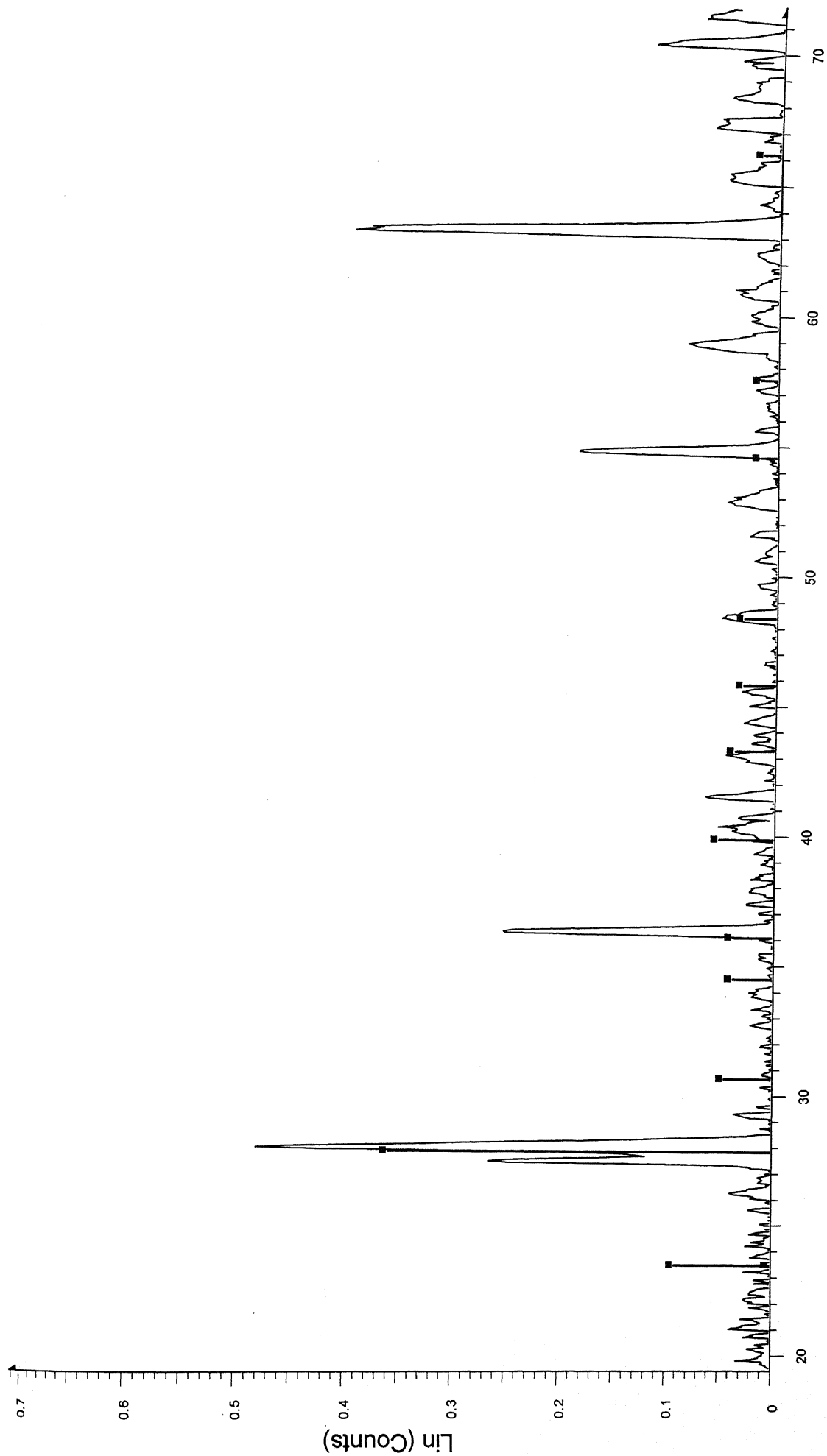## Monolithic TiB$_2$ – 1h

Lin (Counts)

2-Theta - Scale

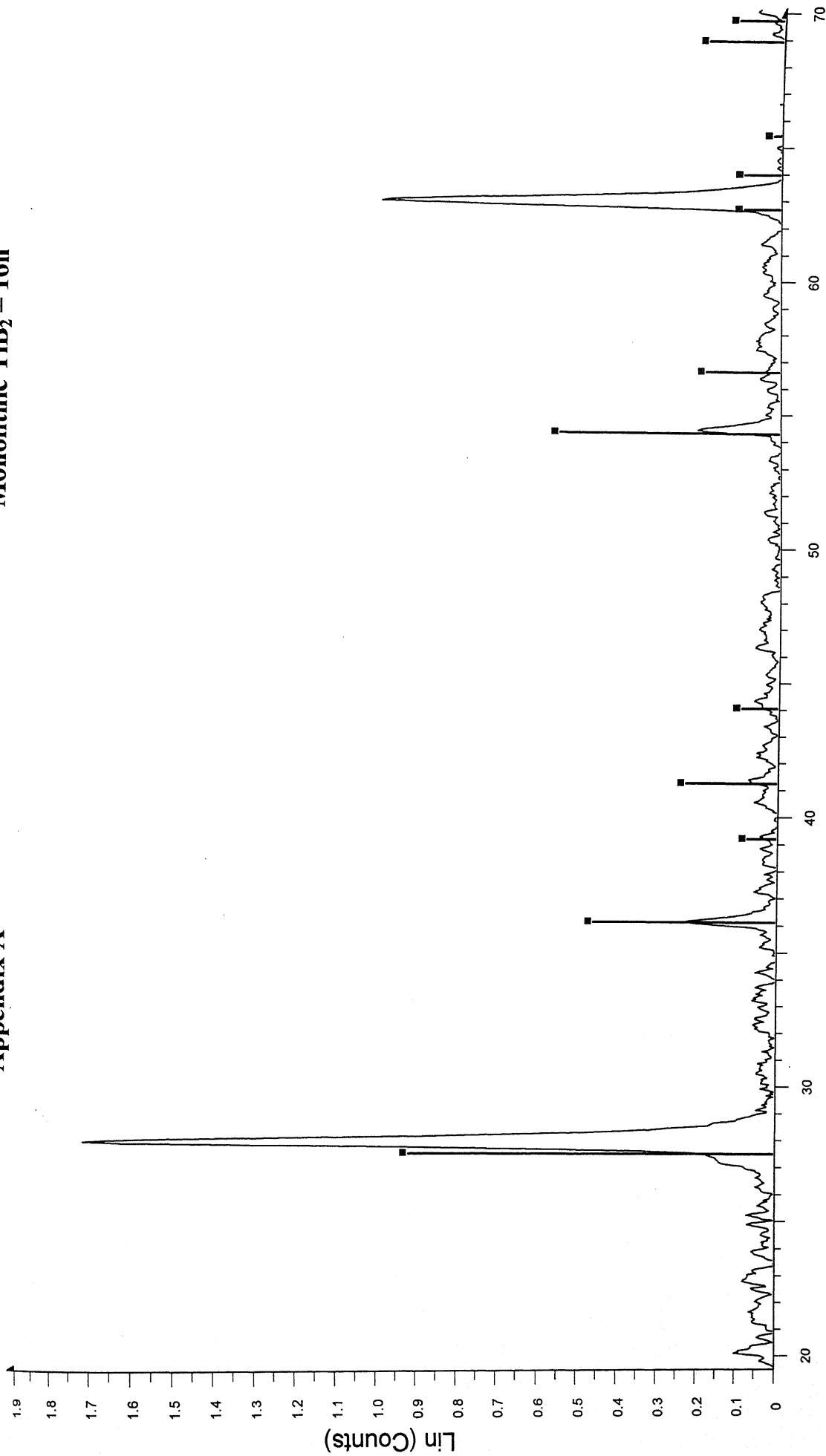M-1h - File: M-1h.raw - Type: 2Th/Th locked - Start: 19.470 ° - End: 100.970 ° - Step: 0.050 ° - Step time: 1. s - Temp.: 25 °C (Room) - Time Started: 0 s - 2-Theta: 19.470 ° - Theta: 9.735 ° - Chi: 0.00 ° -

Operations: Background 1.000,1.000 | Import

21-1276 (*) - Rutile, syn - TiO2 - Y: 50.00 % - d x by: 1. - WL: 1.5406 - 0 - I/Ic PDF 3.4 -
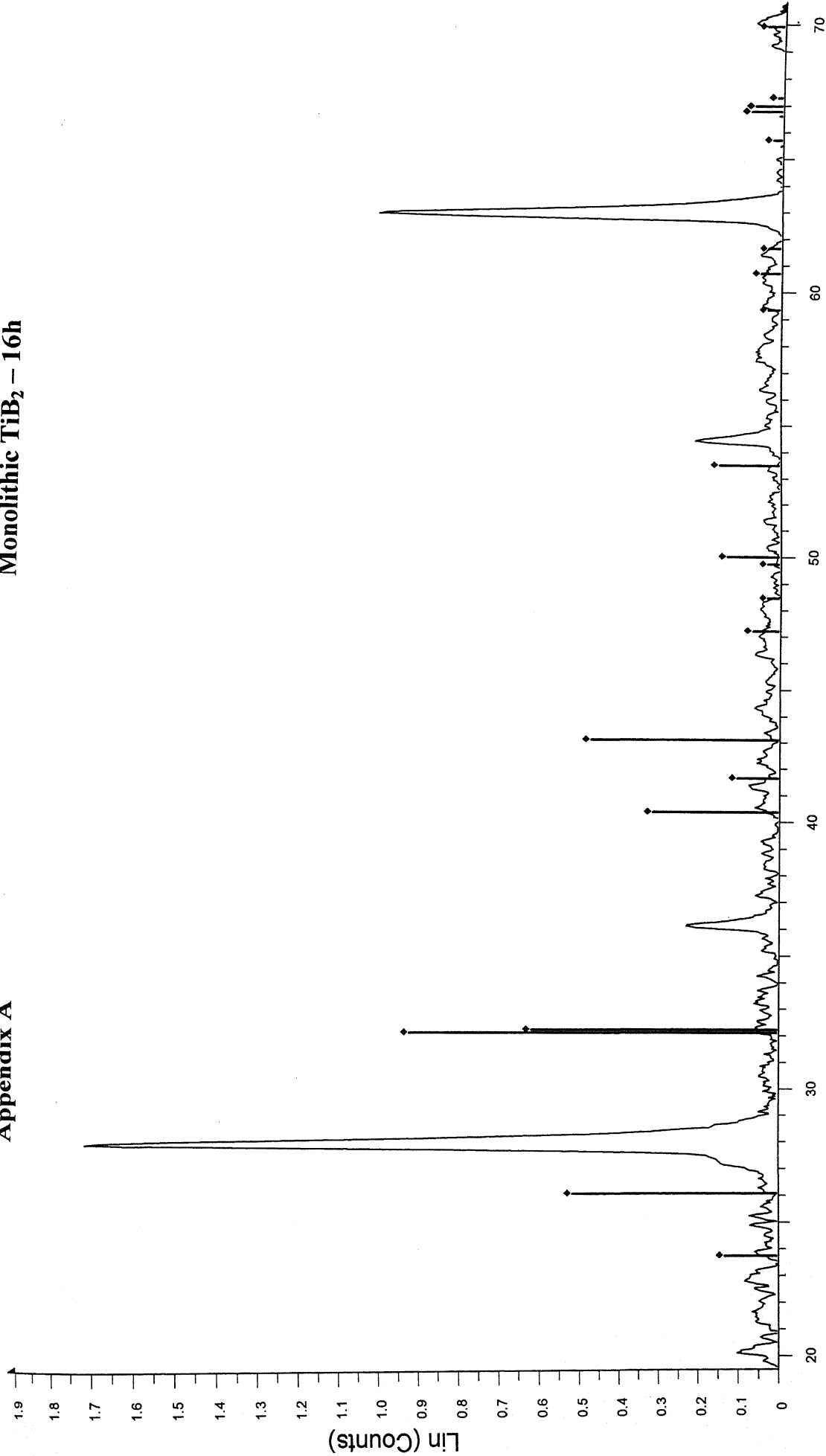
Monolithic TiB$_2$ – 1h

2-Theta - Scale

M-1h - File: M-1h.raw - Type: 2Th/Th locked - Start: 19.470 ° - End: 100.970 ° - Step: 0.050 ° - Step time: 1. s - Temp.: 25 °C (Room) - Time Started: 0 s - 2-Theta: 19.470 ° - Theta: 9.735 ° - Chi: 0.00 ° -

Operations: Background 1.000,1.000 | Import

73-1550 (C) - Boron Oxide - B2O3 - Y: 50.00 % - d x by: 1. - WL: 1.5406 - 0 - I/Ic PDF 0.8 -
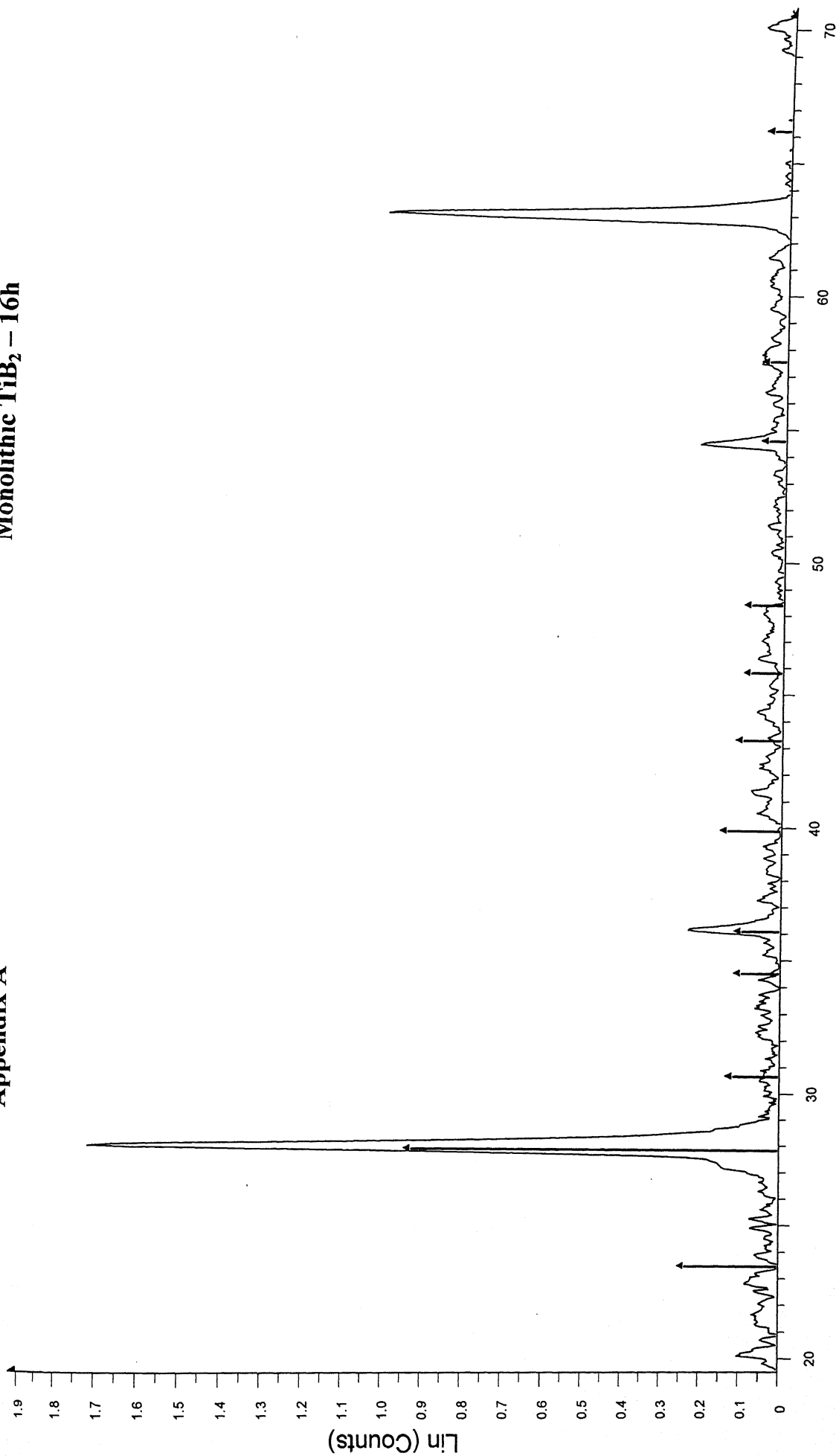
Appendix A

Monolithic TiB$_2$ – 1h

M-1h - File: M-1h.raw - Type: 2Th/Th locked - Start: 19.470 ° - End: 100.970 ° - Step: 0.050 ° - Step time: 1. s - Temp.: 25 °C (Room) - Time Started: 0 s - 2-Theta: 19.470 ° - Theta: 9.735 ° - Chi: 0.00 ° -

Operations: Background 1.000,1.000 | Import

13-0570 (D) - Boron Oxide - B2O3 - Y: 50.00 % - d x by: 1. - WL: 1.5406 -

Appendix A

Monolithic TiB$_2$ – 4h

2-Theta - Scale

Lin (Counts)

M-3-4h - File: M-3-4h.raw - Type: 2Th/Th locked - Start: 19.460 ° - End: 102.060 ° - Step: 0.050 ° - Step time: 1. s - Temp.: 25 °C (Room) - Time Started: 0 s - 2-Theta: 19.460 ° - Theta: 9.730 ° - Chi: 0.0

Operations: Background 1.000,1.000 | Background 1.000,1.000 | Import

21-1276 (*) - Rutile, syn - TiO2 - Y: 50.00 % - d x by: 1. - WL: 1.5406 - Tetragonal - I/Ic PDF 3.4 -

Monolithic TiB₂ – 4h

2-Theta - Scale
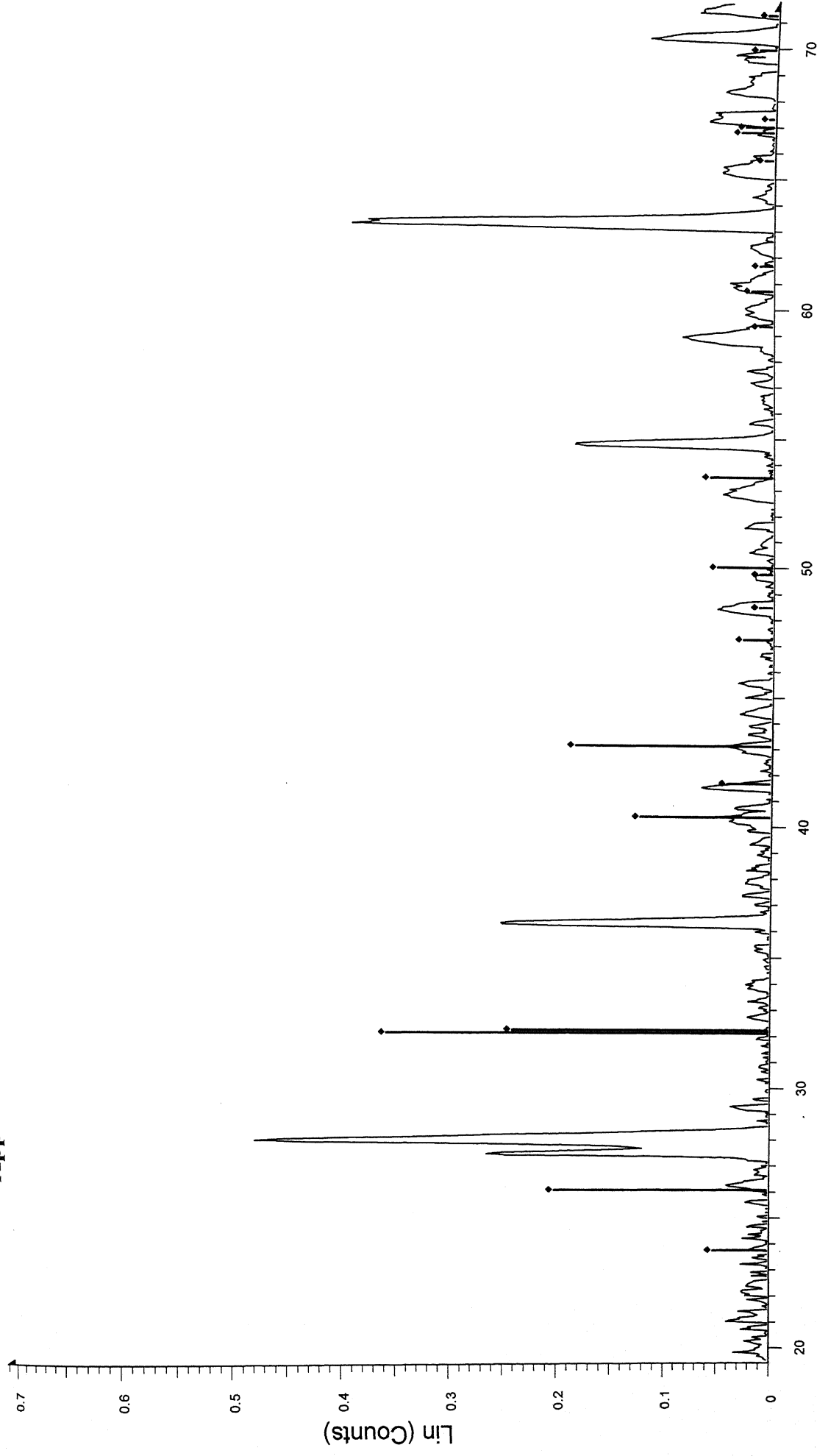
☒M-3-4h - File: M-3-4h.raw - Type: 2Th/Th locked - Start: 19.460 ° - End: 102.060 ° - Step: 0.050 ° - Step time: 1. s - Temp.: 25 °C (Room) - Time Started: 0 s - 2-Theta: 19.460 ° - Theta: 9.730 ° - Chi: 0.0
Operations: Background 1.000,1.000 | Background 1.000,1.000 | Import
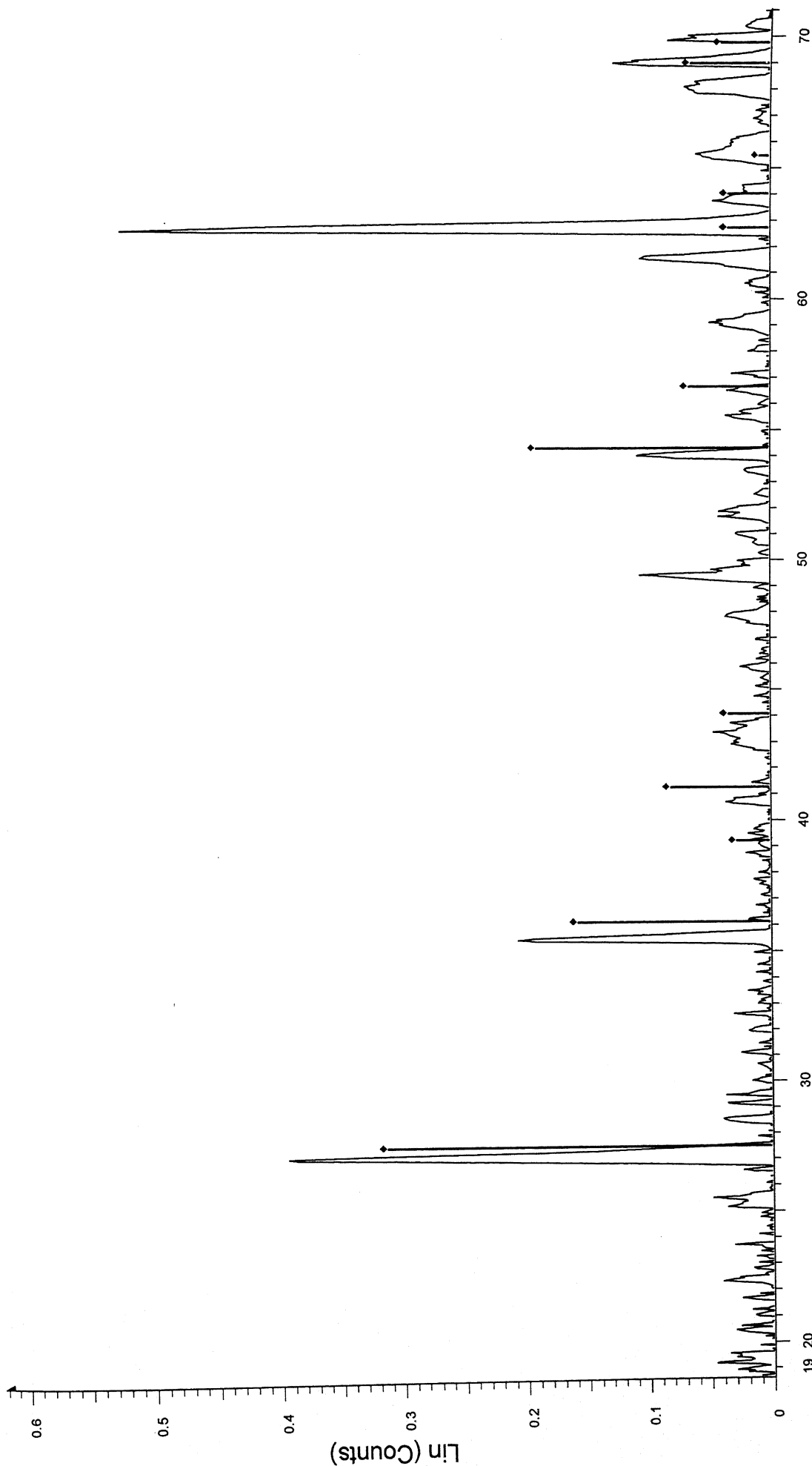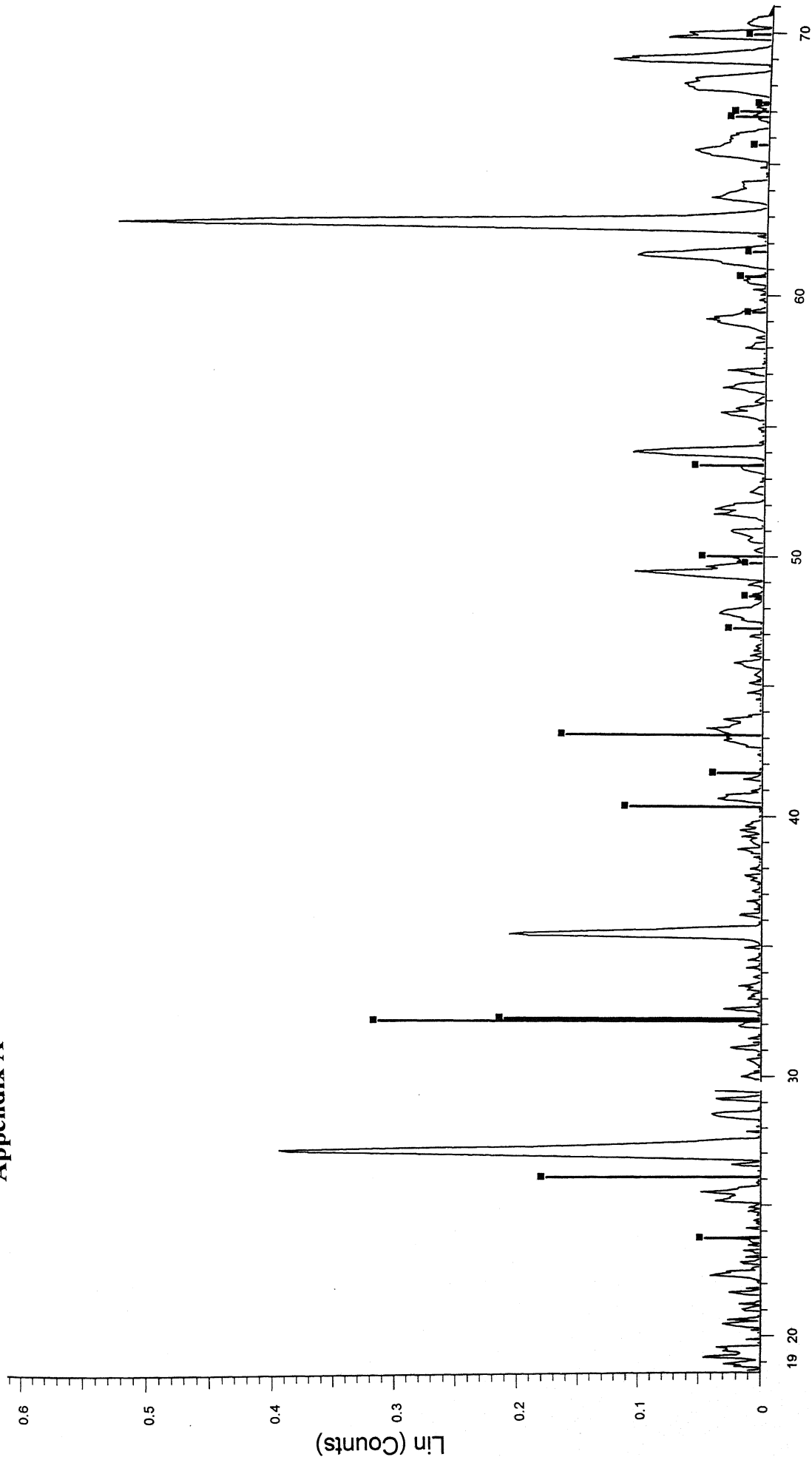◆73-1550 (C) - Boron Oxide - B2O3 - Y: 50.00 % - d x by: 1. - WL: 1.5406 - Hexagonal - I/Ic PDF 0.8 -

M-3-4h - File: M-3-4h.raw - Type: 2Th/Th locked - Start: 19.460 ° - End: 102.060 ° - Step: 0.050 ° - Step time: 1. s - Temp.: 25 °C (Room) - Time Started: 0 s - 2-Theta: 19.460 ° - Theta: 9.730 ° - Chi: 0.0
Operations: Background 1.000,1.000 | Background 1.000,1.000 | Import
13-0570 (D) - Boron Oxide - B2O3 - Y: 50.00 % - d x by: 1. - WL: 1.5406 -

2-Theta - Scale

Lin (Counts)

Appendix A

Monolithic TiB$_2$ – 16h

2-Theta - Scale

M-16h - File: M-16h.raw - Type: 2Th/Th locked - Start: 19.490 ° - End: 100.290 ° - Step: 0.050 ° - Step time: 1. s - Temp.: 25 °C (Room) - Time Started: 0 s - 2-Theta: 19.490 ° - Theta: 9.745 ° - Chi: 0.0

Operations: Background 1.000,1.000 | Import

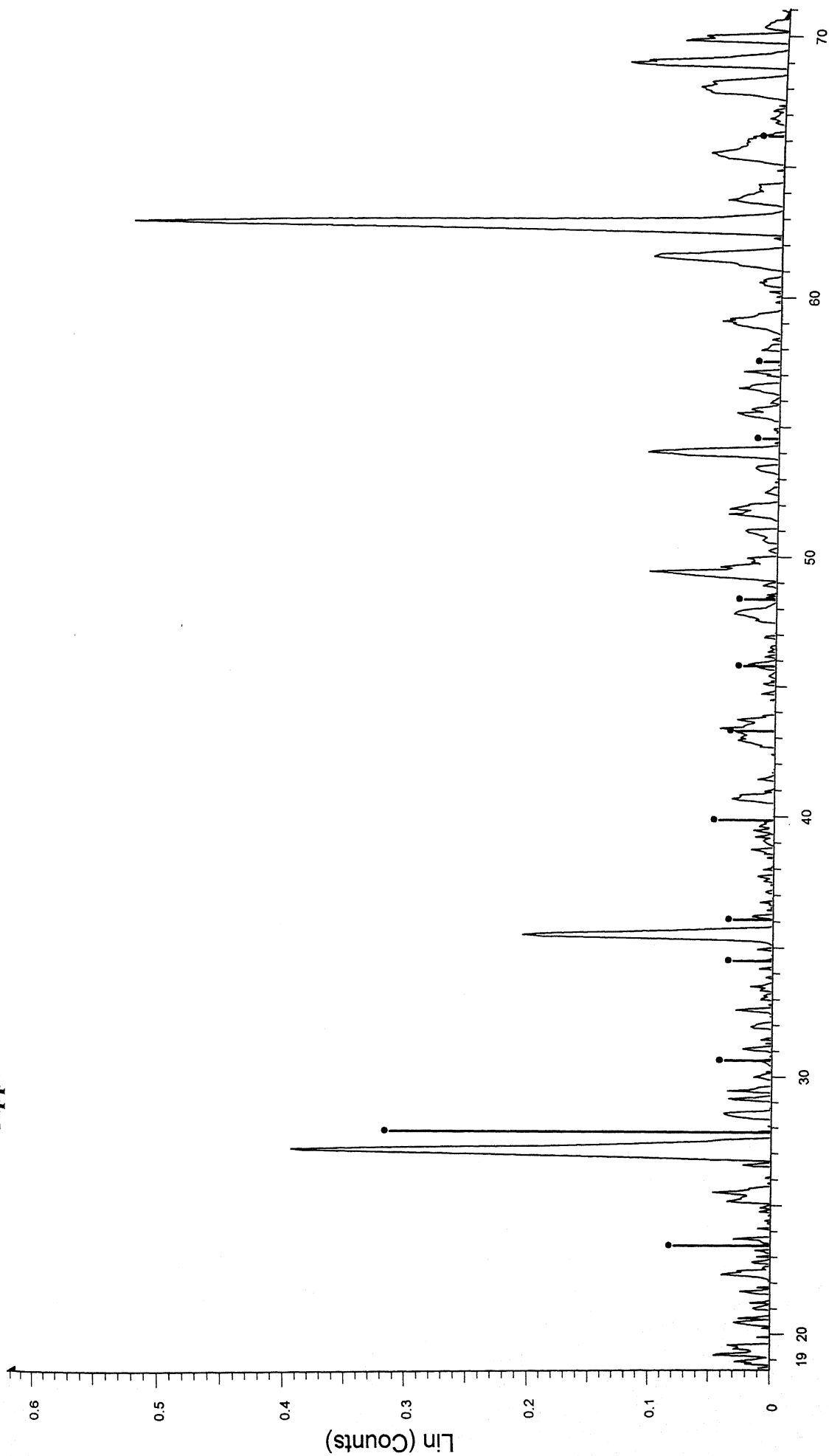21-1276 (*) - Rutile, syn - TiO2 - Y: 50.00 % - d x by: 1. - WL: 1.5406 - 0 - I/Ic PDF 3.4 -

Monolithic TiB₂ – 16h

2-Theta - Scale

☒M-16h - File: M-16h.raw - Type: 2Th/Th locked - Start: 19.490 ° - End: 100.290 ° - Step: 0.050 ° - Step time: 1. s - Temp.: 25 °C (Room) - Time Started: 0 s - 2-Theta: 19.490 ° - Theta: 9.745 ° - Chi: 0.0
Operations: Background 1.000,1.000 | Import
◆73-1550 (C) - Boron Oxide - B2O3 - Y: 50.00 % - d x by: 1. - WL: 1.5406 - 0 - I/Ic PDF 0.8 -

Appendix A

Monolithic TiB$_2$ – 16h

2-Theta - Scale

Lin (Counts)

M-16h - File: M-16h.raw - Type: 2Th/Th locked - Start: 19.490 ° - End: 100.290 ° - Step: 0.050 ° - Step time: 1. s - Temp.: 25 °C (Room) - Time Started: 0 s - 2-Theta: 19.490 ° - Theta: 9.745 ° - Chi: 0.0
Operations: Background 1.000,1.000 | Import
13-0570 (D) - Boron Oxide - B2O3 - Y: 50.00 % - d x by: 1. - WL: 1.5406 -

Monolithic TiB₂ – 64h

2-Theta - Scale
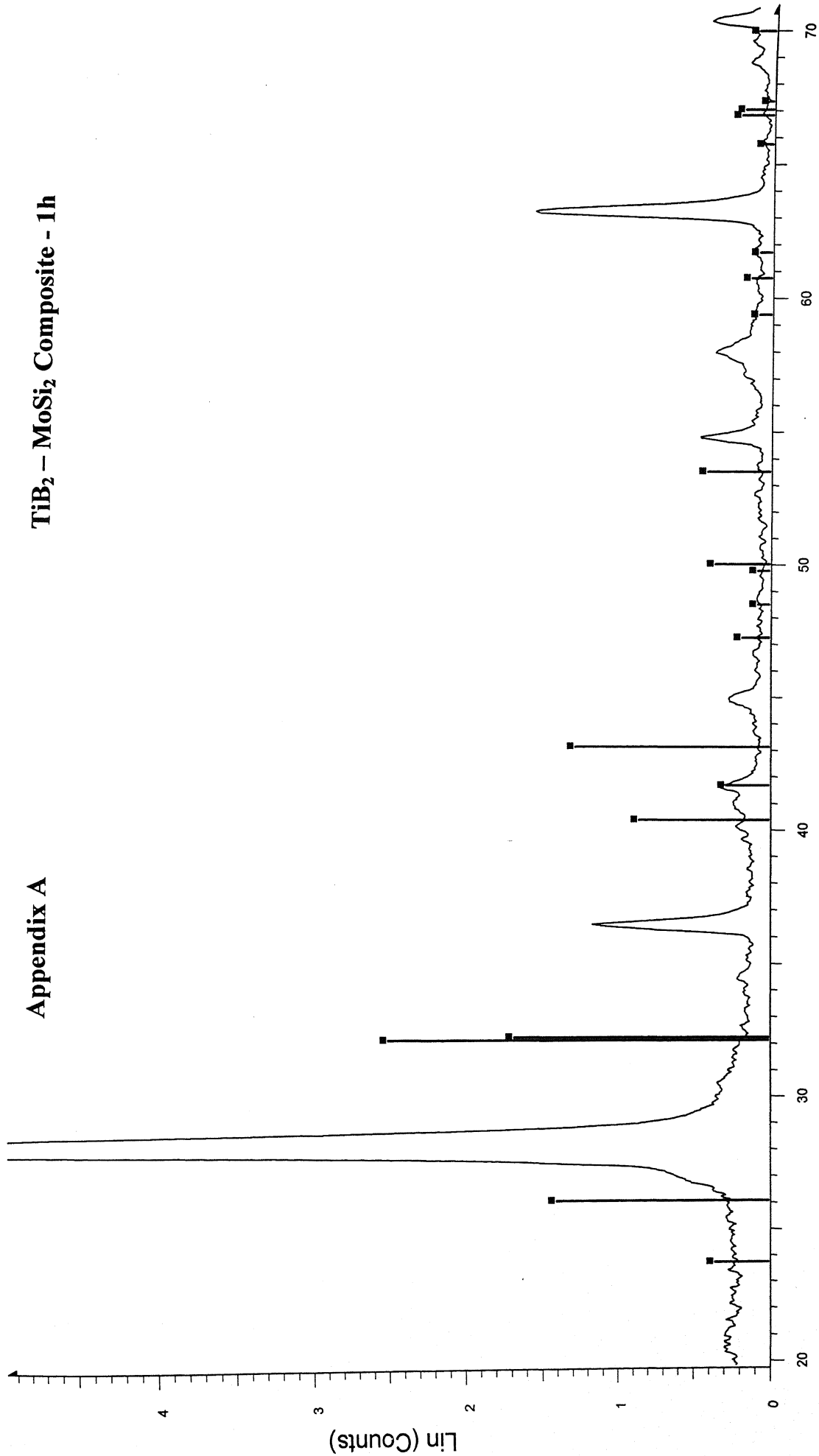
Lin (Counts)

M-5-64h - File: M-5-64h.raw - Type: 2Th/Th locked - Start: 18.570 ° - End: 115.270 ° - Step: 0.050 ° - Step time: 1. s - Temp.: 25 °C (Room) - Time Started: 0 s - 2-Theta: 18.570 ° - Theta: 9.285 ° - Chi:

Operations: Background 1.000,1.000 | Background 1.000,1.000 | Import

21-1276 (*) - Rutile, syn - TiO2 - Y: 50.00 % - d x by: 1. - WL: 1.5406 - Tetragonal - I/Ic PDF 3.4 -
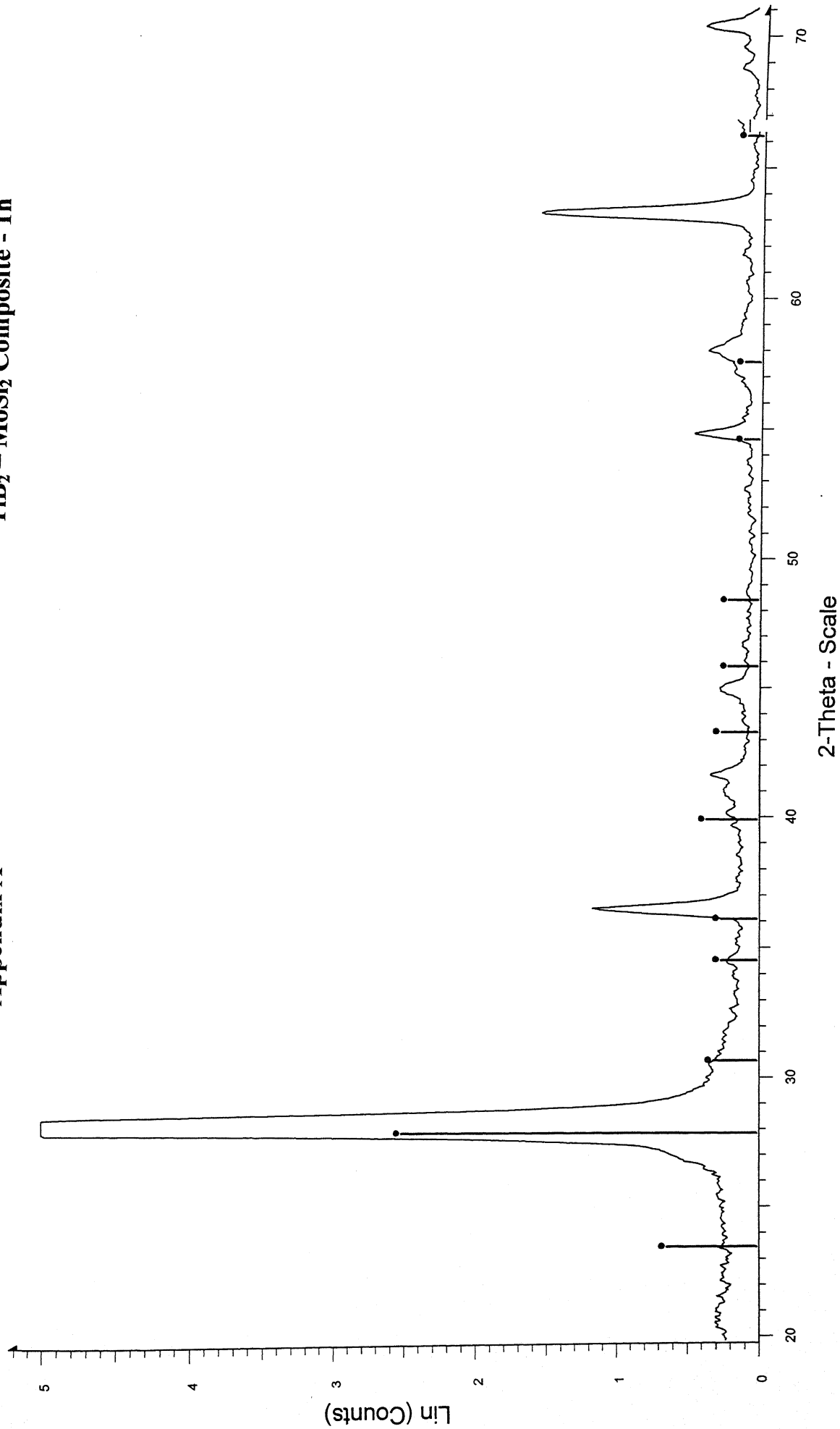
Monolithic TiB$_2$ – 64h

2-Theta - Scale

M-5-64h - File: M-5-64h.raw - Type: 2Th/Th locked - Start: 18.570 ° - End: 115.270 ° - Step: 0.050 ° - Step time: 1. s - Temp.: 25 °C (Room) - Time Started: 0 s - 2-Theta: 18.570 ° - Theta: 9.285 ° - Chi:
Operations: Background 1.000,1.000 | E ickground 1.000,1.000 | Import
73-1550 (C) - Boron Oxide - B2O3 - Y: ⦂).00 % - d x by: 1. - WL: 1.5406 - Hexagonal - I/Ic PDF 0.8 -

Monolithic TiB$_2$ – 64h

2-Theta - Scale

M-5-64h - File: M-5-64h.raw - Type: 2Th/Th locked - Start: 18.570 ° - End: 115.270 ° - Step: 0.050 ° - Step time: 1. s - Temp.: 25 °C (Room) - Time Started: 0 s - 2-Theta: 18.570 ° - Theta: 9.285 ° - Chi:
Operations: Background 1.000,1.000 | Background 1.000,1.000 | Import
13-0570 (D) - Boron Oxide - B2O3 - Y: 50.00 % - d x by: 1. - WL: 1.5406 -

Appendix A

TiB$_2$ – MoSi$_2$ Composite - 1h
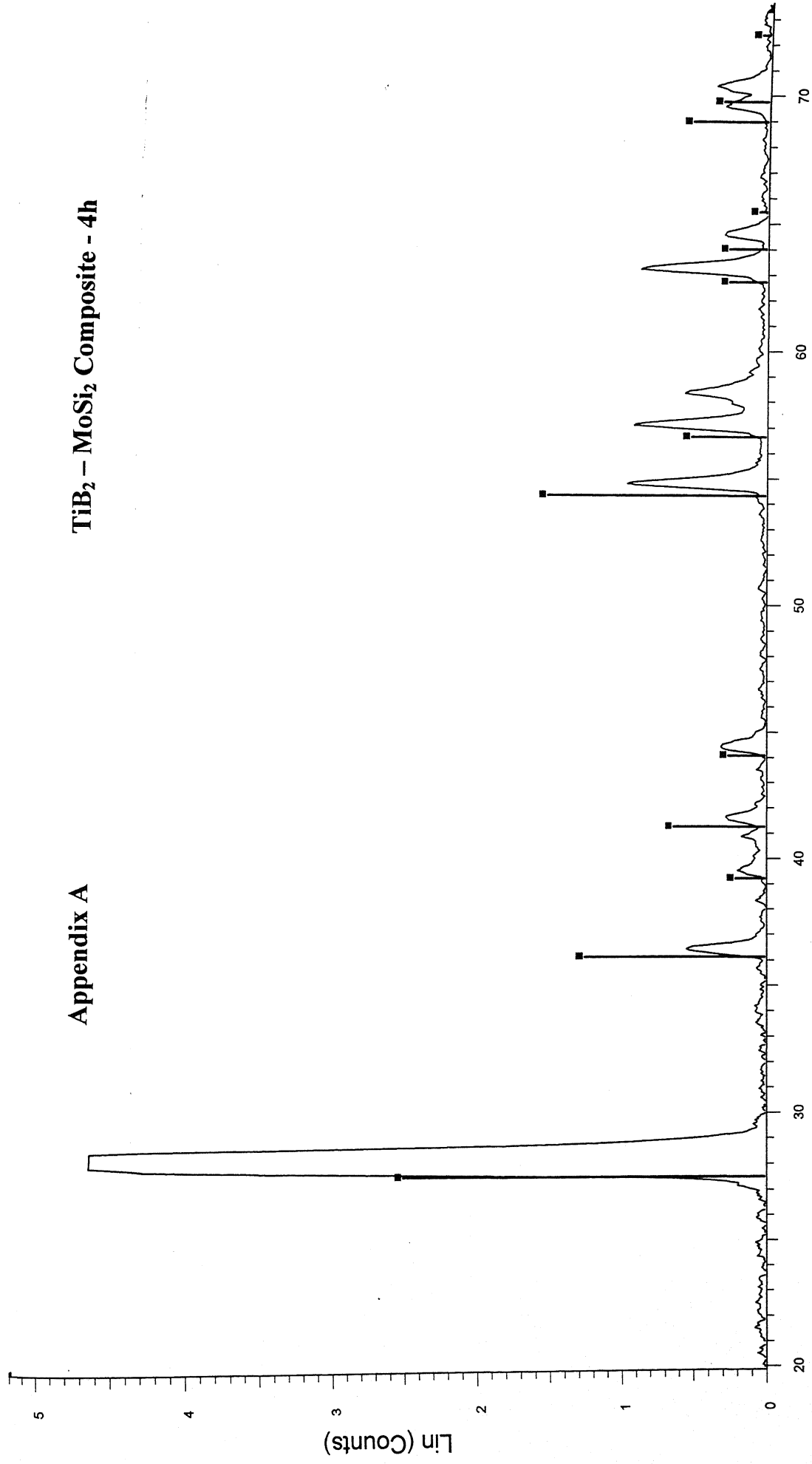

2-Theta - Scale

Lin (Counts)
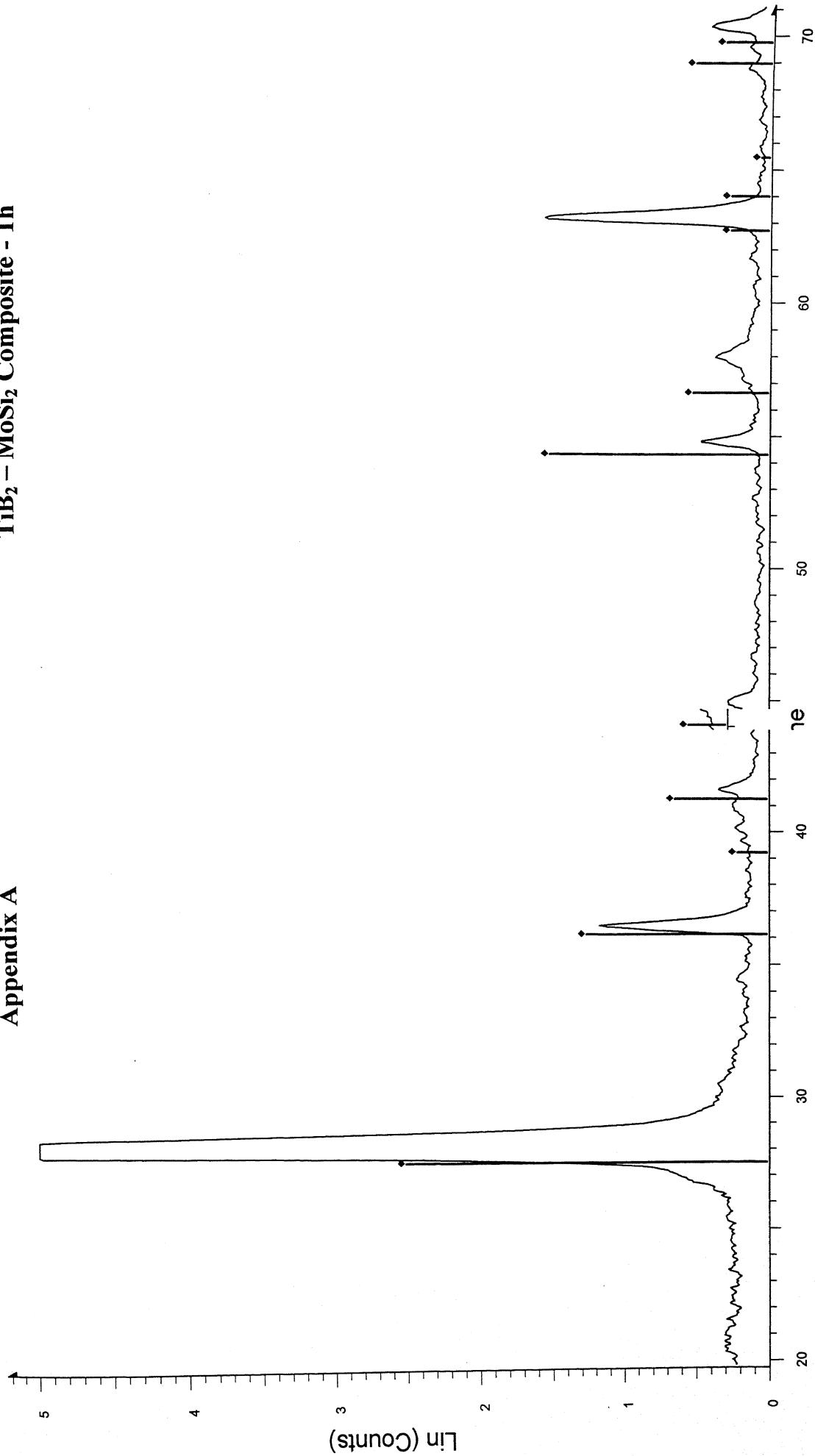
C-7-1h - File: C-7-1h.raw - Type: 2Th/Th locked - Start: 19.780 ° - End: 102.080 ° - Step: 0.0504 ° - Step time: 1. s - Temp.: 25 °C (Room) - Time Started: 0 s - 2-Theta: 19.780 ° - Theta: 9.890 ° - Chi: 0.0
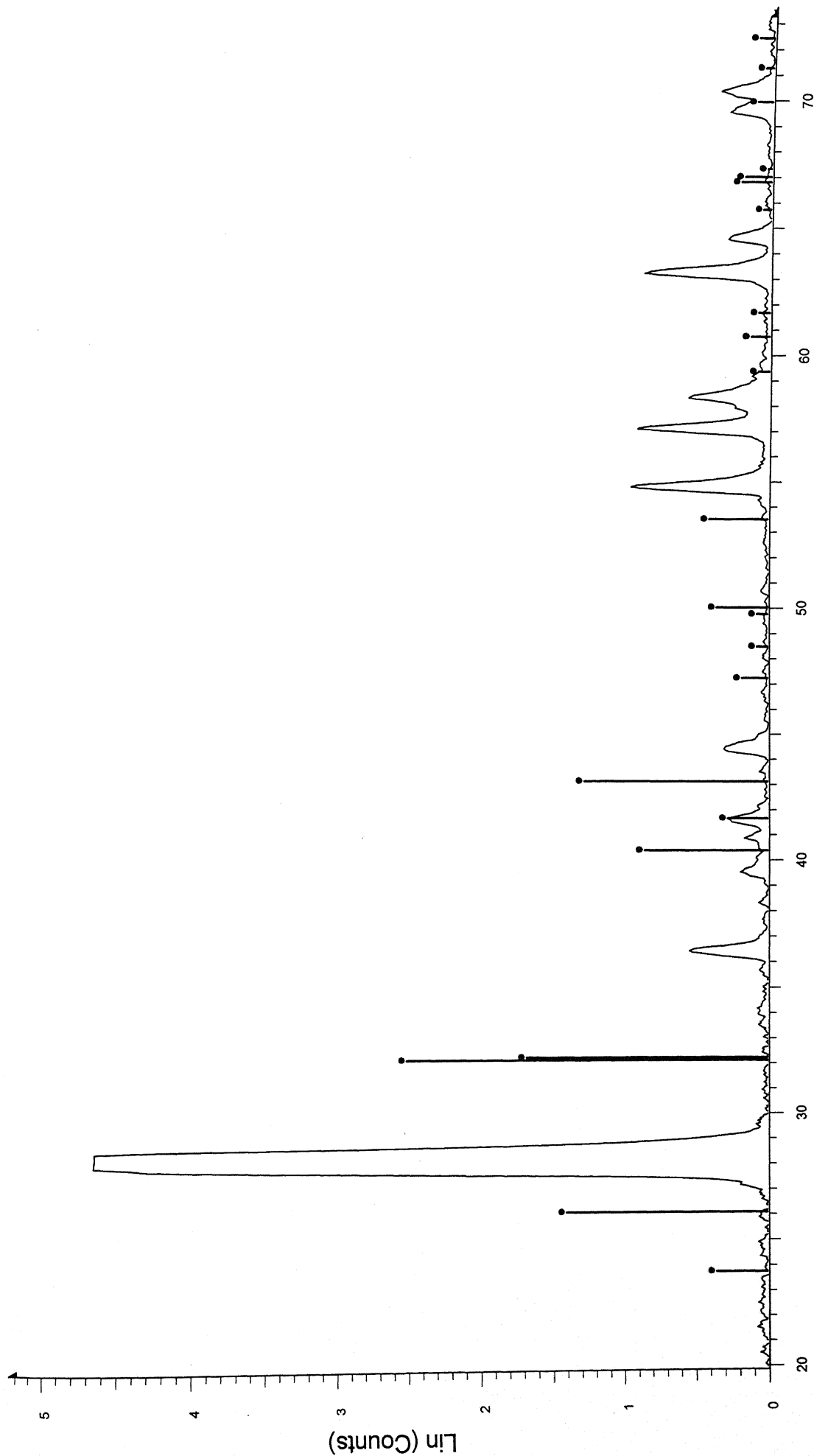
Operations: Import

21-1276 (*) - Rutile, syn - TiO2 - Y: 50.00 % - d x by: 1. - WL: 1.5406 - Tetragonal - I/Ic PDF 3.

Appendix A
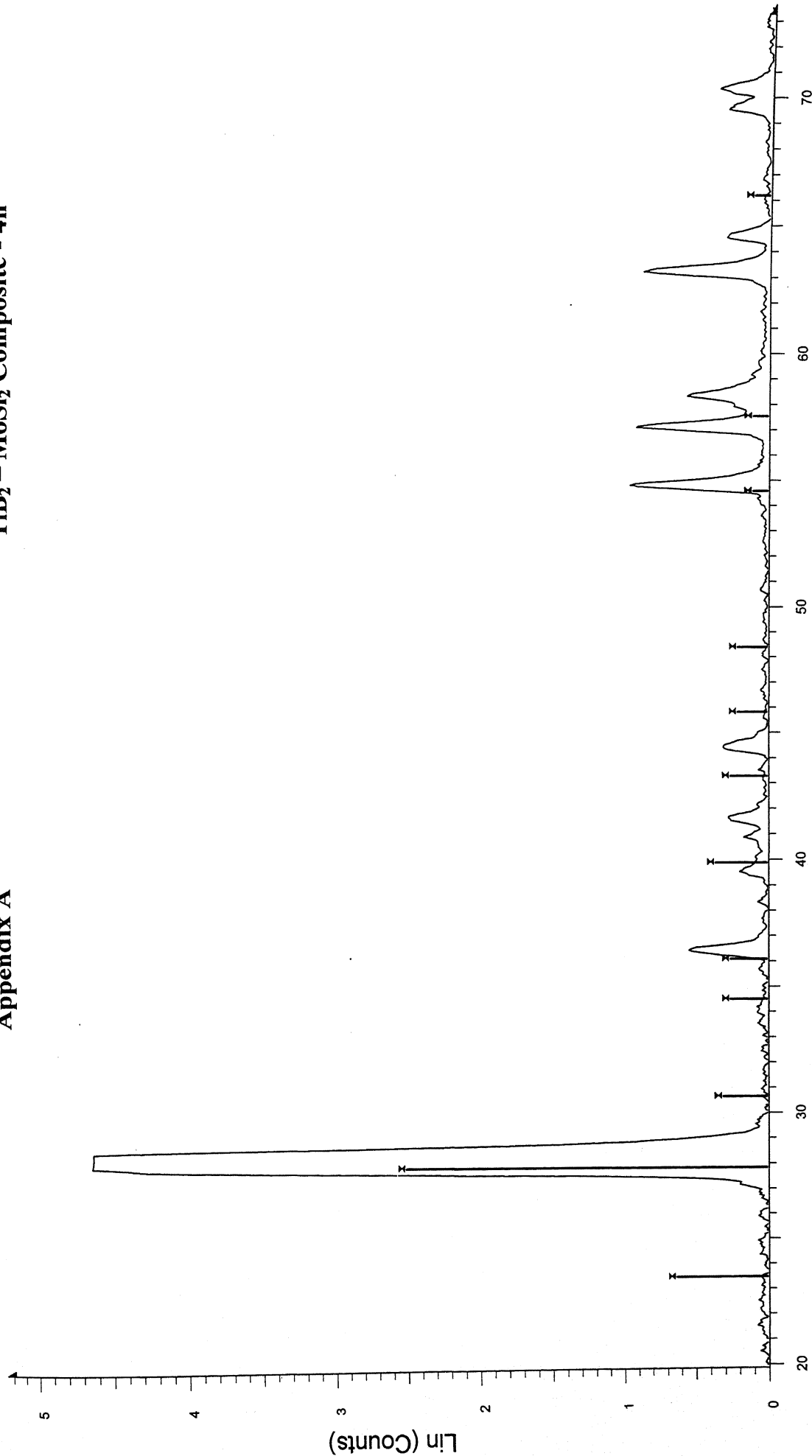
TiB$_2$ – MoSi$_2$ Composite – 1h

2-Theta - Scale

C-7-1h - File: C-7-1h.raw - Type: 2Th/Th locked - Start: 19.780 ° - End: 102.080 ° - Step: 0.050 ° - Step time: 1. s - Temp.: 25 °C (Room) - Time Started: 0 s - 2-Theta: 19.780 ° - Theta: 9.890 ° - Chi: 0.0
Operations: Import
73-1550 (C) - Boron Oxide - B2O3 - Y: 50.00 % - d x by: 1. - WL: 1.5406 - Hexagonal - I/Ic PDF 0.8 -

Appendix A

TiB₂ – MoSi₂ Composite - 1h

⊠C-7-1h - File: C-7-1h.raw - Type: 2Th/Th locked - Start: 19.780 ° - End: 102.080 ° - Step: 0.050 ° - Step time: 1. s - Temp.: 25 °C (Room) - Time Started: 0 s - 2-Theta: 19.780 ° - Theta: 9.880 ° - Chi: 0.0

Operations: Import

⬤13-0570 (D) - Boron Oxide - B2O3 - Y: 50.00 % - d x by: 1. - WL: 1.5406 -

Appendix A

TiB₂ – MoSi₂ Composite - 4h

2-Theta - Scale

Lin (Counts)

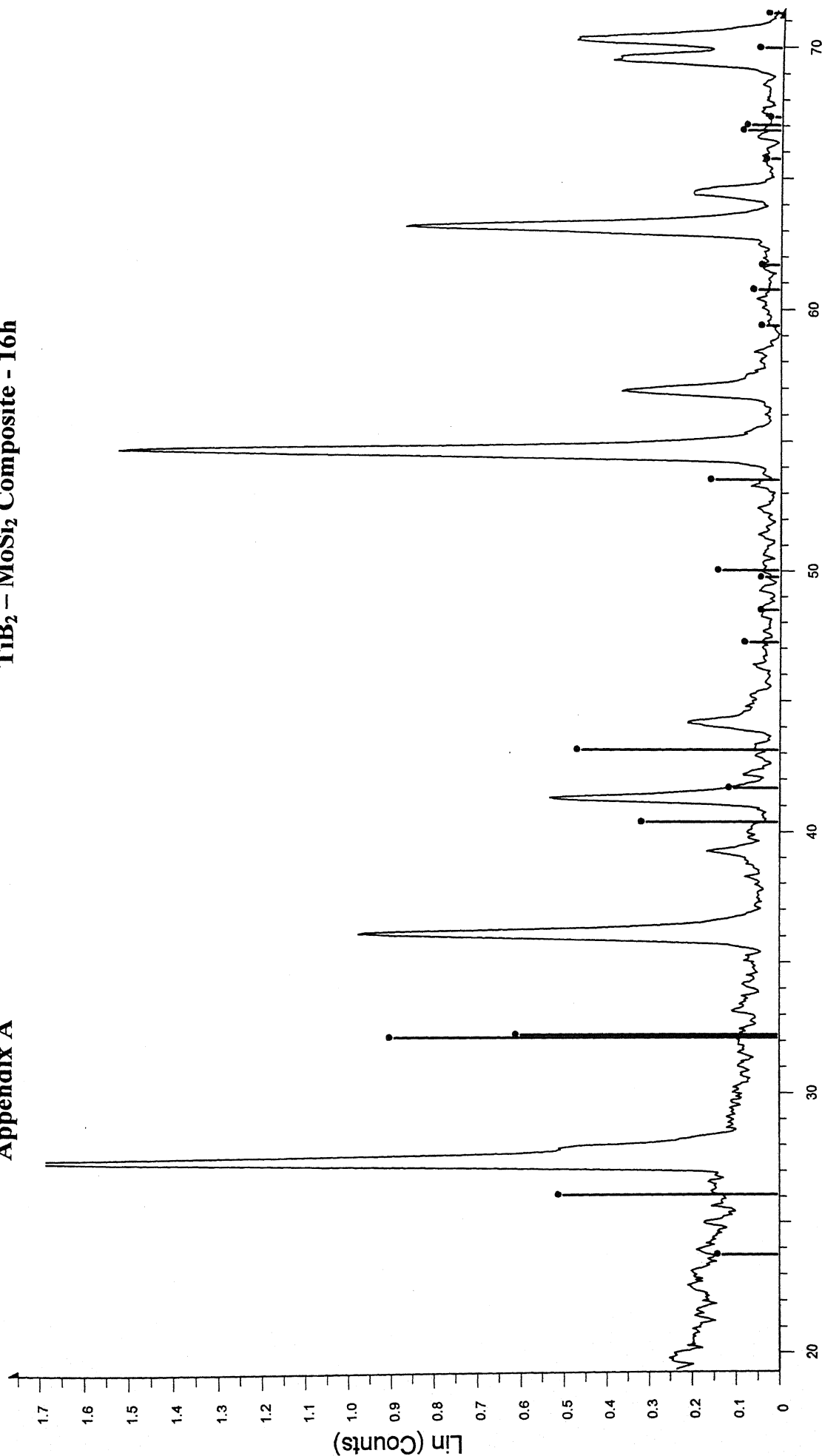⟨⟨⟩⟩C-4h - File: C-4h.raw - Type: 2Th/Th locked - Start: 19.900 ° - End: 101.650 ° - Step: 0.050 ° - Step time: 1. s - Temp.: 25 °C (Room) - Time Started: 0 s - 2-Theta: 19.900 ° - Theta: 9.950 ° - Chi: 0.00 ° -
Operations: Background 1.000,1.000 | Import
■21-1276 (*) - Rutile, syn - TiO2 - Y: 50.00 % - d x by: 1. - WL: 1.5406 - 0 - I/Ic PDF 3.4 -

TiB₂ – MoSi₂ Composite - 4h

2-Theta - Scale

Lin (Counts)

C-4h - File: C-4h.raw - Type: 2Th/Th locked - Start: 19.900 ° - End: 101.650 ° - Step: 0.050 ° - Step time: 1. s - Temp.: 25 °C (Room) - Time Started: 0 s - 2-Theta: 19.900 ° - Theta: 9.950 ° - Chi: 0.00 ° -
Operations: Background 1.000,1.000 | Import
73-1550 (C) - Boron Oxide - B2O3 - Y: 50.00 % - d x by: 1. - WL: 1.5406 - 0 - I/Ic PDF 0.8 -

Appendix A

TiB$_2$ – MoSi$_2$ Composite – 4h

2-Theta - Scale

Lin (Counts)

[X] C-4h - File: C-4h.raw - Type: 2Th/Th locked - Start: 19.900 ° - End: 101.650 ° - Step: 0.050 ° - Step time: 1. s - Temp.: 25 °C (Room) - Time Started: 0 s - 2-Theta: 19.900 ° - Theta: 9.950 ° - Chi: 0.00 ° -
Operations: Background 1.000,1.000 | Import
[X] 13-0570 (D) - Boron Oxide - B2O3 - Y: 50.00 % - d x by: 1. - WL: 1.5406 -
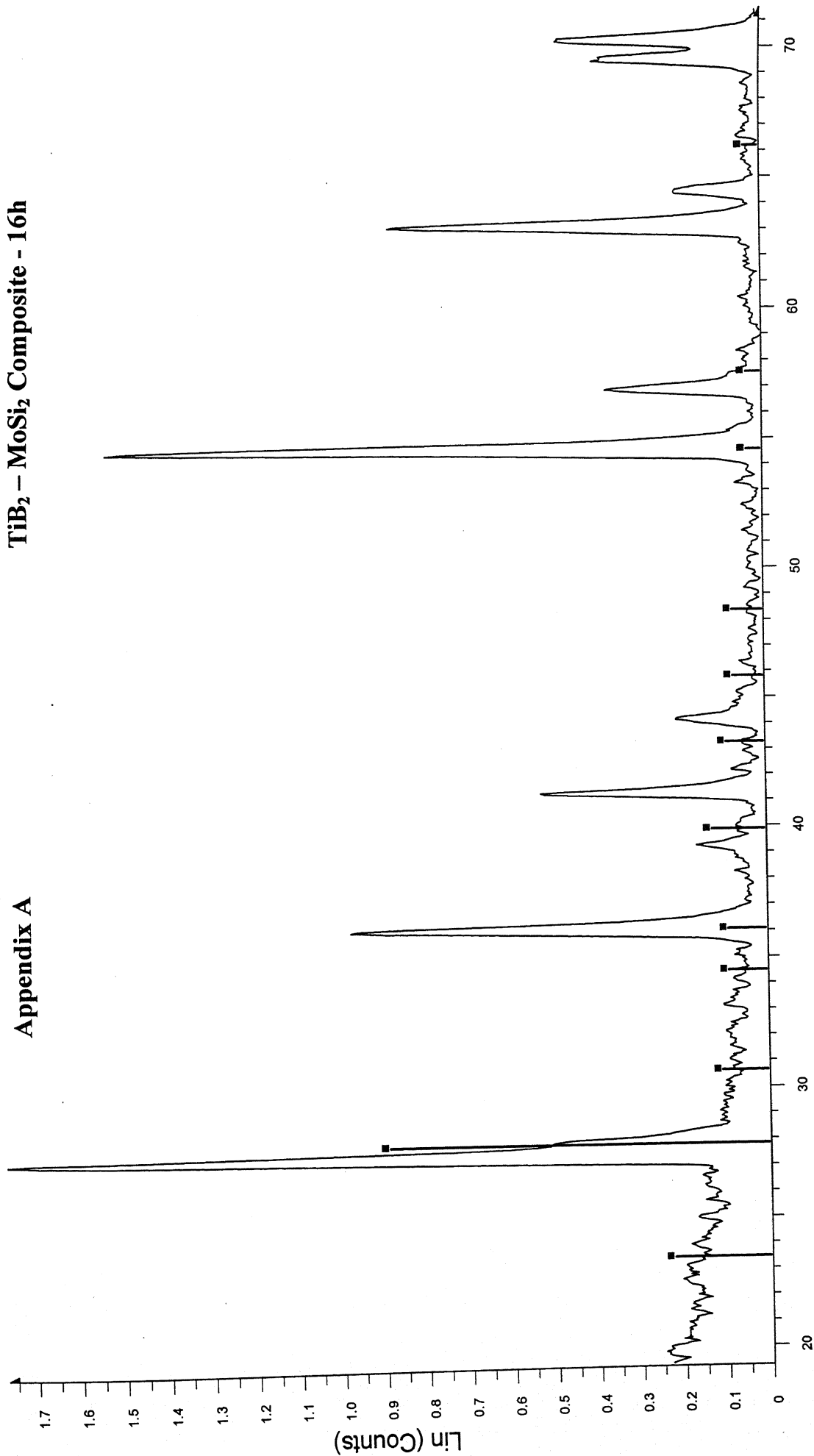
Appendix A

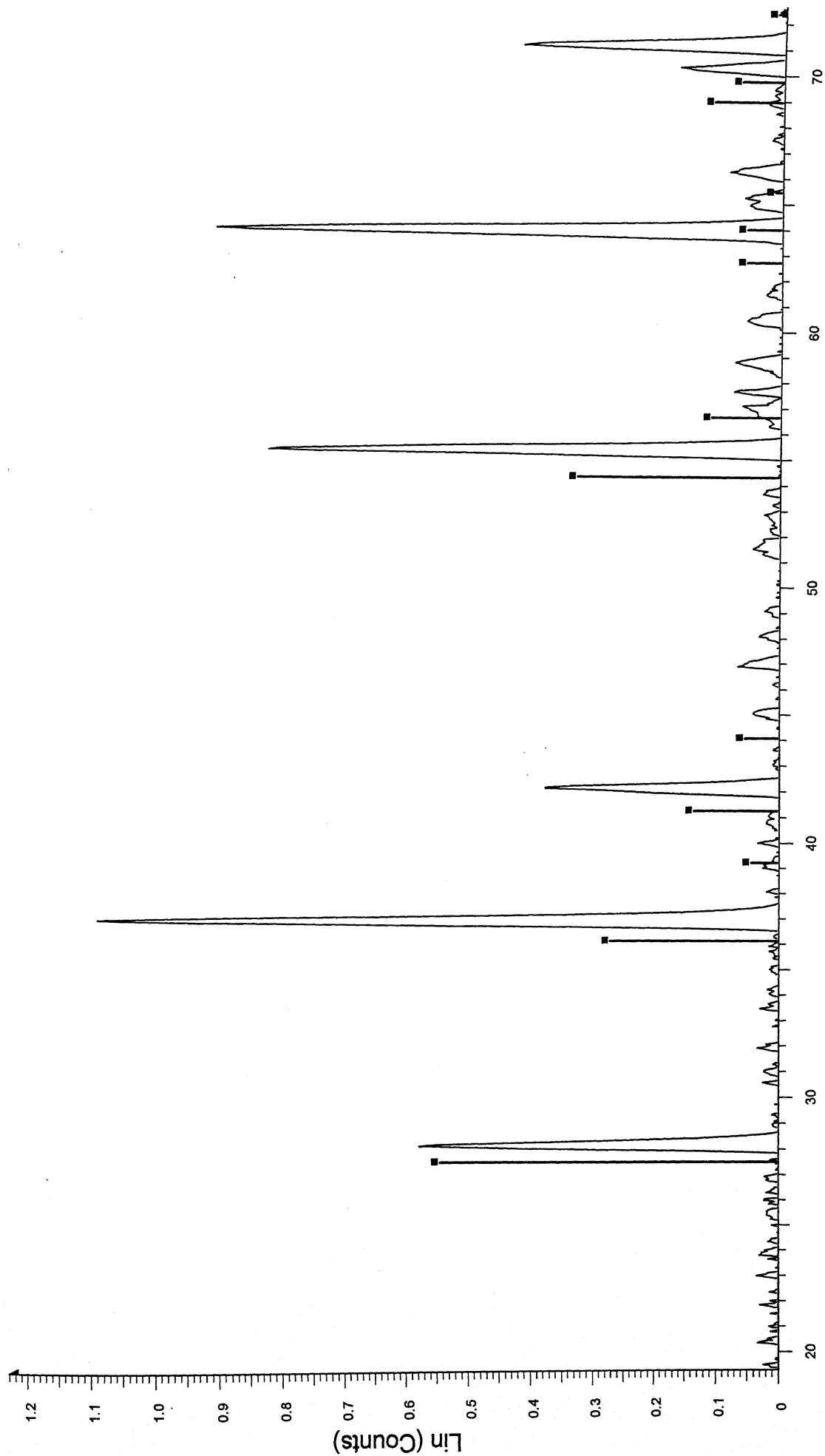## TiB₂ – MoSi₂ Composite - 16h

2-Theta - Scale

[X] C-13-16h - File: C-13-16h.raw - Type: 2Th/Th locked - Start: 19.280 ° - End: 111.030 ° - Step: 0.050 ° - Step time: 1. s - Temp.: 25 °C (Room) - Time Started: 0 s - 2-Theta: 19.280 ° - Theta: 9.640 ° - Chi
Operations: Import
[●] 73-1550 (C) - Boron Oxide - B2O3 - Y: 50.00 % - d x by: 1. - WL: 1.5406 - Hexagonal - I/Ic PDF 0.8 -

Appendix A

TiB$_2$ – MoSi$_2$ Composite - 16h

Lin (Counts)

2-Theta - Scale

Appendix A
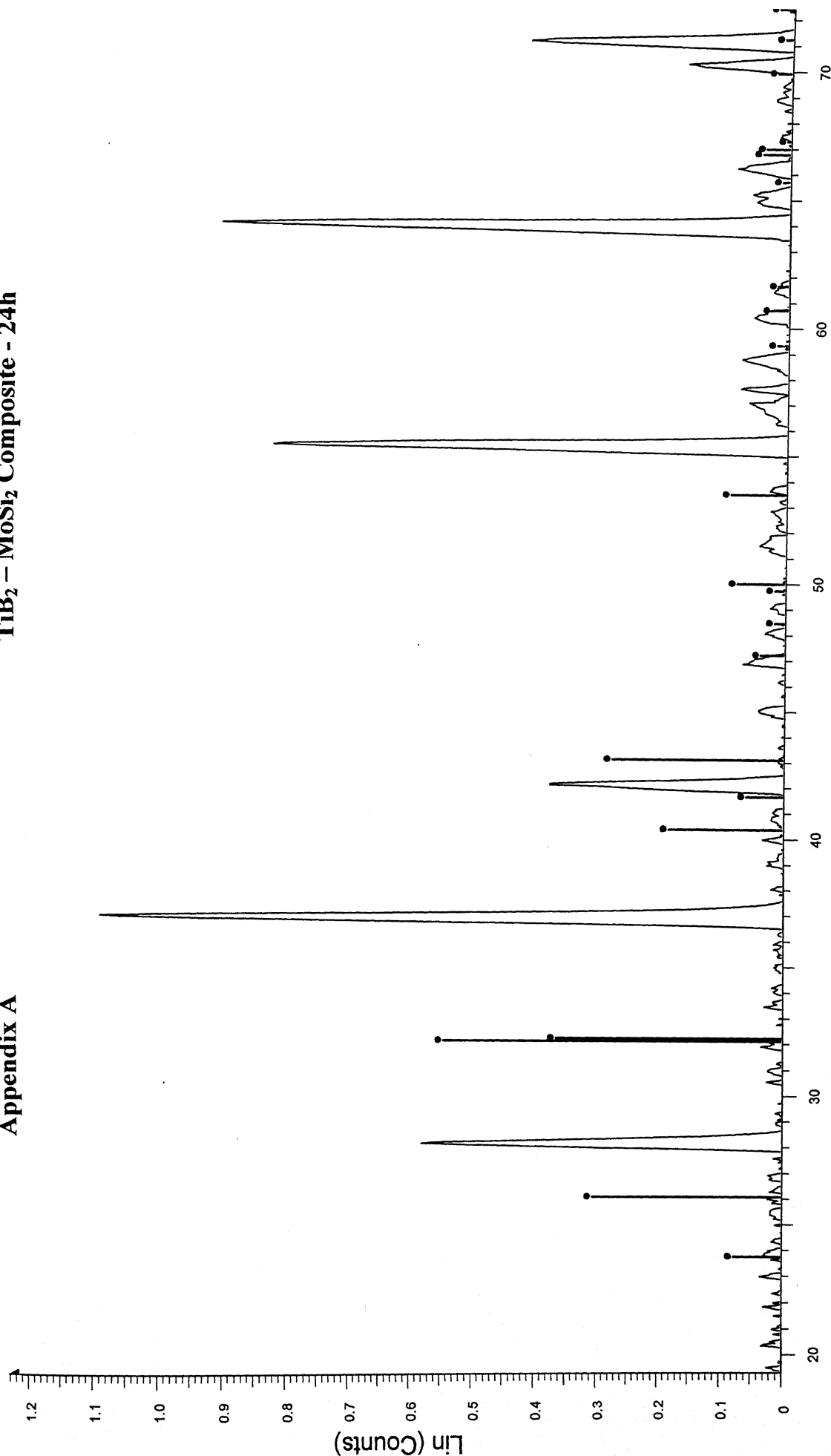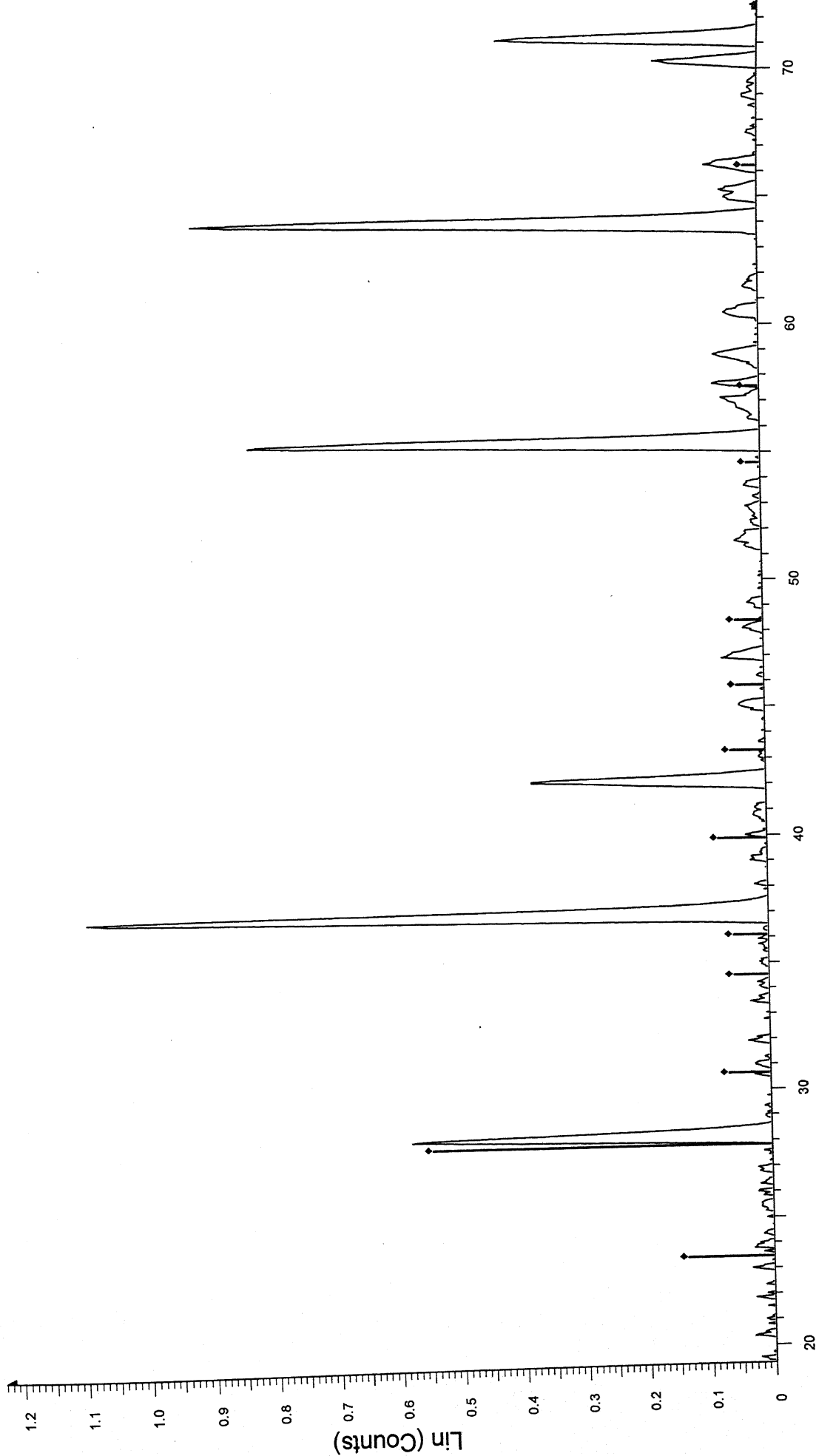
TiO_2 – MoS$_2$ Composite – 24h

2-Theta - Scale

Cn-2-24h - File: Cn-2-24h.raw - Type: 2Th/Th locked - Start: 19.230 ° - End: 102.430 ° - Step: 0.050 ° - Step time: 1. s - Temp.: 25 °C (Room) - Time Started: 0 s - 2-Theta: 19.230 ° - Theta: 9.615 ° - Chi

Operations: Background 1.000,1.000 | Background 1.000,1.000 | Import

21-1276 (*) - Rutile, syn - TiO2 - Y: 50.00 % - d x by: 1. - WL: 1.5406 - Tetragonal - I/Ic PDF 3.4 -

Appendix A

TiB$_2$ – MoSi$_2$ Composite – 24h

2-Theta - Scale

Cn-2-24h - File: Cn-2-24h.raw - Type: 2Th/Th locked - Start: 19.230 ° - End: 102.430 ° - Step: 0.050 ° - Step time: 1. s - Temp.: 25 °C (Room) - Time Started: 0 s - 2-Theta: 19.230 ° - Theta: 9.615 ° - Chi

Operations: Background 1.000,1.000 | Background 1.000,1.000 | Import

73-1550 (C) - Boron Oxide - B2O3 - Y: 50.00 % - d x by: 1. - WL: 1.5406 - Hexagonal - I/Ic PDF 0.8 -

TiB₂ – MoSi₂ Composite – 24h
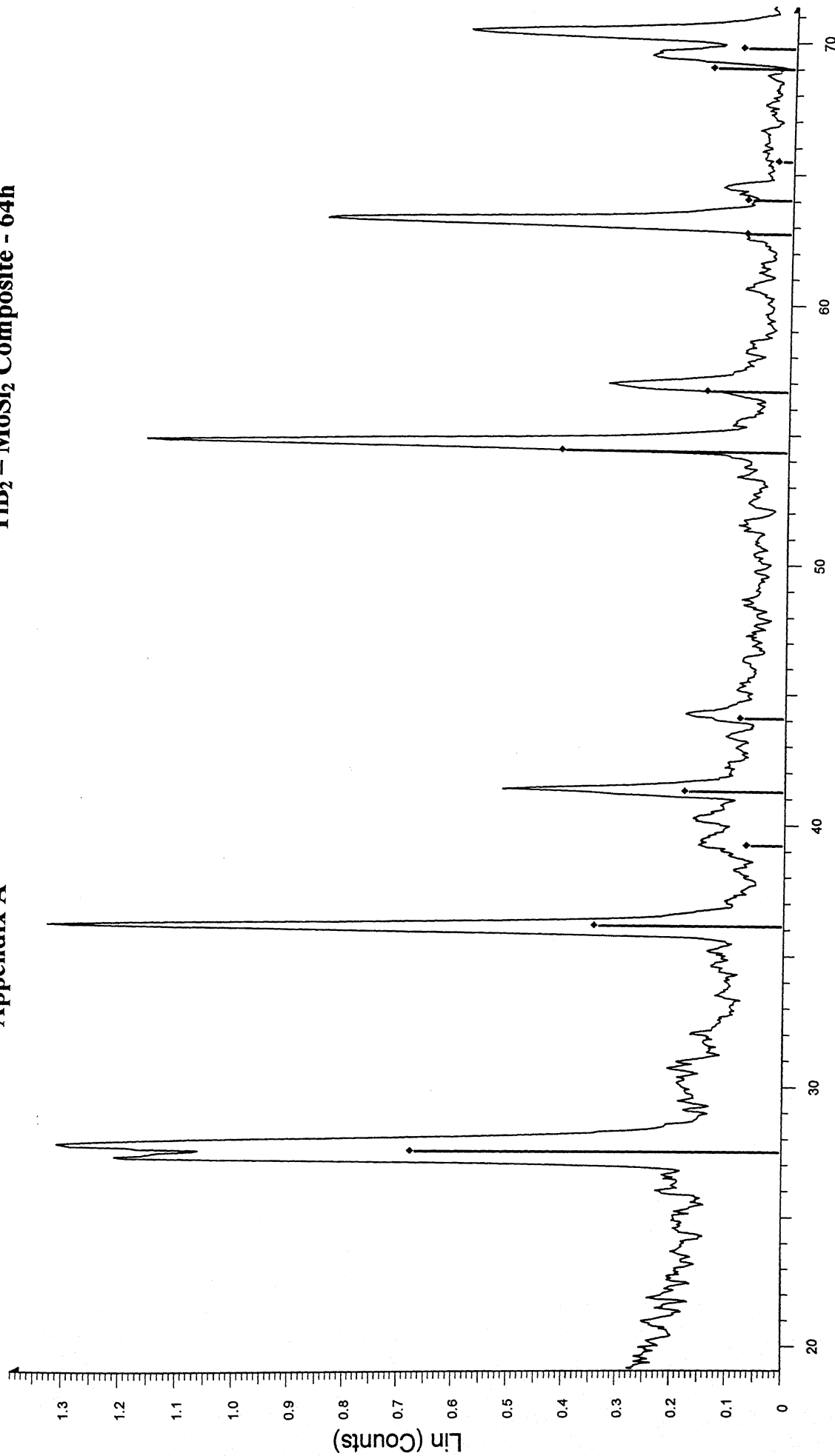

2-Theta - Scale

☒ Cn-2-24h - File: Cn-2-24h.raw - Type: 2Th/Th locked - Start: 19.230 ° - End: 102.430 ° - Step: 0.050 ° - Step time: 1. s - Temp.: 25 °C (Room) - Time Started: 0 s - 2-Theta: 19.230 ° - Theta: 9.615 ° - Chi
Operations: Background 1.000,1.000 | Background 1.000,1.000 | Import
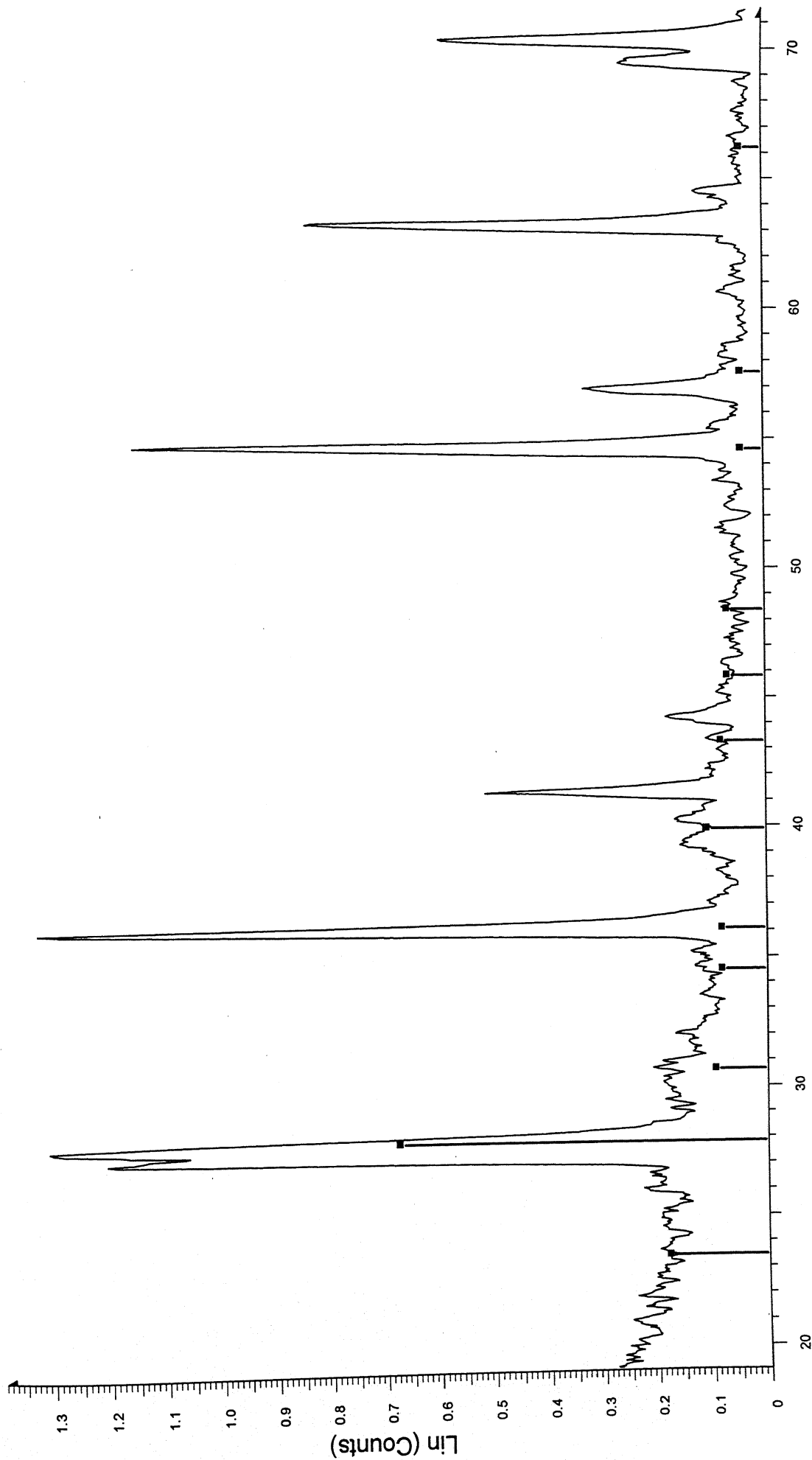◆ 13-0570 (D) - Boron Oxide - B2O3 - Y: 50.00 % - d x by: 1. - WL: 1.5406 -

Appendix A

$TiB_2 - MoSi_2$ Composite - 64h

2-Theta - Scale

ⅧC-1-64h - File: C-1-64h.raw - Type: 2Th/Th locked - Start: 19.020 ° - End: 100.770 ° - Step: 0.050 ° - Step time: 1. s - Temp.: 25 °C (Room) - Time Started: 0 s - 2-Theta: 19.020 ° - Theta: 9.510 ° - Chi: 0

Operations: Import

◆21-1276 (*) - Rutile, syn - TiO2 - Y: 50.00 % - d x by: 1. - WL: 1.5406 - Tetragonal - I/Ic PDF 3.4 -

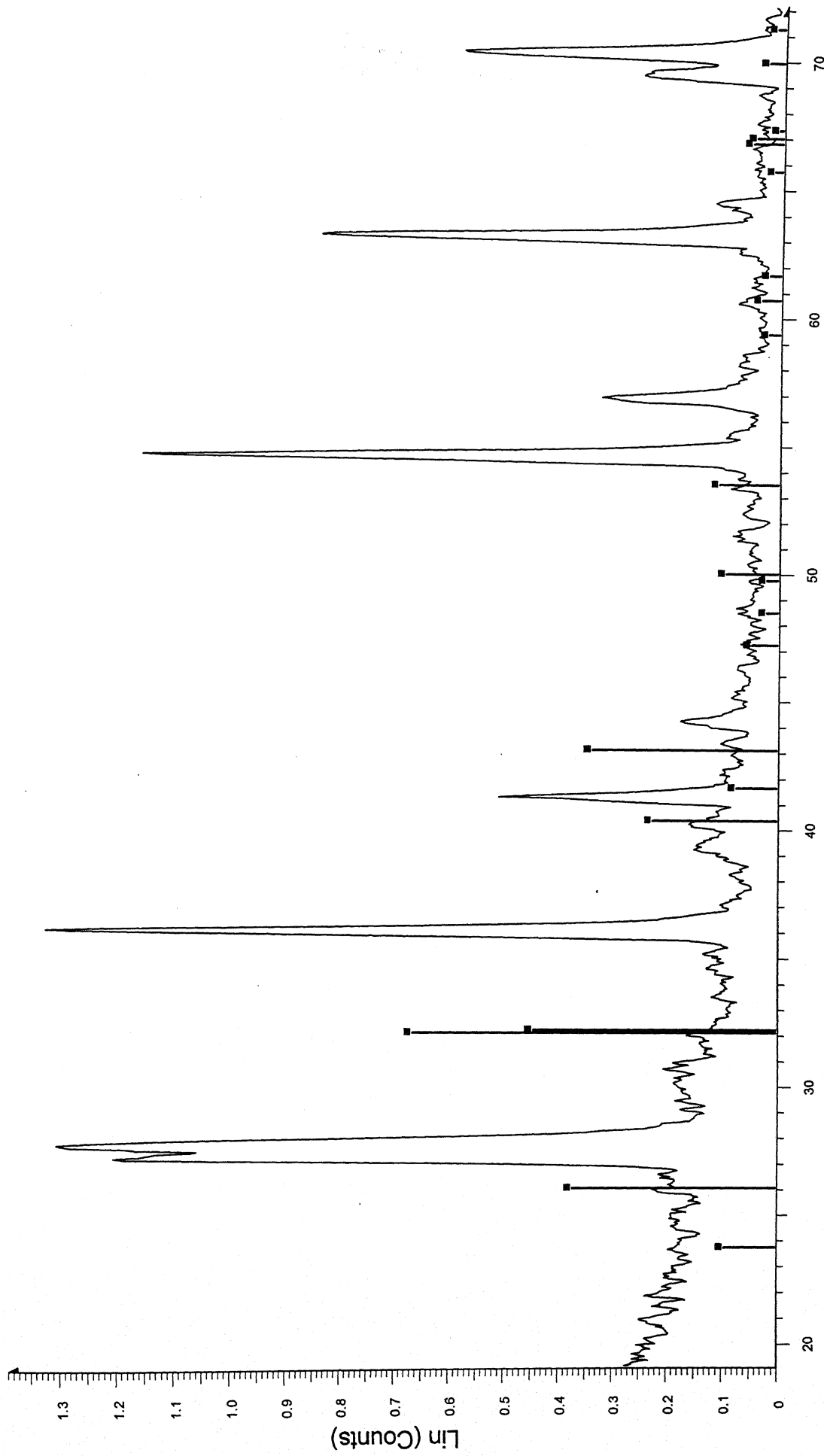# TiB$_2$ – MoSi$_2$ Composite – 64h

2-Theta - Scale

Lin (Counts)

C-1-64h - File: C-1-64h.raw - Type: 2Th/Th locked - Start: 19.020 ° - End: 100.770 ° - Step: 0.050 ° - Step time: 1. s - Temp.: 25 °C (Room) - Time Started: 0 s - 2-Theta: 19.020 ° - Theta: 9.510 ° - Chi: 0
Operations: Import
13-0570 (D) - Boron Oxide - B2O3 - Y: 50.00 % - d x by: 1. - WL: 1.5406 -

Appendix A

TiB$_2$ – MoSi$_2$ Composite - 64h

2-Theta - Scale

Lin (Counts)

C-1-64h - File: C-1-64h.raw - Type: 2Th/Th locked - Start: 19.020 ° - End: 100.770 ° - Step: 0.050 ° - Step time: 1. s - Temp.: 25 °C (Room) - Time Started: 0 s - 2-Theta: 19.020 ° - Theta: 9.510 ° - Chi: 0
Operations: Import
73-1550 (C) - Boron Oxide - B2O3 - Y: 50.00 % - d x by: 1. - WL: 1.5406 - 0 - I/Ic PDF 0.8 -